Solvation Dynamics and Ion Transport in Conventional Solvents and Plasticizers

Marco Masia

Departament de Física i Enginyeria Nuclear

Universitat Politècnica de Catalunya

Barcelona, October 24, 2005

Dissertation of the Doctoral Thesis supervised by Dr. Rossend Rey Oriol

[...] primum Graius homo mortalis tollere contra
est oculos ausus primusque obsistere contra;
quem neque fama deum nec fulmina nec minitanti
murmure compressit caelum, sed eo magis acrem
inritat animi virtutem, effringere ut arta
naturae primus portarum claustra cupiret

Lucretius, De Rerum Natura, Liber I

[...] Un uomo greco per la prima volta osò levare contro di lei (la superstizione)
gli occhi mortali, e per primo resistere contro di lei.
Né le favole intorno agli dèi, né i fulmini, né il cielo
col minaccioso rimbombo lo trattennero: anzi più gli accesero
il fiero valore dell'animo, sì che volle, per primo,
infrangere gli stretti serrami delle porte della natura.

[...] A Greek it was who first opposing dared
Raise mortal eyes that terror to withstand,
Whom nor the fame of Gods nor lightning's stroke
Nor threatening thunder of the ominous sky
Abashed; but rather chafed to angry zest
His dauntless heart to be the first to rend
The crossbars at the gates of Nature old.

Working on this thesis project for the last four years has been a valuable experience. Besides the scientific gain, I will always remember this period for the personal growth. For this reason, and *since it is the only part of the thesis people read with real interest (!!)*, before entering into technical details, I would like to dedicate some words to the people who made a simple scientific experience, special.

Prima di tutto vorrei dedicare questa a tesi a Chicca, con la quale ho condiviso quattro anni meravigliosi e intensi. É lei che mi ha spinto nelle decisioni piú coraggiose e che mi ha dato la forza di portarle avanti. Ma sopratutto é lei che ha reso felici (e divertenti!) tutti i momenti passati insieme.

Un pensiero speciale va a mia madre, mio padre, Carletto e Paoletto che, nella lontananza, ho sentito sempre vicini. Ricordo con particolare gioia i miei soggiorni a casa durante le vacanze e le chiaccherate al telefono con tutti loro.

A mia nonna, la mia piú grande tifosa!

A Mario, Titina e Silvia, che mi hanno sopportato con tanta pazienza nelle mie incursioni estive a casa loro.

Un homenaje especial a mi tutor de tesis, Rossend, con el cual he tenido charlas muy interesantes y divertidas sobre los temas más diversos. Con él he aprendido a ser más riguroso en la investigación, más profundo en la interpretación de los resultados y más cuidadoso en la composición de un texto (¡aunque espero no volver nunca a tener 13 versiones de un artículo antes de enviarlo!).

Sorry Michael, but the only words I know in German are *weissenbier* and *prost* (which has a suspicious similarity with your surname!)...so I use English to thank you for the time you spent with me in Innsbruck, at the University, at the bar, at the restaurants and at the sky resort, and for having introduced me in the field of quantum chemical calculations.

I would also like to thank the people involved in the European project which financed part of my thesis: Kersti (thanks to her I could partecipate to this project), Klaus, Casey, Jan, Rudi, Barbara (with whom we had a very good

time in Innsbruck), Wiktor, Sami, Ewa, Daniel and Bruno.

Una dedicatoria a parte va a mis colegas de despacho: Claudi que ha sido la primera persona con la que he salido de marcha en Barcelona y que me ha entrenado para las "curses dels bombers" todos estos años; Ester (sense "h") amb la que he tingut xerrades molt llargues sobre temes diversos i que han fet els dies més amens; ese $\mu\alpha\lambda\alpha\kappa\alpha$ de Kostas, que me ha provocado muchos dolores de cabeza con su lógica loca!

¿Y cómo podría olvidar a los amigos del departamento, con los cuales he compartido más de una comida y de una cerveza? En orden alfabético (¡para no ofender a nadie!): Agustí (¡el hombre más rápido en comer mejillones!), Alfredo (el informático más deportista del mundo), Michele (cioé quello cioé voglio dí, proprio con mille interessi!), Óscar (el chico más polifacético que conozco), Núria (¿y quién olvida sus bizcochos?), Rubén (que me ha introducido a los misterios del "rol"), Pere (otro que me ha provocado muchos dolores de cabeza con sus razonamientos imposibles), Toni (y su sentido del humor) y Vicente (el *zaborrero* medio maño).

Quiero agradecer la paciencia y la disponibildad de Ana, Cristina, Montse y Sílvia por el tiempo que me han dedicado, por las charlas sobre comidas, viajes y vacaciones y por las recetas que me pasaron!

Finalmente quiero agradecer a los amigos de aquí (*e gli amici che stanno in italia o fuori*), especialmente el peregrino llorón (Miguel), Teresa, Alessandra, Giancarlo, Mario, Majo, Luca, Sandra, Marc, Giuseppe M., Matteo, Paolo, Giuseppe L., Francesco y todos los que he olvidado porqué se me ha ido la olla después de haberla exprimido para escribir esta *magnífica obra literaria y científica*!

Barcelona: October 24, 2005

Marco Masia

Contents

Part I

Introduction

Chapter 1

Introduction

Arrhenius is known to have considered the chemistry of 19^{th} century as "liquid state chemistry". Although modern chemistry does not deal solely with solution chemistry, the Arrhenius' statement is still valid more then 100 years later. Nearly 95% of all published chemical reactions proceed in solution. The development of organic, inorganic and physical chemistry, as well as electrochemistry, is closely associated with investigations on solution chemistry. A determining role in the entire variety of chemical and physico-chemical properties of solutions and the processes which proceed in them is played by *solvation*. In particular, *ion solvation* is a topic which has been thoroughly studied both experimentally and theoretically for a long time. It is known that the behaviour of molecules in salty solutions can be dramatically altered by the type and concentration of the salt; moreover charged species play an important role in many chemical (and biochemical) reactions [1–3]. In biochemistry the presence of ions is critical to the structure and function of nucleic acids, enzymes and proteins [4]; the manner in which water solvates alkali cations is relevant to problems such as the mechanism of enzymatic catalysis and the structural stability of DNA and RNA. Furthermore ion hydration dynamics plays an important role in the selectivity and the mechanism of ion channels in the cell membranes. Ion solvation and transport

is also fundamental for areas of great technological interest, such as surfactants, colloids and polyelectrolytes. Among these, solvated ions play a key role in electrochemical applications, where ion-solvents interactions affect ion mobility and conductivity, it suffices to mention the well known Lithium Ion Batteries, used in mobile phones, digital cameras and laptops [5].

Until quite recently, theoretical descriptions of ion-solvent dynamics were relatively heterogeneous. The main reason is that the ion-solvent interaction has both short- and long-range character. A proper treatment of solvent structure in the vicinity of an ion should incorporate detailed short range interactions; indeed accurate equilibrium theories of this structure have only recently evolved. Also, collective effects should play an important role but in this case the electrostatic interactions are quite strong, and the question of how long range electrical forces influence the collective motion of solvent molecules is difficult to address. Continuum theories have been proposed since Born (1920) but a proper theory needs a microscopic description of the system. The solvation of ions in solution involves ion-molecular, ion-ion and intermolecular interactions, which are related to the chemical nature of the species. The ability of faithfully reproducing these interactions is central to the understanding of solvation processes from the atomistic point of view.

For the experimental study of ion solvation various methods are used, such as X-ray and Neutron Diffraction, Nuclear Magnetic Resonance, Infra Red and Raman Spectroscopy, Dielectric Relaxation. The experimental measurements often yield an incomplete description of ionic solvation, due to, e.g., the lack of suitable isotope substitutions in neutron diffraction experiments, or difficulties in separating the atomic correlations of different species or incompatibility among the instrument and the observed phenomenon time scales.

In recent years, computer calculations have emerged as a successful complement to experimental techniques and to the theoretical approach, leading to a greater understanding of the solvation process. They allow to study the microscopic nature of the phenomenon with realistic models, that allow to go beyond the results obtained with a pure analytic description. Furthermore they permit to pursue a detailed interpretation of the experiment. The three most important computational techniques are Monte Carlo, Molecular Dynamics and Quantum Chemical calculations. In this thesis issues regarding ion solvation are studied using the last two approaches.

1.1 A European Project

The research work presented in this thesis has been developed within the framework of the European Research Training Network on *Solvation Dynamics and Ionic Mobility in Conventional Solvents and Plasticizers - by Computational Chemistry and Experiment*. The overall goal of this Network (which involves the collaboration between six European research groups) was to seek firm knowledge about the mechanisms of the dynamical processes present, and their relative importance. The primary scientific aims were:

1. to discover unifying and differentiating features in ligand and solvent exchange processes around metal ions in conventional and polymer solvents;

2. to study the connection between the solvation dynamics and the ionic diffusion/conduction mechanism in these systems;

3. to help in the search for new applied polymeric systems by providing a more detailed understanding of the basic phenomena occurring in model electrolytes

In this thesis this endeavour is approached from the microscopic point of view, making use of computer simulations and calculations. The way solvent molecules interact with the ion, and how this interaction affects the physicochemical properties of the system is looked into. The contributions of the present work to the Network objectives listed above can be divided into three main topics which constitute the backbone of this thesis:

Solvation and Ionic Mobility: the exchange processes between first and second hydration shells of cations are studied; the interplay between diffusion and the exchange mechanism is addressed, together with rotational and transport dynamics of first shell molecules.

Plasticizers: *ad hoc* intra- and inter-molecular force fields are developed for two plasticizers* used in Lithium Ion Batteries: ethylene carbonate (EC) and γ-butyrolactone (GBL). Structural and dynamical (diffusional and vibrational motion) properties of the solvent and of the ion are studied.

*Small, often volatile solvents added to plastics to make them softer.

Polarization: to improve the modeling of intermolecular interactions in computer simulations, the inclusion of polarization effects seems fundamental. The performance of the most commonly used polarization methods is studied for chosen model systems, using ab initio calculations as benchmark.

The outline of this thesis is as follows: the present Part I is dedicated to introduce the main topics studied (chapter 1), and to give a brief introduction of the computational methods used (chapter 2). Parts II, III and IV contain the results and discussion of specific studies, respectively on *Solvation and Ionic Mobility*, *Plasticizers* and *Polarization*. Finally, concluding remarks are given in Part V.

We now proceed to a more detailed exposition of the issues involved in the three topics addressed in this thesis.

1.2 Solvation and Ionic Mobility

Besides the theory of electrical conductivity in solutions, one aspect that has always fascinated physical chemists is the simplest ligand substitution reaction known as *solvent exchange reaction*:

$$[\mathrm{IL}_n]^z + n\mathrm{L}^* \overset{\text{exchange}}{\longleftrightarrow} [\mathrm{IL}_{(n-1)}\mathrm{L}^*]^z + (n-1)\mathrm{L}^* + \mathrm{L} \tag{1.1}$$

where I is the ion of charge z and L is the ligand. The first solvation shell is formed by the n molecules, first neighbours to the ion (where n is called the solvation number). The replacement of a solvent molecule from the first solvation shell, is an important step in complex formation reactions of metal cations (I=M and $z > 0$) and in many redox processes. In exchange reactions the reactant and the product are identical and the Gibbs energy change is zero. The exchange process can take place according to different mechanisms, the following two being the limiting cases [6]:

Associative: the ligand L^* enters the first solvation shell and then L leaves it.

Dissociative: L leaves the first solvation shell and then L^* enters it.

Knowing and understanding the exchange mechanism is of great importance since it affects the kinetics and stereochemistry of chemical reactions on the ion center.

For obvious reasons, water represents the most studied ligand. The chemistry of aqua ions has been the subject of recent books and reviews [6–10]. Determination of ionic hydration numbers, mechanisms and rates of exchange of coordinated

water molecules and interaction energies between ions and water has constituted a goal since Arrhenius.

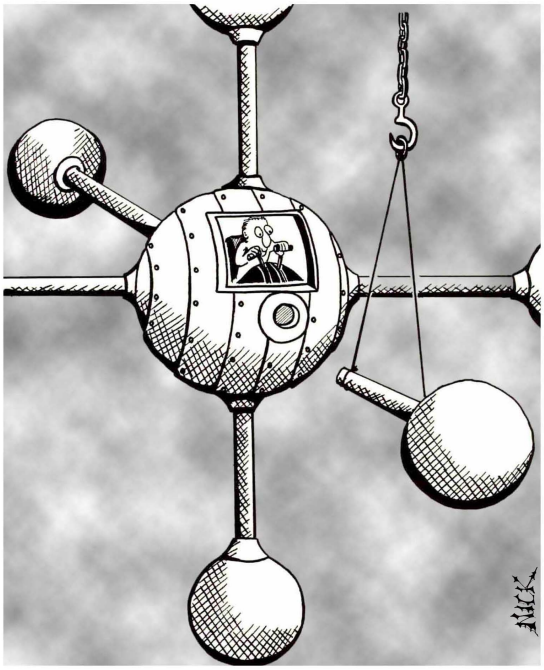

The mysterious world of ligand substitution.

Figure 1.1. The chemist's concern for the ligand exchange process.

The observed exchange rates cover more than 18 orders of magnitude [9]. The most inert (slow exchanges) are trivalent transition metal ions, while the most labile (fast exchanges) are alkali, alkaline earth and halide ions. Experimentally, exchange constants are determined mainly from nuclear magnetic resonance measurements [11]. For labile complexes this information is not experimentally accesible and other techniques are required. Recently, it has been shown that specific information on solvation shells can be obtained by vibrationally exciting and detecting a solvation shell probe molecule using ultrafast infrared nonlinear spectroscopy [12–15]. A disadvantage of this technique is that it probes the solvating water molecules indirectly, but it has been found that it provides information on the time scale on which solvation shell exchange takes place [16].

Molecular Dynamics simulation can provide a deeper insight on the structure and dynamics of aqueous solvation shells [17–20]. For example, while the solvation free energy for a salt can be measured, it is impossible to separate by experiment cation and anion contributions. In contrast, with computer simulations it is straightforward to directly simulate a single cation or anion in any solvent. Moreover the microscopic nature of the exchange reaction can be understood by following the trajectories of the MD simulation.

The majority of earlier simulation studies on ion solvation primarily concerned the structure and thermodynamics [21–47]. Theoretical aspects of ion solvation dynamics have been studied in Refs. [48–59]. Some studies were also concerned with first shell dynamics [60–78], most of them focused on residence times and exchange rates for systems characterized by fast exchanges. Rey and Hynes [66, 67] introduced the use of the reactive flux method for the study of the exchange

process, which allows to study slow exchanges. Finally some investigations examined the detailed mechanism, or the effect of ion solvation on hydrogen bond dynamics [79–82].

Part II of this thesis is devoted to the study of solvent exchange around ions. In particular the following three questions have been posed:

1. *how do the static and dynamical properties of water exchange around an ion vary with the change of thermodynamical conditions?* One could expect that, varying the density and/or the temperature of the system, different behaviours might be found. On the contrary the activated process shows similar features for a large variety of thermodynamic conditions, spanning from liquid to supercritical conditions, for Li^+ in water [Masia et al. *J. Phys. Chem. B* **107**, 2651 (2003)].

2. *what is the relation between the diffusion coefficient of the ion and that of first shell molecules?* For tightly bound ion-shell systems, they should be identical since the complex diffuses as a unit. Contrary to this expectation, this equality is not found in computer simulations for cases where it is manifest that no exchanges have taken place during the calculation. This apparent inconsinstency is explained as an artifact due to the insufficient length of the simulations [Masia at al. *J. Chem. Phys.* **122**, 094502 (2005)].

3. *is there any connection between solvent shell exchange and ion mobility?* Given the different time scales over which the two phenomena occur, the extent of the coupling between both processes is unclear. Nevertheless, it will be shown that the interplay is two-fold: *(i)* the onset of solvation exchange *mechanism* is affected by ion diffusion and *(ii)* ionic diffusion is enhanced by the disruption of local solvent structure that takes place during exchanges [Møller et al. *J. Chem. Phys.* **122**, 114508 (2005)].

1.3 Plasticizers

Battery technology has achieved spectacular progress in recent years [83] (see figure 1.2). A most successful product is the rechargeable Lithium Ion Battery (LIB), which has reached an established commercial status with a production rate of several millions of units per month. The technology of LIBs is still in progress and important steps forward have been achieved in the development of

battery systems using lithium metal as the anode. Currently, the lithium salt electrolyte is not held in an organic solvent like in the past models, but in a solid polymer gel electrolyte [84–91] such as polyacrylonitrile, polyvinylidene fluoride, polyethilene oxide etc. There are many advantages of this design, for instance, the solid polymer electrolyte is not flammable, like the organic solvent that the Li-Ion cell uses. Thus these batteries are less hazardous if mistreated [92].

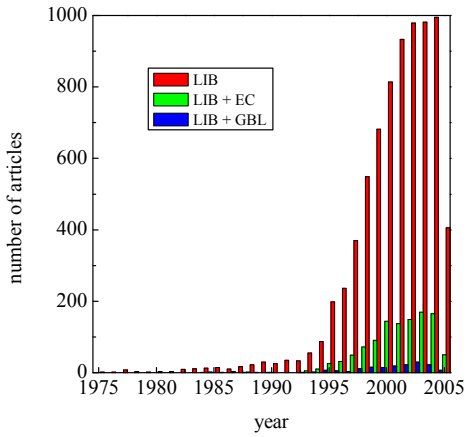

Figure 1.2. Number of articles per year on LIBs up to may 2005; EC and GBL are the plasticizers studied in this thesis (source: SCIFINDER Scholar [93]).

The vast majority of the electrolytes are electrolytic solution-types that consist of salts (also called "electrolyte solutes") dissolved in solvents (also called *plasticizers*), either water (aqueous) or organic molecules (nonaqueous), and remain in the liquid state within the service-temperature range. The most used solvents are ethylene carbonate, tetrahydrofuran, propylene carbonate, and γ-butyrolactone [94].

The electrolyte is in close interaction with both electrodes and serves as a medium of transport for the ions involved in the charge/discharge cycle [95]. Conceptually, it should undergo no net chemical changes during the operation of the battery, and all Faradaic processes are expected to occur within the electrodes. Therefore, in an oversimplified description, the electrolyte could be viewed as the inert component in the battery, and it should demonstrate stability against both cathode and anode surfaces. Experimentally it has been found that a mixture of two or more plasticizers is more convenient, as it allows to optimize the balance between different features (such as dielectric constant, viscosity, ionic diffusion, salt dissociation, and chemical stability) and thus to enhance the battery performace and cyclability [96].

Even if the functioning scheme described above is quite simple, it should be stressed that many phenomena occurs inside the battery which are complex and difficult to interpret through experiment. Understanding the molecular mechanisms by which these phenomena take place is of great interest.

Part of the theoretical work addresses degradation processes, like electrolyte decomposition and surface chemistry on the electrode [97–101]. A different line of

work focuses on the plasticizer and on its interaction with lithium ions [102–106]. Following this line and the objectives of the European Project, we studied two plasticizers: ethylene carbonate (EC) and γ-butyrolactone (GBL). EC and GBL (and their mixtures with other solvents) are quite widespread in LIBs, and seem to be good candidates for next generation magnesium ion batteries [107–111]. Few computational studies exist on these two molecules and on their solutions with lithium. The parameters used so far to model both the intra- and inter-molecular interactions (*force field*) were generic and could not adequately reproduce quantities of experimental interest. For instance, huge errors were found in the simulated vibrational spectrum of the two molecules. Moreover the diffusion coefficient both of the ion and of the molecules were underestimated, with respect to NMR measurements.

In part III, we study the main properties of the interaction of EC and GBL with lithium ion, addressing the following questions [Masia et al. *J. Phys. Chem. B* **108**, 2016 (2004) and Masia et al. *J. Phys. Chem. B* **108**, 17992 (2004)]:

1. *what is the structure of EC and GBL?* This issue is still controversial mainly for EC; we have tried to clarify which structure is the most stable in the gas phase, making use of ab initio calculations, and which is the most probable in liquid phase, making use of MD simulations.

2. *is it possible to develop more accurate intramolecular force fields for these medium sized molecules?* Given that the commonly used force fields do not fairly reproduce the vibrational spectrum (mainly at low wavenumbers), an improved model for the intramolecular interactions was required. To achieve this objective the problem was addressed with a technique which makes use of ab initio calculations in a novel way.

3. *what are the differences in vibrational properties between gas and liquid phases?* New assignments of vibrational modes are done for the gas phase and the shifts induced in the liquid are studied using the newly derived force fields.

4. *how does the lithium ion coordinate EC and GBL, and how does it affect their geometrical and dynamical properties?* The interaction with lithium changes the structure of the plasticizers, also inducing vibrational shifts. MD simulations are used to asses the extent of such perturbation and explain the experimental measures.

1.4 Polarization

The fast evolution of computers has allowed one to go from the simulation of simple systems to more complex ones. Recently, much efforts have been devoted to the simulation of heterogenous environments such as biological systems, polymers and surfaces. To realistically model this kind of system, the classical force fields are evolving towards the inclusion of polarization effects. Taking into account these effects is fundamental to reproduce and to understand the behaviour of molecules in such non-homogeneus surroundings.

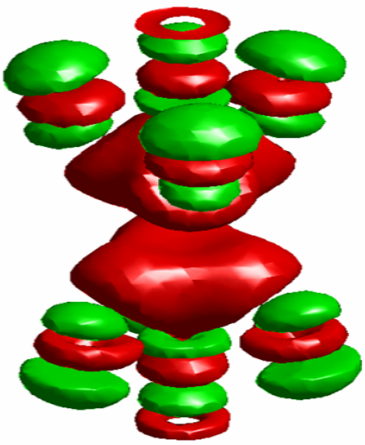

Figure 1.3. Lithium ion is "sandwiched" between two carbon tetrachloride molecules to form the $[Li(CCl_4)_2]^+$ complex. The ion electric field causes electrons to rearrange, yielding to regions with more (red colour) or less (green) electron density than in neutral CCl_4.

Polarization refers to the redistribution of a particle's (or molecule's) electron density due to an electric field, and generally is a complex process (see figure 1.3). In terms of molecular interactions, polarization leads to nonadditivity. In Molecular Dynamics simulations there are two ways of including polarization effects: *implicitly* or *explicitly*. In implicit models it is considered that a mean polarization can be averaged out and its effect is included in the functional form of the interaction potential. For instance, in condensed phase simulations, the dipole moment of dipolar molecules is artificially overestimated with respect to gas phase values. When systems with high polarizabilities and/or highly charged species are studied, both static and dynamic properties are strongly correlated with dipole moments [112]. That is why a great effort is being done to develop explicit models, i. e. to include the many body dipolar interactions so to obtain a more appropriate description.

Water is the substance for which several polarizable potentials have been developed. The available literature on the simulation of water is extensive enough to deserve separate reviews [112–114]. Some studies were also done on halogenated organic compounds which play an important role from a technological and environmental perspective [115–119]. Due to their physical properties they are used

as propellants, refrigerants, pesticides, solvents, etc. Within this family, chlorinated solvents are specially relevant, being among the top organic groundwater pollutants.

Since the interaction of water and chlorinated molecules with ions is of particular interest, in part IV we dedicate our attention to the approaches used to implement polarization in MD simulations. A response to the following queries is given:

1. *how can we judge the goodness of a polarizable model?* From the analysis of Potential Energy Surface (see chapter 2) it is not easy to disentangle the effects of all types of interaction, so that obtaining a clear view of the range of validity and limits of polarization methods is difficult. Here, a series of ab initio calculations for ion-molecule dimers will be used to "rank" the methods according to their efficiency. Moreover, since the ion-molecule electric interactions are very strong, these systems represent the limiting situation which coud be found in the liquid phase. Once having explored the limits of existing polarization methods, we will show how they can be improved to reproduce *(i)* the total dipole moment for the charge-molecule system and, *(ii)* the molecular polarizability tensor.[Masia et al. *J. Chem. Phys.* **121**, 7362 (2004) and Masia et al. *Comp. Phys. Comm.* **169**, 331 (2005)].

2. *is the cation-molecule interaction different from the charge-molecule one?* When short ion-molecule distances are considered, nonlinear effects arise due to orbital overlap and electron repulsion, which are not present for a point charge. Polarization methods do not take into account this effect, so that a damping needs to be introduced. It will be shown how a well known method for introducing damping in the case of intramolecular interactions can be parameterized for ion-molecule dimers [Masia et al. *J. Chem. Phys.* in press].

3. *is polarization damping also required for halides?* It will be shown that while the behaviour is rather similar to cations, the phenomenological description needs to be sligthly more sophisticated. Moreover it will be argued that such effort might be important in order to understand the existence of surface states for halides in water [Masia et al. *to be submitted*].

References

[1] J. N. Murrell and A. D. Jenkins, Properties of Liquids and Solutions, 2^{nd} Ed., Wiley, Chichester (1994).

[2] G. A. Krestov, N. P. Novosyolov, I. S. Perelygin, A. M. Kolker, L. P. Safanova, V. D. Ovchinnikova and V. N. Trostin, Ionic Solvation, Ellis Horwood, Chichester (1994).

[3] R. R. Dogonadze, E. Kálmán, A. A. Kornyshev and J. Ulstrup, The Chemical Physics of Solvation, Elsevier, Amsterdam (1988).

[4] D. P. Tielman, P. C. Biggin, G. R. Smith. and M. S. P. Sansom *Q. Rev. Biophys.* **34**, 473 (2001).

[5] Special Issue on "Batteries and Fuel Cells" *Chem. Rev.* **104** (10), (2004).

[6] L. Helm and A. E. Merbach *Coord. Chem. Rev.* **187**, 151 (1999).

[7] D. T. Richens, The Chemistry of Aqua Ions, Wiley, Chichester (1997).

[8] H. Ohtaki and T. Radnai *Chem. Rev.* **93**, 1157 (1993).

[9] H. L. Friedman *Chem. Scripta* **25**, 42 (1985).

[10] P. G. Wolynes *Ann. Rev. Phys. Chem.* **31**, 345 (1980).

[11] U. Frey and A. E. Merbach, Dynamics of Solutions and Fluid Mixtures by NMR, Wiley, Chichester (1995).

[12] R. Jiménez, G. R. Fleming, P. V. Kumar and M. Maroncelli *Nature* **369**, 471 (1994).

[13] S. Woutersen, U. Emmerichs and H. J. Bakker *Science* **278**, 658 (1997).

[14] S. Woutersen and H. J. Bakker *Nature* **402**, 507 (1999).

[15] S. Woutersen and H. J. Bakker *Phys. Rev. Lett.* **83**, 2077 (1999).

[16] B. Nigro, R. Rey and J. T. Hynes, submitted.

[17] L. X. Dang, J. E. Rice, J. Caldwell and P. A. Kollman *J. Am. Chem. Soc.* **113**, 2481 (1991).

[18] S.-B. Zhu and G. W. Robinson *J. Chem. Phys.* **97**, 4336 (1992).

[19] D. E. Smith and L. X. Dang. *J. Chem. Phys.* **100**, 3757 (1994).

[20] A. Chandra *Phys. Rev. Lett.* **85**, 768 (2000).

[21] K. Heinzinger and P. C. Vogel *Z. Naturforsch.* **29**, 1164 (1974).

[22] G. I. Szász, K. Heinzinger and W. O. Riede *Z. Naturforsch.* **36**, 1067 (1981).

[23] P. Bopp, I. Okada, H. Ohtaki and K. Heinzinger *Z. Naturforsch.* **40**, 116 (1985).

[24] D. G. Bounds *Mol. Phys.* **54**, 1335 (1985).

[25] B. M. Pettitt and P. J. Rossky *J. Chem. Phys.* **84**, 5836 (1986).

[26] T. Yamaguchi, E. Spohr, G. Pálinkas, K. Heinzinger, M. Probst and H. Ohtaki *Z. Naturforsch., A: Phys. Sci.* **41**, 1175 (1986).

[27] M. Probst, E. Spohr and K. Heinzinger *Chem. Phys. Lett.* **161**, 405 (1989).

[28] P. Cieplak and P. Kollman *J. Chem. Phys.* **92**, 6761 (1990).

[29] J. Åqvist *J. Phys. Chem.* **94**, 8021 (1990).

[30] E. Guàrdia, R. Rey and J. A. Padró *Chem. Phys.* **155**, 187 (1991).

[31] E. Guàrdia, R. Rey and J. A. Padró *J. Chem. Phys.* **95**, 2823 (1991).

[32] F. M. Floris, M. Persico, A. Tani and J. Tomasi *Chem. Phys. Lett.* **199**, 518 (1992).

[33] F. M. Floris, M. Persico, A. Tani and J. Tomasi *Chem. Phys.* **195**, 2078 (1995).

[34] X. Periole, D. Allouche, J. P. Daudey and Y. H. Sanejouand *J. Phys. Chem. B* **101**, 5018 (1997).

[35] A. Tongraar, K. R. Liedl, and B. M. Rode *Chem. Phys. Lett.* **286**, 56 (1998).

[36] X. Periole, D. Allouche, A. Ramírez-Solís, I. Ortega-Blake, J. P. Daudey and Y. H. Sanejouand *J. Phys. Chem. B* **102**, 8579 (1998).

[37] E. Guàrdia, G. Sesé, J. A. Padró and S. G. Kalko *J. Solution Chem.* **28**, 1113 (1999).

[38] R. Sansone, C. Ebner and M. Probst *J. Mol. Liq.* **88**, 129 (2000).

[39] A. Lauenstein, K. Hermansson, J. Lindgren, M. Probst and P. A. Bopp *Int. J. Quantum Chem.* **80**, 892 (2000).

[40] G. H. Peslherbe, B. M. Ladanyi and J. T. Hynes *J. Phys. Chem. A* **104**, 4533 (2000).

[41] A. Grossfield, P. Ren and J. W. Ponder *J. Am. Chem. Soc.* **125**, 15671 (2003).

[42] D. Spångberg and K. Hermansson *J. Chem. Phys.* **119**, 7263 (2003).

[43] S. Amira, D. Spångberg and K. Hermansson *Chem. Phys.* **303**, 327 (2004).

[44] D. Spångberg and K. Hermansson *J. Chem. Phys,* **120**, 4829 (2004).

[45] S. Amira, D. Spångberg, M. Probst and K. Hermansson *J. Phys. Chem. B* **108**, 496 (2004).

[46] S. Amira, D. Spångberg, V. Zelin, M. Probst and K. Hermansson *J. Phys. Chem. B* **109**, 14235 (2005).

[47] Y. Umebayashi, B. Mroz, M. Asada, K. Fujii, K. Matsumoto, Y. Mune, M. Probst and S. Ishiguro *J. Phys. Chem. A* **109**, 4862 (2005).

[48] J.-H. Chen and S. A. Adelman *J. Chem. Phys.* **72**, 2819 (1980).

[49] R. W. Impey, P. Madden and I. R. McDonald *J. Phys. Chem.* **87**, 5071 (1983).

[50] I. Rips, J. Klafter and J. Jortner *J. Chem. Phys.* **88**, 3246 (1988).

[51] A. Chandra and B. Bagchi *J. Phys. Chem.* **93**, 6996 (1989).

[52] A. Chandra, D. Wei and G. N. Patey *J. Chem. Phys.* **99**, 4926 (1993)

[53] B. M. Ladanyi and R. M. Stratt *J. Phys. Chem.* **99**, 2502 (1995).

[54] A. Chandra *Chem. Phys. Lett.* **235**, 133 (1995).

[55] A. Chandra *Chem. Phys. Lett.* **244**, 314 (1995).

[56] S. Tucker and M. W. Maddox *J. Phys. Chem. B* **102**, 2437 (1998).

[57] B. Bagchi and R. Biswas *Adv. Chem. Phys.* **109**, 207 (1999).

[58] K. Ando and J. T. Hynes *Adv. Chem. Phys.* **109**, 381 (1999).

[59] S. A. Egorov *Phys. Rev. Lett.* **93**, 023004 (2004).

[60] G. I. Szász and K. Heinzinger *J. Chem. Phys.* **79**, 3467 (1983).

[61] R. Rey and E. Guàrdia *J. Phys. Chem.* **96**, 4712 (1992).

[62] S. H. Lee and J. C. Rasaiah *J. Chem. Phys.* **101**, 6964 (1994).

[63] R. Åkesson, L. G. M. Pettersson, M. Sandström and U. Wahlgren *J. Am. Chem. Soc.* **116**, 8705 (1994).

[64] S. H. Lee and J. C. Rasaiah *J. Phys. Chem.* **100**, 1420 (1996).

[65] T. Kowall, F. Foglia, L. Helm and A. E. Merbach *J. Am. Chem. Soc.* **117**, 3790 (1995).

[66] R. Rey and J. T. Hynes *Phys. Condens. Matter* **8**, 9411 (1996).

[67] R. Rey and J. T. Hynes *J. Phys. Chem.* **100**, 5611 (1996).

[68] T. Kowall, F. Foglia, L. Helm and A. E. Merbach *Chem.-Eur. J.* **2**, 285 (1996).

[69] G. Sesé, E. Guàrdia and J. A. Padró *J. Chem. Phys.* **105**, 8826 (1996).

[70] M. Hartmann, T. Clark and R. van Eldik *J. Am. Chem. Soc.* **119**, 7843 (1997).

[71] F. P. Rotzinger *J. Am. Chem. Soc.* **119**, 5230 (1997).

[72] D. Spångberg, M. Wojcik and K. Hermansson *Chem. Phys. Lett.* **276**, 114 (1997).

[73] S. Obst and H. J. Bradaczek *Phys. Chem.* **100**, 15677 (1996).

[74] K. Hermansson and M. Wojcik *J. Phys. Chem. B* **102**, 6089 (1998).

[75] S. Koneshan, J. C. Rasaiah, R. M. Lynden-Bell and S. H. Lee *J. Phys. Chem. B* **102**, 4193 (1998).

[76] E. Guàrdia and R. Pinzón *J. Mol. Liq.* **85**, 33 (2000).

[77] A. P. Lyubartsev, K. Laasonen and A. Laaksonen *J. Chem. Phys.* **114**, 3120 (2001)

[78] D. Spångberg, R. Rey, J. T. Hynes and K. Hermansson *J. Phys. Chem. B* **107**, 4470 (2003).

[79] K. Hermansson *J. Phys. Chem. A* **106**, 4695 (2002).

[80] E. Guàrdia, J. Martí, J. A. Padró, L. Saiz and A. V. Komolkin *J. Mol. Liq.* **96-97**, 3 (2002).

[81] L. Pejov, D. Spångberg and K. Hermansson *J. Phys. Chem. A* **109**, 5144 (2005).

[82] E. Guàrdia, J. Martí, L. Garcia-Tarrés and D. Laria *J. Mol. Liq.* **117**, 63 (2005).

[83] B. Scrosati *Nature* **373**, 557 (1995).

[84] M. Watanabe, M. Kanba, K. Nagaoka and I. Shinohara *J. Appl. Polym. Sci.* **27**, 4191 (1982).

[85] E. Tsuchida, H. Ohno and K. Tsunemi *Electrochim. Acta* **28**, 591 (1983).

[86] M. Z. A. Munshi and B. B. Owens *Solid State Ionics* **26**, 41 (1988).

[87] K. M. Abraham and M. Alamgir *J. Electrochem. Soc.* **137**, 1657 (1990).

[88] O. Bohnke, G. Frand, M. Rezrazi, C. Rousselot and C. Truche *Solid State Ionics* **66**, 97 (1993).

[89] S. Passerini, S. Looutzky and B. Scrosati *J. Electrochem. Soc.* **141**, 80 (1994).

[90] J.-M. Tarascon. A. S. Gozdz, C. Schmutz, F. Shokoohi and P. C. Warren *Solid State Ionics* **86-88**, 49 (1996).

[91] M. Kono, E. Ayashi, M. Nishiura and M. Watanabe *J. Electrochem. Soc.* **147**, 2517 (2000).

[92] B. Scrosati, F. Croce and S. Panero *J. Power Sources* **100**, 93 (2001).

[93] SCIFINDER Scholar is a software used to explore the CAS database. It's available at `http://www.cas.org/SCIFINDER/SCHOLAR/`.

[94] J. Y. Song, Y. Y. Wang and C. C. Wan *J. Power Sources* **77**, 183 (1999).

[95] W. H. Meyer *Adv. Mater.* **10**, 439 (1998).

[96] S. S. Sekhon, M. Deepa and S. A. Agnihotry *Solid State Ionics* **136-137**, 1189 (2000).

[97] K. Tasaki *J. Phys. Chem. B.* **109**, 2920 (2005).

[98] Y. Wang, and P. B. Balbuena *J. Phys. Chem. B* **106**, 4486 (2002).

[99] Y. Wang, S. Nakamura, K. Tasaki and P. B. Balbuena *J. Am. Chem. Soc.* **124**, 4408 (2002).

[100] Y. Wang, S. Nakamura, M. Ue and P. B. Balbuena *J. Am. Chem. Soc.* **123**, 11708 (2001).

[101] T. Li and P. B. Balbuena *Chem. Phys. Lett.* **317**, 422 (2000).

[102] R. Blint *J. Electrochem. Soc.* **142**, 696 (1995).

[103] J. C. Soetens, C. Millot and B. Maigret *J. Phys. Chem. A* **102**, 1055 (1998).

[104] B. Klassen, R. Aroca, M. Nazri and G. A. Nazri *J. Phys. Chem. B* **102**, 4795 (1998).

[105] T. Li and P. B. Balbuena *J. Electrochem. Soc.* **146**, 3613 (1999).

[106] J. C. Soetens, C. Millot, B. Maigret and I. Bakó *J. Mol. Liq.* **92**, 201 (2001).

[107] D. Aurbach, I. Weissman, Y. Gofer and E. Levi *The Chemical Record* **3**, 61 (2003).

[108] O. Chusid, Y. Gofer, H. Gizbar, Y. Vestfrid, E. Levi, D. Aurbach and I. Reich *Adv. Mater.* **15**, 627 (2003)

[109] N. Yoshimoto, S. Yakushiji, M. Ishikawa and M. Morita *Electrochem. Acta* **48**, 2317 (2003).

[110] D. Aurbach, Z. Lu, A. Schechter, Y. Gofer, H. Gizbar, R. Turgeman, Y. Cohen, M. Moshkovich and E. Levi *Nature* **407**, 724 (2000).

[111] G. G. Kumar and N. Munichandraiah *J. Electroanal. Chem.* **495**, 42 (2000).

[112] S. W. Rick and S. J. Stuart *Rev. Comput. Chem.* **18**, 89 (2002).

[113] S.-H. Zhu, S. Singh and G. W. Robinson *Adv. Chem. Phys.* **85**, 627 (1994).

[114] A. Wallqvist and R. D. Mountain *Rev. Comput. Chem.* **12**, 137 (1998).

[115] E. Llanta, K. Ando and R. Rey *J. Phys. Chem. B* **105**, 7783 (2001).

[116] E. Llanta and R. Rey *Chem. Phys. Lett.* **340** (1-2), 173 (2001).

[117] M. Chang, K. A. Peterson and L. X. Dang *J. Chem. Phys.* **103**, 7502 (1995).

[118] J. C. Soetens, G. Jansen and C. Millot *Mol. Phys.* **96**, 1003 (1999).

[119] R. Veldhuizen and S. W. de Leeuw *J. Chem. Phys.* **105**, 2828 (1996).

Chapter 2

Computational Methods

This chapter contains an overview of the computational techniques used in this thesis. *Quantum chemical calculations* (also called *first principles* or *ab initio* calculations) and *molecular dynamics simulations* constitute the main topics of this chapter. The last part of the chapter gives a brief introduction to other computational techniques used. Some of the programs used for these calculations are commercial and/or available for download as freeware; others have been developed within the research group.

2.1 Quantum Chemical Calculations

Quantum chemistry is a discipline which, over the past three decades, has become an essential tool in the study of atoms and molecules and, increasingly, in modelling complex systems such as those arising in biology and materials science [1–5]. It is based on the numerical solution of the Schrödinger equation. The fundamental assumption (known as the Born-Oppenheimer approximation) is that, in the adiabatic limit, we can decouple the nuclear and the electronic degrees of freedom; in this way the time-independent electronic Schrödinger equation is obtained

$$(\hat{H}_{el} + V_{nu})\Psi_{el}(\mathbf{q}_{el}; \mathbf{q}_{nu}) = E_{el}\Psi_{el}(\mathbf{q}_{el}; \mathbf{q}_{nu}), \tag{2.1}$$

where the electronic coordinates ($\mathbf{q}_{el}$) are independent variables while the nuclear coordinates ($\mathbf{q}_{nu}$) are parameters. For a given set of nuclear coordinates, the nuclear-nuclear potential energy V_{nu} is a constant. The electronic Hamiltonian $\hat{H}_{el}$ is defined as the sum of the kinetic energy, the electron-electron and the electron-nuclei Coulomb potential energy

$$\hat{H}_{el} = T_{el} + V_{el} = -\sum_{i=1}^{n_{el}} \frac{\nabla_i^2}{2} + \sum_{i=1}^{n_{el}} \left[\sum_{k=i+1}^{n_{el}} \frac{e^2}{|\mathbf{q}_{ik}|} - \sum_{j=1}^{n_{nu}} \frac{z_j e^2}{|\mathbf{q}_{ij}|} \right]. \tag{2.2}$$

Solutions of equation 2.1 are the wave functions $\Psi_{el,i}$ and the energy spectrum $E_{el,i}$; equation 2.1 is usually solved without the inclusion of V_{nu}, in which case the eigenvalue is called the *pure electronic energy*, and then $E_{el,0}$ is obtained by adding V_{nu}. The (hyper)surface defined by $E_{el,0}(\mathbf{q}_{nu})$ over all possible nuclear coordinates, is called the *Potential Energy Surface* (PES). The nuclear motion is ruled by the PES, so that molecular vibration, rotation and traslation are described by the nuclear Schrödinger equation:

$$\left(-\sum_{i=1}^{n_{nu}} \frac{\nabla_i^2}{2M_i} + E_{el,0}(\mathbf{q}_{nu}) \right) \Psi_{nu}(\mathbf{q}_{nu}) = \hat{H}_{nu} \Psi_{nu}(\mathbf{q}_{nu}) = E_{nu} \Psi_{nu}(\mathbf{q}_{nu}), \tag{2.3}$$

where M_i is the mass of the i^{th} nucleus. In the following subsections we will always refer to the electronic Schrödinger equation 2.1, so that the subscript *el* will be dropped. Finding and describing approximate solutions to equation 2.1 has been a major preoccupation of quantum chemists since the birth of quantum mechanics. Two highly productive approaches to this problem have arisen over the past 50 years. Wave function based approaches expand the electronic wave function as a sum of Slater determinants, the coefficients of which are optimized by various numerical procedures. The second class of theoretical approaches is based on *density functional theory* (DFT), which expresses the total energy of the system as a functional of the electron density (see subsection 2.1.5). However the "correct" functional of the energy is unknown and has to be constructed by heuristic approximation. Below we offer a brief summary of the methods used (or cited) within this thesis.

2.1.1 The Hartree-Fock Approximation

The wave function $\varphi(\mathbf{x})$ which describes both the single electron spatial distribution and its spin is called *spin orbital*. It is usually expressed as a linear combination of spatial basis functions ($\phi(\mathbf{x})$) multiplying a given spin function

(χ)

$$\varphi(\mathbf{x}) = \chi\left[\sum_{i=1}^{\infty} a_i \phi_i(\mathbf{x})\right]. \tag{2.4}$$

In general, the set of spin orbitals would have to be infinite; however, in practice only a finite set is used (further details on basis sets are given in subsection 2.1.6). Starting from single electron spin orbitals, how can the N-electrons wave function be constructed? To a first approximation we can consider that the electrons do not interact. The total Hamiltonian will be the sum of N individual Hamiltonians

$$\hat{h}(i)\varphi(\mathbf{x}_i) = \varepsilon\varphi(\mathbf{x}_i), \tag{2.5}$$

where $\hat{h}(i)$ contains both the electron kinetic energy operator and the potential energy operator for the Coulomb interaction with nuclei. The total wave function is the product of N spin orbitals: $\Psi = \prod \varphi(\mathbf{x}_i)$. Such a many electrons wave function is called the *Hartee product*. For the Pauli exclusion principle, the electronic wave function should be antisymmetric; since the Hartree product does not satisfy this condition, another form of the wave function is needed. The simplest one which can be used to describe the ground state on an N-electron system is a sum of Hartree products known as the *Slater determinant*:

$$\Psi_0(\mathbf{x}_1, \mathbf{x}_2, \ldots, \mathbf{x}_N) = \begin{vmatrix} \varphi_i(\mathbf{x}_1) & \varphi_j(\mathbf{x}_1) & \ldots & \varphi_k(\mathbf{x}_1) \\ \varphi_i(\mathbf{x}_2) & \varphi_j(\mathbf{x}_2) & \ldots & \varphi_k(\mathbf{x}_2) \\ \vdots & \vdots & \ddots & \vdots \\ \varphi_i(\mathbf{x}_N) & \varphi_j(\mathbf{x}_N) & \ldots & \varphi_k(\mathbf{x}_N) \end{vmatrix}. \tag{2.6}$$

The resulting wave function incorporates *exchange correlation*, which means that two electrons with parallel spins are correlated. Still, since electrons with opposite spins remain uncorrelated, it is customary to refer to a single determinantal wave function as *uncorrelated*.

Since electrons interact among them, eq. 2.5 constitutes a crude approximation. In the Hartree-Fock approximation, the Coulomb interaction among electrons is averaged and the many electrons wave function (and energies) is obtained in an iterative way. Namely, one introduces in 2.5 the *average potential* v^{HF} experienced by the i^{th} electron due to the presence of the other electrons, obtaining a one-electron eigenvalue equation of the form

$$(\hat{h}(i) + v^{HF})\varphi(\mathbf{x}_i) = \hat{f}(i)\varphi(\mathbf{x}_i) = \varepsilon\varphi(\mathbf{x}_i), \tag{2.7}$$

where $\hat{f}(i)$ is called the Fock operator. According to the variational principle, the best wave function is the one which gives the lowest possible energy

$$E_0\left[\Psi_0\right] = \langle\Psi_0|\hat{H}|\Psi_0\rangle \geq E_0^{true}, \tag{2.8}$$

where H is the electronic Hamiltonian defined in 2.1. If the coefficients a_i appearing in equation 2.4 are varied to minimize the functional $E_0\left[\Psi_0\right]$ with respect to the choice of spin orbitals, equation 2.7 is obtained. It should be reminded that the value of the field v^{HF} depends on the spin orbitals of the rest of electrons. Thus, equation 2.7 is nonlinear and must be solved iteratively. The procedure used is called the *self consistent field* (SCF) method.

In practice the Hartree-Fock equation is solved by introducing a finite set of K basis functions, which lead to a set of N occupied spin orbitals and $K - N$ virtual ones (obviously K is always greater than N). As a rule of thumb, the larger and more complete the set of basis functions $\{\varphi(\mathbf{x})\}$, the greater is the degree of flexibility in the expansion for the spin orbitals, and the lower will be the expectation value E_0 (eq. 2.8). Larger and larger basis sets will lower the Hartree-Fock energy E_0 until a limit is reached, called the Hartree-Fock limit [6].

2.1.2 Configuration Interaction

Energies calculated by the Hartree-Fock method are typically in error by 0.5% to 1%. In absolute terms this is not much, but for the chemist it is too large. For example the total energy of the carbon atom is about 1000 eV, and 0.5% of this is 5 eV, of the same magnitude as single bond energies. A way of improving Hartree-Fock wave functions and energies is, thus, of fundamental importance. The main drawback of Hartree-Fock methods is that interactions between electrons are taken into account only in an average way.

The *Configuration Interaction* (CI) method, in order to account for electron correlation, uses a variational wave function that is a linear combination of determinants built from spin orbitals. Mathematically, CI consists of the linear combination of Slater determinants [2, 7–9]:

$$\Phi = \sum_{i=0}^{L} c_i \Psi_i. \tag{2.9}$$

The number L of different single determinants that can be formed from N electrons and K spin orbitals is given by the binomial coefficient

$$L = \binom{K}{N} = \frac{K!}{N!(K-N)!}, \tag{2.10}$$

the Hartree-Fock ground state is just one of these. The other determinants can be taken to represent approximate excited states of the system; indeed they are considered to be the Hartree-Fock singly, doubly, triply,..., N-tuply excited states. In the limit $L \to \infty$, the lowest eigenvalue of the Hamiltonian matrix, denoted by E_{CI}, is the **exact** nonrelativistic ground state energy of the system within the Born-Oppenheimer approximation. Unfortunately, the *full* CI procedure cannot be implemented in practice because the number of determinants is too large (even for finite L); only a small fraction of the L possible determinants is typically used.

2.1.3 Perturbative Methods

Configuration Interaction is a systematic procedure for going beyond the Hartree-Fock approximation. It has the important advantage that it is variational (at each level, it gives an upper bound to the exact energy), but it has the disadvantage that it is only *size consistent** when all possible excitations are incorporated into the trial function. A different procedure to find the correlation energy, which is not variational but size consistent at each level [10], is the *Perturbation Theory* (PT). In 1934 Møller and Plesset [11] proposed a perturbation treatment of atoms and molecules in which the unperturbed wave function is the Hartree-Fock function; this is called the *Møller-Plesset* (MP) perturbation theory. In this approach the total Hamiltonian of the system is divided into two pieces: a zeroth-order part $\hat{H}_0$, which has known eigenvalues ($E^{(0)}$) and eigenfunctions ($\Psi^{(0)}$), and a perturbation $\hat{H}_P$

$$\hat{H} = \hat{H}_0 + \lambda \hat{H}_P. \tag{2.11}$$

The assumption is that the perturbation is small so that the exact energy and wave function can be expressed as a power series of $\hat{H}_P$. The usual way of doing it is in terms of the parameter λ:

$$\Psi = \lim_{n\to\infty} \sum_{i=0}^{n} \lambda^i \Psi_{(i)}, \tag{2.12}$$

$$E = \lim_{n\to\infty} \sum_{i=0}^{n} \lambda^i E_{(i)}. \tag{2.13}$$

*A size-consistent calculation gives the same energy for two atoms (or molecular fragments) separated by a large distance as is obtained from summing the energies for the atoms (or molecular fragments) computed separately. So for a size-consistent method, the bond energy in N_2 is $D_e = 2E(N) - E(N_2)$. For a method that is not size-consistent, a calculation with a big distance (e.g. 100 Å) is required: $D_e = E(N \cdots\cdots N) - E(N_2)$.

Substitution of these series into the time-independent Schrödinger equation gives

$$(\hat{H}_0 + \lambda \hat{H}_P)\left(\sum_{i=0}^{n} \lambda^i \Psi_{(i)}\right) = \left(\sum_{i=0}^{n} \lambda^i E_{(i)}\right)\left(\sum_{i=0}^{n} \lambda^i \Psi_{(i)}\right). \tag{2.14}$$

The expression for 2.12 and 2.13 contain the eigenvalues of $\hat{H}_0$ and matrix elements of the perturbation between the eigenfunctions of $\hat{H}_0$. Terms involving products of n such matrix elements are grouped together and constitute the nth-order perturbation energy. If the perturbation $\hat{H}_P$ is chosen to be small enough, the perturbation expansion converges quickly. The solution of equation 2.14 at zeroth order ($n = 0$) gives the unperturbed Hartree-Fock wave function and energy. A wave function through n^{th} order is sufficient to calculate the energy to $(2n + 1)^{th}$ order. Second (MP2) and fourth (MP4) order Møller-Plesset calculations (where we refer to the order of the energies) are standard levels used for small systems and are implemented in many computational chemistry codes [12].

2.1.4 Coupled Cluster Methods

Coupled Cluster (CC) method is a technique used for description of many-body systems. It was initially developed in 1950's for studying nuclear physics phenomena but it became more frequently used after Jiři Čížek and Josef Paldus reformulated the method for studying electronic correlation in atoms and molecules [13]. It is now one of the most prevalent methods in quantum chemistry that include electronic correlation. The method is based on the exponential Ansatz:

$$|\Phi\rangle = e^{\hat{T}}|\Phi_0\rangle, \tag{2.15}$$

where $|\Phi\rangle$ is the wave function, $|\Phi_0\rangle$ is the reference function (e.g. Hartree-Fock function), and $\hat{T}$ is the cluster operator:

$$\hat{T} = \hat{T}_1 + \hat{T}_2 + \cdots, \tag{2.16}$$

where the cluster operators, $\hat{T}_n$, are frequently referred to as *excitation* operators, since the determinants they produce resemble excited states in Hartree Fock theory. The coupled cluster equations are usually derived using diagrammatic techniques and result in nonlinear equations which can be solved in an iterative way.

In the simplest version one considers only the $\hat{T}_2$ operator (double excitations). This method is called coupled cluster with doubles (CCD in short). The method

gives the exact non-relativistic solution of the Schrödinger equation of the n-body problem if one includes up to the $\hat{T}_n$ cluster operator. However, the computational effort of solving the equations grows steeply with the order of the cluster operator and in practical applications the method is limited to the first few orders.

Most frequently, one solves the CC equation using the operator $\hat{T} = \hat{T}_1 + \hat{T}_2$, which produces all Slater determinants which differ from the reference determinant by one or two spin-orbitals. This approach, called coupled-cluster singles and doubles (CCSD), has the effect of describing coupled two-body electron correlation effects and orbital relaxation effects. It is also fairly common (although also more computationally expensive) to include an approximate, non-iterative correction accounting for three-body electron correlations in a method designated CCSD(T). For ground electronic states near their equilibrium geometries, CCSD(T) is often called a *gold standard* of quantum chemistry because it provides results very close to those of full configuration interaction (full CI).

2.1.5 Density Functional Theory

Hohenberg and Kohn (HK) [14], in 1964, suggested that the many-electron wavefunction was too complicated an entity to deal with as the fundamental variable in a variational approach. Firstly, it cannot adequately be described without $\sim 10^{23}$ parameters, and secondly it has the complication of possessing a phase as well as a magnitude. They chose instead to use the *electron density* $\rho(\mathbf{x})$ as their fundamental variable

$$\rho(\mathbf{x}) = \langle \Psi | \hat{\rho}(\mathbf{x}) | \Psi \rangle, \tag{2.17}$$

where $\hat{\rho}(\mathbf{x}) = \sum_{i=1}^{N} \delta(\mathbf{x} - \mathbf{x}_i)$ is the density operator. HK proved that the relation expressed above can be reversed, i.e. for a given ground state density $\rho(\mathbf{x})$ it is in principle possible to calculate the corresponding ground state wave function $\Psi(\mathbf{x})$. In other words, $\Psi(\mathbf{x})$ is a unique functional of $\rho(\mathbf{x})$, i.e.

$$\Psi = \Psi\left[\rho(\mathbf{x})\right], \tag{2.18}$$

and consequentely all ground state properties of the system (e.g. lattice constant, cohesive energy, etc.) are functionals of the ground state electron density. The most common present-day implementation of density functional theory is through the Kohn-Sham method (KS) [15]. Within the framework of KS DFT, the intractable many-body problem of interacting electrons in a static external potential is reduced to a tractable problem of non-interacting electrons moving in

an effective potential. The effective potential includes the external potential and the effects of the Coulomb interactions between the electrons. They considered the ground state of the system to be defined by that electron density distribution which minimizes the total energy

$$E_0\left[\rho(\mathbf{x})\right] = \langle \Psi\left[\rho(\mathbf{x})\right] | \hat{H} | \Psi\left[\rho(\mathbf{x})\right] \rangle. \tag{2.19}$$

The variational problem of minimizing the energy functional above can be solved using the fact that the functional in the equation above can be written as a fictitious density functional of a non-interacting system

$$E_{KS}\left[\rho(\mathbf{x})\right] = \langle \Psi\left[\rho(\mathbf{x})\right] | \hat{H}_{KS} | \Psi\left[\rho(\mathbf{x})\right] \rangle, \tag{2.20}$$

where $\hat{H}_{KS}$ contains the non-interacting potential energy and an *external effective potential* v_{KS} in which the particles are moving. Thus, one can solve the so-called Kohn-Sham equations of this auxiliary non-interacting system

$$(\hat{h}(i) + v_{KS})\varphi(\mathbf{x}_i) = \hat{k}(i)\varphi(\mathbf{x}_i) = \varepsilon\varphi(\mathbf{x}_i), \tag{2.21}$$

which yields the orbitals $\varphi(\mathbf{x}_i)$ that reproduce the density $\rho_{KS} = \sum_{i=1}^{N} |\varphi(\mathbf{x}_i)|^2$ of the original many-body system (notice the resemblance with the Hartree-Fock equation 2.7). The effective single-particle potential v_{KS} can be written in more detail as

$$v_{KS} = v + \int \frac{e^2 \rho_{KS}(\mathbf{x}')}{|\mathbf{x} - \mathbf{x}'|} \mathrm{d}^3\mathbf{x}' + v_{XC}\left[\rho_{KS}(\mathbf{x})\right], \tag{2.22}$$

where v represents the static external potential where electrons are moving, the second term denotes the so-called Hartree term describing the electron-electron Coulomb repulsion, while the last term v_{XC} is called *exchange correlation potential*. It includes all the many particle interactions. Since the Hartree term and v_{XC} depend on ρ, which depends on the φ_i, which in turn depend on v_{KS}, the problem of solving the Kohn-Sham equation has to be done in a self-consistent way.

A variety of exchange-correlation functionals have been developed for chemical applications. The most popular is known as B3LYP [16–18]. The adjustable parameters of these functionals are generally fitted to a "training set" of molecules. Unfortunately, although the results obtained with these functionals are usually relatively accurate for most applications, there is no systematic way of improving them (in contrast to some of the traditional wave function-based methods like CI). Hence, in the current DFT approach it is not possible to rigorously estimate the error of the calculations without comparing them to other methods or experiment.

2.1.6 Implementation

From the above discussion, it appears clear that, given the positions of a collection of atomic nuclei, and the total number of electrons, the computational solution of the electronic Schrödinger equation is "at hand". Depending on the requested degree of accord with *true* values, one can use one of the approaches listed above (or others). When a quantum chemical calculation is set up, the first step is the choice of the *model chemistry*, i.e., the combination of the method (HF, CI, MP2, MP4, DFT etc.) and the basis set. The model chemistry defines the *level of theory* (degree of approximation) of the calculation; the higher the level, the more expensive and time consuming is the calculation.

Basis Sets

In the previous subsections we gave an overview of the methods, while nothing was said about basis sets. The molecular orbitals are expressed as linear combinations of a predefined set of one-electron functions known as basis functions, usually centered on the atomic nuclei. In usual commercial packages (such as Gaussian [19], the one used for this research work) they are chosen to be gaussian type atomic functions, as their mathematical properties allow to easily solve the integrals appearing in equation 2.8. By performing electronic structure calculations on a small variety of molecules, a hierarchy of basis sets can be devised [20]. A vast literature exists on this topic (see references [1–4,21] and references therein for more details).

When more than one molecule (dimers, trimers etc.) are considered in quantum chemical calculations, the *basis set superposition error* (BSSE) [22] needs to be considered. Given a dimer $A - B$, the BSSE originates in the possibility that the unused basis functions of unit B in the associated complex may augment the basis set of unit A, thereby lowering its energy compared to a calculation of this unit alone (and vice versa). There is a large literature dealing with this problem, which becomes particularly acute when subtle energy differences occur between a variety of conformational forms, such as in H-bonded water or ammonia dimers: BSSE causes the intermolecular interactions to be artifactually too attractive. One obvious solution to the basis set superposition error is the use of extremely large basis sets [23]. This is, however, hardly feasible for most of the chemically interesting systems. The second approach, termed the *Counterpoise Method* (CP) [23–25], is an approximate method for estimating the size of the

BSSE. It calculates each of the units with just the basis functions of the other (without the nuclei or electrons), using so called "ghost orbitals". In the general case of a supermolecular aggregate containing n units, the counterpoise corrected energy is given by

$$E_{CP} = E + CP, \tag{2.23}$$

$$CP = \sum_{i=1}^{n} \left(E_i - E_i^* \right), \tag{2.24}$$

where E_i and E_i^* represent the energies of the individual units calculated respectively with the complete and with the ghost orbitals. There have been extensive discussions in the literature about the ability of the counterpoise correction to correct for BSSE. Be this as it may, it is clear that the use of the CP correction significantly improves the convergence behaviour of molecular properties [20]. The CP method has been employed in this thesis in parts III and IV when ion-molecule dimers are studied.

Types of Calculations

Different types of calculations can be made with a typical quantum chemical package [21, 26]; here we give a brief description of the ones used in this thesis (see parts III and IV):

Single Point Energy: given a molecule with a specified geometric structure, its *total energy* and related properties are calculated.

Geometry Optimization: the global minimum of the potential energy surface is searched using special algorithms [27] (see also section 2.3). This point represents the lowest energy (equilibrium) structure of the molecule. This type of calculations could end up in a transition structure (local maximum). A good test is to perform a vibrational analysis: if all the normal mode frequencies are real, the structure found is an equilibrium one.

Vibrational Analysis: nuclei move in the PES as described by equation 2.3. Molecular frequencies can be computed directly from the second derivatives of the total energy with respect to nuclear positions. In this way normal mode harmonic frequencies are computed, and the IR and Raman spectra of the molecules predicted.

Population Analysis: one property of great interest for molecular simulations are atomic partial charges. Unfortunately, in contrast to the three-dimensional electronic charge distribution, they are not quantum observables and cannot be obtained uniquely from the wave function. Nevertheless, starting from Mulliken's *population analysis* [28], different methodologies have been devised. They produce, for instance, charge fits to the electrostatic potential at given points in space, constraining them to reproduce the total dipole moment of the molecule (itself computed from the wave function) [29].

2.2 Molecular Dynamics Simulations

In section 2.1 we explained how, within the Born-Oppenheimer approximation, it is possible to express the Hamiltonian of the system as a function of nuclear variables, once the electron motions have been averaged out. Making the additional approximation that a classical description is adequate, we may write the Hamiltonian of a system of N particles as the sum of their kinetic and potential energies. From this Hamiltonian it is straightforward to construct the Newton equations of motion to describe the time evolution of the system:

$$H(\mathbf{q}_{nu}, \mathbf{p}_{nu}) = K(\mathbf{p}_{nu}) + V(\mathbf{q}_{nu}) \quad \Rightarrow \quad \frac{\mathrm{d}\mathbf{p}_{nu}}{\mathrm{d}t} = -\nabla V(\mathbf{q}_{nu}), \tag{2.25}$$

where the potential energy $V(\mathbf{q}_{nu})$[†] is the PES. The equations of motion govern the time evolution of the system and all its mechanical properties [30–32].

2.2.1 Numerical Integrators

For many particle systems, such as molecular systems, it is not possible to find an analytical solution to the equations of motion; so an approximate solution is sought. The phase space trajectory is discretized in time and the Newton equations are solved using *finite difference methods*. Molecular Dynamics (MD) simulations are based on these concepts [33–38]. The general idea of the finite difference

[†]The use of generalized coordinates $\mathbf{q}(t)$ is not practical for computer simulations, while with cartesian coordinates $\mathbf{r}(t) = [x(t), y(t), z(t)]$ it is much simpler to implement and carry out the simulation. So in the rest of the chapter we will make use only of cartesian coordinates.

approach, is that, given a configuration (positions and velocities) at time t, we can approximate the configuration at time $t + \delta t$, provided that δt is sufficiently small. For the last 40 years (since the advent of computers), algorithms for the simulation of atomic and molecular systems have been developed and remarkable progresses have been made in condensed matter theory; in this thesis we have mostly used the so-called half step *leapfrog* scheme [39]. Within this algorithm, position and velocity of the i^{th} particle are given by

$$\mathbf{v}_i(t + 1/2\delta t) = \mathbf{v}_i(t - 1/2\delta t) + \delta t \mathbf{a}_i(t), \tag{2.26}$$

$$\mathbf{r}_i(t + \delta t) = \mathbf{r}_i(t) + \delta t \mathbf{v}_i(t + 1/2\delta t). \tag{2.27}$$

Since the velocities are calculated at mid step intervals, the velocity at time t are given by

$$\mathbf{v}_i(t) = \frac{1}{2}\left[\mathbf{v}_i(t + 1/2\delta t) + \mathbf{v}_i(t - 1/2\delta t)\right]. \tag{2.28}$$

The above scheme is repeated iteratively to calculate the time evolution of the system for a total time $T = N\delta t$, N being the total number of time steps. An advantage of using the leapfrog algorithm is that at no stage the difference of two large quantities is calculated to obtain small ones: this minimizes loss of computational precision during the calculation.

For long simulations a drift in the temperature could be observed. Several different methods to keep a constant temperature in a MD simulation exist. In this thesis we have used the velocity rescaling approach as proposed by Berendsen et al. [40]. At each time step, velocities are scaled by a factor

$$\chi = \left[1 + \frac{\delta t}{\tau}\left(\frac{T}{\mathcal{T}} - 1\right)\right], \tag{2.29}$$

where $\mathcal{T} = \left(\sum_i^N m_i |\mathbf{v}_i|^2\right) / 3k_{\mathrm{B}}N$ is the instantaneous kinetic temperature, and τ is a preset time constant. This method forces the system towards the desired temperature at a rate determined by τ. This method should be used only during equilibration runs, and constant energy simulations should be conducted for production runs (if possible), particularly for the calculation of time dependent quantities.

2.2.2 Force Fields

One of the main concerns of the simulator is that the model being studied is "realistic" enough. All the information regarding molecular interactions is contained

in the potential $V(\{\mathbf{r}\})$, the potential energy surface of ground state electrons which rules the classical motion of nuclei. A knowledge of the PES would allow to calculate the "exact" dynamics of the system. Unfortunately, calculating the full many body PES is not feasible for a large system and its functional description would be very complex. That is why it is usual to approximate the PES with an *effective classical potential*. The expressions for this potential and the associated adjustable parameters are known as *force field* (FF) [3, 41]. A large majority of condensed phase simulations have invoked pairwise additivity such that the total potential energy for a collection of molecules and/or ions is given by the sum of *intermolecular* interaction energies between all components, plus the sum of *intramolecular* energies

$$V(\{\mathbf{r}\}) = \sum_{a<b} V_{ab}^{inter} + \sum_{a} V_{a}^{intra}, \tag{2.30}$$

The intermolecular energy V_{ab}^{inter} is given by the *non-bonded* interactions between intermolecular atom pairs. The short range interaction is usually modelled with the Lennard-Jones potential, which contains a repulsive and an attractive term, respectively falling off as $1/r^{12}$ and $1/r^6$. The charge-charge Coulomb interaction has a long range character, so that special algorithms are needed to take into account the long range tails of the force (such as Ewald sum or the reaction field method [30]). In molecular simulations, interaction sites $i, j, \ldots$ are considered which bear a charge $q_i, q_j, \ldots$ and/or the short range interaction parameters (in the case of Lennard-Jones potential the parameters are σ and ϵ). The intermolecular term of eq. 2.30 thus reads

$$V_{ab}^{inter} = \sum_{i}^{\in a} \sum_{j}^{\in b} \left\{ \frac{q_i q_j}{r_{ij}} + 4\epsilon_{ij} \left[\left(\frac{\sigma_{ij}}{r_{ij}} \right)^{12} - \left(\frac{\sigma_{ij}}{r_{ij}} \right)^{6} \right] \right\}, \tag{2.31}$$

where r is the distance between atoms.

The intramolecular potential energy is typically represented by harmonic (and higher order) terms for bond stretching (V^{bond}) and angle bending (V^{angle}), and a Fourier series for torsional angles (V^{dihed}):

$$V_a^{intra} = V_a^{bond} + V_a^{angle} + V_a^{dihed}, \tag{2.32}$$

$$V_a^{bond} = \sum_n \left[\sum_i^{\in a} k_{i,n}^{r} \left(r_i - r_{i,eq} \right)^n \right], \tag{2.33}$$

$$V_a^{angle} = \sum_n \left[\sum_i^{\in a} k_{i,n}^{\theta} \left(\theta_i - \theta_{i,eq} \right)^n \right], \tag{2.34}$$

$$V_a^{dihed} = \sum_m \left\{ \sum_i^{\in a} A_{i,m}^{\varphi} \left[1 + (-1)^{(m-1)} \cos(m\varphi_i) \right] \right\}, \tag{2.35}$$

where $n = 1, 2, \ldots$ and $m = 1, 2, \ldots$, depending respectively on the accuracy of the model and on the periodicity of the angle. Further details are given in part III.

The above functional (eqs. 2.32, 2.33, 2.34 and 2.35) provides a compromise between speed and accuracy [42–44]. More complex FF [45, 46] have been developed that add, for example, stretch-bend cross-terms, or nonbonded interactions (Coulomb and/or Lennard-Jones) between atoms separated by three or more bonds in 2.32, or that replace the Lennard-Jones interaction in 2.31 by more flexible potentials. Such force fields, developed primarily for isolated molecules, have not been used significantly in liquid simulations.

Force field parameters are obtained by an optimization process which can have a rather different nature depending on the goals, and which makes use of data from a training set, itself constituted of both experimental data (of gas and liquid phases) and/or quantum mechanical calculations for intra and intermolecular interactions. Recently, to extend the coverage and increase the quality of the parametrization, many automated optimization techniques have become quite popular, such as Simplex (see also subsection 2.3.1), Artificial Neural Networks and Genetic Algorithms [47–51]. In part III we develop the intramolecular force field for single molecules. The difference among our approach and the most common force fields, is that our parametrization is not universal, i.e., it is not portable to a vast class of molecules, but heavily relies on ab initio calculations.

2.2.3 Polarizable Models

When an electric field is applied to an individual atom or molecule, the electron distribution is modified and the molecular geometry is distorted [52]. In a uniform electric field $\mathbf{E}$, the total dipole moment μ is [53]

$$\mu = \mu_0 + \tilde{\alpha}\mathbf{E} + \frac{1}{2}\mathbf{E}\tilde{\beta}\mathbf{E} + \ldots, \tag{2.36}$$

where μ_0 is the permanent dipole moment and the tensors $\tilde{\alpha}$ and $\tilde{\beta}$ are respectively the polarizability and the first hyperpolarizability of the molecule (atom). In fields of ordinary strength we can neglect the hyperpolarizability contribution and consider that the dipole moment increases linearly with the field. $\tilde{\alpha}$ is often interpreted as a measure of the *softness* of a charge cloud, that is, the ease with which it can be "distorted". In the case of atoms, it usually correlates well with the element's size. Large alkali atoms are highly polarizable, whereas the

relatively small inert gas atoms have low polarizabilities. Positive ions generally have polarizabilities much smaller than the corresponding neutral atoms; both their smaller sizes and the decreased shielding of the nuclei make it harder to overcome the electron-nuclear attraction. Negative ions are much more polarizable than neutral atoms for the converse reason: they are large and the outer electrons are not strongly bounded to their nuclei [54].

Since the total energy can be written as a Taylor expansion in the electric field, we have

$$U = U_0 - \mu_0 \cdot \mathbf{E} - \frac{1}{2}\mathbf{E}\tilde{\alpha}\mathbf{E} + \ldots, \tag{2.37}$$

U_0 being the energy in absence of the field. When molecules are free to orient themselves in the presence of an electric field, they of course tend to occupy the lowest energy orientations. A dipolar molecule in a uniform field, for example, will tend to align itself so that μ and $\mathbf{E}$ are parallel.

A major simplification in the minimalist model introduced in the subsection 2.2.2 is that the atomic charges are held fixed and there is no explicit treatment of polarization [55]. The Lennard-Jones interaction (equation 2.31) contains an attractive part, falling off as r^{-6}, which shows the same dependence as the dipole-dipole London dispersion energy $U \propto -\alpha^2/r^6$, α being the particle polarizability [56]. The Lennard-Jones parameters are not typically assigned [57] using known values of α, but this interaction is one way in which polarizability, in an average sense, is included in nonpolarizable models. Another way in which polarizability is included implicitly is the value of the partial charges q_i; for condensed phase simulations, they are often enhanced from the values that would be consistent with the gas phase dipole moment. In this way the polarization of electron distributions by the electric fields of other particles in a condensed phase environment are taken into account. Nevertheless, they cannot respond dynamically to fluctuations in the electric field due to molecular motion. Furthermore, this approximation is well known to be problematic for interactions with highly charged atomic ions and for interactions of ions with π-electron systems. Treating such systems requires the implementation of a polarizable model. For a discussion of polarizable FF and their properties, we refer to part IV.

2.2.4 Rigid Molecules

Forces acting within molecules are at least one order of magnitude greater than those acting between molecules. A direct consequence of this fact is that the time

scales associated with intramolecular motions are typically a factor 10-50 shorter than the time over which the translational velocity of a molecule changes appreciably. In a Molecular Dynamics simulation, the time step for the integration of the equation of motions should be "sufficiently" shorter than the shortest relevant time scale. If the intramolecular dynamics of the system is explicitly simulated (e.g. to compute vibrational spectra as in part III), the time step is chosen to be shorter than the highest vibrational frequency. This makes the simulation of molecular substances very time consuming. To tackle this problem *multiple time step algorithms* [58] can be implemented. If the intramolecular motion is not of interest, a reasonable alternative is to treat the bonds (and other intramolecular degrees of freedom) as rigid. The equations of motion are then solved under the constraint that the molecular structure does not change during the simulation. *Constrained dynamics* calculations have been performed in this thesis for all simulations in part II, where water molecules were always considered as rigid. Moreover, in part III the optimal geometry of single molecules was calculated under given constraints, using the same computational technique, namely the *SHAKE* algorithm [59–61]. Given a set of n constraints

$$\sigma_k = \sigma_k\left(\{\mathbf{r}\}\right) = 0 \qquad (k = 1, 2, \ldots, n), \tag{2.38}$$

the Newton equations for the constrained system can be written as

$$\frac{\mathrm{d}\mathbf{p}_i}{\mathrm{d}t} = -\nabla_i V(\mathbf{r}) - \sum_{k=1}^{n} \lambda_k \left(\frac{\partial \sigma_k}{\partial \mathbf{r}_i}\right), \tag{2.39}$$

where we have introduced the Lagrange multipliers λ_k, which have to be determined by the equations defining the constraints 2.38. The set $\{\lambda\}$ can be calculated simply solving a set of linear equations. Unfortunately this formal solution if of little practical use; since simulations are performed with discretized difference equations instead of continuos differential equations (see subsection 2.2.1), the round-off errors accumulated during the (time consuming) matrix inversion do not satisfy accurately the constraints which will break. In the SHAKE method, the set of exact $\{\lambda\}$ is substituted with a set of approximate parameters $\{\tilde{\lambda}\}$ which guarantees that the constraints are *always satisfied within a certain tolerance.*

To see how this works, let's consider the leapfrog algorithm (subsection 2.2.1). The constrained accelerations are

$$\mathbf{a}_i(t) = \frac{\mathbf{F}_i}{m_i} - \frac{1}{m_i} \sum_{k=1}^{n} \tilde{\lambda}_k \left(\frac{\partial \sigma_k}{\partial \mathbf{r}_i}\right)_t. \tag{2.40}$$

We can rewrite the equation 2.26 of the algorithm in the following form

$$\mathbf{r}_i(t+\delta t) = \mathbf{r}_i^{\text{unconst}}(t+\delta t) - \frac{\delta t^2}{m_i}\sum_{k=1}^{n}\tilde{\lambda}_k\left(\frac{\partial\sigma_k}{\partial\mathbf{r}_i}\right)_t, \tag{2.41}$$

which means that we can calculate the new positions $\{\mathbf{r}_i^{\text{unconst}}\}$ neglecting the effect of constraints, and correct the effect posteriorly. The set $\{\tilde{\lambda}\}$ should be determined by equation 2.38 at time $t+\delta t$. The process to find the corrected positions is iterative and sequential. At loop M we consider constraint k, being $\{\mathbf{r}_i^{\text{old}}\}$ the set of approximate positions at loop $M-1$. The new position for each particle i involved in constraint k is

$$\mathbf{r}_i^{\text{new}}(t+\delta t) = \mathbf{r}_i^{\text{old}}(t+\delta t) - \frac{\delta t^2}{m_i}\tilde{\lambda}_k^M\left(\frac{\partial\sigma_k}{\partial\mathbf{r}_i}\right)_t, \tag{2.42}$$

where the value $\tilde{\lambda}_k^M$ is found substituting $\{\mathbf{r}_i^{\text{new}}\}$ into the equation that defines the k^{th} constraint, and keeping only the first order result:

$$\tilde{\lambda}_k^M = \delta t^{-2}\frac{\sigma(\{\mathbf{r}_j^{\text{old}}\})}{\sum_{j=1}^{N} m_j^{-1}\left(\frac{\partial\sigma_k}{\partial\mathbf{r}_i}\right)_{\mathbf{r}^{\text{old}}}\cdot\left(\frac{\partial\sigma_k}{\partial\mathbf{r}_j}\right)_t}. \tag{2.43}$$

The process begins with the values $\{\mathbf{r}_i^{\text{unconst}}\}$ as the first input for $\{\mathbf{r}_i^{\text{old}}\}$, and finishes when the positions $\{\mathbf{r}_i^{\text{new}}\}$, after completing a loop, satisfy the constraints within a certain level of tolerance.

2.2.5 Calculated Properties

Once a Molecular Dynamics calculation is set up, structural, thermodynamical, dynamical and statistical properties of the system can be easily calculated [30, 31]. In particular, in this thesis, we concentrated our attention on the properties introduced below.

Radial Distribution Function (RDF)

Liquid structure is characterized by a set of distribution functions for the atomic (molecular center of mass) positions, the simplest of which is the pair or radial distribution function $g(r)$. This function gives information on the local structure as a function of the distance r from a chosen origin (atom or molecule):

$$g(r) = \frac{\rho(r)}{\rho} = \frac{\text{density of particles at distance } r \text{ from the origin}}{\text{density of the bulk}}, \tag{2.44}$$

From the above definition of $g(r)$ it is clear how to calculate it in a molecular simulation. We consider as origin a given molecule and explore the n^{th} spherical shell at distance $r + n\delta r$, where δr is a small separation. Then, an histogram $h(r + \delta r)$ is compiled of all pair separations falling within each spherical shell of volume $v_{shell} = 4\pi r^2 \delta r$. To gather higher statistical accuracy, the same operation is repeated for all N molecules and S steps. The discrete radial distribution function is then calculated as

$$g(r) = \frac{h(r + \delta r)}{\rho \times v_{shell} \times N \times S}. \tag{2.45}$$

In liquid state theory, $g(r)$ serves to calculate all thermodynamic properties of the system if the potential is pairwise additive. In our case, the RDF is useful to investigate the local structure around the ion and the spatial extension of each solvation shell; this information can be compared with X-ray and neutron diffraction experiments.

Potential of Mean Force

One property we are interested in is the potential of mean force (PMF) between the ion and a solvent molecule. Strictly speaking, the PMF is the potential that gives the force averaged over all the configurations of all the $N - 2$, molecules acting on one particle (j) at any fixed configuration of a pair of molecules:

$$-\nabla_j W^{(2)} = \frac{\int e^{-\beta V}(-\nabla_j V)\mathrm{d}\mathbf{q}_1 \ldots \mathrm{d}\mathbf{q}_{N-2}}{\int e^{-\beta V}\mathrm{d}\mathbf{q}_1 \ldots \mathrm{d}\mathbf{q}_{N-2}}, \tag{2.46}$$

where V is the potential energy and $\beta = 1/K_{\mathrm{B}}T$. $\nabla_j W^{(2)}$ is the average force and therefore $W^{(2)}$ is called the potential of mean force. In our studies we calculated the $W^{(2)}(r_{\mathrm{ion-solvent}})$, that describes the ion-solvent interaction at a distance r when the remaining $N - 2$ molecules are averaged over all configurations. It represents the free energy as a function of the ion-solvent distance. In molecular simulations it can be calculated from the RDF

$$W(\mathbf{r}) = -\frac{\ln g(\mathbf{r})}{\beta}. \tag{2.47}$$

In the *transition state theory* (see below), the one dimensional centrifugally averaged effective potential is used instead of the PMF; this is easily calculated from the PMF as

$$W_{eff}(r) = W(r) - \frac{2}{\beta}\ln\frac{r}{r^{\ddagger}}, \tag{2.48}$$

where $r^{\ddagger}$ corresponds to the barrier top distance.

Time Correlation Functions

The time correlation function (TCF) of a phase space function A is of great interest in computer simulations because it is connected with observable quantities. It is defined as

$$C_{AA}(t) = \langle A(t)A(0)\rangle, \tag{2.49}$$

and at equilibrium depends upon the separation between times only and not on the absolute value of time. In molecular dynamics simulations, where the phase space trajectory is determined at discrete time steps, the TCF C_{AA} is expressed as a sum:

$$C_{AA} = \frac{1}{n-k}\sum_{j=1}^{n-k} A(\mathbf{x}_k)A(\mathbf{x}_{k+j}) \qquad (k = 0, 1, 2, \ldots, n_c), \tag{2.50}$$

where n is the total number of time steps Δt, and $n_c << n$.

Within linear response, the dynamical properties of a system (transport coefficients, rate constant, spectra, etc.) are related with the TCF of an appropriate variable at equilibrium [62]:

1. the diffusion coefficient D_i of species i is given by

$$D_i = \frac{1}{3}\int_0^\infty \langle \mathbf{v}_i(t)\mathbf{v}_i(0)\rangle \mathrm{d}t, \tag{2.51}$$

   where $\mathbf{v}_i$ is the center of mass velocity of the i^{th} molecule. Alternatively it can be computed using the corresponding Einstein relation, valid at long times:

$$D_i = \frac{1}{6t}\langle |\mathbf{r}_i(t) - \mathbf{r}_i(0)|^2\rangle, \tag{2.52}$$

   where $\mathbf{r}_i$ is the molecule center of mass position. In practice this averages are computed for each of the N molecules in the simulation, the results added and divided by N to improve statistical accuracy.

2. the vibrational spectrum $S(\omega)$ of a molecule is

$$S(\omega) = (2\pi)^{-1}\int_{-\infty}^{\infty} \exp(-i\omega t)\langle \dot{\mathbf{M}}(t)\cdot\dot{\mathbf{M}}(0)\rangle \mathrm{d}t, \tag{2.53}$$

   where $\dot{\mathbf{M}}$ denotes the time derivative of the total dipole moment. Given that

$$\dot{\mathbf{M}} = \sum_i^{N_{mols}} \dot{\mu} = \sum_i^{N_{mols}}\sum_j^{N_{at}} \frac{\mathrm{d}}{\mathrm{d}t} q_j^i \mathbf{r}_j^i = \sum_i^{N_{mols}}\sum_j^{N_{at}} q_j^i \mathbf{v}_j^i, \tag{2.54}$$

   we can write the time correlation function $C_{\dot{\mathbf{M}}\dot{\mathbf{M}}}$ as a sum of modified velocity TCF (due to the charges multiplying the velocity). Its implementation is

straightforward, but long simulations are needed to sample good correlation functions with a low level of noise. As will be shown in part III, numerical techniques can be used to lower the noise in the final spectrum.

3. the solvent shell exchange can be seen as a dissociation-association reaction and can be studied in the framework of *transition state theory* (TST). In Molecular Dynamics simulations we can calculate the kinetic constant k using the *reactive flux* approach: we consider q^* the reaction coordinate at TS[‡], and $\theta(q) = 1$ if $q > 0$ and zero elsewhere (Heaviside function). We can calculate the kinetic constant as the correlation function

$$k(t) = \langle v(0)\delta[q(0) - q^*]\theta[q(t)]\rangle. \tag{2.55}$$

The right hand side of this equation gives the average flux crossing the TS surface, given that the trajectory ends up in the product basin; $k(t)$ is known as the reactive flux correlation function. The kinetic constant is given by the long time plateau of it [62].

The *residence time* of a first shell molecule can be obtained by the following TCF:

$$C(t) = \langle \theta(0)\theta(t)\rangle, \tag{2.56}$$

where θ is the Heaviside function defined above. The decay time τ of this function is the inverse of k; this represents an alternative method to the reactive flux for the calculation of the rate constant for first shell exchange [63, 64].

2.3 Optimization Algorithms

In subsections 2.1.6 and 2.2.2 we alluded to the concepts of geometry optimization and function minimization. Both problems belong to the same (vast) family of a mathematical discipline which is concerned with finding the maxima and minima of functions, possibly subject to constraints. Phenomena are described as functions of variable parameters $\mathbf{x} = (x_1, x_2, \ldots, x_n)$, and a single measure of quality $\chi(\mathbf{x})$, the objective function, is defined, whose extremum (maximum or

[‡]The Transition State (TS) is defined as the surface dividing two stable basins of the phase space (reactants and products).

minimum) corresponds to the optimal solution. Frequently, the optimum is constrained by additional equations (or inequalities) that have to be satisfied. The extremum could be either *global* or *local*; usually, finding a global extremum is a difficult task which is tackled in two ways: *(i)* shift the solution by a finite amplitude perturbation and check if the same solution is found again; *(ii)* compare the local extrema found starting from different initial conditions and take the best among them. Many different methods exist for solving minimization problems of various kinds [65]. None of them is universally applicable, although some are robust for many problems, e.g. the *simplex method*. Besides the geometry optimization algorithm which was already implemented in the Gaussian package, for the research faced in this thesis (part IV) two methods have been implemented: the cited simplex method and the *conjugate gradients method* [66]. In this section we give a brief overview of each of them.

2.3.1 The Simplex Algorithm

The simplex method [67] is an efficient iterative algorithm to solve unconstrained minimization problems numerically for several but not too many variables. It attempts to enclose the extremum inside an irregular volume defined by a *simplex*, an n-dimensional convex volume bounded by $(n-1)$-dimensional hyperplanes and defined by $n+1$ linearly independent corners, e.g. a triangle for $n=2$ and a tetrahedron for $n=3$. The algorithm starts with a first guess of $n+1$ initial conditions defining a simplex at $\mathbf{P}_0$. Then n versors $\mathbf{e}_i$ are defined and other n simplex are formed

$$\mathbf{P}_i = \mathbf{P}_0 + \lambda \mathbf{e}_i, \tag{2.57}$$

where λ represents the problem's characteristic length scale. The simplex size is continuously changed and mostly diminished. The operations of changing its form optimally with respect to the minimal/maximal function values found at the corners are *contraction, expansion* and *reflection*, each determining new simplex corner points by linear combinations of selected existing corner points. Finally the simplex becomes small enough to contain the extremum with the desired accuracy [65]. The simplex method has the advantage that it requires no gradient information. In part IV it has been used to optimize the Thole parameters for ion-molecule dimers.

2.3.2 The Conjugate Gradients Method

In part IV we will introduce the *shell model* which is used to implement molecular polarization in Molecular Dynamics simulations. The main point is that the atoms forming a molecule can be thought to consist of two charges: one is fixed in the molecular structure, while the other is linked to the first by a harmonic spring (which force constant is k). The problem of finding the equilibrium point of all the shells (which interact among them) is analogous to minimize the potential energy. It has been tackled formerly both with *steepest descent* [68] and conjugate gradients methods [69], the latter being used in this thesis. It consists of iterative relaxations which end when the forces are null. Consider $\mathbf{r}_i^{(n)}$ and $\mathbf{F}_i^{(n)}$ the position and force acting on the i^{th} shell at the n iteration. At the following iteration we displace this solution along the vector $\mathbf{d}_i^{(n)}$

$$\mathbf{r}_i^{(n+1)} = \mathbf{r}_i^{(n)} + \lambda \mathbf{d}_i^{(n)}, \tag{2.58}$$

where λ specifies the size of the displacement; the search vector is

$$\mathbf{d}_i^{(n)} = \mathbf{F}_i^{(n)} + \eta^{(n)} \mathbf{d}_i^{(n-1)}, \tag{2.59}$$

and the parameter $\eta^{(n)}$ is chosen to be

$$\eta^{(n)} = \frac{\sum_i \left|\mathbf{F}_i^{(n)}\right|^2}{\sum_i \left|\mathbf{F}_i^{(n-1)}\right|^2}. \tag{2.60}$$

At each time step, the position considered for the 1^{st} iteraction is taken from the equilibrium position of the previous time step; in this way less iteractions are needed to reach convergence of the algorithm. Finally, the last assumption needed is that, since the shells are never too far from the equilibrium position, the energy is nearly quadratic in $\mathbf{r}$. Given the above premises, the iterative cycle terminates when we arrive at a search direction in which no progress proves to be possible. As a convenient test of performance, the progress of minimization can be monitored calculating the root mean square force.

References

[1] A. Szabo and N. S. Ostlund, Modern Quantum Chemistry, Dover Publications, New York (1996).

[2] I. N. Levine, Quantum Chemistry (4^{th} edition), Prentice Hall International, Elglewood Cliffs (1991).

[3] C. J. Cramer, Essentials of Computational Chemistry, John Wiley and Sons, Chichester (2002).

[4] R. A. Friesner *P. Natl. Acad. Sci. USA* **102**, 6648 (2005).

[5] Capelle K. `http://arxiv.org/abs/cond-mat/0211443`

[6] C. C. J. Roothaan *Rev. Mod. Phys.* **23**, 69 (1951).

[7] R. Krishnan, H. B. Schlegel and J. A. Pople *J. Chem. Phys.* **1980**, 72 (4654).

[8] K. Raghavachari and J. A. Pople *Int. J. Quant. Chem.* **20**, 167 (1981).

[9] J. B. Foresman, M. Head-Gordon, J. A. Pople and M. J. Frisch *J. Phys. Chem.* **96**, 135 (1992).

[10] S. R. Langhoff and E. R. Davidson *Int. J. Quantum Chem.* **8**, 61 (1974).

[11] C. Møller and M. S. Plesset *Phys. Rev.* **46**, 618 (1934).

[12] S. Sabeo and P. Pulay *Ann. Rev. Phys. Chem.* **44**, 213 (1991).

[13] J. Čížek and J. Paldus *Physica Scripta* **21**, 251 (1980).

[14] P. Hohenberg and W. Kohn *Phys. Rev.* **136**, B864 (1964).

[15] W. Kohn and L. J. Sham *Phys. Rev.* **140**, A1133 (1965).

[16] A. D. Becke, *J. Chem. Phys.* **98**, 5648 (1993).

[17] C. Lee, W. Yang and R. G. Parr *Phys. Rev. B* **37**, 785 (1988).

[18] P. J. Stephens, F. J. Devlin, C. F. Chabalowski and M. J. Frisch *J. Phys. Chem.* **98**, 11623 (1994).

[19] M. J. Frisch, G. W. Trucks, H. B. Schlegel, G. E. Scuseria, M. A. Robb, J. R. Cheeseman, J. A. Montgomery, Jr., T. Vreven, K. N. Kudin, J. C. Burant, J. M. Millam, S. S. Iyengar, J. Tomasi, V. Barone, B. Mennucci, M. Cossi, G. Scalmani, N. Rega, G. A. Petersson, H. Nakatsuji, M. Hada, M. Ehara, K. Toyota, R. Fukuda, J. Hasegawa, M. Ishida, T. Nakajima, Y. Honda, O. Kitao, H. Nakai, M. Klene, X. Li, J. E. Knox, H. P. Hratchian, J. B. Cross, V. Bakken, C. Adamo, J. Jaramillo, R. Gomperts, R. E. Stratmann, O. Yazyev, A. J. Austin, R. Cammi, C. Pomelli, J. W. Ochterski, P. Y. Ayala, K. Morokuma, G. A. Voth, P. Salvador, J. J. Dannenberg, V. G. Zakrzewski, S. Dapprich, A. D. Daniels, M. C. Strain, O. Farkas, D. K. Malick, A. D. Rabuck, K. Raghavachari, J. B. Foresman, J. V. Ortiz, Q. Cui, A. G. Baboul, S. Clifford, J. Cioslowski, B. B. Stefanov, G. Liu, A. Liashenko, P. Piskorz, I. Komaromi, R. L. Martin, D. J. Fox, T. Keith, M. A. Al-Laham, C. Y. Peng, A. Nanayakkara, M. Challacombe, P. M. W. Gill, B. Johnson, W. Chen, M. W. Wong, C. Gonzalez and J. A. Pople, Gaussian, Inc., Wallingford CT. (`http://www.gaussian.com`).

[20] T. H. Dunning Jr. *J. Phys. Chem A* **104**, 9062 (2000).

[21] Æ. Frisch and M. J. Frisch, Gaussian 98 User's Reference (2^{nd} edition), Gaussian Inc., Pittsburgh (1999).

[22] J. Lipinski, H. Chojnacki *Int. J. of Quantum Chem.* **19** (5), 891 (1981).

[23] S. Simon, M. Duran and J. J. Dannenberg *J. Chem. Phys.* **105**, 11024 (1996).

[24] S. F. Boys and F. Bernardi *Mol. Phys.* **19**, 553 (1970).

[25] F. B. van Duijneveldt, J. G. C. M. van Duijneveldt-van de Rijdt and J. H. van Lenthe *Chem. Rev.* **94**, 1873 (1994).

[26] J. R. Thomas, B. J. DeLeeuw, G. Vacek, T. D. Crawford, Y. Yamaguchi and H. F. Schaefer III *J. Chem. Phys.* **99**, 403 (1993).

[27] H. B. Schlegel *J. Comp. Chem.* **3**, 214 (1982).

[28] R. S. Mulliken *J. Chem. Phys.* **23**, 1833 (1955).

[29] G. Tasi and I. Palinko, Topics In Current Chemistry Vol. 174, p. 45, Springer, Berlin (1995).

[30] M. P. Allen and D. J. Tildesley, Computer Simulation of Liquids, Clarendon Press, Oxford (1987).

[31] D. Frenkel and B. Smit, Understanding Molecular Simulation, Academic Press, San Diego (2002).

[32] M. E. Tuckerman and G. J. Martyna *J. Phys. Chem. B* **104**, 159 (2000).

[33] E. Fermi, J. Pasta and S. Ulam *Los Alamos Preprint* LA-1940 (1955).

[34] E. Fermi *Collected Papers* **II**, 978 (1965).

[35] B. J. Alder and T. E. Wainwright *J. Chem. Phys.* **26**, 1208 (1957).

[36] B. J. Alder and T. E. Wainwright *J. Chem. Phys.* **31**, 459 (1959).

[37] A. Rahman *Phys. Rev.* **136A**, 405 (1964).

[38] L. Verlet *Phys. Rev.* **159**, 98 (1967).

[39] R. W. Hockney *Methods Comput. Phys.* **9**, 136 (1970).

[40] H. J. C. Berendsen, J. P. M. Postma, W. F. Van Gunsteren, A. di Nola and J. R. Haak *J. Chem. Phys.* **81**, 3684 (1984).

[41] W. L. Jorgensen and J. Tirado-Rives *P. Natl. Acad. Sci. USA* **102**, 6665 (2005).

[42] W. D. Cornell, P. Cieplak, C. I. Bayly, I. R. Gould, K. M. Merz, D. M. Ferguson, D. C. Spellmeyer, T. Fox, J. W. Caldwell and P. A. Kollman *J. Am. Chem. Soc.* **117**, 5179 (1995).

[43] W. L. Jorgensen, D. S. Maxwell and J. Tirado-Rives *J. Am. Chem. Soc.* **118**, 11225 (1996).

[44] A. D. MacKerell, Jr., D. Bashford, M. Bellott, R. L. Dunbrack, Jr., J. D. Evanseck, M. J. Field, S. Fischer, J. Gao, H. Guo, S. Ha, D. Joseph-McCarthy, L. Kuchnir, K. Kuczera, F. T. K. Lau, C. Mattos, S. Michnick, T.

Ngo, D. T. Nguyen, B. Prodhom, W. E. Reiher, III, B. Roux, M. Schlenkrich, J. C. Smith, R. Stote, J. Straub, M. Watanabe, J. Wirkiewicz-Kuczera, D. Yin and M. Karplus *J. Phys. Chem. B* **102**, 3586 (1998).

[45] T. A. Halgren *J. Comput. Chem.* **17**, 490 (1996).

[46] N. L. Allinger, K. Chen and J.-H. Lii *J. Comput. Chem.* **17**, 642 (1996).

[47] T. H. Fischer, W. P. Petersen and H. P. Lüthi *J. Comput. Chem.* **16** (8), 923 (1995).

[48] P.-O. Norrby and T. Liljefors *J. Comput. Chem.* **19** (10), 1146 (1998).

[49] J. Hunger and G. Huttner *J. Comput. Chem.* **20** (4), 455 (1999).

[50] J. Wang and P. A. Kollman *J. Comput. Chem.* **22** (12), 1219 (2001).

[51] T. Strassner, M. Busold and W. A. Herrmann *J. Comput. Chem.* **23** (2), 282 (2002).

[52] P. W. Atkins and R. S. Friedman, Molecular Quantum Mechanics, Third Edition, Oxford University Press (1997).

[53] C. J. F. Böttcher, Theory of Electric Polarization, Second Edition, Elsevier, New York (1973).

[54] R. S. Berry, S. A. Rice and J. Ross, Physical Chemistry, Second Edition, Oxford University Press (2000).

[55] S. W. Rick and S. J. Stuart *Rev. Comput. Chem.* **18**, 89 (2002).

[56] M. Rigby, E. B. Smith. W. A. Wakeham and G. C. Maitland, The Forces Between Molecules, Oxford Science Publications, Oxford (1986).

[57] T. A. Halgren *J. Am. Chem. Soc.* **114**, 7827 (1992).

[58] M. E. Tuckerman, B. J. Berne and G. J. Martyna *J. Chem. Phys.* **97**, 1990 (1992).

[59] J. P. Ryckaert, G. Ciccotti and H. J. C. Berendsen *J. Comput. Phys.* **23**, 237 (1977).

[60] J. P. Ryckaert *Mol. Phys.* **55**, 549 (1985).

[61] G. Ciccotti and J. P. Ryckaert *Comput. Phys. Rep.* **4**, 345 (1986).

[62] D. Chandler, Introduction to Modern Statistical Mechanics, Oxford University Press, Oxford (1987).

[63] R. Rey and J. T. Hynes *Phys. Condens. Matter* **8**, 9411 (1996).

[64] R. Rey and J. T. Hynes *J. Phys. Chem.* **100**, 5611 (1996).

[65] W. H. Press, S. A. Teukolsky, W. T. Vetterling and B. P. Flannery, Numerical Recipes in Fortran 77 (2nd ed.), Cambridge University Press, Cambridge (1992).

[66] R. Fletcher, Pratical Methods of Optimization (vol 1, p. 63), Wiley, New York (1980).

[67] J. A. Nelder and R. Mead *Computer Journal* **7**, 308 (1965).

[68] M. J. Sangster and M. Dixon *Adv. Phys.* **25**, 247 (1976).

[69] P. J. D. Lindan and M. J. Gillan *J. Phys.: Condens. Matter* **5**, 1019 (1993).

Part II

Solvation and Ionic Mobility

This Part is devoted to the study of the solvation shell exchange mechanism, its thermodynamic state dependence and on its relationship with ion and solvent diffusion. A short summary of each chapter is given below:

Chapter 3 Hydration shell exchange of $Li^+(aq)$ is analysed from the standpoint of reaction rate theory for a wide set of thermodynamic conditions, with an emphasis on the supercritical regime, viewing the exchange as an association-dissociation process. It is found that the free energy dependence upon the reaction coordinate of the ion-water complex maintains similar features in ambient and supercritical water, in contrast with related activated processes such as ion pair association. The activation free energy increases with decreasing density (with an inflexion point *circa* 0.3 g cm^{-3}) although it does not parallel the strong decrease in dielectric constant that takes place, at variance with continuum theory. The substantial increase in exchange rate from ambient to supercritical conditions cannot be simply adscribed to the temperature difference, but to an interplay of temperature and thermodynamic state dependence of the activation free energy, while the dynamic features of the exchange are substantially independent of bulk properties. The present system provides a first computational test of Transition State Theory in supercritical fluids, showing that it overestimates the rate constant by approximately a factor of two, being slightly more successful than in ambient water.

Chapter 4 It is shown that, for a tightly bound ion-solvation shell complex, the mean square displacement for solvation molecules is characterized by a long lasting transitory. This initial portion is related to the rotational relaxation of the complex and can reach up to several hundred picoseconds for a representative example such as the Mg^{2+} ion in water. As the diffusion coefficient is usually fitted using much shorter time spans, unnoticed overestimations are possible. It is argued that, instead of computing the aforementioned diffusion coefficient from the mean square displacement, it should be defined taking as a basic guideline the ratio between the rotational relaxation time of the complex and the lifetime within the first solvation shell.

Chapter 5 The connection between diffusion and solvent exchanges between first and second solvation shells is studied by means of Molecular Dynamics simulations and analytic calculations, with detailed illustrations for water

exchange for the Li^+ and Na^+ ions, and for liquid argon. First, two methods are proposed which allow, by means of simulation, to extract the quantitative speed-up in diffusion induced by the exchange events. Second, it is shown by simple kinematic considerations that the instantaneous velocity of the solute conditions to a considerable extent the character of the exchanges. Analytic formulas are derived which quantitatively estimate this effect, and which are of general applicability to molecular diffusion in any thermal fluid. Despite the simplicity of the kinematic considerations, they are shown to well describe many aspects of solvent exchange/diffusion coupling features for non-trivial systems.

Chapter 3

Reaction Rate Theory Approach to Thermodynamic State Dependence of Hydration Shell Exchange for $Li^+(aq)$

The exchange of a water molecule in the first hydration shell of an ion is a phenomenon of long standing interest [1], particularly for ionic transport [2] and for reactions of the ion with other species, where the hydration shell must rearrange [3]. However, computational studies have usually focused on the calculation of hydration shell lifetimes from equilibrium simulations, paying little attention to the detailed character of the exchange. Moreover, such an approach is limited in its scope, as it is not computationally feasible in cases with exchange times exceeding the nanosecond time scale. To overcome these limitations, a method based on reaction rate theory was implemented by Rey and Hynes to study the aqueous Na^+ ion [4] in a unimolecular dissociation perspective. It is similar to that used for contact ion pair to solvent-separated ion pair interconversion reactions [5–7], being equivalent to the usual equilibrium simulations regarding the final value

for the exchange time. As a major advantage, the exchange process is viewed from a richer point of view, as it highlights the equilibrium and nonequilibrium contributions [4], and the computation focuses on the critical parts of the exchange process, which can therefore be easily analysed [8]. This methodology has been recently applied to $Li^+(aq)$, allowing for a detailed study of the exchange mechanisms [9].

Here this perspective is extended to a broad set of thermodynamic conditions for Li^+. Starting from ambient water (AW), where the aforementioned studies were performed, the calculations extend to supercritical water (SCW), a regime that has attracted considerable theoretical attention, due to its technological applications and to the challenge of providing a convenient theoretical framework [10, 11]. Concerning the behaviour of small ions in SCW, several computational studies have addressed equilibrium ion solvation [12–17] (see Ref. [18] for a review) and dynamics [19–25]— mainly analysing diffussion and conductivity, but including the computation of hydration shell exchange times as well [20, 22–24]. From this body of results a couple of aspects constitute a main motivation for the present work. First, from the solvation studies it is clear that large changes of the ion-oxygen radial distribution function ($g(r)$) take place when entering SCW. In Figure 3.1(a,b) the results for Li^+ in liquid water (along the coexistence curve) and in SCW (at several densities) are displayed. While in the liquid phase the first peak shows only slight variations in height, never exceeding a value of ≈ 14, in SCW the first peak reaches values of up to 35, while the first minimum seems rather low in all cases. This suggests interesting dynamical changes with thermodynamic state, if viewed from the unimolecular dissociation perspective. The activation free energy for ion-water dissociation (in units of k_BT) is approximately obtained from the expression (see below)

$$\frac{\Delta G}{k_BT} \approx ln\left[\frac{g(r_{max})}{g(r_{min})}\right], \tag{3.1}$$

where r_{max} and r_{min} denote the positions of the first maximum and first minimum respectively. Inspection of the plots (Fig. 3.1), together with formula 3.1, are strongly suggestive of the possibility of substantial variations in $\Delta G/k_BT$, which would increase as the density was lowered, hindering the exchange process. The dielectric behaviour of water in the supercritical regime would in principle support such variations. It is known [11] that a variation in density from 0.5 g/cm^3 to 0.14 g/cm^3, results in a variation of the dielectric constant from a polar value of

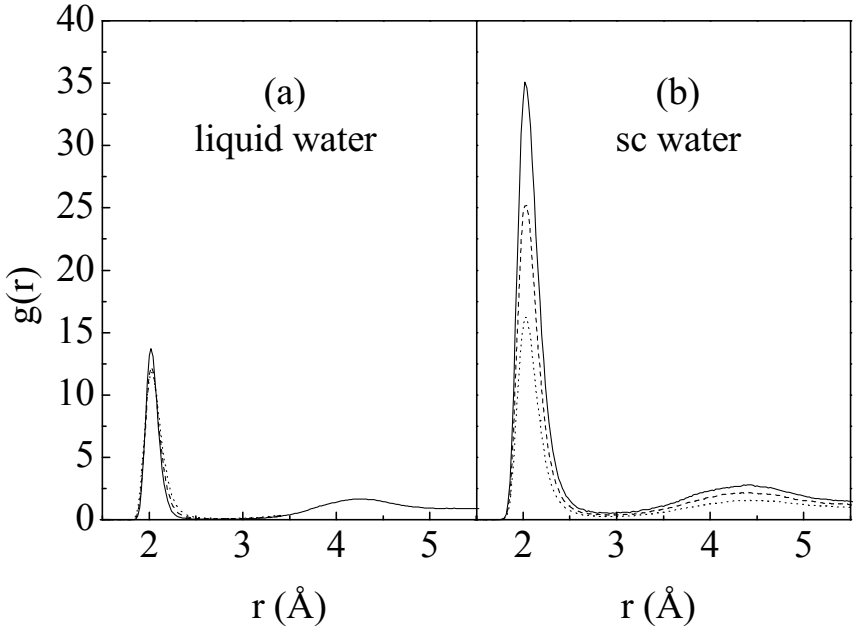

Figure 3.1. Ion-water center of mass radial distribution functions. (a) Li^+ in liquid water at T=298 K, ρ=0.997 g cm^{-3} (solid line), T=373 K, ρ=0.958 g cm^{-3} (dashed line) and T=473 K, ρ=0.850 g cm^{-3} (dotted line); (b) Li^+ in supercritical water at T=683 K and ρ=0.22 g cm^{-3} (solid line), ρ=0.31 g cm^{-3} (dashed line) and ρ=0.48 g cm^{-3} (dotted line).

$\epsilon = 10$ to a nonpolar value of $\epsilon = 2$. Given the strong electrostatic forces present it seems reasonable to expect that for lower densities, and therefore smaller dielectric constants, much higher activation barriers should result, as the bulk solvent would not decrease the activation barrier as much as in AW. Precisely such behaviour has been found for ion pair association in SCW [26, 27], where the contact ion pair configuration is substantially more stable (by a factor of ≈ 20) as the density is lowered [26] down to 0.2 g/cm^3.

Finally, regarding the possible effect on the exchange times, given that in the Transition State Theory (TST) approximation there is an exponential relationship between the rate constant and $\Delta G/k_BT$, one could also expect a noticeable increase (see below) of the hydration shell exchange time (the inverse of the reaction rate constant) as the density of SCW is lowered (at constant temperature).

At variance with these considerations, computational studies focusing on dynamics have shown that very fast exchange times (on the order of 3-6 ps) are obtained in SCW which, in addition, show almost no dependence with density. This is in contrast with AW, where times of about 30 ps for Na^+ and in the order of 100 ps for Li^+ are obtained [4, 9]. Certainly, since the temperature of SCW is

higher, shorter times should be obtained. However, the temperature contribution is in principle already taken into account in Eq. 3.1, as ΔG is given in units of k_BT. Such results suggest that the increase in ΔG, from AW to SCW, with decreasing density is not substantial. The almost null effect of large variations in density, within the supercritical regime, is probably more suprising, as it contrasts with the strong variations in peak height of the maximum of $g(r)$ as a function of density (Fig. 3.1(b)), as previously argued.

From the reaction rate theory standpoint adopted here there are two, possibly overlapping, explanations. In one limit the height of the first minimum ($g(r^{\ddagger})$) would increase with decreasing density, compensating exactly the increase of the first maximum and thus keeping $\Delta G/k_BT$ almost constant. This would be consistent with the known fact that the first shell hydration number does not change down to very small densities [14]. A second explanation makes use of the transmission coefficient (κ), the dynamical correction to TST, which would tend to one as the density is lowered, consistent with a decrease of recrossings with lower density. Such an increase of κ would compensate any increase in activation energy and render the exchange time constant, signaling a change in the dynamics as the density is lowered and possibly, the validity of TST. In this work we intend to clarify which mechanism is dominant or if a combination of both is required to explain the results, depending on the phase.

Finally, it is interesting to note that the computational study of reaction kinetics in SCW at the molecular level has just started, so that simple questions such as the likelihood of TST breakdown in SCW are being asked [11]. Only two activated processes have been addressed so far (a S_N2 type reaction [14] and ion pair association [26,27]), limited to the calculation of free energy barriers. We are not aware of any computational study of the dynamical corrections (transmission coefficient) to the TST estimates in supercritical fluids. While hydration shell exchange constitutes a most simple case, it allows for a comprenhesive study of κ over a broad range of thermodynamic conditions. Moreover, given that there is a large variation in density from AW to SCW, it is of interest to explore any possible effect stemming from changes of the friction. The theory of reactions in condensed phase predicts the existence of a reaction rate turnover as a function of viscosity, arising from purely dynamical effects [28–30]. Therefore, the present study may offer the possibility of directly obtaining, from simulation of a realistic system, the reaction rate turnover which has been experimentally observed in other more standard reactive processes [10].

ρ (g cm^{-3})	(ρ_r)	T (K)	(T$_r$)	ΔG (kJ mol^{-1})	$\Delta G/k_BT$	ΔW (kJ mol^{-1})	ω_0 (ps^{-1})	N$_{hyd}$
0.04	0.112	673	1.052	21.4	3.8	25.8	102	4.1
0.10	0.345	”	”	21.7	3.7	25.6	104	4.1
0.15	0.517	”	”	20.6	3.7	24.7	103	4.1
0.18	0.621	”	”	20.3	3.6	24.3	99	4.1
0.22	0.758	”	”	20.1	3.6	24.2	102	4.1
0.31	1.069	”	”	19.8	3.5	23.9	103	4.2
0.48	1.655	”	”	19.6	3.5	23.6	103	4.2
0.20	0.699	683	1.067	20.3	3.6	24.3	101	4.1
0.35	1.207	”	”	19.8	3.5	24.0	103	4.2
0.48	1.655	”	”	19.3	3.4	23.5	103	4.2
0.67	2.310	”	”	18.3	3.2	22.3	103	4.1
0.85	2.931	”	”	16.9	3.0	20.9	102	4.2
0.958	3.290	”	”	16.0	2.4	19.9	99	4.2
0.997	3.438	”	”	15.6	2.7	19.5	97	4.5
0.67	2.310	573	0.835	18.1	3.8	21.3	103	4.2
0.85	2.931	473	0.739	16.8	4.3	19.0	103	4.2
0.958	3.290	373	0.583	14.9	4.7	16.8	103	4.2
0.997	3.438	298	0.466	14.5	5.9	15.8	104	4.1

Table 3.1. Equilibrium properties obtained for the thermodynamic state points studied.

In the following section we summarize the theoretical framework and we describe the simulation techniques, models and thermodynamic points studied. The main results are presented and discussed in Section III, while the final conclusions are summarized in Section IV.

3.1 Theory and Simulation

3.1.1 Theory

The reaction coordinate is defined as the distance (r) from the ion to the water molecule center of mass [4], viewing the process in a unimolecular dissociation perspective. In general, the dissociation rate constant can be written as the product $k = \kappa k^{TST}$, where k^{TST} denotes the Transition State Theory (TST) rate constant, and κ the transmission coefficient. In the particular case of ion hydration, given that each ion is surrounded by several waters, the free energy or potential of mean force (pmf) can be determined with acceptable statistics (for the ions studied here) from the radial distribution function [31], without recourse to lengthy calculations of free energy differences

$$W(r) = -\beta^{-1} \ln(g(r)). \tag{3.2}$$

Notice that from this equation we easily obtain the approximate (see below) relationship for the activation free energy embodied in Eq. 3.1. Once the pmf is computed, k^{TST} can be readily determined from the following expression [6],

$$k^{TST} = \sqrt{\frac{k_B T}{2\pi\mu}} \frac{r^{\ddagger 2} e^{-\beta W(r^\ddagger)}}{\int_0^{r^\ddagger} dr r^2 e^{-\beta W(r)}} = \sqrt{\frac{k_B T}{2\pi\mu}} \frac{e^{-\beta W_{eff}(r^\ddagger)}}{\int_0^{r^\ddagger} dr e^{-\beta W_{eff}(r)}}, \tag{3.3}$$

which defines the centrifugally averaged effective potential [7, 30, 32]

$$W_{eff}(r) = W(r) - \frac{2}{\beta} \ln(r/r^\ddagger), \tag{3.4}$$

from which the activation free energy will be computed. μ is the ion-water molecule pair reduced mass, and $r^\ddagger$ indicates the barrier top position (Transition State, TS). Finally, there is an approximate expression for the TST rate which is particularly illustrative [33] for its simplicity, and which results from fitting a parabola to the first well of the effective pmf

$$W_{eff}(r) \cong W_{eff}(r_0) + \frac{1}{2}\mu\omega_0^2 (r - r_0)^2. \tag{3.5}$$

Here r_0 denotes the position of the first minimum of $W_{eff}(r)$ (or equivalently, the first *maximum* of $g(r)$) and ω_0 the associated frequency. If an approximate integration of Eq. 3.3 is performed [33], the following expression is obtained

$$k^{TST} \cong \frac{\omega_0}{2\pi} e^{-\beta \Delta G}, \tag{3.6}$$

where $\Delta G \equiv W_{eff}(r^\ddagger) - W_{eff}(r_0)$. This relation clearly shows how the rate constant can be understood as the frequency of attempts to jump over the barrier times a correction factor with an Arrhenius like dependence on the activation barrier. In the present context we get (see Eqs. 3.2 and 3.4)

$$k^{TST} \cong \frac{\omega_0}{2\pi} \frac{g(r^\ddagger)}{g(r_0)}, \tag{3.7}$$

which evidences the direct relationship between the rate and the height of the radial distribution function (as succinctly described in the Introduction), with no explicit temperature dependences. This relation shows how the rate constant decreases if $g(r)$ increases the value of its first maximum $g(r_0)$, explaining why one might expect a noticeable increase in exchange time with decreasing density from inspection of Fig. 3.1(b).

In principle, the transmission coefficient can be determined from the plateau value of the normalized reactive flux [34], computed in the constrained reaction

coordinate ensemble [35]. This calculation requires the generation of configurations with the reaction coordinate constrained at the TS, which after the release of this constraint and the sampling of velocities according to a thermal distribution, are followed in time. Fortunately, the present problem also allows a direct calculation of κ, given the short time scale for the escape from the first hydration shell. Given an initial equilibrium configuration, we start a long simulation run and compute the residence time correlation function (tcf) [4, 20, 36]

$$n(t) = \frac{1}{N_h} \sum_{i=1}^{N_h} \theta_i(r,t)\theta_i(r,0), \tag{3.8}$$

where $\theta(r,t)$ is 1 if the molecule is within the first hydration shell (defined by a maximum separation $r^{\ddagger}$ between the ion and the water molecule center of mass), and 0 otherwise. N_h denotes the number of water molecules initially within the first shell. The behaviour of $n(t)$ is well represented by an exponential with characteristic exchange time $\tau_{ex} = k^{-1}$. It was shown in the case of Na^+ in AW that this method provides results coincident with those obtained from reactive flux simulations [4].

To summarize, both the TST estimation for the rate (k^{TST}) and the transmission coefficient (κ) can be obtained from rather short simulations (if the exchange time is below the nanosecond time scale). The former involves the calculation of $g(r)$ (Eq. 3.2), while the latter is obtained after the total rate constant k is fitted from the residence time tcf. In this way, it is possible to scan a broad range of thermodynamic conditions and study the behaviour of these (k, κ, k^{TST}) and other relevant quantities (like activation free energy, diffussion coefficient and hydration number) with a reasonable computational effort.

3.1.2 Computational Details

We have performed simulations of an ion (Li^+) plus 215 water molecules in a cubic box with standard periodic conditions. The water model is SPC/E [37], keeping the water molecules rigid via the shake algorithm [38]. In order to ease comparison with previous work, the interaction parameters chosen in this work are those developed by Dang [39], as these have been amply used in recent studies of supercritical ionic solutions [17, 23, 24]. Long-range forces were computed by the Ewald summation method [40], and a leap-frog integration algorithm with coupling to a thermal bath [41] has been used, with a 1 fs time step, and the value of the coupling set to 0.1 ps. Experimental values for the critical properties

ρ (g cm^{-3})	(ρ_r)	T (K)	(T$_r$)	τ (ps)	k (ps^{-1})	k^{TST} (ps^{-1})	k$^{TST}_{approx}$(ps^{-1})	κ
0.05	0.112	673	1.072	8.7	0.11	0.30	0.35	0.38
0.10	0.345	673	”	7.4	0.13	0.33	0.39	0.41
0.15	0.517	673	”	7.0	0.14	0.35	0.41	0.41
0.18	0.621	673	”	7.0	0.14	0.36	0.42	0.39
0.22	0.758	673	”	6.7	0.15	0.37	0.45	0.39
0.31	1.069	673	”	6.2	0.16	0.40	0.48	0.40
0.48	1.655	673	”	6.0	0.17	0.42	0.46	0.40
0.20	0.699	683	1.067	6.9	0.14	0.38	0.46	0.38
0.35	1.207	683	”	6.3	0.16	0.42	0.50	0.38
0.48	1.655	683	”	5.9	0.17	0.45	0.54	0.38
0.67	2.310	683	”	5.0	0.20	0.53	0.65	0.38
0.85	2.931	683	”	4.0	0.25	0.66	0.83	0.38
0.958	3.290	683	”	3.6	0.28	0.76	0.95	0.36
0.997	3.438	683	”	3.4	0.30	0.81	0.99	0.37
0.69	2.310	573	0.895	8.5	0.12	0.31	0.36	0.38
0.85	2.931	473	0.739	13.6	0.07	0.20	0.23	0.36
0.958	3.290	373	0.583	25.4	0.04	0.12	0.13	0.33
0.997	3.438	298	0.466	56.8	0.02	0.07	0.05	0.26

Table 3.2. Kinetic data obtained for the thermodynamic state points studied; $k^{TST}_{approx} = \omega_0/2\pi \exp(-\Delta W_{eff}/k_B T)$.

of water (T_c = 647.13 K, ρ_c = 0.322 g cm^{-3} and P_c = 220.55 bar) [42] are reasonably reproduced by SPC/E water (T_c = 640 K, ρ_c = 0.29 g cm^{-3} and P_c = 160 bar) [43]. The system has been studied over a wide range of thermodynamic conditions both above and under the critical point (see table 1). The simulations can be grouped in two different sets:

(a) Above the critical point ($T > T_c$) the density of the system has been changed continuosly from the values typical of ambient liquid water down to very small densities, for two different temperatures (673 K and 683 K).

(b) Temperature and density of liquid water was varied along the liquid-vapour coexistence curve from AW up to close to the critical point.

In each case, after an equilibration of 500 ps, data collection is performed over 3-blocks of 500 ps. The calculation of the diffusion coefficient in SCW at very low densities is particularly difficult [25], with noticeable variances in the mean square displament tcf, and long lived velocity self correlation functions. Nevertheless, both methods provide coincident estimates within statistical error, which is estimated to be roughly a 10% of the computed value [25] of the diffusion coefficient.

3.2 Simulation Results and Analysis

3.2.1 Potentials of Mean Force

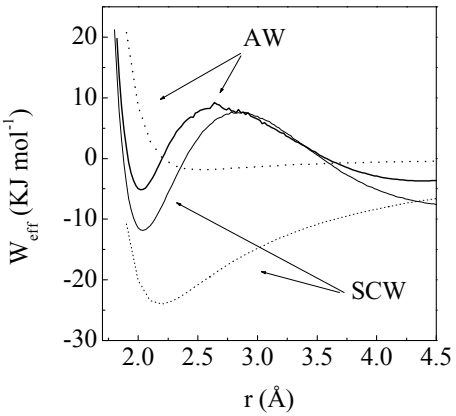

Figure 3.2. Potential of mean force for Li^+-water. Solid line: ambient water ($\rho = 0.997 g/cm^3$, $T = 298K$) and supercritical water ($\rho = 0.20 g/cm^3$, $T = 683K$) as obtained from the MD simulations; dashed line: same conditions using the continuum model.

From the computed ion-water center of mass radial distribution function it is straightforward to obtain the effective pmf for each thermodynamic state (see Eqs. 3.2 and 3.4). Figure 3.2 displays the pmf at two selected state points: ambient water ($\rho = 0.997 g/cm^3$, $T = 298K$) and supercritical water ($\rho = 0.20 g/cm^3$, $T = 683K$). A first minimum corresponding to the water molecule in the first hydration shell of the ion appears in both cases, with no noticeable differences in position. From this plot the process can be viewed, borrowing the definitions from ion pair association, as a transition between what might called contact ion-water (CIW) to a solvent separated ion-water (SSIW) complex.

Contrary to the ion pair case [26,27] both configurations can be found for any thermodynamic condition (with the interconversion barriers actually increasing for lower densities), while for ion pair association SSIP (solvent separated ion pair) is not present at low densities. Regarding the barrier to dissociation, while it is larger in SCW, the increase of the first well (CIW) depth is rather modest if we compare it with that found for the Na^+-Cl^- ion pair. While for the latter it deepens by a factor of roughly 20 [26], here it increases by a mere 40 %. This is surprising if we consider that activation energies for ion pair dissociation in AW are comparable to those of ion-water dissociation. The Na^+-Cl^- pair has been extensively studied in AW and the barrier from CIP (contact ion pair) to SSIP has consistently resulted to be in the range 3-5 k_BT [26, 44–50]. This value is *lower* in AW than the Li^+-water barrier to dissociation, which is found here to be of 5.9 k_BT (see Table 3.1), and $5k_BT$ in a model including 3-body

interactions [9]. Therefore, it turns out that this situation is largely inverted in supercritical conditions, a fact highlighted by the following simple continuum model estimations.

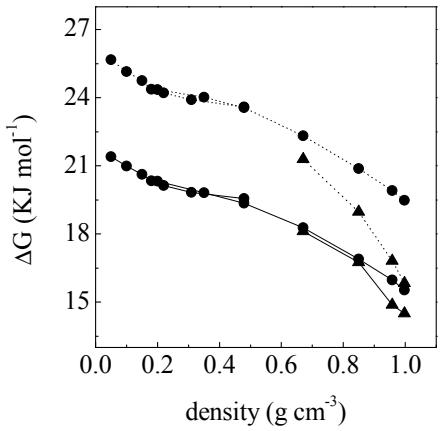

Figure 3.3. Solid line: ΔG from effective potential of mean force ($W_{eff}(r)$); dashed line: ΔW from 3-D potential of mean force ($W(r)$). Circles: supercritical water; triangles: liquid water.

Fig. 3.2 includes the pmf obtained if the ion-water interaction were simply screened by the bulk solvent dielectric constant. It can be seen that the first minimum in AW is substantially deeper than the one from continuum theory, a feature that also differences it from ion pair association [26, 48] (although for like charged ion pairs the first minimum can be slightly lower than the continuum estimation [51]). While the continuum estimates show differences in well depth of roughly a factor of 20, much smaller differences for the computed pmf are observed. It is to be noted that this small difference results from a twofold effect: the first well is deeper in AW than predicted by the continuum theory and, in addition, it is much shallower in SCW than predicted by this same approximation. Therefore, the charge-charge interaction of the ion pair is comparatively much less screened at lower dielectric constants, compared to the more feeble charge-dipole interaction of the ion-water system. The comparably smaller effect for the ion-water interaction must be attributed to smaller changes in local structure, which will be the subject of the following section. This modest increase in well depth is largely responsible for the noticeable acceleration of exchange rate, as will be described in more detail within.

Figure 3.3 displays the values of ΔG for each thermodynamic point studied, with a steady increase in activation energy from AW to very low density SCW. It should be noted that down to a density of 0.6 g/cm^3 two curves have been computed. The lower one corresponds to the liquid-gas coexistence region, *i.e.*, both density and temperature are varied. To disentangle the effects of temperature and density, a second set of calculations has been performed with the same densities but for a constant (supercritical) temperature of 683 K. The differences between

both of them are almost negligible, so that we must attribute most of the change in activation free energy to density variations. For densities below, and including, 0.48 g/cm^3, which corresponds to the supercritical region for both density and temperature, two different temperatures have been used (673 K and 683 K). The results from both sets are indistinguishable on the plot, again reflecting a feeble dependence on temperature. While, as expected, there is an increase of ΔG with decreasing density, from Eq. 3.6 the dissociation rate constant depends on the quotient $\Delta G/k_BT$ (see Fig. 3.4 and Table 3.2). Obviously the high temperature in SCW is critical in diminishing this factor, and thus speeding up the exchange time, what will be discussed in more detail within.

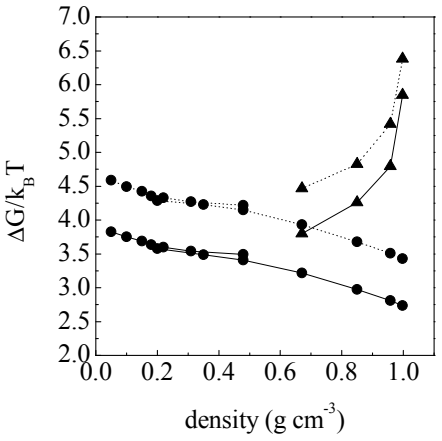

Figure 3.4. $\Delta G/k_BT$ for the thermodynamic states studied; same symbols as in Fig. 3.3.

While the focus of this work is on hydration shell exchange rather than mobility, it is interesting to observe that within the fully supercritical regime (points with density below 0.6 g/cm^3 in Fig. 3.3) there is an inflexion point near ≈ 0.3 g/cm^3, where the activation energy as a function of density changes its curvature, so that the increase in ΔG gets comparatively faster with decreasing density from that point on. This fact might be related with the conductivity slow down found experimentaly [52] in that region, which has been the focus of intense computational study [20–22, 25]. While the present model for Li^+ is not specially well suited as it underestimates the slow down compared with experiment [22], it is remarkable that such inflexion is found even in this case. Preliminary calculations for other ions show a rather similar behaviour. Therefore, the activation energy calculated here might be a pertinent quantity in this connection, as it is the single factor controling the exchange dynamics (it will be seen within that other factors are secondary), which in turn might be coupled to diffusion and explain the conductivity slow down. While the mean ion-water energy for first shell molecules shows a steady increase with decreasing density, and thus has been used to explain mobility changes [20, 22], it does not seem to show the curvature change displayed by ΔG, and is only indirectly related with

the exchange process. The possible implications for ion mobility of an approach based on the activation free energy of exchange will be addressed in future work.

Returning to the factors that condition the behaviour of ΔG, indirect temperature effects can be found if the 3-D pmf $W(r)$ (Eq. 3.2) is used to compute ΔG rather than the 1-D effective potential of mean force $W_{eff}(r)$ (see Figure 3.3). The effective potential has a contribution explicitly dependent on temperature (last term in Eq. 3.4), which results from averaging over different orientations [30, 32], and which gives rise to substantial differences. In AW this contribution is barely noticeable, rougly a 7 % (similar results were obtained for Na^+-water dissociation in AW [7]). As this term is directly proportional to T, the difference grows steadily as the supercritical regime is approached (as measured by the temperature), where it attains its maximum. For a supercritical temperature of 683 K the effective potential barrier is a substantial 25 % lower than what might be inferred from $W(r)$. Therefore it is important to distinguish between both types of potentials when discussing the application of TST to the present problem.

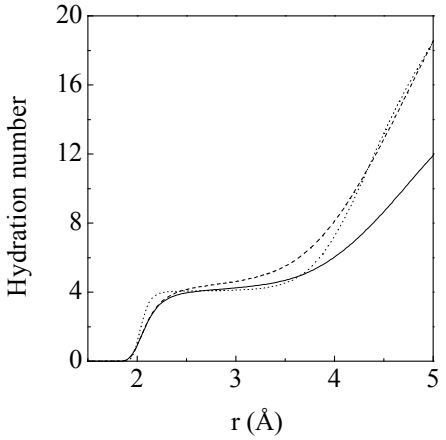

Figure 3.5. Hydration number as a function of the distance ion-water centre of mass, as defined in Eq. 3.9, for three thermodynamic states: T=683 K and ρ=0.48 g cm^{-3} (solid line), T=683 K and ρ=0.997 g cm^{-3} (dashed line) and T=298 K and ρ=0.997 g cm^{-3} (dotted line).

3.2.2 Structure

Radial Dependence

We now turn to the structural changes that take place with decreasing density in order to understand the modest increase of activation energy. All simulation studies to date have shown that the hydration number is almost constant down to very low densities, which is indicative of only slight changes in structure. It is worth investigating the distance at which this robust first shell hydration declines, or any feature of the first shell that might have been averaged out in computing the hydration number. Radial distribution functions are not convenient in this connection as they do not inform on the absolute number of hydration molecules.

A simple alternative consists in computing the hydration number as a function of the distance (R) to the ion [12]

$$n(R) = 4\pi\rho \int_0^R g(r) r^2 dr. \tag{3.9}$$

Results for $n(R)$, for a few representative thermodynamic conditions, are displayed in Figure 3.5. For their interpretation it is worth noting, from Fig 3.1, that the first hydration shell can be defined by the interval [2,2.7] Å, and the second shell by [2.7, 5] Å, although there is a marked minimum (small density) in the interval [2.5,3.5] Å. From Fig. 3.5 we see that the plateau reaching up to 3.5 Å is common to almost all thermodynamic conditions, with an hydration number of roughly 4 (a probable value for Li^+, lacking an unambiguous experimental measure, see Ref. [9]). The only marked departure is for liquid densities at high temperatures, for which roughly an additional molecule can fit within the space [2.5,3.5] Å in which ordinarily there is almost null density. Therefore, excepting this case, the only noticeable difference is a slight decrease in the first shoulder (at about 2.1 Å) for decreasing density. The more marked differences are found within the second shell. While for AW the total number of molecules within a sphere up to 5 Å is of roughly 18, for SCW ($\rho = 0.48$ g/cm^3, $T = 683$ K) it is of ≈ 12, a 30 % lower. Liquid density at 683 K shows again a peculiar behaviour, the total number of molecules including the second shell is the same as in AW (thus compensating the first shell differences). Values for the hydration number (integration up to the first minimum of $g(r)$) are summarized in Table 3.1 and Figure 3.6. A rather constant value of ≈ 4.15 results for the hydration number, excepting liquid densities at high temperature (T=683 K), where it climbs up to ≈ 4.5. A slightly decreasing number is also clearly displayed for densities below 0.3 g/cm^3, an effect which will be further discussed in the analysis of the exchange

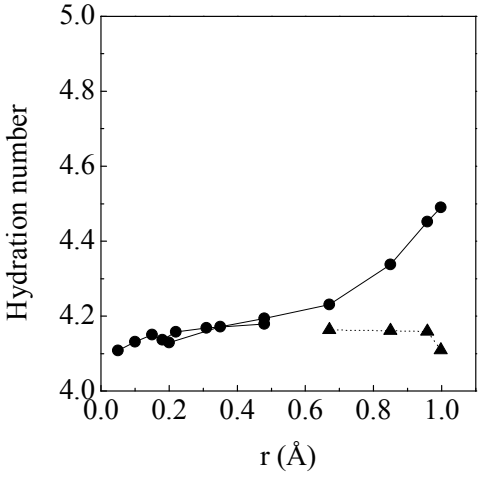

Figure 3.6. First shell hydration number as a function of thermodynamic state. Circles and solid line: supercritical water; triangles and dotted line: liquid water.

dynamics.

The present results have been averaged over all configurations, while it might be the case that the supercritical regime might demand a more detailed approach. In particular, there might be a broad distribution of hydration numbers, which the mean values computed here averages out, providing a wrong picture. It has been pointed for instance that in order to explain self diffusion in pure supercritical fluids a proper account of the distribution of environments might be required [53]. This issue has been analysed here only for first shell hydration, as a detailed analysis including the outer shells would demand a high amount of computation. From the results displayed in Fig. 3.7(a,b), we can conclude that the instantaneous hydration number shows small fluctuations, except for high densities and temperatures. The number of 4-coordinated configurations found for AW and SCW (at low densities) is quite similar ($\approx$ 80 %), differing by less than 10 % from each other (Fig. 3.7(a)), so that the strong electrostition of the ion is able to maintain a stable 4-coordinated first shell at any instant. The small decrease in four coordinated ions with density is approximately compensated by a slight increase in five coordinated ions ($\approx$ 15 %). Again, the peculiar behaviour of liquid densities and high temperatures (683 K) is evidenced by a progressive equilibration of four and five coordinated ions with increasing density. Configurations with 3 and 6 molecules play a largely negligible role, although specific trends can also be found (Fig. 3.7(b)). While along the coexistence curve there is an almost equal proportion of 3 and 6-coordinated configurations (less of 1 % in each case), within the low density supercritical regime the 3-coordinated ions outweight the 6-coordinated cases by a factor of $\approx$ 7, a proportion which is inverted (albeit to

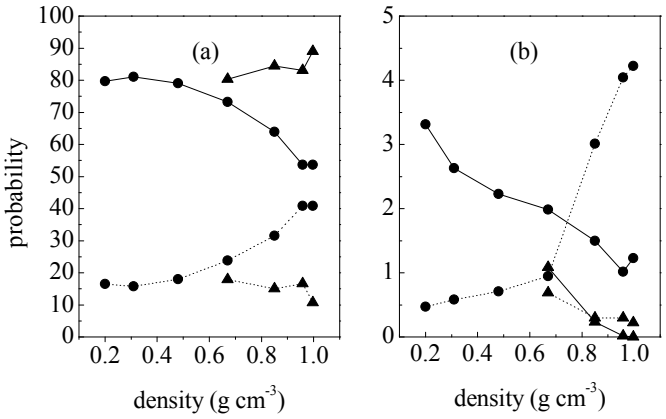

Figure 3.7. Probabilities for each hydration number as a function of thermodynamic state in supercritical (circles) and liquid water (triangles). (a) 4-coordinated (solid line) and 5-coordinated ions (dotted line); (b) 3-coordinated (solid line) and 6-coordinated ions (dotted line).

a lesser extent) for high densities and temperatures.

The link between structure and activation free energy can only be qualitatively explored from the present results, a quantitative approach might require for instance the computation of the pmf for increasingly larger clusters. Nevertheless, it can be seen from Fig. 3.3 that first shell changes have a noticeable influence on the 3-D potential $W(r)$. A strong increase in ΔW ($\equiv W(r^{\ddagger}) - W(r_0)$) is found when, for AW density, the temperature is increased from 298 K to 683 K (dotted line in Fig. 3.3). However, this difference is muted by the temperature dependent correction in $W_{eff}(r)$ when the values for ΔG are compared (solid line in Fig. 3.3). Therefore, given the almost constant first shell hydration it seems reasonable to relate the increase in ΔG with the progressive depopulation of the second shell and beyond as the density is lowered, and the limited extend of this increase with the first shell hydration robustness. In this connection, the fast increase of ΔG for ion pairs [26] might be indicative of substantial first shell changes. It might be interesting to investigate in this case how the local water structure is altered in comparison with AW, where a characteristic electrostatic bridging by shared hydration molecules has been described [48, 51].

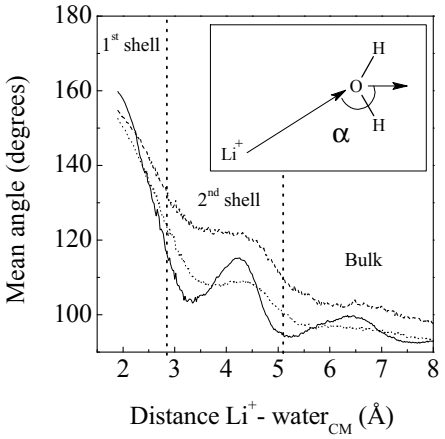

Figure 3.8. Mean angle between the ion-water/water dipole vectors (see the inset) as a function of ion-water center of mass distance for three thermodynamic states: T=298 K and $\rho = 0.997$ g cm^{-3} (solid line), T=683 K and $\rho = 0.48$ g cm^{-3} (dashed line) and T=683 K and $\rho = 0.997$ g cm^{-3} (dotted line).

Orientational Dependence

The previuos analysis has been focused on distance dependent properties, it is also of interest to study the changes in orientational order. The basic finding is that even though the temperature is substantially higher in SCW, the mean orientation of water molecules around the ion is generally *stronger* than in AW. To investigate orientational properties, the angle between the ion-oxygen vector

and the dipole vector of the water molecule has been computed during the MD runs (see inset of Fig. 3.8 for its definition). In principle, for an isolated ion-water pair the most favourable orientation is characterized by an angle of 180^o (this configuration has been used for the computation of the pmf from continuum theory in the previous section), and complete lack of any orientational order would result in a mean angle of 90^o.

Fig. 3.8 displays the mean angle as a function of the ion-water distance, for AW and SCW. Orientational order is slightly higher in AW only up to a distance of ≈ 2.2 Å (at which both curves cross), well before the TS distance of 2.7 Å is reached. From that point on, orientational order in SCW is always stronger and extends into the bulk region, where all curves tend to 90^o. Within the second shell, differences of up to a factor of two can be found. This overall stronger order (which includes a substantial part of the first shell) is remarkable given the considerably higher temperature, and probably contributes to the robustness of the dissociation free energy as a function of density. The lower second shell density previuosly discussed probably allows the water molecules in the second shell and beyond to adopt more optimal configurations, a possibility which might be hindered in AW.

3.2.3 Kinetics

Residence Times

Results for the residence times are summarized in Table 3.2 and displayed in Fig. 3.9. For the particular model used here the lifetime in AW is of 57 ps ($\approx$ 115 ps has been found in a model including 3-body interactions [9]), consistent with the experimentally estimated bound ($\tau < 100$ ps [54]). The results for SCW are in good accord with previous work [23]. The main feature is a sharp decrease of the exchange time along the coexistence curve, in marked contrast with the almost constant value within the supercritical regime. Nevertheless, for the latter, although the effect of density if largely secondary at supercritical temperatures, there is a steady increase in the exchange time from ≈ 3 ps at liquid density to ≈ 8 ps at very low densities. In the following these results will be interpreted in the light of reaction rate theory.

Transition State Theory Estimates

In order to apply reaction rate theory to the exchange process it is important to ask to which extent is this an activated process, rendering the present approach useful. The main indicator in this connection is the activation free energy for dissociation. In the first study of this sort for $Na^+(aq)$ [4], with a barrier of ≈ 4 k_BT, it was demonstrated that the process could be adequately addressed as an activated process.

From Table 3.1 and Fig. 3.4 it is clear that here the exchange process involves several k_BT in all cases, with a worst case of 2.7 k_BT and an exchange time of $\approx$ 3.4 ps (see Table 3.2). It is worth noting that a similar approach has proven its value in an even more labile system, such as the relevant case of hydrogen bond breaking in pure water [55], with typical times in the order of 1 ps. Here, the reaction rate approach has provided a unifying view of a number of previous observations on hydrogen bond lifetimes.

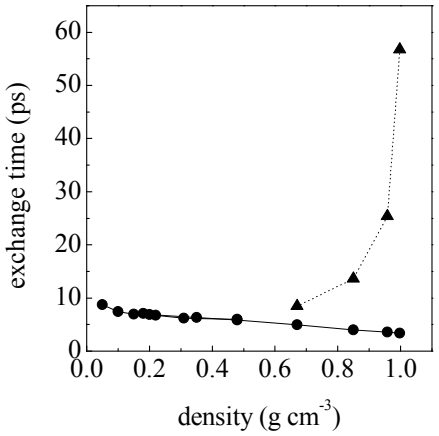

Figure 3.9. Exchange times for the thermodynamic states studied. Solid line and circles: supercritical water; dotted line and triangles: liquid water.

The TST approximation results, obtained from the equation 3.3 are summarized in Table 3.2. The same table contains the values obtained from the approximate formula for k^{TST} embodied in Eq. 3.6, from which we see that it is a satisfactory approximation. We will therefore use the latter as it is particularly clear, with all the relevant information condensed in only two parameters (ω and ΔG), plus the mean energy (k_BT). Regarding ω_0 (obtained from a fit to the first well of the effective pmf), this parameter is independent of thermodynamic state (see Table 3.1), with a value of ≈ 103 ps^{-1}. Therefore, all the equilibrium aspects of the exchange are contained in the single quotient $\Delta G/k_BT$, displayed in Fig. 3.4, so that the previous discussion on the thermodynamic state dependence of ΔG and $\Delta G/k_BT$ is particularly useful here. The equilibrium picture is rather simple: the steady increase of dissociation free energy with decreasing density hinders the exchange process, damping

to some extent the acceleration due to the much higher temperature in SCW as compared with AW. No effects stemming from possible shape changes in $W_{eff}(r)$ (represented by ω_0) are present. Moreover, the dissociation energy increase is not as fast as might be expected from continuum theory due to the robustness of first shell hydration, and short exchange times are still obtained in SCW.

A simple explanation for the fast exchange rates in SCW would attribute them to the higher temperature, missing important effects associated to the dissociation energy increase, as it can be shown in a simple calculation. If the exchange times in SCW would be estimated from Eq. 3.6, using the same dissociation free energy as in AW, a rate of 1.2 ps^{-1} at 683 K is obtained. This result is to be compared (see Table 3.2) with the actual value of ≈ 0.4 ps^{-1} obtained for k^{TST} in the supercritical region. The assumption of a constant dissociation free energy overestimates the TST rate by a factor of 3. Therefore, the increase in temperature by itself predicts considerably shorter exchange times (1-2 ps). It is the activation energy increase, hinted in the plots of the radial distribution function (Fig. 3.1), which slows down the process, although not to the extent that (as argued in the Introduction) might have been expected from these same plots.

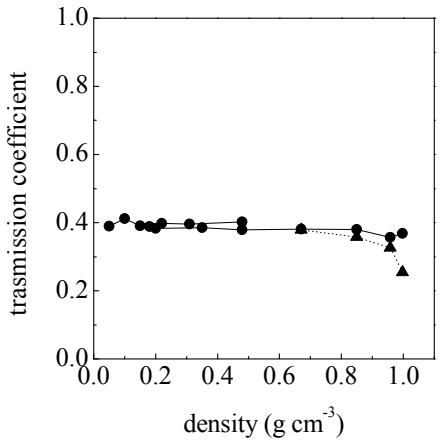

Figure 3.10. Transmission coefficient for the thermodynamic states studied. Solid line and circles: supercritical water; dotted line and triangles: liquid water.

Transmission Coefficients

The previous discussion has ignored the dynamic effects contained in the transmission coefficient (κ), which will be addressed here. The only systems for which this correction has been computed so far are Na^+ [4] and Li^+ [9] in AW. In both cases TST does not account for the exchange rate, and transmission coefficients of 0.21 and 0.14 respectively are obtained.

Such important corrections are due to extensive recrossings of the TS, which for these particular systems are specially long ranged, explaining the failure of theories based on the concept of small excursions around the TS [4]. The results

for κ (see Table 3.1) in AW are slightly higher (0.25) than those in Ref. [9], which should be attributed to the differences between force fields. Fig. 3.10 displays the values obtained for each thermodynamic state, from which two main features stand out. First, in SCW the transmission coefficient is rouhgly 60 % higher ($\kappa \approx 0.4$) than in AW, but is still far from unity, implying a substantial degree of recrossings, and the failure of TST in supercritical conditions. This is the first case that we know where dynamical corrections have been computed in this regime, showing that TST performs only slightly better than in the liquid phase.

A second important feature from Fig. 3.10 is that κ is constant and independent of density at supercritical temperatures. Therefore, the slight increase in residence time with decreasing density must be fully attributed to the increase in dissociation free energy discussed previously. This behaviour differs from what is found along the coexistence curve, where κ increases as the supercritical regime is approached, along with a corresponding increase in dissociation free energy. From the theoretical standpoint it is interesting that the transmission coefficient is constant for a wide range of densities, since it suggests that the exchange times can be obtained (except for a constant correction factor) from purely equilibrium calculations for the dissociation free energy, which itself can be obtained from the radial distribution function. This simple scenario might facilitate modelling at supercritical conditions.

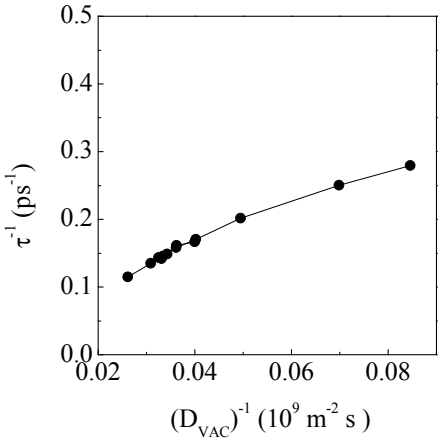

Figure 3.11. Dissociation rate as a function of the system friction (as estimated from D^{-1}) at constant supercritical temperature (673 K).

The finding that κ is constant is also relevant in connection with the theories of reaction rates in condensed phase, which predict a reaction rate turnover as a function of viscosity [28–30] (the latter usually monitored by the inverse of the diffusion constant). Figure 3.11 displays the dissociation rate constant as a function of D^{-1} for supercritical conditions, at constant temperature. There is a clear decrease of the rate with decreasing viscosity (that is, for lower D^{-1}), which on first sight might be interpreted as the left wing of the reaction rate turnover. However, the turnover is predicted to be a purely dynamical effect, and

therefore should be present for the transmission coefficient as well, which as discussed is constant over the whole range of densities. In consequence, the decrease of the rate should not be confused in this case with the friction induced turnover. The explanation is based on the fact that the theoretical predictions assume that the barrier height does not change with viscosity or temperature. As discussed in detail, for the present case it is precisely this effect, variation of the barrier height with density, that is taking place. Such situation is rather similar to the paradigmatic example of the photoisomerization dynamics of dimethylaminobenzonintrile [29, 56], where the phenomenological inverse dependence with solvent viscosity was explained as a decrease of activation free energy with increasing solvent polarity, which is precisely the case for the system under study.

3.3 Conclusions

It has been shown that considerable insight of the hydration shell exchange process can be obtained from an analysis based on a reaction rate perspective, notably in what concerns its dependence on thermodynamic conditions. Regarding the initial question, namely the origin of the tenfold speed up of the exchange rate from AW to SCW, the answer lies in the interplay of two factors. First, it is not simply due to the temperature increase, as this would give rise to much faster exchanges. The role of the increase in dissociation free energy is crucial in damping this temperature induced acceleration. However, this effect is muted by the strong electrostition of the ion down to rather low densities, which is able to keep a rather constant environment (particularly for the first shell), and induce an increase in orientational order with decreasing density. It has been shown that other possible contributions play a negligible role. Examples of these are the possible variation of shape of the pmf, which is negligible (as indicated by the curvature of the first well, ω_0), or the dynamic correction represented by the transmission coefficient, which does not change noticeably from AW to SCW, and which shows a constant behaviour at supercritical temperatures. This last aspect has served to illustrate that this system, when viewed as a reactive process, does show a behaviour similar to other reactive processes, in that the reaction rate decrease with decreasing viscosity is not due to a dynamical effect, but rather to an increase in activation free energy with decreasing solvent polarity.

Some aspects have not been addressed in detail but do have some interest for future work. The fact that the exchange process does show rather similar

characteristics in both AW and SCW, except for a substantially lower exchange time for the latter, might be useful for cases in which the process is particularly slow in AW. By running simulations in supercritical conditions, sufficient reactive events might be obtained to help define proper reaction coordinates in the liquid state. It is to be noted that such study of reaction types in SCW is not feasible in the present case due to the very short exchange times involved, which renders a classification of exchange events in terms of a reduced set of reaction classes unfeasible, a situation similar to the one previously found for Na^+ in AW [8]. However, it seems reasonable to expect that such limitation will not be present for instance in the case of multiply charged ions. The inflexion point shown by the dissociation free energy at low densities, which has been discussed in connection with mobility is also an interesting aspect for future study. Finally, given their technological interest, the present conclusions should be tested in apolar polarizable solvents. While for water the inclusion of polarizability does not seem to result in any significant change in the supercritical regime [24], this might change for apolar solvents [57] in the environment of an ion.

References

[1] H. L. Friedman *Chemica Scripta* **25**, 42 (1985).

[2] P. G. Wolynes *Annu. Rev. Phys. Chem.* **31**, 345 (1980).

[3] K. Ando and J. T. Hynes *J. Mol. Liq.* **64**, 25 (1995).

[4] R. Rey and J. T. Hynes *J. Phys. Chem.* **110**, 5611 (1996).

[5] O. A. Karim and J. A. McCammon *Chem. Phys. Lett.* **132**, 219 (1986).

[6] (a) G. Ciccotti, M. Ferrario, J. T. Hynes and R. Kapral *Chem. Phys.* **129**, 241 (1989); (b) *J. Chem. Phys.* **93**, 7137 (1990).

[7] R. Rey and E. Guàrdia *J. Phys. Chem.* **96**, 4712 (1992).

[8] R. Rey and J. T. Hynes *J. Phys. Cond. Matt.* **8**, 9411 (1996).

[9] D. Spangberg, R. Rey, K. Hermansson and J. T. Hynes *J. Phys. Chem. B* **107**, 4470 (2003).

[10] O. Kajimoto *Chem. Rev.* **99**, 355 (1999).

[11] S. C. Tucker and M. W. Maddox *J. Phys. Chem. B* **102**, 2437 (1998).

[12] P. T. Cummings, H. D. Cochran, J. M. Simonson, R. E. Mesmer and S. Karaboni *J. Chem. Phys.* **94**, 5606 (1991).

[13] G. Kalinichev *Z. Naturforsch.* **46A**, 433 (1991).

[14] (a) P. B. Balbuena, K. P. Johnston and P. J. Rossky *J. Am. Chem. Soc.* **116**, 2689 (1994); (b) P. B. Balbuena, K. P. Johnston and P. J. Rossky *J. Phys. Chem.* **99**, 1554 (1995); (c) L. W. Flanagin, P. B. Balbuena, K. P. Johnston and P. J. Rossky *J. Phys. Chem.* **99**, 5196 (1995).

[15] L. W. Flanagin, P. B. Balbuena, K. P. Johnston and P. J. Rossky *J. Phys. Chem. B* **101**, 7998 (1997).

[16] A. A. Chialvo, P. T. Cummings, J. M. Simonson and R. E. Mesmer *J. Chem. Phys.* **110**, 1064 (1999).

[17] J. C. Rasaiah, J. P. Noworyta and S. Koneshan *J. Am. Chem. Soc.* **122** , 11182 (2000).

[18] A. A. Chialvo and P. T. Cummings *Adv. Chem. Phys.* **109**, 115 (1999).

[19] A. G. Kalinichev Ber. Bunsenges. *Phys. Chem.* **97**, 872 (1993).

[20] S. H. Lee, P. T. Cummings, J. M. Simonson and R. E. Mesmer *Chem. Phys. Lett.* **293**, 289 (1998).

[21] P. B. Balbuena, K. P. Johnston, P. J. Rossky and J. K. Hyun *J. Phys. Chem. B* **102**, 3806 (1998).

[22] S. H. Lee and P. T. Cummings *J. Chem. Phys.* **112**, 864 (2000).

[23] J. P. Noworyta, S. Koneshan and J. C. Rasaiah *J. Am. Chem. Soc.* **122**, 11194 (2000).

[24] S. Koneshan, J. C. Rasaiah and L. X. Dang *J. Chem. Phys.* **114**, 7544 (2001).

[25] J. K. Hyun, K. P. Johnston and P. J. Rossky *J. Phys. Chem. B* **105**, 9302 (2001.

[26] J. Gao *J. Phys. Chem.* **98**, 6049 (1994).

[27] A. A. Chialvo, P. T. Cummings, H. D. Cochran, J. M. Simonson and R. E. Mesmer *J. Chem. Phys.* **103**, 9379 (1995).

[28] J. T. Hynes Theory of Chemical Reaction Dynamics, Baer, M., Ed.; CRC Press: Boca Raton, FL, 1985; p 171.

[29] B. J. Berne, M. Borkovec and J. E. Straub *J. Phys. Chem.* **92**, 3711 (1988).

[30] P. Hänggi, P. Talkner and M. Borkovec *Rev. Mod. Phys.* **62**, 250 (1990).

[31] T. L. Hill Statistical Mechanics, McGraw-Hill, New York (1956).

[32] M. G. Sceats *Adv. Chem. Phys.* **70**, 357 (1988).

[33] G. Ciccotti, M. Ferrario, J. T. Hynes and R. Kapral *J. Chem. Phys.* **93**, 7137 (1990).

[34] D. Chandler *J. Chem. Phys.* **68**, 2959 (1978).

[35] E. A. Carter, G. Cicotti, J. T. Hynes and R. Kapral *Chem. Phys. Lett.* **156**, 472 (1989).

[36] R. W. Impey, P. Madden and I. R. McDonald *J. Phys. Chem.* **87**, 5071 (1983).

[37] H. J. C. Berendsen, J. R. Grigera and T. P. Straatsma *J. Phys. Chem.* **91**, 6269 (1987).

[38] J. P. Ryckaert *Mol. Phys.* **55**, 549 (1985).

[39] (a) L. X. Dang *J. Chem. Phys.* **96**, 6970 (1992); (b) *J. Am. Chem. Soc.* **117**, 6594 (1995).

[40] (a) M. P. Allen and D. J. Tildesley Computer Simulation of Liquids, Oxford, New York (1989); (b) J. S. Bader and D. Chandler *J. Phys. Chem.* **96**, 6424 (1992).

[41] H. J. C. Berendsen, J. P. M. Postma, W. F. van Gunsteren, A. di Nola and J. R. Haak *J. Chem. Phys.* **81**, 3683 (1984).

[42] R. C. Reid, J. M. Prausnitz and T. K. Sherwood The Properties of Liquids and Gases, McGraw-Hill, New York (1977).

[43] Y. Guissani and B. Guillot *J. Chem. Phys.* **98**, 8221 (1993).

[44] M. Berkowitz, O. A. Karim, J. A. McCammon and P. J. Rossky *Chem. Phys.* **105**, 577 (1984).

[45] B. M. Pettitt and P. J. Rossky *J. Chem. Phys.* **84**, 5836 (1986).

[46] J. van Earden, W. J. Briels, S. Harkema and D. Feil *Chem. Phys. Lett.* **164**, 370 (1989).

[47] L. X. Dang, J. E. Rice and P. A. Kollman *J. Chem. Phys.* **93**, 7528 (1990).

[48] E. Guàrdia, R. Rey and J. A. Padró *Chem Phys.* **155**, 187 (1991).

[49] L. X. Dang *J. Chem. Phys.* **97**, 1919 (1992).

[50] S. B. Zhu and G. W. Robinson *J. Chem. Phys.* **97**, 4336 (1992).

[51] E. Guàrdia, R. Rey and J. A. Padró *J. Chem. Phys.* **95**, 2823 (1991).

[52] G. H. Zimmerman, M. S. Gruszkiewicz and R. H. Wood *J. Phys. Chem.* **99**, 11612 (1995).

[53] A. N. Drozdov and S. C. Nucker *J. Chem. Phys.* **114**, 5912 (2001).

[54] P. S. Salmon, W. S. Howells and R. Mills *J. Phys. C: Solid State Phys.* **20**, 5727 (1987).

[55] A. Luzar *J. Chem. Phys.* **113**, 10663 (2000).

[56] J. Hicks, M. Vandersall, Z. Babarogic and K. B. Eisenthal *Chem. Phys. Lett.* **18**, 116 (1985).

[57] E. Llanta and R. Rey *Chem. Phys. Lett.* **340**, 173 (2001).

Chapter 4

On the Diffusion Coefficient of Ionic Solvation Shell Molecules

Diffusion of molecules belonging to the ionic solvation shell has been studied for a variety of systems in the liquid phase [1–16]. Generally, their motion is found to be substantially slowed down with respect to bulk solvent molecules but still somewhat faster than that of the ion. This conclusion is usually founded on the computation of the diffusion coefficient for the subset of first solvation shell molecules: its value is larger than that of the ion and lower than that of the bulk. While a hindered motion seems perfectly reasonable on physical grounds, in this work it will be argued that some care must be taken in assigning a diffusion coefficient, a point that can be illustrated with a simple example. For a tightly bound ion-shell system, one in which no exchanges can take place between first and second solvation shells, it is obvious that the diffusion coefficient of first shell molecules must be identical to that of the ion (as the complex diffuses as a unit). Contrary to this expectation, this equality is not found in computer simulations for cases where it is manifest that no exchanges have taken place during the calculation. Fig.

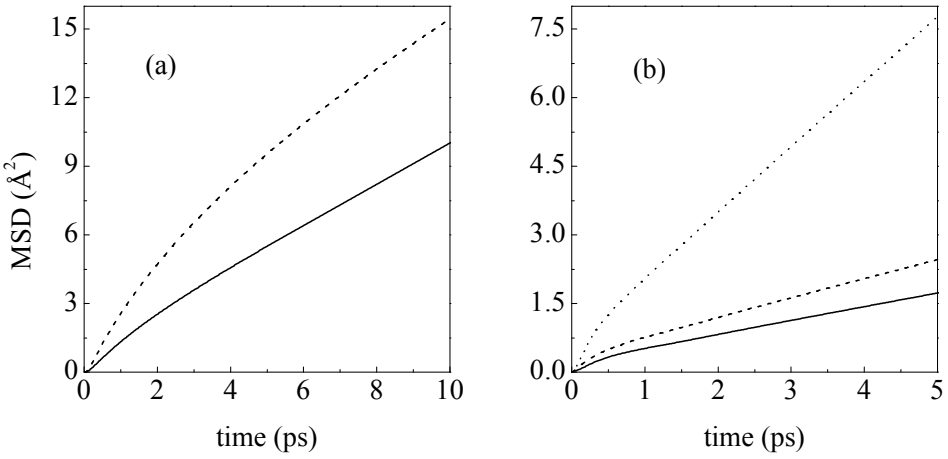

Figure 4.1. Short time behaviour of the mean square displacement for the systems studied. (a) Carbon (solid line) and chlorine (dashed line) atoms in CCl_4. (b) Mg^{2+} (solid line), first shell molecules (dashed line) and bulk water (dotted line).

4.1(b) displays results obtained for Mg^{2+} in water (see below for computational details), a representative case for which the previous considerations apply. A linear regime is (apparently) attained after ≈1 ps for the mean square displacement (MSD) of the ion, for first solvation shell molecules and for bulk solvent. The slope of the ion's MSD is clearly the smallest one, so that the conclusion that first shell molecules have a larger diffusion coefficient, but still smaller than that of bulk solvent, seems inescapable (the same conclusion is reached from analysis of the corresponding velocity autocorrelation functions, VACF). The computational origin of this artifact, together with the physical interpretation of the apparent faster diffusion of solvation molecules, will be studied here in detail. Moreover, the implications for the estimation of the mean diffusion coefficient in different scenarios will also be addressed.

The paper is organized as follows: the basic formulas are derived in the next section, results for a couple of illustrative examples are described in section 4.2, and the final section is devoted to sketch a general picture and to summarize the main conclusions.

4.1 Theory

The rather simple explanation is that too short a cut-off is used for the MSD or VACF of the solvation shell molecules. Although, strictly speaking, the diffusion coefficient is a long time property, it is usually determined with rather short simulations, to the point that within the time span usually taken for the MSD ($\approx$ 5-10 ps) the ion only diffuses by roughly one ionic diameter. If we take for instance a diffusion coefficient of $\approx$ 1 ($10^{-9}\mathrm{m}^2/\mathrm{s}$), the square root of the corresponding MSD after 10 ps is $\approx$ 2.5 Å, i.e. of the order of the ionic diameter (a much shorter distance is obtained if computing the diffusion coefficient from the VACF). Although, remarkably, this suffices to produce an accurate diffusion coefficient for the ion, it will be shown within that this is not so for solvation shell molecules.

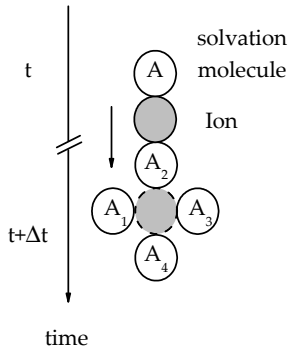

Figure 4.2. Sketch of possible configurations after the ion and a first solvation shell molecule diffuse for a given time: a molecule initially located in position A can move to any of the sites A_i.

The physical process that explains the apparently higher diffusion of the latter is easily understood from the sketch in Fig. 4.2 where, for the sake of clarity, the ion diffuses two diameters from its original position. During that time, a given solvation molecule (A) will travel the same distance as the ion (ending in position A_1) only if it follows the ion rigidly. However, the motion of solvation molecules is a combination of translation and rotation around the ion, so that the molecule is also likely to end up in positions A_2, A_3 or A_4, which imply a net displacement larger than that of the ion. If the MSD is averaged over all these possible outcomes an apparently higher diffusion of solvation molecules will be found. Obviously no such effect would be present if the ion would be allowed to diffuse by a large enough distance before computing the MSD, as the effect of rotations in random directions would cancel out.

These considerations can be readily translated into mathematical form. The position vector of a solvation molecule ($\vec{r}_M$) can be expressed in terms of that of the ion ($\vec{r}_I$) and the relative vector ($\vec{r}$)

$$\vec{r}_M = \vec{r}_I + \vec{r}. \tag{4.1}$$

The MSD of the molecule

$$\Delta_M(t) = \left\langle [\vec{r}_M(t) - \vec{r}_M(0)]^2 \right\rangle, \tag{4.2}$$

can thus be written in terms of the ion position and relative vector as

$$\Delta_M(t) = \Delta_I(t) + \left\langle [\vec{r}(t) - \vec{r}(0)]^2 \right\rangle + 2 \left\langle [\vec{r}_I(t) - \vec{r}_I(0)] \cdot [\vec{r}(t) - \vec{r}(0)] \right\rangle. \tag{4.3}$$

The last term is zero since there is no correlation on average between the ion position and the molecule-ion relative vector, so that one gets

$$\Delta_M(t) = \Delta_I(t) + \left\langle [\vec{r}(t) - \vec{r}(0)]^2 \right\rangle, \tag{4.4}$$

which can be rewritten

$$\Delta_M(t) = \Delta_I(t) + 2 \left[\bar{r}^2 - \langle \vec{r}(t) \cdot \vec{r}(0) \rangle \right], \tag{4.5}$$

where $\bar{r}$ denotes the mean distance between the ion and the solvating molecule.

At long times the time correlation function contained into the last term will tend to zero so that the ion and solvation molecule mean square displacements ($\Delta_I(t)$, $\Delta_M(t)$) will only differ by a constant value ($2\bar{r}^2$). Therefore, since the diffusion coefficient is obtained as

$$D = \frac{1}{6} \lim_{t \to \infty} \frac{d[\Delta(t)]}{dt}, \tag{4.6}$$

the corresponding diffusion coefficients will be identical as expected. Of course this is only strictly valid under the assumption of no exchanges between first and second shells, the limit in which $\bar{r}$ is well defined.

To a very good approximation formula 4.5 can be written in a form that highlights the role of solvation shell rotation. For tight solvation shells the ion-molecule distance is almost constant, as reflected for instance in the steep first peak of the corresponding radial distribution function. Assuming a constant separation equal to the mean value, the relative vector can be written as $\vec{r} \cong \bar{r}\hat{r}$ (where $\hat{r}$ denotes the unit vector). From this approximation it follows

$$\Delta_M(t) \cong \Delta_I(t) + 2\bar{r}^2 \left[1 - \langle \hat{r}(t) \cdot \hat{r}(0) \rangle \right] = \Delta_I(t) + 2\bar{r}^2 \left[1 - P_1(t) \right], \tag{4.7}$$

where $P_1(t)$ stands for the Legendre polynomial which appears in the theory of rotational absorption spectroscopy [17], and which after very short times is

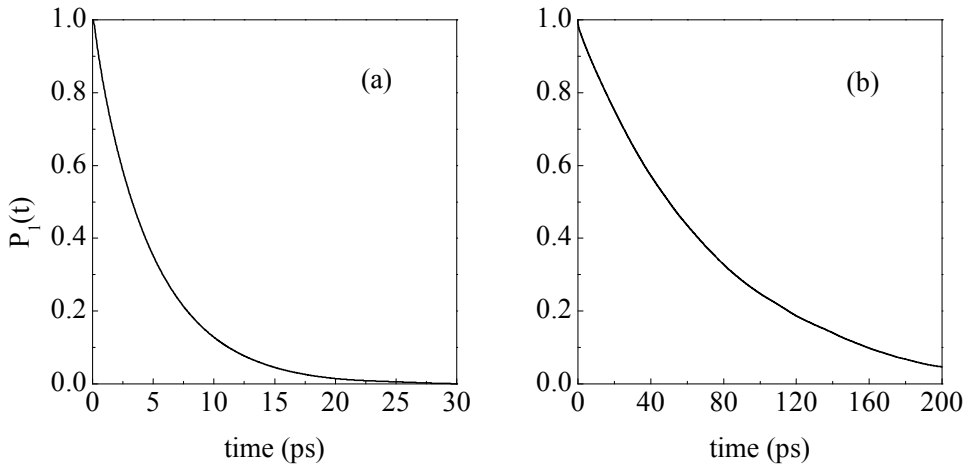

Figure 4.3. $P_1(t)$ for (a) chlorine atoms in CCl_4 and (b) water molecules around Mg^{2+}.

characterized by an almost exponential decay [18] ($P_1(t) = e^{-t/\tau_1}$). $\Delta_M(t)$ will only get parallel to $\Delta_I(t)$ after $P_1(t)$ has decayed to zero. As the rotation of a solvation complex made of several molecules will be slow, τ_1 can be longer than the time it takes the ion to reach diffusive behaviour, this is why a MSD shorter than 10 ps is not capable of displaying the same diffusion coefficient for the ion and for the solvation shell molecules. Thus, Eq. 4.7 summarizes the basic idea of this work: at short times the mean square displacement of first solvation shell molecules (Δ_M) results from ion translation (Δ_I) plus rotation around the ion (embodied in the term containing $P_1(t)$), while at longer times, after rotational correlation is lost, both MSD differ by just a constant and yield the same diffusion coefficient. It is interesting to note that the present image, according to which the ions with their solvation shells should be regarded as rigid spheres on a picosecond time scale, is in line with the conclusions reached from recent measures of rotational relaxation within the solvation shell [19].

From Eq. 4.7 it is possible to get a pretty good idea of the time length required in order to obtain the expected identical values for the ion and solvation molecules diffusion coefficients. An estimate for the reorientational time can be derived from the rotational version of the Stokes-Einstein relation [20], here applied to the ion plus first solvation shell complex

$$\tau = \frac{8\pi\eta R^3}{k_B T}, \tag{4.8}$$

where η stands for the bulk solvent viscosity and R for the radius of the complex. The time obtained for Mg^{2+} in water falls in the vicinity of 70 ps (see Section 4.2.2 for details). The important point is that this time is more than one order of magnitude larger than the 5 ps used in Fig. 4.1(b).

Eq. 4.7 also makes it clear why one can be mislead by the shape of the MSD at such short times and assume that diffusive behaviour has already been attained and a diffusion coefficient can be fitted. As previously stated, at intermediate times (shorter than $\approx$ 10 ps) the ion will have attained diffusive translation (so that its MSD will be linear in time: $\Delta_I(t) = 6D_I t$, where D_I denotes the ion's diffusion coefficient), but $P_1(t)$ can still be approximated by its short time expansion ($P_1(t) = 1 - \frac{t}{\tau_1} + \cdots$). If both expressions are inserted into Eq. 4.7 we get

$$\Delta_M(t) \approx 6D_I t + 2\bar{r}^2 \frac{t}{\tau_1} = \left(6D_I + \frac{2\bar{r}^2}{\tau_1}\right) t, \tag{4.9}$$

i.e. a linear behaviour is obtained, which mimics the characteristic diffusive behaviour. From the latter expression one would estimate the solvation molecule diffusion coefficient as

$$D_M = D_I + \frac{\bar{r}^2}{3\tau_1}, \tag{4.10}$$

which in all cases exceeds the true value by a constant value $\frac{\bar{r}^2}{3\tau_1}$. Since $\bar{r}^2$ is close to the shortest distance that can be attained and τ_1 is a rather long time, the overestimation is usually not substantial (as can be inferred for instance from Fig. 4.1(b)), but is noticeable enough to suggest that solvation molecules diffuse faster than the ion.

4.2 Numerical Results

In this section a couple of illustrative examples will be described, both studied by means of Molecular Dynamics simulations. In all cases a time step of 1 fs was used and the temperature was kept constant by applying a Berendsen thermostat with a coupling constant of 10 ps [21]. Molecules were kept rigid using the SHAKE algorithm [22]. Further details for each system are given in the next subsections.

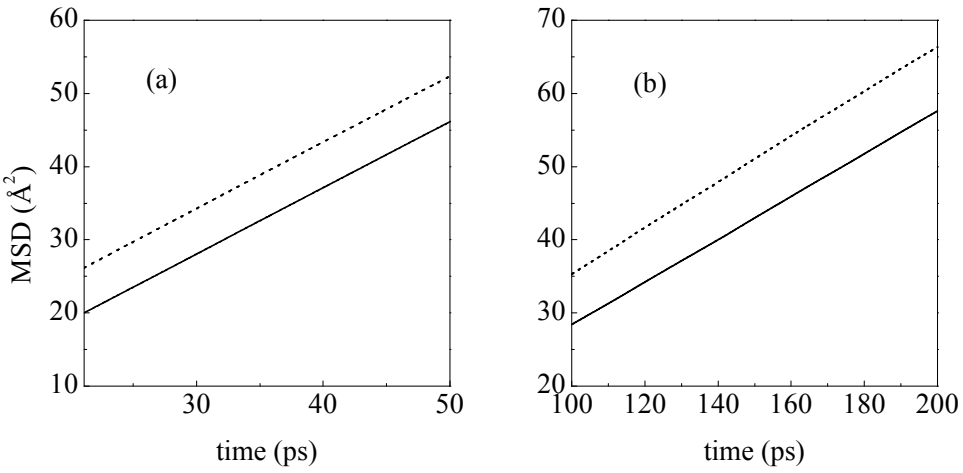

Figure 4.4. Long time behaviour of the mean square displacement for the systems studied. (a) Carbon (solid line) and chlorine (dashed line) atoms in CCl_4. (b) Mg^{2+} (solid line) and first shell molecules (dashed line).

4.2.1 Carbon Tetrachloride

Liquid CCl_4 will be used as a toy model: the C center will play the role of the ion and the Cl centers that of the solvation molecules. In this way one can eliminate several sources of statistical noise in order to check unambiguously the formulas developed above. For ion diffusion it takes a long simulation time to get enough statistics as there is only one ion surrounded by several hundred solvent molecules, while in neat CCl_4 statistics can be collected for every molecule. In addition, the approximation used to obtain formula 4.7, namely that the ion-molecule distance is constant, here is exact. Finally, the rotation time for the molecule is known to be shorter than 10 ps [23], so that no extremely long simulations are required. Molecular Dynamics simulations of 1.5 ns were done for a system of 215 molecules. The reference temperature and density were respectively 298.15 K and 1.579 g cm^{-3}. The geometric and interaction parameters for carbon tetrachloride are given in ref. [23]. Fig. 4.1(a) displays the MSD for carbon and for chlorine up to 10 ps. They both attain, to a good approximation, a linear behaviour with different slopes within that time window. As in the case of Mg^{2+} in water (Fig. 4.1(b)) it is tempting to conclude that the chlorine centers have a larger diffusion coefficient than the carbon, which is obviously impossible for a rigid molecule. In order to analyze this case, formula 4.7 applies exactly, as the distances are fixed.

The rotational correlation function ($P_1(t)$) is displayed in Fig. 4.3(a), it is well represented by an exponential decay with $\tau_1 = 4.8$ ps, so that it is safe to consider it has vanished after $\approx 20 - 30$ ps for practical purposes. Therefore, according to Eq. 4.7, after that time the MSD for the C center and that for the Cl centers should be parallel and differ by a constant amount of $2\bar{r}^2$ (which in this case, with a C-Cl bond of 1.766 Å, is equal to 6.24 Å^2). The results from the simulation are in perfect quantitative agreement with this expected behaviour, as displayed in Fig. 4.4(a).

4.2.2 Mg^{2+} in Liquid Water

For this system the lifetime of a molecule within the first solvation shell (estimated to fall in the μs range [24]) is much longer than the time required for the rotational relaxation of the first shell solvation complex (estimated in Section 4.1 to be lower than 100 ps). Therefore, the formulas developed in Section 4.1 for tightly bound complexes should be valid. Simulations of 15.0 ns were done for a system of 215 SPC/E water molecules [25] and one magnesium ion. The reference temperature and density were set respectively to 298.15 K and 0.997 g cm^{-3}. The Lennard-Jones interaction parameters for Mg^{2+}-water were taken from Ref. [26]. With these parameters the first solvation shell contains six molecules, and none of them is observed to leave the first shell during the course of the simulation.

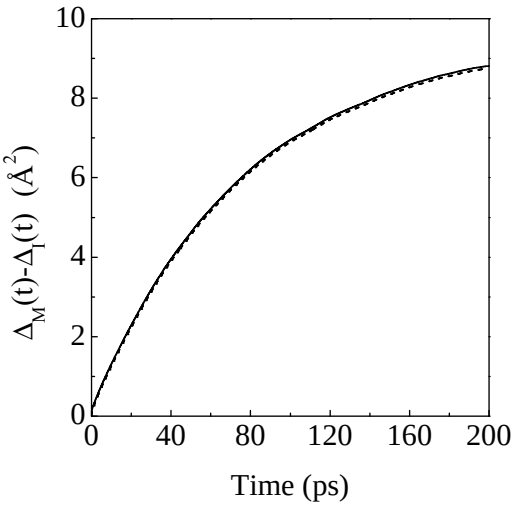

Figure 4.5. Dashed line: difference between ion and solvation molecules mean square displacements. Solid line: approximate result predicted by Eq. 4.7 ($2\bar{r}^2[1 - P_1(t)]$).

As previously stated, the estimated rotational relaxation time can be rather long. The theoretical prediction is only approximate since, besides the phenomenological character of Eq. 4.8 on which it relies, water viscosity (η), for the SPC/E model used here, is estimated [27,28] to fall in the range 0.71-0.91 (which

brackets the experimental value of 0.85 cP [29]). Regarding the radius of the complex, we have taken 2.41 Å, the distance at which first solvation shell population has decayed to zero, as estimated from the ion-oxygen radial distribution function, which is consistent with the results from a variety of (polarizable and non-polarizable) models [27, 30, 31]. The rotational time thus obtained applying Eq. 4.8 is 68-87 ps (depending on the value of the viscosity). This theoretical estimation is confirmed to a large extent in Fig. 4.3(b), which displays the computed $P_1(t)$.

An exponential fit results in a time of $\tau_1 = 78$ ps, so that even for a time as long as 200 ps this function will have a nonnegligible contribution. This implies, according to the considerations in Section 4.1, that in order to get a diffusion coefficient for solvation shell molecules equal to that of the ion, the corresponding MSD should be several hundred picoseconds long, what is in stark contrast with the 5-10 ps range usually chosen. Fig. 4.4(b) shows that for times larger than 100 ps both MSD are parallel to a good approximation and differ by a constant value which approaches (see below) the theoretical prediction $2\bar{r}^2 = 9.24$ Å^2, where we have taken $\bar{r} = 2.15$ Å (the position of the first maximum of the radial distribution function). The accord is excellent considering that in this case the ion-molecule distance is only approximately constant. The rather small disagreement is more visible in Fig. 4.5, where the function $2\bar{r}^2[1-P_1(t)]$ is compared with the difference $\Delta_M(t)-\Delta_I(t)$. According to Eq. 4.7 both functions are only approximately equal, although from Fig. 4.5 it is clear that the deviation is negligible in this case, particularly considering that the statistics obtained from a single ion simulation can be subject to some noise at such long times. It can also be easily appreciated in Fig. 4.5 how $\Delta_M(t) - \Delta_I(t)$ asymptotically approaches the theoretical value (9.24 Å^2).

4.3 Discussion

The role played by exchanges between first and second solvation shells remains to be addressed. The corresponding time scale is critically dependent on the system under study: for monoatomic ions dissolved in water it spans 18 orders of magnitude [24], with the lower limit estimated to fall within the picosecond range and the upper limit reaching up to Ms. The very long times involved in most cases constitute a barrier for computational studies, it is only recently that the dynamics and kinetics of this process have started to be addressed [32–36]

using numerical methods borrowed from reaction rate theory. The bottom line of the previous sections is that, as long as the exchange time scale is much longer than that for rotational relaxation, the diffusion coefficient of first solvation shell molecules should be taken equal to that of the ion. Indeed, the case of Mg^{2+} is probably representative of the majority of cases for multiply charged monoatomic ions in water [24]: the rotational relaxation time will be of the order of 0.1 ns and the exchange time higher than 1 ns. Overestimations of the diffusion coefficient (close to the value given in Eq. 4.10) will be obtained if short MSD (of the order of 0.01 ns) are used, and are due to the transient rotational relaxation of the complex at short times. The situation is less well defined for singly charged ions in water, while for other liquids and/or ions the field is largely unexplored.

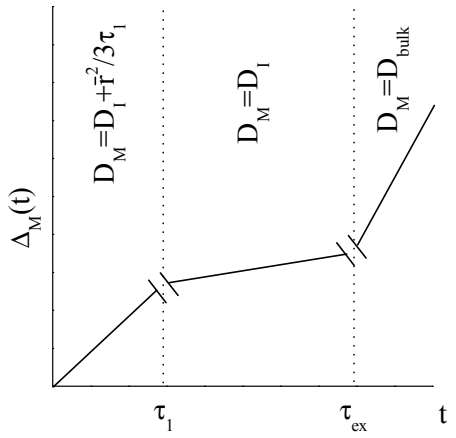

Figure 4.6. Sketch of the typical expected behaviour for the MSD of molecules initially belonging to the first solvation shell. The case shown here corresponds to a tightly bound shell as $\tau_{ex} \gg \tau_1$.

In order to get a general view that includes systems for which the time scales are not so clear-cut it is important to note that, indeed, any diffusion coefficient for first shell molecules (D_{first}) is a temporary one since, eventually, exchanges will occur and the molecule will diffuse as bulk solvent. This formulation makes it clear that the value taken for D_{first} is actually a matter of definition, which will only be valid for times lower than τ_{ex}. In other words, $\Delta_M(t)$ (a function that results from an average over all molecules initially belonging to the first solvation shell) will go through different (linear) regimes, each one characterized by a temporary diffusion coefficient. This expected behaviour is sketched in Fig.4.6 for a tightly bound solvation shell: a fit of the MSD for times lower than τ_1 would result in the value given in Eq. 4.10, for times in the range $\tau_1 < t < \tau_{ex}$ the fit would yield $D_M = D_I$ and, finally, for times larger than τ_{ex} it is clear that one would obtain $D_M = D_{bulk}$. This suggests that a sensible definition of the diffusion coefficient should be based on the ratio between the exchange time (τ_{ex}) and the rotational relaxation time (τ_1) for the system of interest. As previously stated, if $\tau_{ex} >> \tau_1$ it seems reasonable to define $D_{first} \equiv D_{ion}$, without requiring the actual calculation of the MSD.

Indeed such calculation would not provide any new information and, in addition, it would involve extremely long simulations (as illustrated by the Mg^{2+} case). If $\tau_{ex} \geq \tau_1$ (both falling within the same order of magnitude), i.e. if (on average) solvation molecules leave the first shell shortly after rotation of the complex has relaxed, then according to Eq. 4.10 it should probably be a reasonable choice to take $D_{first} \equiv D_{ion} + \bar{r}^2/3\tau_1$. To stress that this is in fact a definition one can note that it is not possible to obtain such result from simulation. If all solvation molecules would be used for the calculation, given that a fraction of them would escape during the simulation run, a mean between diffusion in the first shell and (the much faster) bulk diffusion would be obtained; on the contrary, if one would try to compute D_{first} only using those solvation molecules that do not escape, the result would initially be equal to Eq. 4.10 and subsequently be followed by a value equal to D_{ion}. Finally, if $\tau_{ex} \leq \tau_1$, i.e. most of the molecules are exchanged before the complex can rotate significantly, it does not seem possible to talk of a D_{first} clearly different from that of bulk solvent molecules. To summarize, simple definitions for D_{first} seem possible which take into account the role of exchanges. The computer simulations required to estimate the diffusion coefficient are not direct calculations of the MSD for solvation shell molecules (which have been argued to be problematic in all cases), but rather the solvation shell lifetime and rotational relaxation time of the complex.

References

[1] R. W. Impey, P. A. Madden and I. R. McDonald *J. Phys. Chem.* **87**, 5071 (1983)

[2] K. Heinzinger *Physica B* **131**, 196 (1985).

[3] E. Guàrdia and J. A. Padró *Chem. Phys.* **144**, 353 (1990).

[4] E. Guàrdia and J. A. Padró *J. Phys. Chem.* **94**, 6049 (1990).

[5] D. Marx, K. Heinzinger, G. Pálinkás and I. Bakó *Z. Naturforsch.* **46A**, 887 (1991).

[6] S. Koneshan, R. M. Lynden-Bell and J. C. Rasaiah *J. Am. Chem. Soc.* **120**, 12041 (1998).

[7] D. Roccatano, H. J. C. Berendsen and P. D'Angelo *J. Chem. Phys.* **108**, 9487 (1998).

[8] E. Hawlicka and D. Swiatla-Wojcik *J. Mol. Liq.* **78**, 7 (1998).

[9] J. M. Martínez, R. R. Pappalardo, E. Sánchez Marcos, K. Refson, S. Díaz-Moreno and A. Muñoz-Pérez *J. Phys. Chem. B* **102**, 3272 (1998).

[10] T. M. Chang and L. X. Dang *J. Phys. Chem. B* **103**, 4714 (1999).

[11] O. N. Kalugin, M. N. Volobuev, A. V. Ishchenko and A. K. Adya *J. Mol. Liq.* **85**, 299 (2000).

[12] E. Hawlicka and D. Swiatla-Wojcik *Phys. Chem. Chem. Phys.* **2**, 3175 (2000).

[13] E. Guàrdia and R. Pinzón *J. Mol. Liq.* **85**, 33 (2000).

[14] F. Floris and A. Tani *J. Chem. Phys.* **115**, 4750 (2001).

[15] A. Chandra *J. Phys. Chem. B* **107**, 3899 (2003).

[16] S. Amira, D. Spångberg, M. Probst and K. Hermansson *J. Phys. Chem. B* **108**, 496 (2004).

[17] R. G. Gordon, *J. Chem. Phys.* **43**, 1307 (1965).

[18] J. P. Hansen and I. R. McDonald, Theory of Simple Liquids, Academic Press, London, (1986).

[19] A. W. Omta, M. F. Kropman, S. Woutersen and H. J. Bakker *Science* **301**, 347 (2003).

[20] A. J. Masters and P. A. Madden *J. Chem. Phys* **. 74**, 2470 (1981).

[21] H. J. C. Berendsen, J. P. M. Postma, W. F. van Gunsteren, A. di Nola and J. R. Haak *J. Chem. Phys.* **81**, 3683 (1984).

[22] J. P. Ryckaert *Mol. Phys.* **55**, 549 (1985).

[23] E. Llanta, K. Ando and R. Rey *J. Phys. Chem. B* **105**, 7783 (2001).

[24] H. L. Friedman *Chemica Scripta* **25**, 42 (1985).

[25] H. J. C. Berendsen, J. R. Grigera and T. P. J. Straatsma *J. Phys. Chem.* **91**, 6269 (1987).

[26] J. Åqvist *J. Phys. Chem.* **94**, 8021 (1990).

[27] D. Spångberg and K. Hermansson *J. Chem. Phys.* **120**, 4829 (2004).

[28] A. Glätti, X. Daura and W. van Gunsteren *J. Chem. Phys.* **116**, 9811 (2002).

[29] Handbook of Chemistry and Physics, 56th ed., edited by R. C. Weast (CRC, Boca Raton, 1976).

[30] E. Guàrdia, G. Sesé, J. A. Padró and S. G. Kalko *J. Sol. Chem.* **28**, 1113 (1999).

[31] D. Spångberg and K. Hermansson *J. Chem. Phys.* **119**, 7263 (2003).

[32] R. Rey and J. T. Hynes *J. Phys. Chem.* **100**, 5611 (1996).

[33] R. Rey and J. T. Hynes *J. Phys.: Condens. Matter* **8**, 9411 (1996).

[34] M. Masia and R. Rey *J. Phys. Chem. B* **107**, 2651 (2003).

[35] D. Spångberg, R. Rey, J. T. Hynes and K. Hermansson *J. Phys. Chem. B* **107**, 4470 (2003).

[36] K. B. Møller, R. Rey, M. Masia and J. T. Hynes *J. Chem. Phys.* **122**, 114508 (2005).

Chapter 5

On the Coupling between Molecular Diffusion and Solvation Shell Exchange

Although we are close to the centennial of the first theoretical studies on molecular diffusion [1] this fundamental process is rich enough to constitute an area of active research for years to come. While the subject has extended in many interesting directions, here we revisit some not fully understood features of diffusion in thermal fluids. In these conditions the basic picture is one in which the diffusing molecule (hereinafter referred to as the solute) undergoes random collisions, which hinder its motion and result in a mean square displacement only linear in time. It is interesting to note that the role and fate of the colliding neighbors (solvation molecules) tend to be often overlooked, as in most instances the interaction is feeble and only coarse-grained aspects (like solute size and solvent viscosity) are considered to be of relevance. The remarkable numerical success of the macroscopic Stokes law down to the atomic scale for a large variety of systems [2](including a prominent example such as liquid water self diffusion [3]) might be taken as a reflection of the unimportance of the neighbours dynam-

ics, even when the sizes of the solute and the solvent molecules are comparable. However, it has been argued that microscopic aspects of diffusion are in fact important [4, 5]. A particular instance in which this Stokes-Einstein macroscopic approach is generally agreed to fail qualitatively is that of ionic diffusion (of evident interest if taking place in water), where for instance an increase of the diffusion coefficient with decreasing radius of the ion is not observed [6], while it is a direct prediction of the macroscopic theory. The qualitative explanation [7,8] focuses on the nature of the electrostatic interaction, which for the ion in a polar solvent case is strong enough (specially for the smaller ions) so that the solvation molecules follow the ion motion in time, with occasional exchanges between solvation shells: one molecule from the first solvation shell escapes to the second shell while a second shell molecule enters into the immediate vicinity of the ion (both events being simultaneous or asynchronous, with no general priority rule in the latter case). The increased drag on the ion exerted by this cohort of nearest neighbors explains the breakdown of the macroscopic approach, with a diffusion constant lower than what should be expected for the bare ionic radius. Nevertheless, in the strong interaction limit (small ionic radius and/or high charge, so that the first shell solvation molecules do not undergo any exchange) the macroscopic theory regains at least its numerical validity, as applied to the complex defined by the ion plus nearest neighbors (an approach known as the "solventberg" model).

The previous considerations highlight the potential role of the exchanges for the diffusion process in what might be called the intermediate regime, where the dynamics of the solvation shell molecules is highly correlated with that of the solute and yet, the exchanges are still not rare (on the time scale for diffusion). We believe that in this scenario the effect of the solvation shell exchange is not fully understood. Actually, not even the exchange process by itself can be regarded as a solved issue: although the exchange times for ions in solution have been the subject of study for quite some time [6, 9–12] (by means of Molecular Dynamics simulations), the mechanisms and stereochemistry of the exchange process are just starting to be scrutinized [13–16], usually motivated by its key role in other important processes such as ion reactivity. To evidence some unclear aspects of the influence of exchange on diffusion with an example, an issue such a characterization of the quantitative speed-up in diffusion induced by exchanges, remains unaddressed. Moreover, it is known that the exchange times for ions in water are typically larger than (roughly) 10 ps [10] while the time span required to obtain the diffusion coefficient with a high degree of accuracy (from the mean

square displacement or from the velocity correlation function) is of the order of 1 ps. It is then somewhat puzzling that the solventberg picture is not mandatory in all cases, given that on the time scale required to reach a diffusive behaviour there seem to be no exchanges in either case (as for a multiple charged ion). These questions constitute a first topic of attention in this work.

The main line of study, though, will focus on the inverse problem, namely, on the possible influence of diffusion on solvation shell exchange. The basic question here is if a given exchange event is conditioned in some way by the instantaneous state of motion of the solute, what we believe constitutes a rather new approach on this issue. At first sight, it might be thought that any such effect should be feeble. To start with, it is easy to show that exchanges are independent of diffusion in some instances: in the simple case of a massive particle (compared with the solvent molecules' mass), there will be many exchanges occurring while there is almost no diffusion of the solvated particle. In addition, these exchanges will obviously take place with a (very nearly) symmetric distribution around the solute so that no correlation will exist with its motion. Certainly this is a limiting case, but if we consider for instance the (random) oscillatory motion of an ion inside its cage of (first shell) solvating molecules while the whole complex diffuses, and that exchanges are rather infrequent, a correlation of the *instantaneous* ion velocity with the exchange between a second shell molecule and a first shell one may not seem likely a priori. Remarkably, it will be shown within that an important aspect of this problem allows for an exact analytical approach, which should apply to any thermal fluid. It so happens that the stereochemistry of the exchanges is effectively driven (in a probabilistic way) by the instantaneous velocity of the solute: the exchange events occur according to a nonsymmetric probability distribution around this direction, the counterexample starting this paragraph being a limiting (symmetric) case. While most of the results presented to illustrate these issues will correspond to the particular case of ionic diffusion in water (selected both for its relevance as well as for computational convenience), given the general character of the previous considerations, examples corresponding to simple liquids will also be included for the sake of completeness.

The outline of the paper is as follows. A summary of the simulation details is given in the following section. The results and discussion on the influence of solvation shell exchange on diffusion are presented in Sec. 3, while the inverse problem (the influence of diffusion on the exchange process) is addressed in Sec. 4. The main conclusions are summarized in Sec. 5. An Appendix is also included,

with the details of the derivation of some analytical expressions used in the main text.

5.1 Computational details

As just described most of the Molecular Dynamics (MD) simulations correspond to single ions dissolved in water. The simulated systems consist of an ion (Li^+ or Na^+) plus 215 water molecules in a cubic box with standard periodic conditions. The water model is SPC [17] (if not stated otherwise), keeping the water molecules rigid via the shake algorithm [18]. The ion-water interaction parameters for ions are those of Ref. [19] for sodium and those of Ref. [20] for lithium. Long-range forces were computed by the Ewald summation method [21], and a leap-frog integration algorithm with coupling to a thermal bath [22] has been used, with a 1 fs time step, and the value of the coupling set to 0.1 ps.

A second set of simulations has also been done for pure simple liquids (Argon at liquid conditions), with the interaction parameters taken from Refs. [23, 24]. A leap-frog integration algorithm has been used without thermal control and with a time step of 5 fs. Periodic boundary conditions for 500 Ar atoms in a cubic box were applied.

5.2 Effect of solvation shell exchange on diffusion

As previously described in the Introduction, within the regime of interest the first solvation shell follows the solute in its diffusive motion, with the exchange events being relatively uncommon. Thus, we seek to connect two phenomena that take place on rather different time scales, and which consequently are usually studied with different tools. Diffusion is usually addressed with long (typically hundreds of ps) equilibrium runs, from which the mean square displacement (MSD) is computed up to a certain time limit (much shorter than the total simulation time): for ionic diffusion in liquid water the typical length required for the MSD is of substantially less than 10 ps, but certainly *longer* than ≈ 1 ps, in order to get a sufficiently accurate value of the diffusion coefficient (D). On the other hand, the onset and completion of an exchange event last typically less than 1 ps, so that exchanges must be studied with short runs starting from properly selected initial conditions [13, 15]. These time scales suggest that asking for instance about the

value of the diffusion coefficient during an exchange does not seem to be meaningful, since the exchange event lasts less than the time required to observe diffusive behaviour in the MSD. Nevertheless, an indirect method is possible to study the signature of exchanges on diffusion: the portions of the long equilibrium run during which no exchanges take place are used to compute a new MSD function (and a new velocity self correlation function), from which a different diffusion coefficient results (D'). It should be obvious that the effect of the exchanges on diffusion will be reflected in a quantitative difference between D and D': one should expect that D is in all cases larger than D', as the latter corresponds to the first shell moving concertedly with the ion, with no exchanges. Since it is only needed that the aforementioned portions have a length of some 10 ps, and exchanges occur on this time scale or longer [10], the computation of D' is perfectly feasible from a statistical point of view. The interesting feature of this simple approach is that, to our knowledge, it will provide the first *quantitative* estimation on the effect of exchanges: although, as argued in the Introduction, it is generally accepted that diffusion is slower if no exchanges take place, the extent of this slowdown is unknown.

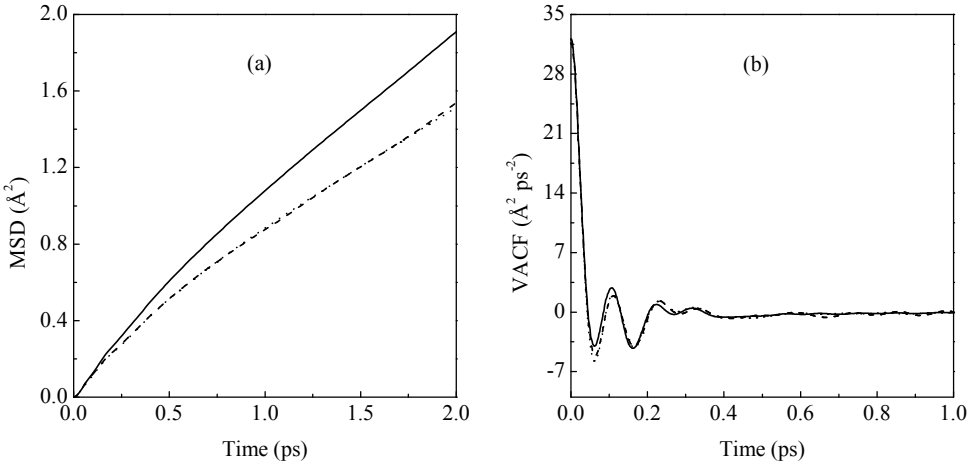

Figure 5.1. Na^+ diffusion in ambient liquid water. Solid line: results from equilibrium simulation; dashed line: results only including portions of equilibrium run without exchanges; points: results from simulations including an effective "wall" between first and second hydration shells. (a) Ion mean square displacement; (b) ion velocity self correlation function.

We have first addressed the case of Na^+ in liquid water, a system for which

kinetic [13] and dynamic [14] characteristics of the exchanges have been studied in detail. The MSD and velocity self correlation functions have been computed in the manner just described, from a run of 3 ns. Figure 5.1(a) displays the results for the MSD obtained from the whole simulation, together with the one obtained from trajectories with no exchanges. As expected, the latter has a clearly smaller slope, consistent with a slower diffusion, with the actual values of the diffusion coefficients being: $D = 1.37$ in front of $D' = 1.05$ (both in units of $10^{-5} cm^2/s$). We see that exchanges increase the diffusion coefficient by a 30 % with respect to the value obtained if exchanges do not occur, which constitutes a basic result of this work. Identical results for the diffusion coefficients are obtained from the velocity self correlation functions obtained in each case. The qualitative differences between the latter functions are evident in Fig. 5.1(b): the initial backscattering to negative values is stronger if no exchanges occur, which can be understood considering that in this case the ion is at all times constrained to an oscillatory motion within the cage of first neighbors.

A second independent methodology has also been devised to doublecheck the previous results. The interaction between the ion and its solvation molecules is altered in order to preclude any exchange between first and second shells, while trying to minimally alter other properties of the system. The ion-oxygen interaction potential for water molecules initially within the first shell is augmented by a term

$$V_{in}(r) = \beta e^{\alpha(r-r^{\ddagger})}, \tag{5.1}$$

while for those molecules initially outside the first shell we use

$$V_{out}(r) = \beta e^{-\alpha(r-r^{\ddagger})}. \tag{5.2}$$

Both contributions together establish a sort of "wall" between first and second shells, which effectively results in the absence of exchanges. The parameters are chosen so that this wall has a fairly short range: $\alpha = 10$ Å^{-1}, $\beta = 5$ kJ/mol, with $r^{\ddagger}$ corresponding to the limit of the first hydration shell ($r^{\ddagger} \approx 3.2$ Å). The effect of these new potential contributions can be graphically understood upon consideration of the ion-water potential of mean force (pmf) defined as

$$W(r) = -k_B T \ln(g(r)), \tag{5.3}$$

where $g(r)$ denotes the ion-oxygen radial distribution function.

Figure 5.2 displays the pmf obtained for the Na^+-water pair for the case of free dynamics (no "wall" included). This figure also displays the curves that

result when the interactions embodied in Eq. 5.1 and Eq. 5.2 are added to the pmf. It can be seen how the molecules within the first shell ($r < 3.2$ Å) are effectively constrained to a well with a wall which raises steeply for increasing distance, while molecules initially beyond $r^{\ddagger}$ cannot get inside the first shell due to a second barrier, which also rises steeply when the distance is reduced. The MSD and velocity tcf have been computed for a system subject to the constraints described above. The results are included in Figs. 5.1(a,b): the new curves are almost indistinguishable from those obtained from the subset of trajectories which do not display any exchange, confirming the previous conclusions.

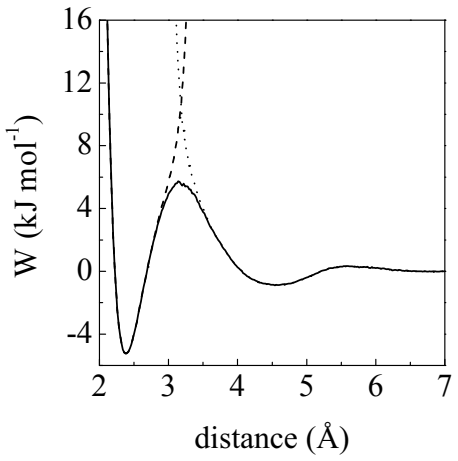

Figure 5.2. Solid line: potential of mean force (Eq. 5.3) between Na^+ and a water molecule; dashed line: same plus the contribution of $V_{in(r)}$ (Eq. 5.1); points: same plus the contribution of $V_{out}(r)$ (Eq. 5.2).

While exchanges around Na^+ cannot be assigned to any well-defined type [14], those around Li^+ have in almost all cases an associative character [15]: a second shell molecule enters the first shell, and after a short (variable) time a second molecule leaves. Therefore, the exchange event is characterized by a temporary hydration number *larger* than the mean. This behaviour suggests that, contrary to the Na^+ case, diffusion might be slower during an exchange for Li^+, considering the larger radius of the complex formed by the ion plus (five) first shell molecules. To examine this point, calculations similar to those described for Na^+ have been performed for Li^+ in ambient water. The results displayed in Figs. 5.3(a,b) indicate that, in line with the results for Na^+, diffusion is again faster if exchanges are included: $D = 1.2$ in front of $D' = 1.1$ (again in units of $10^{-5} cm^2/s$). Although the effect does not seem to be so marked, a 10 % speed-up, it needs to be considered that exchanges are more uncommon for Li^+ than for Na^+: while the lifetime of a first shell molecule is 57 ps for the former [25] (with four hydration molecules), it is of only 34 ps for the latter [13] (with six hydration molecules). Therefore, the small difference in this case is in part due to the increased weight of trajectories which do not contain any exchange. It is worth noting in this connection that this 10 % increase (30 % in the Na^+ case) cannot be directly interpreted in the sense that diffusion is faster

by a 10 % (or 30 %) during an exchange: it should be recalled that the concept of diffusion coefficient during an exchange is ill defined, given that its duration is shorter than the time required for diffusive behaviour to become established.

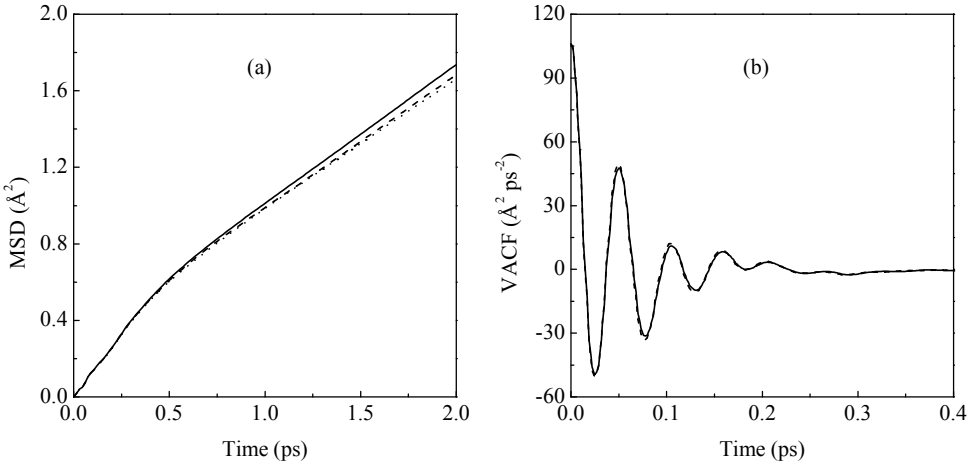

Figure 5.3. Li^+ diffusion in ambient liquid water. Solid line: results from equilibrium simulation; dashed line: results only including portions of equilibrium run without exchanges; points: results from simulations including an effective "wall" between first and second hydration shells. (a) Ion mean square displacement; (b) ion velocity self correlation function.

A basic lesson to be learned, though, is that neither the increased local density during the exchanges (which in principle should hinder the ion mobility), nor the larger volume of the hydrated ion complex (which again should produce an slowdown, since e.g. from a Stokes-Einstein point of view diffusion is slower for larger radius) are important factors. In consequence, together with the previous analysis for Na^+, solvent structure disruption during the exchange seems to be the basic factor explaining the increased mobility, due to the more feeble interactions resulting from less than optimal solvent molecule orientations. Finally, comparing the results for Na^+ an Li^+ we see that certainly in the latter case, since the effect of exchanges is scarce, it is a good approximation to use a "solventberg" picture to understand its diffusion.

The previous results also answer one of the questions raised in the Introduction: given that the exchange times are typically longer than 10 ps and the diffusion coefficient is well determined from a shorter portion of the MSD, it is, as we remarked there, somewhat puzzling that the solventberg picture is not manda-

tory in all cases. The answer is evident in Fig. 5.1(a) (Na^+ diffusion in water), the MSD curves that correspond to trajectories with no exchanges diverge from the curve corresponding to all trajectories for times as short as 0.2 ps. The explanation is rather simple, while it is certainly true that molecules take a mean time of some 34 ps to leave the first shell, it is a key point that nothing prevents an exchange to take place immediately after a new time origin is set during the computation of the MSD. Again, Fig. 5.3(b), illustrates why the solventberg picture is more convenient in the case of Li^+: the curves only start to (slightly) diverge for times of the order of 2 ps, when a rather good approximation of the diffusion coefficient can already be obtained.

5.3 Effect of diffusion on solvation shell exchange

We now turn to the inverse problem, summarized in the present Section title. As described in the Introduction, some arguments suggest a negligible influence of the instantaneous velocity of the solute on the onset of a solvent exchange event and, actually, a thought example which supports this view was detailed there. However, a simple link is uncovered if we take upon consideration that the particle velocity and the *relative* velocity between the particle and a solvation molecule are correlated via simple kinematic considerations. For a solute moving inside a solvent, and assuming random directions of motion for each individual, it is evident that there will be a higher probability for head-on collisions with solvation molecules in front of the solute. It is important to notice that this is a probabilistic statement; collisions from behind the solute are not precluded, they are just less probable. A different way to put it is that given an instantaneous velocity for the solute, say to the right, then all molecules on the right are approaching the particle on the average (although of course some of them might be getting farther away). Note that this alternative formulation is not limited to those molecules in the immediate vicinity of the particle, molecules far away will be approaching or going away from it (for each given instantaneous particle velocity). The formulation also makes no reference to the phase of the solvent; they also apply for a low density gas situation. Despite their very general character, these simple kinematic considerations have something to say about exchange for a translating solute in a solvent. If we particularize to second shell molecules then we conclude that, for instance, those on the right of the solute will on the average get closer to the first solvation shell (with the maximum approach for those on the line of motion of the

particle). Therefore, we see that purely kinetic considerations strongly condition the way in which (attempted) exchanges may start: molecules on the right side of the second solvation shell will have a higher probability of *trying* to enter the first solvation shell while, on the contrary, those on the left side of the *first* solvation shell will have a higher probability of attempting to leave (always assuming an instantaneous solute velocity to the right). The picture that results is one in which, as the solute moves in one direction, molecules in front of it try to enter the first solvation shell and molecules behind it try to exit to the second solvation shell. Of course, trying to enter or leave does not guarantee the success of the exchange but as will be shown within this is, *de facto*, a driving force.

5.3.1 Equilibrium contribution

The above ideas can be expressed in mathematical form assuming thermal equilibrium and a homogeneous phase so that, consequently, the formulas that result are of application to any thermal fluid. Figure 5.4 sketches the typical configuration in which the solute and one of the solvent molecules (of a given solvation shell) have random velocities at a given time. Taking the solute velocity direction as the origin for angles, we ask about the probability (as a function of θ, see Figure 5.4) that a given solvent molecule has an approaching relative velocity (which we will define as positive, and negative when the two particles tend to move away). This probability is given by the expression (see Appendix for mathematical details)

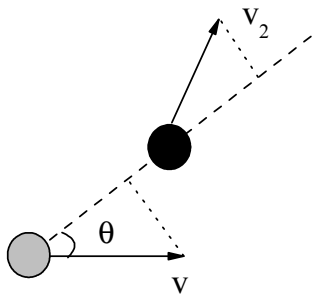

Figure 5.4. Random velocities for solute (grey circle) and solvent molecule (black circle). Also shown projections of both velocities on the intermolecular axis, from which v_r (Eq. 5.13) is defined.

$$p_+(\theta) = \frac{1}{\pi}\left\{\tan^{-1}\left(\sqrt{\frac{m_2}{m_1}}\cos\theta\right) + \frac{1}{2}\sin\left[2\tan^{-1}\left(\sqrt{\frac{m_2}{m_1}}\cos\theta\right)\right] + \frac{\pi}{2}\right\}, \quad (5.4)$$

where m_1 denotes de mass of the solute, m_2 that of a solvent molecule, and the angle θ is defined over the interval $[0, 180]$ degrees. While we will mainly focus on this function, a parallel study can be done for the probability of having a relative velocity in the opposite direction ($p_-(\theta)$), and appropriate distinctions will be

made where required.

A first notable feature is the lack of dependence on temperature, which supports a similar behaviour (for the attempts of solvation shell exchange) at different temperatures, as long as there exists a similar solvation structure (measured for instance by the hydration number). This constitutes an interesting aspect from a computational standpoint, since simulations of the system at higher temperatures, where exchanges are not so rare, might be a convenient starting point to gain some understanding for the behaviour at lower ones (as suggested in Ref. [25]), although we will not pursue this possibility here.

The mass ratio (m_2/m_1) is the single parameter appearing in $p_+(\theta)$ and therefore it is relatively easy to understand its effect. Figure 5.5 displays the behaviour of $p_+(\theta)$ for three selected values (corresponding curves for $p_-(\theta)$ can be constructed as a mirror image with respect to a vertical line at 90^o). The wiggling curve corresponds to $m_2/m_1 = 1$ (equal masses for the solute and the solvent molecules), and is representative of the general situation. It illustrates how the probability of having an approaching relative velocity is larger at $\theta = 0^o$ and attains its lowest value at $\theta = 180^o$, effectively resulting in an asymmetric distribution around the instantaneous solute velocity, which constitutes a central result of this work. Two interesting limiting cases are also included. For $m_2/m_1 \to 0$ (particle mass much larger than that of a solvent molecule) we recover the limiting case that was qualitatively discussed in the Introduction (with no real diffusion). We see how the probability distribution is flat ($p_+(\theta) = 1/2$): all molecules around the central massive particle have an equal (symmetric) probability of attempting to get into its vicinity (and similarly for the probability of attempting to escape). The second limiting case corresponds to $m_2/m_1 \to \infty$, a very light solute in comparison with massive (and slow) solvent molecules. Here we obtain the step function depicted in Fig. 5.5, defined by

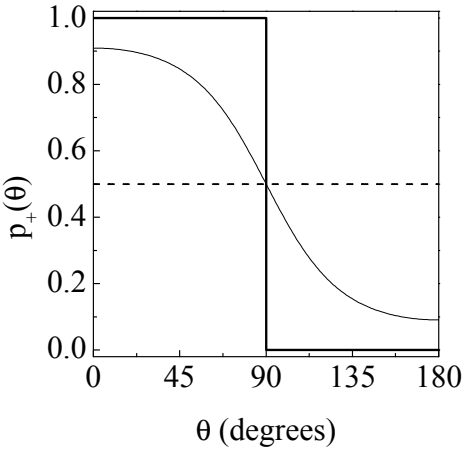

Figure 5.5. $p_+(\theta)$, probability for a solvent molecule to approach the solute. Thick line: $m_2/m_1 \to \infty$; dashed line: $m_2/m_1 \to 0$; thin line: $m_2/m_1 = 1$.

$$p_+(\theta) = \begin{cases} 1 & \text{for } 0 \leq \theta < 90^o \\ 0 & \text{for } 90^o < \theta \leq 180^o \end{cases} , \tag{5.5}$$

which is easily interpreted: the solute undergoes a random motion in a maze of static scatterers, which will never "chase" it and therefore no approaching molecules can be found for any angle greater than 90^o (the corresponding inverted behaviour would be found for $p_-(\theta)$).

Finally, it should be noted that the function just analyzed corresponds to the probability for any given molecule to have an approaching relative velocity with respect to the solute. A related, but different, function is the fraction of molecules found for each angle of all those that have inward velocity (which will be denoted $\wp_+(\theta)$). Given that there is cylindrical symmetry around the solute velocity, more molecules are found for angles close to 90^o than for smaller (close to 0^o) or larger angles (close to 180^o). On the contrary, $p_+(\theta)$, as we have seen before, has a maximum at $\theta = 0^o$. In consequence, the maximum of $\wp_+(\theta)$ will be found somewhere between 0 and 90 degrees. The result is (see the Appendix for details)

$$\wp_+(\theta) = \frac{\sin(\theta)}{\pi} \left\{ \tan^{-1}\left(\sqrt{\frac{m_2}{m_1}}\cos\theta\right) + \frac{1}{2}\sin\left[2\tan^{-1}\left(\sqrt{\frac{m_2}{m_1}}\cos\theta\right)\right] + \frac{\pi}{2} \right\} \tag{5.6}$$

where the only difference with $p_+(\theta)$ is the sine function preceding the braces.

Figure 5.6 displays the function $\wp_+(\theta)$ for each of the three examples that were just discussed above in terms of $p_+(\theta)$. For $m_2/m_1 \to 0$ the distribution displays a maximum at 90^o, showing that $\wp_+(\theta)$ can be somewhat misleading about the process: although all molecules (for any angle) have the same probability of having an approaching velocity (in this particular limit), collecting all the molecules for a given angle results in an apparent nonsymmetric distribution of molecules trying to enter. With this cautionary note in mind, we see how in the opposite limit ($m_2/m_1 \to \infty$) the distribution also peaks at 90^o. Finally, all the intermediate cases are characterized by a maximum at an angle lower than 90^o, which reflects that if the attempted exchanges are monitored and collected as function of θ, a maximum at this angle will be be found, and not along the velocity direction (as might in principle be expected from $p_+(\theta)$). Given the probabilistic nature of the formulas just derived, it is obvious that by themselves they cannot predict when and how an exchange event will start, they should be regarded instead as a sort of "sum-rule". As such, they can help interpret averaged results for the

stereochemistry of the exchanges. We take the case of the hydration shell exchange process around the lithium ion in ambient water as an illustrative example. This system, which has been recently studied [15], is characterized by a tetrahedral equilibrium solvation structure and a substantial variety of distinct exchange classes.

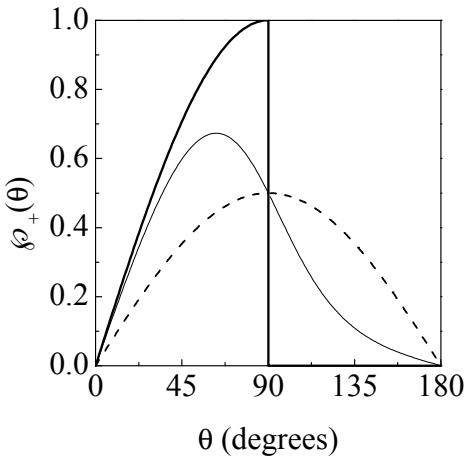

Figure 5.6. $\wp_+(\theta)$, fraction of molecules having an inward velocity for each θ. Thick line: $m_2/m_1 \to \infty$; dashed line: $m_2/m_1 \to 0$; thin line: $m_2/m_1 = 1$.

A priori arguments would suggest that when the exchange is simultaneous (one molecule entering the first shell while another leaves) the mechanism should have a *trans* character. This hypothesis is based on the well-known S_N2 reaction mechanism (Walden inversion), in which the attacking and leaving groups form 180^o. But in contradiction with this hypothesis, it is found [15] that the number of *cis* exchanges is more than half of those assigned to *trans* exchanges. While a satisfactory explanation could not be given in Ref. [15], it now seems clear that this finding is due to the kinetic constraints just described. As we have seen, $\wp_+(\theta)$ peaks at an angle of approximately 60^o (applying formula 5.6 to the pair Li^++H_2O), while $\wp_-(\theta)$ would have a corresponding maximum at a value of 120^o. This implies that the angle between the entering and leaving water molecules may span the range from 60^o ($= 120^o - 60^o$, assuming a null dihedral angle between the plane defined by the ion velocity and the leaving molecule velocity, and the plane formed by the ion velocity and the entering molecule velocity) and up to 180^o (for a dihedral angle of 180^o). This broad range of possibilities results assuming the most probable entrance and exit angles, and thus is further reinforced if we consider the broad dispersion of angles apparent in Fig. 5.6.

Therefore, we see that *cis* exchanges are not precluded at all and that, instead, a continuuum between *cis* and *trans* is most probably the general rule. In short, the substantial number of *cis* exchanges found in the simulations is due to the fact that more molecules are available at angles larger than 0^o. Actually, the con-

siderations above suggest that a classification in terms of *cis* and *trans* exchange classes is a concept which should not be pursued for exchange processes, at least for the types of exchanges considered here [26]. Finally, as explained above, if the exchanges would be normalized by the number of water molecules available at each angle, then the distribution $p_+(\theta)$ is obtained for the entering molecules, and $p_-(\theta)$ for those leaving (which peak respectively at 0^o and 180^o): in consequence, the most probable exchange would have a *trans* character as initially expected.

5.3.2 Nonequilibrium contribution

The previous discussion provides an "equilibrium" estimation for the exchanges, in the sense that we have computed the probability that a given second shell solvent molecule might attempt to enter the first shell ($p_+(\theta)$), or the fraction of molecules trying to enter for a given angle ($\wp_+(\theta)$). However, we now have to consider nonequilibrium effects, meaning that the attempted exchange will fail or succeed depending on the detailed dynamics of the system. In the end, the success or failure depends on the combination of equilibrium (probability of attempting an exchange) and nonequilibrium contributions (dynamics starting at the attempted exchange). A pessimistic view would anticipate that the nonsymmetric distribution just discussed might get blurred by this additional contribution, so that, finally, no noticeable correlation will be found between (successful) exchanges and the instantaneous solute velocity. However, there are strong arguments in the opposite direction stemming from reaction rate theory. The problem of solvation shell exchange, particularly in the vicinity of an ion, was first tackled from the standpoint of activated reactive process for the Na^+-water system [13]. There it was shown that the exchange rate (notice that this is a quantity averaged over all angles) can be expressed as the product of equilibrium contributions (determined from Transition State Theory, TST) and a nonequilibrium contribution dependent on the dynamics (transmission coefficient, κ). This approach has been subsequently applied to the aforementioned case of $Li^+(aq)$ in a broad range of thermodynamic conditions [25] and, at a more detailed level, in ambient water [15]. A first lesson from this work is that TST provides an acceptable estimation of the exchange rate, predicting at least the right order of magnitude, which is remarkable if we consider that exchange rates span more than 15 orders of magnitude [27]. TST assumes, as applied to the present case, that all molecules crossing the Transition State (basically the division between first and second solvation shells) with inward velocity will finally end up in the

first shell. We must conclude that (in this approximation) $p_+(\theta)$ (or $\wp_+(\theta)$) represent not only the probability of attempted exchanges, but the real distribution of successful exchanges and, therefore, that all exchanges (for any sort of solute or solvent) obey exactly the same rules.

It must be said though that the transmission coefficient is rather low in the cases that have been studied so far, with values ranging from ≈ 0.4 (for Li^+ in supercritical water [25]) down to 0.14 (for Li^+ in ambient water [15]), so that its effect certainly has to be considered. However, this correction will affect the estimated distribution of successful exchanges ($p_+(\theta)$ or $\wp_+(\theta)$) only if a sort of angle-dependent transmission coefficient is found, so that the probability for an attempt of being successful would depend on the angle θ. The only way to ascertain this point seems to be a case by case analysis, performed by MD simulation of the systems. In principle, this could be done, but it is a computationally difficult task: for example, the computation has to be performed separately for each angle, so that it has to be lengthened proportionally to the number of intervals in which the interval $[0^o,180^o]$ is divided (for a given statistical tolerance). With these considerations in mind we have chosen three examples where this study is still feasible.

In each case we have computed the previously defined function $\wp_+(\theta)$ (the fraction of molecules found for each angle of all those with inward velocity), which as previously explained takes into account the equilibrium effects. To scrutinize the nonequilibrium effects we have also computed the fraction of molecules found for each angle of all those that finally become stabilized within the first shell (denoted as $\wp_+^{delay}(\theta)$). It is important to note that $\wp_+^{delay}$ is not the fraction of successful molecules from *all* those that tried to enter initially. If defined that way, because of the strong reduction embodied in κ (transmission coefficient), $\wp_+^{delay}(\theta)$ would be very low for any angle, and not easily comparable with $\wp_+(\theta)$. With these definitions, the basic idea is that, if κ is not dependent on θ, then we should obtain $\wp_+(\theta) = \wp_+^{delay}(\theta)$, *i.e.*, all the molecules trying to enter have the same chance of being successful irrespective of the attack angle θ. Any dependence of κ on θ will show up as a difference between $\wp_+(\theta)$ and $\wp_+^{delay}(\theta)$.

First, we have addressed Na^+ in ambient water, a case characterized by a low transmission coefficient (≈ 0.21) and a first solvation shell of six molecules [13]. A long run of 14 ns has been performed at 298 K, during which ≈10,000 attempts by second shell water molecules to enter the first shell have been recorded. The angle between the relative velocity and the instantaneous ion velocity has been

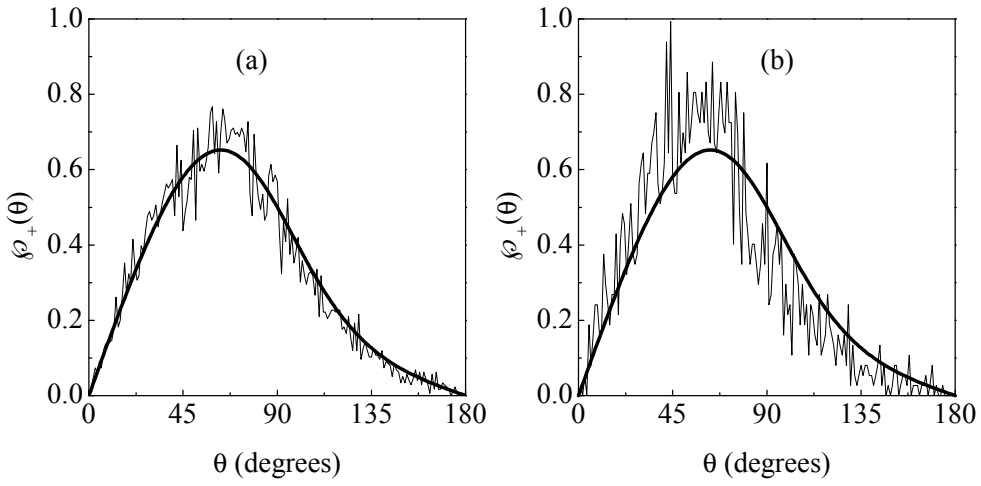

Figure 5.7. (a) Thick line: theoretical $\wp_+(\theta)$ for Na^+ in ambient liquid water; thin line: computed from MD simulation; (b) Thin line: computed $\wp_+^{delay}(\theta)$ for Na^+ in ambient liquid water; thick line: theoretical curve for $\wp_+(\theta)$.

computed in each case, what allows us to estimate $\wp_+(\theta)$. As it can be seen in Fig. 5.7(a), this numerical estimation nicely matches the theoretical prediction of formula 5.4. In order to ascertain the nonequilibrium contribution, each of these attempts has been followed during 1.5 ps. This time is chosen in accordance with the reactive flux function computed in Ref. [13], where it was shown that after $\approx$ 0.5 ps it levels off and reaches a plateau, from which its mean value can be identified with the aforementioned transmission coefficient ($\kappa = 0.21$). It has been found that, consistently with the latter value (which can also be interpreted as the ratio of successful exchanges over total number of attempts), a total of $\approx$ 2,100 second shell molecules become stabilized within the first solvation shell. If these successful attempts are assigned to the corresponding angle (with an angle interval of 1 degree), the curve depicted in Fig. 5.7(b) results. Despite the substantial amount of noise, it is rather clear that this curve is rather similar to the theoretical curve for attempted exchanges, although it seems slightly higher at small angles and closer to zero at larger angles. In conclusion, the probability of attempted exchanges is, *de facto*, the one that conditions the distribution of successful exchanges, with a possible small correction from the nonequilibrium contribution.

Li^+ in supercritical water is the second case that has been analyzed numeri-

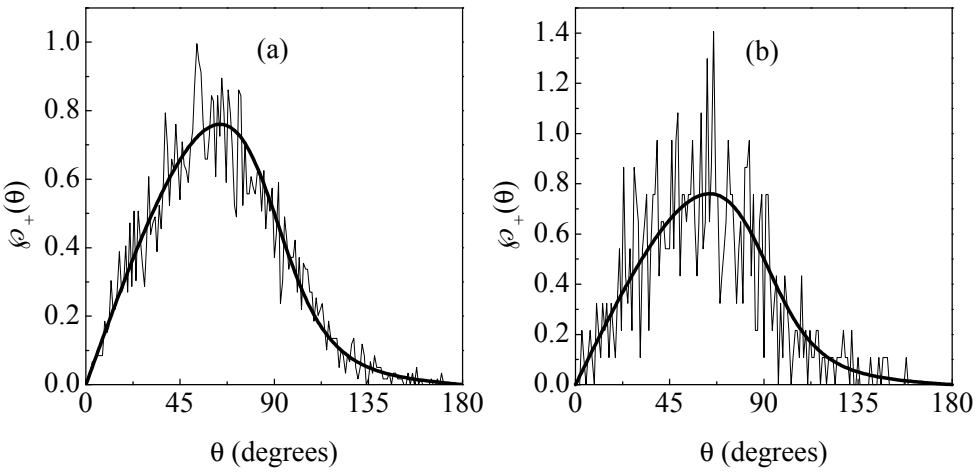

Figure 5.8. (a) Thick line: theoretical $\wp_+(\theta)$ for Li^+ in supercritical water (T = 683 K, $\rho = 0.20$ g cm^{-3}); thin line: computed from MD simulation; (b) Thin line: computed $\wp_+^{delay}(\theta)$ for Li^+ in supercritical water; thick line: theoretical curve for $\wp_+(\theta)$. Same results are found at $\rho = 0.31$ g cm^{-3} and $\rho = 0.48$ g cm^{-3}.

cally. While in ambient water the transmission coefficient seems to be rather low for the systems analyzed so far [13, 15, 25], it has been found that in supercritical water it can exceed 0.4 [25]. Together with the lower number of hydration molecules (four), these constitute interesting differences with the preceding case. Simulation runs of 6 ns were performed during which ~ 4000 trajectories of water molecules entering the first solvation shell were followed (for the simulations of Li^+ in supercritical water we have used the same ion-water interaction parameters as in Ref. [25], where a detailed study of lithium diffusion in this phase was performed, and the SPC/E model for water [28]). Three different densities were chosen at the temperature of 683 K: 0.20, 0.31 and 0.48 g cm^{-3}. The time interval over which the trajectories are followed before deciding if the attempt is successful has been chosen as in the previous case. Fig. 5.8(a,b) displays the corresponding results. Again, the results are rather similar to the case of Na^+ in ambient water.

Despite their differences, the previous examples are both representative of ionic diffusion (albeit in different phases), sharing some important common characteristics such as low hydration number and strong interactions. Since the formulas have general applicability, it is of interest to examine systems that differ markedly as far as these aspects are concerned. We have addressed a neat sim-

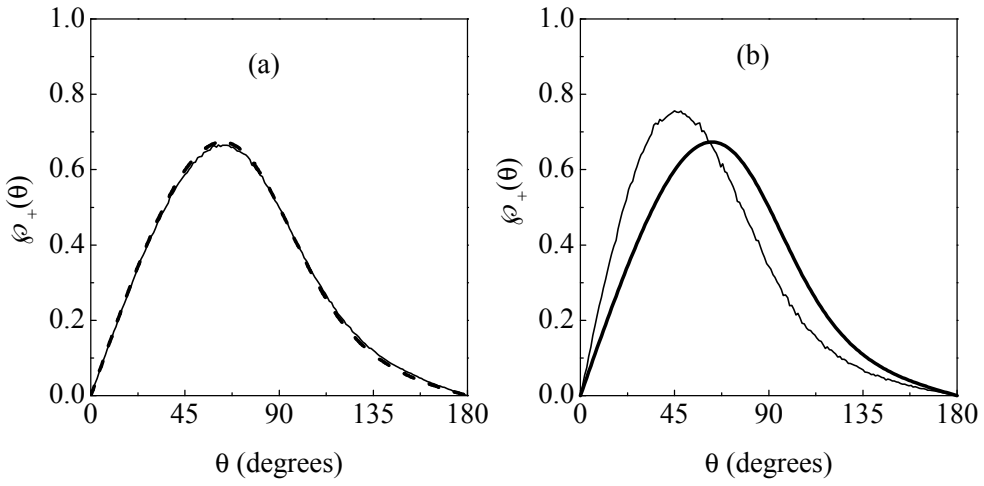

Figure 5.9. (a) Thick dashed line: theoretical $\wp_+(\theta)$ for liquid Ar (T = 112 K, $\rho = 1.479$ g cm^{-3}); thin line: computed from MD simulation; (b) Thin line: computed $\wp_+^{delay}(\theta)$ for liquid Ar; thick line: theoretical curve for $\wp_+(\theta)$.

ple liquid, the much studied liquid Argon [23, 24, 29, 30], which has the following interesting characteristics: a solvation number substantially larger (≈ 12) and almost no free energy barriers to exchange (see below). Furthermore, it constitutes a computationally convenient system: it is easier to obtain good statistics since now all the atoms can be used, instead of a single ion as before. The system is composed of 500 Ar atoms at a temperature of 112 K and a density of 1.479 g cm^{-3}. Since there are no previous studies of which we are aware on the solvation shell exchange process in this case, we have first performed such an analysis.

First, from the radial distribution function we find that the barrier to exchange, viewed in a unimolecular dissociation perspective (as done for ions in water [13, 15, 25]), is ≈ 1.6 k$_B$T (computed from the free energy defined in Eq. 5.3). This low barrier shows that the process is not well described as an activated one, even though we have chosen a state point where the barrier is probably (close to) the highest possible in liquid argon [29]. Since the velocity time correlation function is known to decay in less than 1 ps (comparable to the case of an ion in liquid water, and to the corresponding reactive flux function), we have also followed the incoming atoms during 1.5 ps before checking if they end up in the first shell. The results, at each state point, correspond to equilibration runs of 50000 steps (where the velocities where rescaled to get the reference temperature of the

simulation) followed by production runs of 1000000 steps. Fig 5.9(a,b) displays the corresponding results. Again, there is a perfect match with the theoretical curve for $\wp_+(\theta)$ (Fig. 5.9(a)). Thanks to the better statistical sampling the deviation of the distribution of successful exchanges ($\wp_+^{delay}(\theta)$) from the theoretical curve is now perfectly discernible (Fig. 5.9), and confirms the deviation hinted in the plots corresponding to Na^+ and Li^+. We see that head-on collisions (small angles) have a (slightly) higher probability of being successful (values above $\wp_+(\theta)$) in comparison with those at large angles (curve closer to zero than $\wp_+(\theta)$). A simple explanation suffices to account for this: the mean (approaching) relative velocity is larger at small angles rather than at angles close to 180^o (another reflection of the fact that solvent molecules at small angles are approaching the solute, on the average, and those at large angles are departing from it, on the average). This higher velocity should facilitate the success of the exchange at small angles, and this is what is actually found for liquid argon, and is hinted at in the plots for the cations in water. Evidently, the nonequilibrium contribution slightly enhances the difference between entering and leaving angles.

5.3.3 Effect on the exchange rate

The previous sections have addressed the effect of the instantaneous diffusive state of the solute on the mechanism of the exchange process. It has been shown that a symmetric distribution of entering (and leaving) solvent molecules for a static solute, turns into an asymmetric one if the solute is allowed to diffuse. Since exchanges occur in both cases, we are led to also ask whether the kinetics (exchange time) is affected as well when the solute mass is increased or decreased (without altering the force field). It will be shown that this effect actually exists and can be understood from purely equilibrium considerations. To illustrate this point we have extended our simulations for Li^+, by artificially increasing its mass so that, everything else unchanged, the lithium ion is effectively static. In particular we have taken Li^+ in water at T=683 K and $\rho = 0.2$ g cm^{-3}. We adopt the usual definition of exchange time [9, 13, 25] as the time constant of the exponential fit to the survival function defined

$$n(t) = \frac{1}{N_h} \sum_{i=1}^{N_h} \theta_i(r,t)\theta_i(r,0), \tag{5.7}$$

where $\theta(r,t)$ is 1 if the molecule is within the first hydration shell (defined by a maximum separation $r^\ddagger$ between the ion and the water molecule center of mass),

and 0 otherwise. N_h denotes the number of water molecules initially within the first shell, and a molecule is considered to have left the first shell only if it has been out for more than $\tau^* = 2$ps.

Obviously, we now find that for an ion of infinite mass the distribution of exchanges is symmetric and, what is of interest here, that the exchange time has a value of $\tau_\infty = 10.8$ ps, to be compared with a faster exchange time of $\tau = 6.9$ ps if the lithium ion is assigned its correct mass [25], so that a ratio of $\tau/\tau_\infty = 0.6$ results. To understand the origin of this effect we will adopt the approach that has been cursorily described within the previous sections, namely, to view the exchange as an association-dissociation process [13, 15, 25]. From this standpoint the exchange rate is written, following the usual reaction rate theory formulas, as a product $k = k^{TST}\kappa$, where k^{TST} is obtained from

$$k^{TST} = \sqrt{\frac{k_B T}{2\pi\mu}} \frac{(r^\ddagger)^2 e^{-\beta W(r^\ddagger)}}{\int_0^{r^\ddagger} dr r^2 e^{-\beta W(r)}}, \tag{5.8}$$

where $W(r)$ has been defined in Eq. 5.3.

Equation 5.8 shows that the equilibrium contribution (k^{TST}) depends on the square root of the inverse reduced mass, the only varying parameter since $W(r)$ will remain unchanged even if the masses are varied (as the force field has not been altered). If an infinite mass is assigned to the lithium ion, we will have $\mu_\infty = m_{water}$, *i.e.* the reduced mass is that of the water molecule, whereas for real masses we will have $\mu < \mu_\infty$. Therefore, together with Eq. 5.8 and assuming that κ is the same in both cases, we have the following theoretical (equilibrium) estimation for the ratio of exchange times

$$\frac{\tau}{\tau_\infty} = \frac{k_\infty^{TST}}{k^{TST}} = \sqrt{\frac{\mu}{m_{water}}} = 0.5, \tag{5.9}$$

rather close to the previous value of 0.6 (obtained from direct simulation). Given the indeterminacy in the fits of the survival function, we conclude that the fundamental explanation lies in the variation of the reduced mass: exchanges are slower if the solute mass is increased due to the concomitant larger reduced mass of the pair, with a possibly null effect of the dynamic correction (κ). Indeed, the present example constitutes an extreme case as far as ionic diffusion in water is concerned: for more massive ions the difference between μ and μ_∞ is smaller and therefore the ratio will become closer to unity (as it is obvious that the larger the ion mass, the closer we are to the static solute limit). Finally, it is important to note how useful the association-dissociation perspective has been in order to

easily understand this particular issue. Although the existence of a more optimal (*i.e.* with a higher κ) reaction coordinate for the exchange process would be of interest, it has been just shown that the ion-water distance results in simple analytical formulas (Eq. 5.8) which provide useful (quantitative) understanding on the trends.

5.4 Conclusions

The link between exchange events and the diffusive process has been studied from two different perspectives. First, two independent methods have been devised to quantitatively estimate the commonly accepted diffusion speed up induced by exchanges. This methodology has been applied to Li^+ and Na^+ in liquid water, finding that diffusion increases by a 10 % and 30 % respectively. The former case is particularly interesting: although exchanges are characterised by larger than average hydration shells (associative process), mobility is still faster. Therefore, it is reasonable to infer that solvent structure disruption during the exchange, with its concomitant more feeble interactions, is a key factor explaining the increased mobility. Moreover, it shows that neither the increased local density, nor the larger volume of the hydrated ion complex (in principle relevant from a Stokes theory point of view), are decisive factors for this particular issue, as they would both predict a mobility slowdown. In this work only the Li^+ and Na^+ cations have been addressed, as for these cases the kinetics and dynamics of the exchange have been studied in detail [13–15, 25]. It would be interesting to extend the present study to anions [6,10,31–33], especially in water where hydrogen bonding effects could introduce new features. In this connection it is important to note that a proper modelling of the hydrogen bonds for anions most probably requires the inclusion of polarizability [33], as first shell structure seems to be critically dependent on this effect. An assessment of the different methods available to this end is currently underway [34].

The influence of the instantaneous diffusive state of the solute on the exchange properties has constituted the second main focus of interest in this work. It has been shown that purely kinematic considerations, together with the assumption of thermal equilibrium, are sufficient to derive analytic laws for the probability of entrance to the first solvation shell and, similarly, for that of escape. These expressions are of general applicability and imply that, as a rule of thumb, the majority of the solvent molecules will be found entering at an angle of some

60^o with respect to the instantaneous solute velocity, while those leaving will be mostly found forming an angle of some 120^o. Despite the generality and purely kinematic character of these considerations, they have shown to be extremely useful in characterizing the results for the non-trivial cation in water systems, as well as for liquid argon (as noted above, the case of anions in water remains to be investigated). Furthermore, it has been shown that dynamical corrections to these expressions, while being of secondary importance, tend to slightly increase the difference between entrance and exit angles, with the former becoming closer to 0^o (and to 180^o the latter). Finally, it has been argued that the distinction between *cis* and *trans* exchanges, for exchanges involving the instantaneous exchange of two molecules, is probably not possible for simple ionic exchange processes.

5.5 Appendix

We first derive the probability (p_+) for a solvent molecule to have an approaching relative velocity with the solute. According to the generic configuration depicted in Fig. 5.4, the solute velocity defines the origin for angles. The modulus of this velocity will have the (normalised) probability density

$$p(v) = \frac{4}{\sqrt{\pi}} \left(\frac{m_1}{2k_BT}\right)^{3/2} v^2 e^{-\frac{m_1 v^2}{2k_BT}}, \tag{5.10}$$

where m_1 denotes the solute mass, and the function is defined over $[0, \infty]$.

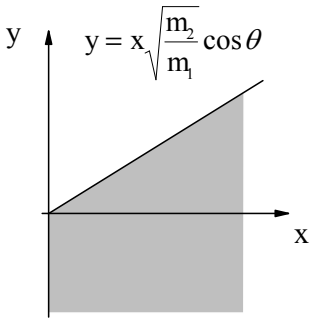

Figure 5.10. Domain of integration indicated by shaded area.

The velocity distribution function for the solvent molecule velocity along the axis joining the solute and the solvent molecule is given by

$$p(v_2) = \sqrt{\frac{m_2}{2\pi k_BT}} e^{-\frac{m_2 v_2^2}{2k_BT}}, \tag{5.11}$$

where m_2 is the mass of a solvent molecule. It should be noted that, in contrast with the previous case, now this function is defined over the interval $[-\infty, \infty]$.

It follows from the previous considerations that the probability density that the modulus of the solute velocity is v and the solvent molecule has a velocity v_2 along the line joining both particles is

$$p(v, v_2) = p(v)p(v_2) = \frac{m_1\sqrt{m_1 m_2}}{\pi(k_BT)^2} v^2 e^{-\frac{m_1 v^2}{2k_BT}} e^{-\frac{m_2 v_2^2}{2k_BT}}, \tag{5.12}$$

A simple projection of the modulus of the solute velocity (see Fig. 5.4) on the intermolecular axis shows that the relative velocity is given by

$$v_r = v\cos\theta - v_2, \tag{5.13}$$

the difference defined so that, when both particles approach each other, v_r is positive.

Finally, the probability we are seeking can be found integrating the two dimensional distribution $p(v, v_2)$ (Eq. 5.12) under the constraint $v_r > 0$, *i.e.*

$$p_+ = \underbrace{\int_0^\infty dv \int_{-\infty}^\infty dv_2}_{v_r>0} p(v, v_2). \tag{5.14}$$

Changing variables ($x \equiv v(m_1/2k_BT)^{1/2}$, $y \equiv v_2(m_2/2k_BT)^{1/2}$), equation 5.14 can be rewritten

$$p_+ = \frac{4}{\pi}\underbrace{\int_0^\infty dx \int_{-\infty}^\infty dy}_{\cos\theta\sqrt{\frac{m_2}{m_1}}x-y>0} x^2 e^{-x^2-y^2}. \tag{5.15}$$

The domain of integration is depicted in Fig. 5.10, which suggests a change to polar coordinates ($x \equiv r\cos\phi$, $y \equiv r\sin\phi$). After this change the 2-d integral is separable

$$p_+ = \frac{4}{\pi}\int_0^\infty dr r^3 e^{-r^2} \int_{-\frac{\pi}{2}}^{\arctan\left(\sqrt{\frac{m_2}{m_1}}\cos\theta\right)} d\phi\cos^2\phi, \tag{5.16}$$

both integrals are trivially done, and the final result is

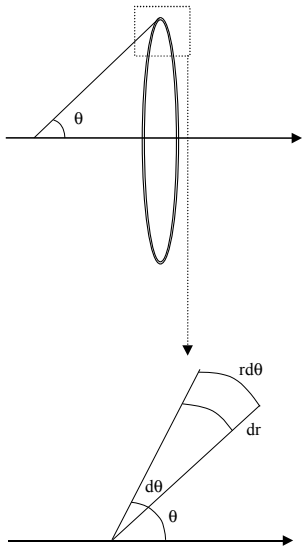

Figure 5.11. Sketch of the volume of the ring at angle θ.

$$p_+(\theta) = \frac{1}{2} + \frac{1}{\pi}\tan^{-1}\left(\sqrt{\frac{m_2}{m_1}}\cos\theta\right) + \frac{1}{2\pi}\sin\left[2\tan^{-1}\left(\sqrt{\frac{m_2}{m_1}}\cos\theta\right)\right] \tag{5.17}$$

We see how the result automatically contains a dependence on θ. As a first trivial check, in the limit case $m_2/m_1 \to 0$ the result is $p_+ = 1/2$, that is, all molecules have equal probability of getting closer or further from the (static) solute, as expected.

Another function of interest, directly related to the former, answers the following question: of all the molecules having inward velocity, which fraction can

be found at angle θ? It will be denoted $\wp_+(\theta)$ and, according to this definition, it can be found (except for a normalisation factor) from the relation

$$\wp_+(\theta)\ \alpha\ (\text{fraction of molecules at angle } \theta) \cdot p_+(\theta). \tag{5.18}$$

The term in brackets ($n(\theta)$) can be expressed (see Fig. 5.11)

$$n(\theta) = \frac{\text{number of molecules in a ring defined by } (\theta, \theta + d\theta) \text{ and thickness dr}}{\text{number of molecules in a spherical shell of thickness dr}}. \tag{5.19}$$

Again, from inspection of Fig. 5.11, it is clear that (if ρ denotes the number density)

$$n(\theta) = \frac{\rho 2\pi r^2 \sin\theta dr d\theta}{(\int_0^\pi sin\theta d\theta)\, \rho 2\pi r^2 dr} = \frac{\sin\theta}{2} d\theta, \tag{5.20}$$

so that (in units of rad^{-1})

$$\wp_+(\theta)\ \alpha\ \frac{\sin(\theta)}{2\pi}\left\{\tan^{-1}\left(\sqrt{\frac{m_2}{m_1}}\cos\theta\right) + \frac{1}{2}\sin\left[2\tan^{-1}\left(\sqrt{\frac{m_2}{m_1}}\cos\theta\right)\right] + \frac{\pi}{2}\right\}. \tag{5.21}$$

Notice that a proper normalisation is still required as, according to its definition, it should satisfy

$$\int_0^\pi \wp_+(\theta) d\theta = 1. \tag{5.22}$$

If this closure relation is imposed for the simple case $m_2/m_1 \to 0$, we obtain the final result

$$\wp_+(\theta) = \frac{\sin(\theta)}{\pi}\left\{\tan^{-1}\left(\sqrt{\frac{m_2}{m_1}}\cos\theta\right) + \frac{1}{2}\sin\left[2\tan^{-1}\left(\sqrt{\frac{m_2}{m_1}}\cos\theta\right)\right] + \frac{\pi}{2}\right\}. \tag{5.23}$$

References

[1] A. Einstein *Ann. Phys.* **17**, 549 (1905).

[2] J. P. Hansen and I. R. McDonald, Theory of Simple Liquids, Accademic, London (1986).

[3] R. Walser, B. Hess, A. E. Mark and W. F. van Gunsteren *Chem. Phys. Lett.* **334**, 337 (2001).

[4] J. T. Hynes *Ann. Rev. Phys. Chem.* **28**, 301 (1977); J. T. Hynes, R. Kapral and M. Weinberg *J. Chem. Phys.* **70**, 871 (1979); J. T. Hynes, R. Kapral and M. Weinberg *J. Chem. Phys.* **67**, 3256 (1977); J. T. Hynes, R. Kapral and M. Weinberg *J. Chem. Phys.* **69**, 2725 (1978).

[5] S. Bhattacharyya and B. Bagchi *J. Chem. Phys.* **106**, 1757 (1997); B. Bagchi and S. Bhattacharyya *Adv. Chem. Phys.* **116**, 67 (2001); S. Pal, S. Balasubramanian and B. Bagchi *Phys. Rev. E* **67**, 61502 (2003).

[6] S. H. Lee and J. Rasaiah *J. Phys. Chem.* **100**, 1420 (1996).

[7] P. G. Wolynes *J. Chem. Phys.* **68**, 473 (1978); P. G. Wolynes *Ann. Rev. Phys. Chem.* **31**, 345 (1980) and references therein.

[8] R. Biswas, S. Roy and B. Bagchi *Phys. Rev. Lett.* **75**, 1098 (1995); R. Biswas and B. Bagchi *J. Chem. Phys.* **106**, 5587 (1997); B. Bagchi and R. Biswas *Acc. Chem. Res.* **31**, 181 (1998).

[9] R. W. Impey, P. Madden and I. R. McDonald *J. Phys. Chem.* **87**, 5071 (1983).

[10] S. Koneshan, J. C. Rasaiah, R. M. Lynden-Bell and S. H. Lee *J. Phys. Chem. B* **102**, 4193 (1998).

[11] T. M. Chang and L. X. Dang *J. Phys. Chem. B* **103**, 4716 (1999).

[12] S. Chowdhuri and A. Chandra *J. Chem. Phys.* **115**, 3732 (2001).

[13] R. Rey and J. T. Hynes *J. Phys. Chem.* **100**, 5611 (1996).

[14] R. Rey and J. T. Hynes *J. Phys. Cond. Matt.* **8**, 9411 (1996).

[15] D. Spångberg, R. Rey, J. T. Hynes and K. Hermansson *J. Phys. Chem B* **107**, 4470 (2003).

[16] L. Helm and A. E. Merbach *Coord. Chem. Rev.* **187**, 151 (1999).

[17] H. J. C. Berendsen, J. P. M. Postma, W. F. van Gunsteren and J. Hermans, Intemolecular Forces, Reidel, Dordrecht (1981).

[18] J. P. Ryckaert *Mol. Phys.* **55**, 549 (1985).

[19] B. M. Pettitt and P. J. Rossky *J. Chem. Phys.* **84**, 5836 (1986).

[20] L. X. Dang *J. Chem. Phys.* **96**, 6970 (1992).

[21] M. P. Allen and D. J. Tildesley, Computer Simulation of Liquids, Oxford, New York (1989).

[22] H. J. C. Berendsen, J. P. M. Postma, W. F. van Gunsteren, A. di Nola and J. R. Haak *J. Chem. Phys.* **81**, 3683 (1984).

[23] A. Rahman *Phys. Rev.* **136**, A405 (1964).

[24] L. Verlet *Phys. Rev.* **159**, 98 (1967).

[25] M. Masia and R. Rey *J. Phys. Chem. B* **107**, 2651 (2003).

[26] It is however certainly the case that the inferences from simple kinematic arguments can be superseded by the effect of strong chemical interactions; the well-known case of the Walden inversion for SN_2 nucleophilic displacement reactions provides an obvious example.

[27] H. L. Friedman *Chemica Scripta* **25**, 42 (1985).

[28] H. J. C. Berendsen, J. R. Grigera, J. R. and T. P. Straatsma *J. Phys. Chem.* **91**, 6269 (1987).

[29] L. Verlet *Phys. Rev.* **165**, 201 (1968).

[30] D. Levesque and L. Verlet *Phys. Rev. A* **2**, 2514 (1970).

[31] A. Chandra *J. Phys. Chem. B* **107**, 3899 (2003).

[32] B. Nigro, R. Rey and J. T. Hynes, submitted.

[33] S. Raugei and M. L. Klein *J. Chem. Phys.* **116**, 196 (2002).

[34] M. Masia, M. Probst and R. Rey *J. Chem. Phys.* **121**, 7362 (2004).

Part III

Plasticizers

In this Part intramolecular force fields are developed for ethylene carbonate and γ-butyrolactone. Furthermore, structural and dynamical properties of both plasticizers and of Li^+ solvated in their liquid phase are studied, according to the following scheme:

Chapter 6 Structural and dynamical properties of the electrolyte system ethylene carbonate - Li^+ are studied. A high level *ab initio* study of the geometry and vibrational spectrum has been performed both for an isolated molecule and for small clusters including the lithium ion. The ethylene molecule is found to be nonplanar in all instances and an assignment of vibrational modes is proposed on this basis. It is shown that the lithium ion induces substantial blue and red shifts, mainly on the ring and carbonyl stretching modes. These issues have also been studied in the liquid phase for the first time and, for that purpose, a new intramolecular force field has been developed. It is shown that this intramolecular potential satisfactorily reproduces a broad range of features, allowing to interpret the shifts measured experimentally for the molecules within the first solvation shell of the ion. Particularly, the broadening of the carbonyl band found experimentally is the result of an ion induced red shift, obscured by the presence of Fermi resonances. Moreover, the study of the shifts as a function of solvation number supports a four coordinated solvation shell.

Chapter 7 A comprehensive study of structural and dynamical properties of γ-butyrolactone (GBL) and the extent to which they are affected in the vicinity of a lithium ion, both in gas and liquid phases, is reported. The isolated GBL molecule is found to be non-planar, with a barrier of ≈ 9 kJ/mol to ring inversion. As expected, the lithium ion coordinates the carbonyl oxygen with an almost collinear configuration relative to the carbon-oxygen bond, but with a slight tilting towards the lactone oxygen. This configuration holds for clusters of up to four molecules and in the liquid phase as well (where a tetrahedral first solvation shell is found). A high level ab initio vibrational analysis, with a new assignment of bands has been performed, which shows substantial red and blued shifts upon lithium solvation, which decrease in a nontrivial way upon increasing the cluster size. In order to study the solvent effect of the vibrational spectrum an accurate intramolecular force field has been developed, based on the concept of relaxed potential energy profiles. The inclusion of stretch and bend anharmonicity is shown

to be essential in order to explain, not only the absolute value, but the sign of the shifts, particularly for the carbonyl stretching which is substantially downshifted. The shifts obtained for the rest of the bands, together with the diffusion coefficients for bulk GBL and for lithium, are in fair agreement with experimental results.

Chapter 6

Ethylene Carbonate-Li^+: a theoretical study of structural and vibrational properties in gas and liquid phases.

In recent years ethylene carbonate has been the subject of an increasing interest due to its important role in polymer-gel lithium-ion batteries [1]. These devices are usually composed of a lithium salt dissolved in a plasticizer (i.e. an organic solvent) that fills a polymer matrix. Some common solvents are ethylene carbonate (EC, see Figure 6.1), tetrahydrofuran (THF), propylene carbonate (PC) and γ-butyrolactone (GBL) [1]. Actually, a mixture of two or more plasticizers is more convenient [2], as it allows to optimize the balance between different features (such as dielectric constant, viscosity, ionic diffusion, salt dissociation and chemical stability) and thus to enhance the battery performace and cyclability. Understanding the molecular mechanisms by which these plasticizers condition

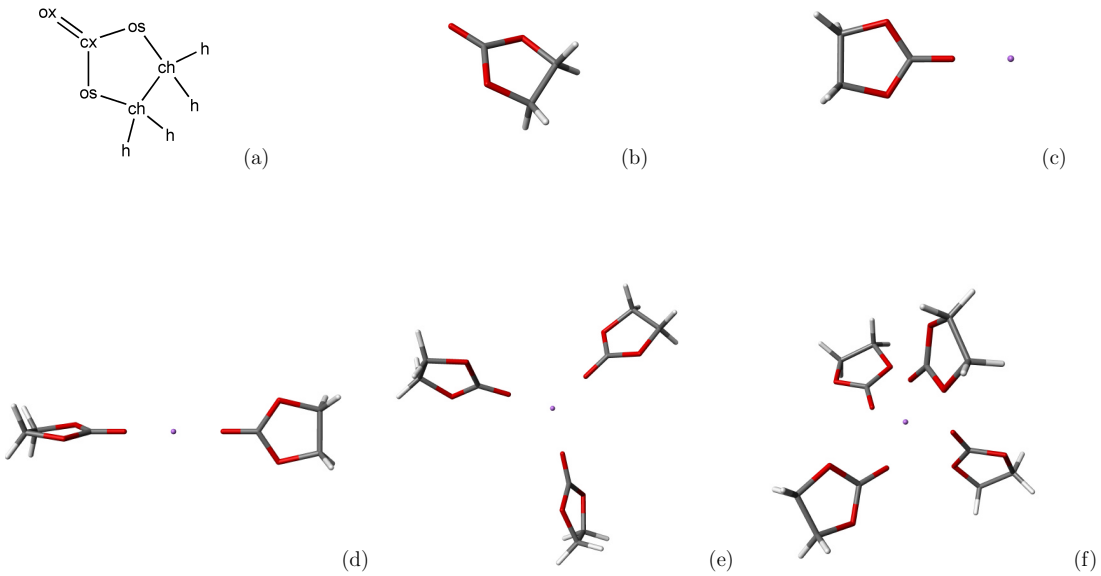

Figure 6.1. Ethylene carbonate and its complexes $[Li(EC)_n]^+$ with $1 \leq n \leq 4$. The labeling of the atoms used in the text is defined in (a). The following colours are assigned to different atomic species: red to oxygen, grey to carbon, white to hydrogen and violet to lithium.

the mobility of lithium is, therefore, of particular interest. Conversely, the strong influence of the ion can substantially affect the surrounding solvent molecules, particularly in their structure and vibrational spectrum. These properties, which can be experimentally probed by a variety of mostly spectroscopical methods, are also amenable to a direct computational study. The motivation of the present work is that a better theoretical understanding of these solvation properties is not only of interest in itself but also a convenient benchmark for the models that will be used to address the basic problem of lithium mobility.

Concerning the structure of the EC molecule, early experimental results of Angell [3] pointed to a planar configuration for EC; later Wang et al. [4], Fortunato et al. [5], Alonso et al. [6, 7] and Matias et al. [8] found that EC has a nonplanar ring structure. On the theoretical side the structural problem has received much attention as well, with the results alternating between both possibilities: the initial computations supported a nonplanar structure [7, 9], subsequent works were in favor of a planar configuration [10–12], while the most recent results favour again a distorted configuration [13–15]. Regarding the vibrational spectrum, many IR and Raman studies have been performed of pure EC and of lithium salts dissolved in liquid EC [5, 11, 16–20]. From the theoretical point of view the vibrational

spectrum has barely been addressed, we only know of the *ab initio* study of Klassen et al. [11] for gas phase EC. For this reason, it will be the main aim of this work to study the dependence of the vibrational modes on geometry and complexation of EC.

We address several issues with both first principles calculations and classical molecular dynamics simulations (MD). First, we have performed the highest level *ab initio* study to date of the single EC molecule, determining which is the most stable geometry and analysing the issue of band assignment. Of particular interest to MD simulations of the liquid, a new intramolecular force field is developed (in terms of valence coordinates) that represents quite satisfactorily not only the vibrational spectrum, but also several other aspects of the full internal potential (particularly the barriers to internal isomerization in the low frequency region, relevant to liquid state dynamics). Moreover, the series of clusters $[Li(EC)_n]^+$ $(n = 1 - 4)$ has also been addressed by analysing the equilibrium geometries and the molecular vibrations in detail. These complexes constitute a useful guide to ascertain which are the EC modes most affected by the ion, and how this effect (and the possible ion-induced geometry distortion) varies as the coordination is increased, what should help understand the liquid state results. In this connection, MD simulations of the liquid phase have been done for pure EC and for one lithium ion dissolved in liquid EC, focusing on the theoretical calculation of the frequency shifts induced on the first shell molecules surrounding the ion. Finally, an analysis of the most probable configurations has also been performed, complementing the MD studies of coordination shell structure by Li et al. [12], and Soetens at al. [13, 21].

The paper is organized as follows: computational details are summarized in section 6.1; results from *ab initio* calculations are discussed in section 6.2 and, those from classical simulations, in section 6.3. Finally, the main conclusions are presented in section 6.4.

6.1 Computational Details

All *ab initio* calculations were performed using the commercial package Gaussian 98 [22]. Vibrational analysis and geometry optimization of a single EC molecule and of the complex $[LiEC]^+$ were performed at the MP2 level with the 6-311G basis set augmented with diffuse and polarization functions [23]. The same model chemistry has been employed for a potential energy surface scan of

EC. We also performed a geometry optimization for the single EC molecule using Dunning's correlation consistent basis set including polarization and diffuse functions aug-cc-pVDZ. As far as we know this is the highest level geometry optimization of EC appearing in literature, providing results in very good agreement with experiment. The additional calculations with the 6-311++G(d,p) basis set were performed to allow for a better comparison between the EC monomer and the $[LiEC]^+$ dimer since the aug-cc-pVDZ basis set is not defined for lithium. Due to the demanding computational effort of *ab initio* calculations on the systems with up to 4 EC molecules, a smaller basis set (6-31G) was used for their geometry optimizations and vibrational analysis.

Classical calculations were performed with both our own Molecular Mechanics code and with the DL_POLY [24, 25] set of programs. The first one was used for the scan of the potential energy surface of a single EC molecule using an internal classical force field and for the vibrational analysis of EC. The DL_POLY package was used to perform the simulations of the chosen liquid phase systems. Data analysis (FFT, curve smoothing and curve fitting) was performed with the commercial package Microcal Origin 6.1 [26].

6.2 Ab Initio Results

6.2.1 Structure

Single EC Molecule

As previuosly described, the equilibrium geometry of an EC molecule is a topic that has received considerable experimental and theoretical attention over the years.

To our knowledge, the only experiment where a planar structure has been inferred was performed by Angell [3], who observed the disappearence of some spectral lines in passing from solid to liquid and gas phase and attributed this to the enhanced symmetry when the molecule passes from C_2 to C_{2v}. Planarity is contradicted by more recent microwave measures [4], where the appearance of doublets of similar intensity for rotational transitions is explained assuming a nonplanar ground state tunneling through the barrier at the planar configuration. A nonplanar structure was also found by Alonso at al. [6, 7] with microwave spectroscopy, and by Matias et al. [8] in a neutron diffraction study.

Surprisingly, rather recent theoretical results support different structures:

	exp. EC	aug-cc-pVDZ EC	6-311++G(d,p) EC	6-311++G(d,p) $[Li(EC)]^+$
Bond length				
ox-cx	1.203	1.203	1.193	1.220
cx-os	1.342	1.370	1.360	1.320
os-ch	1.457	1.440	1.430	1.450
ch-ch	1.522	1.520	1.520	1.520
ch-h	1.091	1.090	1.080	1.080
Bending angle				
ox-cx-os	124.17	124.820	124.970	123.130
cx-os-ch	108.71	108.420	108.140	107.940
os-ch-ch	102.16	102.470	102.050	102.190
os-ch-h	108.30	108.300	108.600	107.552
os-cx-os	111.67	110.350	110.200	113.970
h-ch-h	110.82	110.513	110.610	111.140
ch-ch-h	113.94	114.000	114.030	113.190
Dihedral angle				
ox-cx-os-ch	-	170.550	169.760	171.650
cx-os-ch-ch	21.25	22.900	24.780	20.030
cx-os-ch-h	141.81	143.720	145.580	140.700
os-ch-ch-os	-24.80	-27.180	-29.410	-23.510
os-cx-os-ch	-8.73	-9.443	-10.269	-8.334
os-ch-ch-h	90.88	89.190	86.940	91.780
h-ch-ch-h	-154.32	-154.410	-156.650	-152.910
ox-cx-os-os	171.27	180.000	179.980	179.920

Table 6.1. Comparison of experimental and theoretical geometrical parameters for EC and for the optimized geometry of the EC-Li^+ complex.

Blint [10] points out that the structure of pure EC is planar and that the barrier to reach a distorted configuration is ~ 15 kcal mol^{-1}, making use of a HF/D95V** model chemistry; the same results were obtained by Klassen et al. [11] with the same model chemistry and by Li et al. [12], who made use of a DFT optimized geometry. These findings contradict the expectation of Cremer and Pople who, in their study on general monocyclic rings [27], claimed that a twisted conformation is preferred because a planar ring would imply a more highly strained ring angle at the carbonyl atom. Indeed, in a pioneering study, Alonso et al. [6] found that a double well potential for the ring puckering exists, with two minima different from zero; they argued that this is due to the sum of two opposing contributions where the one that causes the ring to be twisted dominates on the second that would lead to a planar structure; to get a proper description of the molecule

they suggest the use of a rather flexible orbital basis. It is possible that previous studies [10–12] did not find these results because their methods underestimate electron correlation. The nonplanarity of the ring has been recently found with higher level *ab initio* calculations by Soetens and al. [13] and Wang et al. [14].

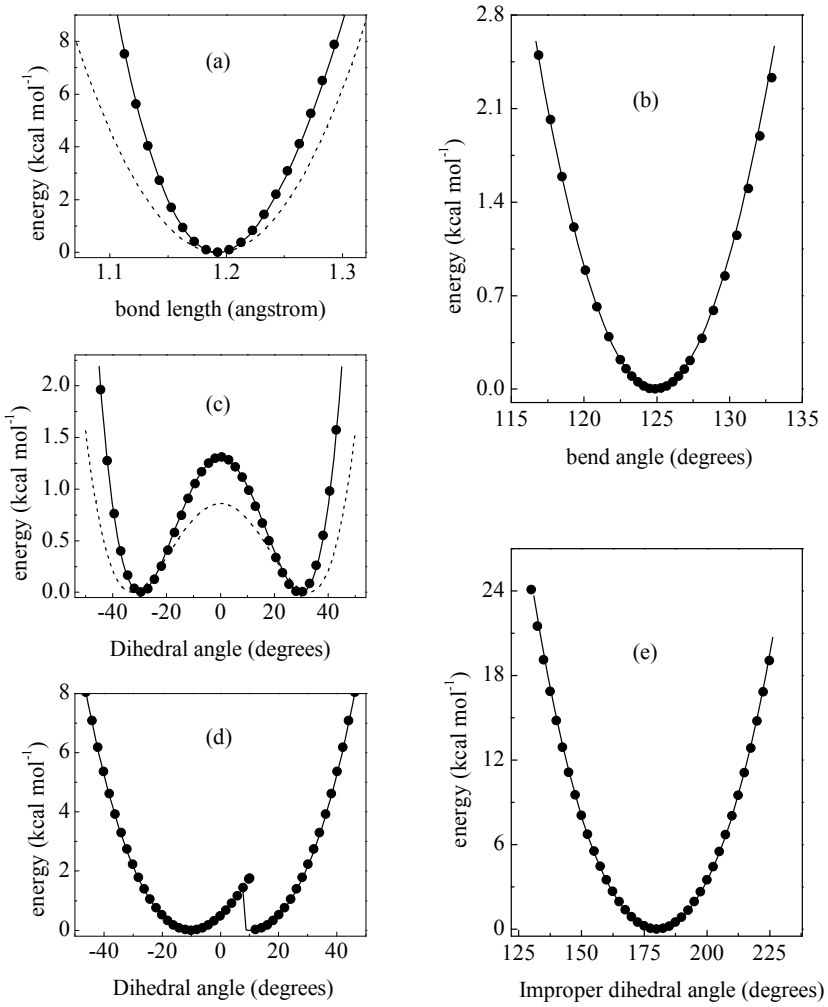

Figure 6.2. rPES curves for (a) ox-cx bond length, (b) ox-cx-os bending angle, (c) os-ch-ch-os dihedral angle, (d) os-cx-os-ch dihedral angle and (e) ox-cx-os-os improper dihedral. The solid lines are obtained with a classical Molecular Mechanics program; dots are the results of the *ab initio* calculations performed with Gaussian 98; dashed lines in panels (a) and (c) are the profiles computed with the AMBER force field.

From the geometry optimization of EC we have also found that the ring shows a nonplanar structure with C_2 symmetry. Table 6.1 contains the values for the internal coordinates (at MP2/aug-cc-pVDZ and MP2/6-311++G(d,p) levels of theory), and the values inferred experimentally for pure EC [8]. It can be seen that

there is good agreement between theory and experiment, mainly at the higher level calculations. Concerning the extent of ring distortion, panel (c) of figure 6.2 displays the double well symmetric potential from an optimized potential energy (rPES) scan of the os-ch-ch-os dihedral angle (see Fig. 6.1 for the labeling of atoms within the EC molecule). A rPES scan computes the energy along a given internal coordinate, simultaneously optimizing all the unconstrained internal degrees of freedom at each step (the Berny geometry optimization algorithm [28] with redundant internal coordinates [29] is used). For this particular coordinate, 60 values of the dihedral angle within -50 and 50 degrees were scanned using an MP2/6-311++G(d,p) model chemistry for the geometry optimization. We find an energy barrier for ring inversion of ~ 1.30 kcal mol^{-1}.

	EC	$[Li(EC)]^+$	$[Li(EC)_2]^+$	$[Li(EC)_3]^+$	$[Li(EC)_4]^+$
Bond length					
li-ox	-	1.760	1.800	1.871	1.947
ox-cx	1.227	1.250	1.240	1.240	1.230
cx-os	1.410	1.360	1.370	1.380	1.380
os-ch	1.490	1.520	1.520	1.510	1.500
ch-ch	1.540	1.550	1.550	1.550	1.540
Bending angle					
li-ox-cx	-	179.98	178.00	179.86	145.32
ox-cx-os	125.36	123.26	123.66	123.99	124.11
os-cx-os	109.51	113.47	112.78	112.00	111.31
Dihedral angle					
ox-cx-os-ch	171.35	175.48	174.83	173.56	172.99
cx-os-ch-ch	21.44	11.14	13.14	15.96	17.93
os-ch-ch-os	-25.28	-12.89	-15.24	-18.59	-21.20
os-cx-os-ch	-8.63	-4.50	-5.35	-6.43	-7.76
ox-cx-os-os	179.95	180.00	179.88	180.00	179.88

Table 6.2. Results of the low-level (MP2/6-31G) geometry optimization results for the structure of EC and its complexes with lithium.

The equilibrium value is $\sim -29°$ (~ 0.78 kcal mol^{-1} at $\sim -27°$ were obtained with the aug-cc-pVDZ basis set). Our values are slightly higher than previous estimations for both the equilibrium angle and barrier height. Alonso et al. [6, 7] found a barrier height of ~ 0.67 kcal mol^{-1} and an equilibrium angle of $\sim -19°$ in the gas phase; Matias et al. [8] found a value of $\sim -24.8°$ in the solid phase using neutron diffraction analysis. The most recent results, though, are rather similar to the ones obtained here, Soetens et al. [13] found an equilibrium dihedral of $\sim 29.5°$

and a barrier of 1.18 kcal mol^{-1} (using an MP2/6-311G** model chemistry). Finally, it is worth to note that the dipole moment of pure EC is 5.3945 Debye (5.4226 Debye was calculated with the 6-311++G(d,p) basis set). These values agree very well with experiment; Alonso et al. [6] report a value of 5.35 ± 0.15 Debye.

$[Li(EC)_n]^+$ ($n = 1 - 4$) Complexes

An interesting issue to look into is how a single EC molecule is affected when it coordinates the lithium ion, and how this is changed by the addition of more molecules since such solvation properties are helpful in understanding the liquid solution. First, as found in previous works [10, 15], the optimized geometry (see figure 6.1(c)) of all complexes studied is characterized by the lithium ion being close to the carbonyl oxygen. The last column of table 6.1 contains the main structural properties of the mono-coordinated lithium complex computed with a MP2/6-311++G(d,p) model chemistry. It is interesting to note that the coordination with Li^+ changes the EC conformation slightly towards a more planar geometry: the os-ch-ch-os dihedral angle reduces from 29.4° to 23.5°, for a given level of theory (two last columns of Table 6.1). The induced distortion is also evident along other internal coordinates: the optimized carbonyl bond length increases from 1.193 Å in the isolated EC molecule to 1.220 Å in the complex. The ch-ch and the ch-h bond lengths do not seem to undergo any significant change as is easily explainable by the proximity of Li^+ to the carbonyl oxygen and its neighbouring atoms.

In addition, we have also studied the effect of coordination in the complexes $[Li(EC)_n]^+$ with n varying from 1 to 4 (theoretical calculations suggest that the four coordinated complex is the one existing in condensed phase [16, 17]). Due to computational limits a smaller basis set (6-31G) was used for the geometry optimization of these complexes. Quantitative values at this level of theory are not sufficiently accurate but certain trends can nevertheless be predicted. As illustrated in figure 6.1, all the complexes are found to be highly symmetrical: there is a linear arrangement for the complexes with 1 and 2 coordinating EC molecules. The three-coordinated complex is trigonal planar with the ring forming an angle of $\sim 55°$ with the plane defined by lithium and the carbonyl oxygens. The four-coordinated complex shows tetrahedral complexation. In the latter one the EC dipole moment does not point straight to the ion, revealing that one of the

two carbonate oxygens is nearer to the metal center. The shorter li-os distance is 3.630 Å and the longer is 4.230 Å. This fact is confirmed by the value of the li-ox-cx angle, which changes from almost 180°(for the dimer) to 145°.

ν		Assignment	Exp.		Assignment
$\nu_1(a)$	3194.2	out of phase CH_2 asym stretch	$\nu_9(a_2)$	3004	CH_2 stretching
$\nu_2(a)$	3109.7	in phase CH_2 sym stretch	$\nu_1(a_1)$	2925	CH_2 stretching
$\nu_3(a)$	1898.8	C=O stretching	$\nu_2(a_1)$	1868	C=O stretching
$\nu_4(a)$	1546.8	in phase CH_2 scissoring	$\nu_3(a_1)$	1483	CH_2 scissoring
$\nu_5(a)$	1420.0	out of phase CH_2 wagging	$\nu_4(a_1)$	1386	CH_2 wagging
$\nu_6(a)$	1271.5	out of phase CH_2 twisting	$\nu_{10}(a_2)$	1157	CH_2 twisting
$\nu_7(a)$	1175.2	**out of phase CH_2 rocking**	$\nu_5(a_1)$	1087	**ring stretching**
$\nu_8(a)$	1123.5	os-ch sym stretch, ch-ch stretch	$\nu_6(a_1)$	960	ring stretching
$\nu_9(a)$	991.6	ring breathing	$\nu_7(a_1)$	881	ring breathing
$\nu_{10}(a)$	895.3	**ring breathing**	$\nu_8(a_1)$	715	**ring bending**
$\nu_{11}(a)$	719.6	**ring stretching**	$\nu_{11}(a_2)$	660	**CH_2 rocking**
$\nu_{12}(a)$	227.2	**out of plane ring bending**	$\nu_{12}(a_2)$	230	**ring puckering**
$\nu_{13}(b)$	3205.8	in phase CH_2 asym stretch	$\nu_{20}(b_2)$	3000	CH_2 stretching
$\nu_{14}(b)$	3112.6	out of phase CH_2 sym stretch	$\nu_{13}(b_1)$	2925	CH_2 stretching
$\nu_{15}(b)$	1539.4	out of phase CH_2 scissoring	$\nu_{14}(b_1)$	1483	CH_2 scissoring
$\nu_{16}(b)$	1420.8	in phase CH_2 wagging	$\nu_{15}(b_1)$	1421	CH_2 wagging
$\nu_{17}(b)$	1267.9	**in phase CH_2 twisting**	$\nu_{16}(b_1)$	1223	**ring stretching**
$\nu_{18}(b)$	1138.4	**ring stretching**	$\nu_{21}(b_2)$	1218	**CH_2 twisting**
$\nu_{19}(b)$	1079.2	os-ch asym stretch	$\nu_{17}(b_1)$	1125	ring stretching
$\nu_{20}(b)$	919.0	in phase CH_2 rocking	$\nu_{22}(b_2)$	768	CH_2 rocking
$\nu_{21}(b)$	779.7	out of plane ring-C=O bending	$\nu_{18}(b_1)$	696	ring bending
$\nu_{22}(b)$	673.4	**in plane ring distortion**	$\nu_{23}(b_2)$	620	**C=O bending**
$\nu_{23}(b)$	526.3	C=O bending	$\nu_{19}(b_1)$	527	C=O bending
$\nu_{24}(b)$	184.9	**ring-C=O bending**	$\nu_{24}(b_2)$	215	**ring puckering**

Table 6.3. Computed harmonic frequencies for EC and band assignment compared to the experimental frequencies and the mode assignment of Fortunato et al. [5]; bold typeface is used where our assignment differs significantly from the experimental one. In-phase and out-of-phase vibrations refer to the synchronization between the two CH_2 groups.

Due to the symmetry in the complexes mentioned above, equilibrium values of the internal coordinates are equal for all coordinating EC molecules in each cluster. They are reported in table 6.2. The most dramatic effect of coordination appears in the 1 : 1 complex where the os-ch-ch-os dihedral angle attains its lowest value and the ox-cx bond is maximally stretched. With increasing number of EC ligands the li-ox distance increases and their geometry approaches the values of

the isolated molecule. The ox-cx-os-os group preserves its planarity, as is expected for the carbonate fragment.

EC		$[Li(EC)]^+$		Assignment	Shift
$\nu_1(a)$	3194.2	$\nu_1(a)$	3227.0	out of phase CH_2 asym stretch	32.8
$\nu_2(a)$	3109.7	$\nu_2(a)$	3147.3	in phase CH_2 sym stretch	37.6
$\nu_3(a)$	1898.8	$\nu_3(a)$	1810.5	C=O stretching	-88.3
$\nu_4(a)$	1546.8	$\nu_4(a)$	1549.2	in phase CH_2 scissoring	2.4
$\nu_5(a)$	1420.0	$\nu_5(a)$	1425.8	out of phase CH_2 wagging	5.8
$\nu_6(a)$	1271.5	$\nu_6(a)$	1272.6	out of phase CH_2 twisting	1.1
$\nu_7(a)$	1175.2	$\nu_7(a)$	1172.0	out of phase CH_2 rocking	-3.2
$\nu_8(a)$	1123.5	$\nu_8(a)$	1146.6	os-ch sym stretch, ch-ch stretch	23.1
$\nu_9(a)$	991.6	$\nu_9(a)$	1012.1	ring breathing	20.5
$\nu_{10}(a)$	895.3	$\nu_{10}(a)$	941.4	ring breathing	46.1
$\nu_{11}(a)$	719.6	$\nu_{11}(a)$	786.7	ring stretching	67.1
-	-	$\omega_1(a)$	504.0	ring-ox-Li^+ stretching	-
$\nu_{12}(a)$	227.2	$\nu_{12}(a)$	184.4	out of plane ring bending	-42.8
$\nu_{13}(b)$	3205.8	$\nu_{13}(b)$	3239.8	in phase CH_2 asym stretch	34.0
$\nu_{14}(b)$	3112.6	$\nu_{14}(b)$	3149.3	out of phase CH_2 sym stretch	36.7
$\nu_{15}(b)$	1539.4	$\nu_{15}(b)$	1545.8	out of phase CH_2 scissoring	6.4
$\nu_{16}(b)$	1420.8	$\nu_{16}(b)$	1477.6	in phase CH_2 wagging	56.8
$\nu_{17}(b)$	1267.9	$\tilde{\nu}_{18}(b)$	1249.1	in phase CH_2 twisting	-18.8
$\nu_{18}(b)$	1138.4	$\tilde{\nu}_{17}(b)$	1281.3	ring stretching	142.9
$\nu_{19}(b)$	1079.2	$\nu_{19}(b)$	1042.9	os-ch asym stretch	-37.2
$\nu_{20}(b)$	919.0	$\nu_{20}(b)$	904.0	in phase CH_2 rocking	-15.0
$\nu_{21}(b)$	779.7	$\nu_{21}(b)$	804.3	out of plane ring-C=O bending	24.6
$\nu_{22}(b)$	673.4	$\nu_{22}(b)$	697.5	in plane ring distortion	24.1
$\nu_{23}(b)$	526.3	$\nu_{23}(b)$	518.7	C=O bending	-7.6
$\nu_{24}(b)$	184.9	$\nu_{24}(b)$	228.4	ring-C=O bending	43.5
-	-	$\omega_2(b)$	105.9	ring-ox-Li^+ bending	-
-	-	$\omega_3(b)$	58.8	cx-ox-Li^+ bending	-

Table 6.4. Harmonic frequencies for EC and $[Li(EC)]^+$. Vibrational modes where lithium is involved are denoted by ω_i. The tilde on two modes of the complex denotes the frequencies which exchange upon complexation (see text for explanation).

6.2.2 Vibrational Spectrum

Single EC Molecule

The first complete assignment of the vibrational frequencies of EC is that of Fortunato et al. [5] more than thirty years ago, based on the assumption of ring

planarity and inferring the nature of the modes from experimental spectra. In accordance with the assumed geometry, the vibrational modes were classified in four symmetry species. More recently, this assignment has been revised by Klassen et al. [11] from *ab initio* calculations at the HF/D95V** level of theory although, again, a planar geometry is assumed. Considering the previously discussed growing theoretical and experimental evidence in favor of a nonplanar structure, it seems justified to revisit this issue and possibly renumber some of the vibrational modes. Table 6.3 contains the assignments proposed from the analysis of the present *ab initio* calculations (and in terms of the two symmetry species corresponding to a C_2 symmetry), together with Fortunato's assignment (this mapping should be useful when comparing future experimental and theoretical results with previous assignments).

	EC	$[Li(EC)]^+$	$[Li(EC)_2]^+$	$[Li(EC)_3]^+$	$[Li(EC)_4]^+$
$\nu_3(a)$	1777.6	1733.8(-43.8)	1752.6(-25.0)	1765.2 (-12.4)	1760.8(-16.8)
$\nu_4(a)$	1584.8	1584.6(-0.2)	1585.1(+0.3)	1584.9 (+0.1)	1584.4(-0.4)
$\nu_5(a)$	1394.6	1394.1(-0.5)	1394.5(-0.1)	1394.5 (-0.1)	1394.3(-0.3)
$\nu_6(a)$	1259.4	1265.0(+5.6)	1264.2(+4.8)	1262.8 (+3.4)	1261.6(+2.2)
$\nu_7(a)$	1147.2	1139.4(-7.8)	1141.0(-6.2)	1142.2 (-5.0)	1143.1(-4.1)
$\nu_8(a)$	1020.3	1050.9(+30.6)	1042.5(+22.2)	1030.7 (+10.4)	1024.4(+4.1)
$\nu_9(a)$	946.0	978.9(+32.9)	974.8(+28.8)	965.6 (+19.6)	957.5(+11.5)
$\nu_{10}(a)$	795.0	835.0(+40.0)	837.6(+42.6)	830.7 (+35.7)	824.2(+29.2)
$\nu_{11}(a)$	680.6	760.6(+80.0)	752.2(+72.2)	723.4 (+42.8)	705.8(+25.2)
$\nu_{12}(a)$	162.0	82.8(-79.2)	102.0(-60.0)	123.2 (-38.8)	138.2(-23.8)
$\nu_{15}(b)$	1578.3	1575.3(-3.0)	1576.3(-2.0)	1576.7 (-1.6)	1576.8(-1.5)
$\nu_{16}(b)$	1402.4	1431.7(+29.3)	1424.2(+21.8)	1416.7 (+14.3)	1412.0(+9.6)
$\nu_{17}(b)$	1216.3	1214.5(-1.8)	1214.9(-1.5)	1215.1 (-1.2)	1214.8(-1.5)
$\nu_{18}(b)$	1025.6	1166.2(+140.6)	1139.5(+113.9)	1106.6 (+81.0)	1087.0(+61.4)
$\nu_{19}(b)$	974.1	944.3(-29.8)	956.4(-17.7)	967.2 (-6.9)	973.9(-0.2)
$\nu_{20}(b)$	886.4	874.1(-12.3)	876.0(-10.4)	878.1 (-8.3)	880.0(-6.4)
$\nu_{21}(b)$	694.3	721.6(+27.3)	718.2(+23.9)	711.5 (+17.2)	708.3(+14.0)
$\nu_{22}(b)$	663.3	701.9(+38.6)	694.7(+31.4)	685.2 (+21.9)	678.8(+15.5)
$\nu_{23}(b)$	487.9	486.6(-1.3)	486.5(-1.4)	485.0 (-2.9)	502.3(+14.4)
$\nu_{24}(b)$	176.5	226.5(+50.0)	218.1(+41.6)	209.5 (+33.0)	202.5(+26.0)

Table 6.5. Results of the low-level (MP2/6-31G) vibrational analysis for EC and its complexes with lithium. Shifts relative to the single EC molecule are given in parenthesis.

In the rest of this paper, we will stick to the new numbering given in the first column of table 6.3. Concerning the dynamics associated with each mode,

in most cases either the experimental assignments coincide with our *ab initio* results, or the differences are minor: for example ν_8 and ν_{19} are ring modes as indicated by Fortunato et al. [5], but we specify which atoms are more involved in these vibrations. Nevertheless, in eight cases the differences are substantial (see assignments marked in bold type in table 6.3: ν_7, ν_{10}, ν_{11}, ν_{12}, ν_{17}, ν_{18}, ν_{22} and ν_{24}). Most of these discrepancies occur in the low-frequency region where, due to the complexity of the vibrational modes, proper assignments are especially difficult. It is interesting to note, for instance, that the C=O bending has an unexpected noticeable weight on the lowest frequency mode (ν_{24}). For the particular case of the ν_{17} and ν_{18} frequencies, the ring stretching mode (ν_{18}) is assigned to a higher frequency than the CH_2 twisting in the experimental assignment [5], while the inverse order is found in the present *ab initio* calculation. Since these frequencies are very close (exp. 5 cm^{-1}), it is difficult to ascertain the proper ordering.

As a rule of thumb modes with (experimental) frequencies below 1139 cm^{-1} (that is, exactly the lower half of the modes) correspond to ring modes and/or C=O bendings (except for ν_{20}), while the higher upper half of the frequencies consists only of CH_2 modes and C=O stretchings. Finally, and as it is usually the case [30], there is a substantial mismatch between the computed harmonic frequencies and the experimental ones for high (stretching) frequencies, with deviations of up to 200 cm^{-1} for the highest frequency mode (CH stretching), due to the increasing role of anharmonicities in that range. On the contrary, the accord is rather good for low frequencies, with some substantial deviations only in the (experimental) range of 700-960 cm^{-1}.

$[Li(EC)_n]^+$ (n=1-4) Complexes

Regarding the effect of the ion on the solvent molecules vibrational frequencies, and considering the results for the structure of the hydrated complexes, it seems reasonable to expect that the strongest effects will be found for the dimer. While no experiments have been reported for this system, the computational estimation of the shift for this case should provide upper bounds of the liquid phase ones. Indeed, we find that many of the frequencies of the single EC molecule coordinated to Li^+ are affected, with both substantial red and blue shifts. In table 6.4 the results for the dimer are compared with those previously discussed for the isolated EC molecule, at the MP2/6-311++G(d,p) level. To ease the comparison with the vibrational frequencies of the single molecule, the notation ν_i is used for the 24

	EC	$[Li(EC)_2]^+$	$[Li(EC)_3]^+$	$[Li(EC)_4]^+$
$\nu_3(a)$	1777.6	1742.6(-35.0)	1755.7(-21.9)	1753.4(-24.2)
		1762.5(-15.1)	1755.8(-21.8)	1753.6(-24.0)
		-	1785.2(+7.6)	1753.6(-24.0)
		-	-	1782.5(+4.9)
$\nu_{10}(a)$	795.0	833.3(+38.3)	828.9(+33.9)	-
		840.2(+45.2)	831.6(+36.6)	-
		-	831.7(+36.7)	-
		-	-	-
$\nu_{11}(a)$	680.6	721.8(+41.2)	714.1(+33.5)	702.7(+22.1)
		782.6(+102.0)	727.9(+47.3)	706.0(+25.4)
		-	728.1(+47.5)	707.3(+26.7)
		-	-	707.3(+26.7)

Table 6.6. Low level (MP2/6-31G) vibrational analysis for EC complexes: details of the modes which show non-negligible splitting of frequencies (shifts relative to the dimer frequencies are displayed in parenthesis).

modes of EC (keeping the same numbering as before) and ω_i is used for the three modes where lithium is involved. The highest shifts occur in the ring stretching and in the carbonyl stretching modes: a blue shift of up to some 143 cm^{-1} for the ν_{18} ring mode, and a red shift of up to 88 cm^{-1} for the important C=O mode (ν_3) are found.

It is interesting to note that the substantial shift experienced by some modes may result in a reordering of frequencies. Two sorts of reordering are observed: the first concerns some frequencies within the same symmetry group. This is the case for the CH_2 twisting and the ring stretching modes which, for the single EC molecule, are $\nu_{17}(b)$ and $\nu_{18}(b)$ respectively; it can be seen that this order is inverted in the lithium complex (see table 6.4). A second type of reordering exists between frequencies corresponding to the two different symmetry groups. The two lowest frequency modes constitute an interesting example: the harmonic value of the ring bending mode ν_{12} (with A symmetry) is downshifted to 184 cm^{-1} which is exactly the harmonic frequency of the unperturbed lowest frequency mode ν_{24} (with B symmetry), which in turn is upshifted by the presence of the ion to 228 cm^{-1}, almost exactly the frequency of the unperturbed ν_{12}. Therefore, the two normal modes with the lowest frequencies are exchanged after EC coordinates the ion even if the same frequencies can still be found in the spectrum (such effects could be validated experimentally due to the different symmetry of both modes). A second example consists of the ν_{10} (A) mode (ring breathing) which

experiences a blueshift and the ν_{20} (B) (CH_2 twisting) which is shifted to lower frequencies, resulting in a crossing of their frequencies.

We have also analyzed the trends in the substantial ion-induced shifts upon addition of more solvent molecules. As mentioned above in section 6.2.1, it is to be expected that all shifts will diminish in absolute value since also the distortion of EC decreases with increasing solvation number. Starting from the optimized structures for the complexes which have been discussed in section 6.2.1, we have performed a vibrational analysis with the same model chemistry (MP2/6-31G) which provides useful insight into the trends. Table 6.5 contains the frequencies obtained for each complex, together with the corresponding shifts relative to the single molecule (hydrogen stretching modes are not included as this region is not relevant for solvation). Focusing on the dimer, the qualitative behaviour of the shifts (see numbers in parenthesis in the third column of Table 6.5) is very similar to that found at the MP2/6-311++G(d,p) level (see last column of Table 6.4). Only in case of very small shifts (< 3 cm^{-1}), found for ν_4, ν_5 and ν_{15}, the two calculations differ with respect to the direction of the shift.

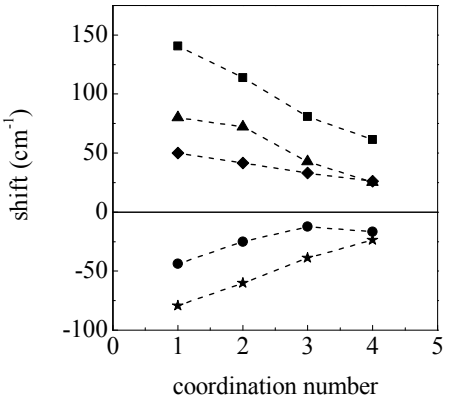

Figure 6.3. Computed shifts for lithium complexes as a function of coordination number; five modes are shown: ν_3 (circles), ν_{11} (triangles), ν_{12} (stars), ν_{18} (squares) and ν_{24} (diamonds).

Regarding the interpretation of table 6.5, it should be noted that the number of normal modes increases rapidly with coordination number n. For every mode found in the single EC molecule, though, it is relatively easy to identify n (closely spaced) corresponding frequencies in the n-coordinated complex. Most of these frequencies are almost identical (differing by less than ~ 1 cm^{-1}) so that just the average value is given. Since the amount of repulsion betwen original degenerate modes depends on the coupling between them, a few modes show a broader dispersion as n increases (see table 6.6), in some cases with both red and blue shifts (see first row, which corresponds to ν_3). It is to be expected that when such a substantial dispersion exists, the band splitting or at least a noticeable band broadening should be observed in liquid phase, as it is indeed the case for ν_3 and

ν_{11} (see section 6.3.2).

Turning to the behaviour (of the averaged shifts) with varying number of molecules we see as expected that the influence of lithium ion decreases upon increase of the coordination number. The two modes that are most affected in the dimer are the ring stretchings ν_{11} and ν_{18}. Figure 6.3 displays their shifts, together with those of the low-frequency ring bendings (ν_{12} and ν_{24}) and of the carbonyl bond stretching (ν_3), which is the mode most indicative of binding to the ion, as a function of the coordination number. In all cases, the shift estimated for the dimer is reduced by more than a 50 % for the $n = 4$ complex. This is in agreement with the more modest shifts that will be shown to occur in the liquid (see below). The crossing of the ν_{12} and ν_{24} modes found for the dimer probably also disappear with increasing solvation number. It should be noted, though, that for the model chemistry used here, the single molecule frequencies are more separated and no crossings occur. Nevertheless, value and sign of the shifts for the dimer are comparable to those obtained with the higher level of theory; since they are reduced by more than a 50 % upon increasing the solvation number, it is likely that the mentioned crossing would disappear too.

6.2.3 Intramolecular Force Field

Finally, our *ab initio* calculations have been used to explore the full internal force field of the EC molecule, the rationale being that for the study of ion mobility in liquid EC it is important to handle properly the internal flexibility of the molecule. From the previous discussion of the spectrum we see that four modes are found below $\approx$ 700 cm^{-1}, *i.e.* $\approx 3\ k_BT$ (at 320 K, a typical temperature for liquid EC). Maybe even more important, the barriers for ring inversion are $\sim$ 2 k$_B$T ($\sim$ 1.2 kcal mol^{-1}), and therefore it is reasonable to expect that some coupling may exist between ion mobility and ring dynamics in the solvation shell.

		New			Amber
Bond	r_0	k_{r_2}	k_{r_3}	k_{r_4}	k_{r_2}
ox-cx	1.193	973.54	-2385.37	-3627.64	540.4
cx-os	1.360	342.61	-931.29	1232.28	401.8
os-ch	1.430	317.74	-658.47	752.67	300.5
ch-ch	1.520	277.68	-552.40	736.85	307.6
ch-h	1.090	398.01	-812.09	1017.74	340.4

Table 6.7. Values of the stretching intramolecular potential constants (Units: [r_0]=Å, [k_{r_2}]=kcal mol^{-1} Å^{-2}, [k_{r_3}]=kcal mol^{-1}Å^{-3}, [k_{r_4}]=kcal mol^{-1}Å^{-4}) and comparison between our new and the Amber force field.

	G98	exp.	New	$diff_a$	$diff_b$	Amber	$diff_a$	$diff_b$
ν_1	3194	3000(w)	3225	31(1.0%)	225(7.5%)	2982	-212(-6.6%)	-18(-0.6%)
ν_2	3110	2925(w)	3143	33(1.1%)	218(7.5%)	2905	-205(-6.6%)	-20(-0.7%)
ν_3	1899	1868(vs)	2035	136(7.2%)	167(8.9%)	1623	-276(-14.5%)	-245(-13.1%)
ν_4	1547	1483[$\perp$]	1611	64(4.2%)	128(8.6%)	1567	20(1.3%)	84(5.7%)
ν_5	1420	1386(m)	1490	70(4.9%)	104(7.5%)	1448	28(2.0%)	62(4.5%)
ν_6	1271	1223(w)	1413	142(11.1%)	190(15.5%)	1402	131(10.3%)	179(14.6%)
ν_7	1175	1157(s)	1277	102(8.7%)	120(10.4%)	1175	0(-0.0%)	18(1.5%)
ν_8	1123	1087(s)	1074	-49(-4.4%)	-13(-1.2%)	992	-131(-11.7%)	-95(-8.7%)
ν_9	992	881(w)	963	-29(-2.9%)	82(9.3%)	938	-54(-5.4%)	57(6.5%)
ν_{10}	895	715(m)	789	-106(-11.9%)	74(10.4%)	792	-103(-11.5%)	77(10.8%)
ν_{11}	720	660(?)B	669	-49(-7.0%)	**9(1.4%)**	544	-176(-24.3%)	-116**(-17.5%)**
ν_{12}	227	230[?]	223	-4(-1.7%)	**-7(-2.9%)**	176	-51(-22.6%)	-54**(-23.5%)**
ν_{13}	3206	3004(w)	3231	25(0.8%)	227(7.6%)	2989	-217(-6.8%)	-15(-0.5%)
ν_{14}	3113	2925(w)	3145	32(1.0%)	220(7.5%)	2910	-203(-6.5%)	-15(-0.5%)
ν_{15}	1539	1483(m)	1608	69(4.4%)	125(8.4%)	1522	-17(-1.1%)	39(2.7%)
ν_{16}	1421	1421(w)	1553	132(9.3%)	132(9.3%)	1464	43(3.1%)	43(3.0%)
ν_{17}	1268	1218[$\|\|$]	1297	29(2.27%)	79(6.5%)	1179	-89(-7.0%)	-39(-3.2%)
ν_{18}	1138	1125[w]	1116	-22(1.9%)	-9(-0.8%)	1044	-94(-8.3%)	-81(-7.2%)
ν_{19}	1079	960(m)	1061	-18(-1.6%)	101(10.6%)	986	-93(-8.6%)	26(2.7%)
ν_{20}	919	768(m)	897	-22(-2.4%)	129(16.8%)	861	-58(-6.3%)	93(12.1%)
ν_{21}	780	696(sh)	710	-70(-8.9%)	**14(2.1%)**	572	-208(-26.6%)	-124**(-17.7%)**
ν_{22}	673	620(?)B	660	-13(-1.9%)	**40(6.5%)**	495	-178(-26.5%)	-125**(-20.2%)**
ν_{23}	526	527(vw)	484	-42(-8.0%)	**-43(-8.2%)**	291	-235(-44.7%)	-236**(-44.8%)**
ν_{24}	185	215(m)B	186	1.0(0.5%)	**-29(-13.5%)**	170	-15(-8.2%)	-45**(-21.1%)**

Table 6.8. Harmonic frequencies obtained with *ab initio* calculations, experimental results and values obtained with classical calculations using our new force field and the Amber force field. The intensity of experimental peaks is given in brackets: [$*$] = solid phase values, B = spectrum in benzene, w = weak, m = medium, s = strong, vs = very strong, ? = not reported in literature, $\perp$ ($\|$) = observed with perpendicular (parallel) polarized light [5]. Column $diff_a$ gives the difference between the values found with classical calculations and with the quantum chemical methods. The difference between classical and experimental values is shown in column $diff_b$. Bold typeface is used to point out the differences among classical simulations and experiment at low frequencies.

In this connection, it is to be noted that a popular force field like AMBER [32–34] performs poorly in reproducing the barriers to inversion and the absolute frequencies in the low frequency range (see below). These considerations have motivated the development of a new force field from high level *ab initio* calculations, tailored for EC. Particular attention has been payed to include effects beyond the simple adjustment of harmonic frequencies. In the most widely used procedure an internal potential is constructed by grafting group (bond, etc) contributions that have been fitted to represent a large body of molecules, usually only including harmonic terms (except for dihedrals).

This method has the drawback that it can result in a rather bad accord for some frequencies. Table 6.8 contains the results for the AMBER force field as applied to EC: the six lowest harmonic frequencies (which are in principle the most relevant for liquid dynamics) are consistently too low by at least a 20 % to 40 % compared with the *ab initio* or experimental values. The advantage in this sort of approach is that the functional form is standard, and therefore implemented in most MD packages. If an accurate intramolecular potential is required, the most successful approach for molecules of a size similar to EC is to expand the internal potential in terms of normal modes [30]. While anharmonicity is treated more consistently, the drawback of this approach is that as the normal modes are computed numerically, it is not evident how to implement it in a MD package.

Here we have devised a different approach to the problem of force field development. We have tried to balance both approaches looking for both an easy implementation and a faithful representation of the actual anharmonic intramolecular potential. Starting from the optimized structure we performed a relaxed potential energy surface (rPES) scan for all valence coordinates (stretchings, bendings and dihedrals, including the ox-cx-os-os improper dihedral, which showed to be important in modeling low frequencies vibrations), with a total of 19 coordinates scanned. At first sight it could seem that we have scanned less coordinates than degrees of freedom, but due to the symmetry of the molecule, we have actually used more internal coordinates (39) than independent degrees of freedom (24: for example the ch-os stretching appears twice with the same force constant). In figure 6.2 we show some results: a bond (panel a), a bending angle (panel b), two dihedrals (panel c and d) and an improper dihedral angle (panel e). Fitting of these curves to suitable polynomials reveals that most of bond-distance rPES have a quartic behaviour while bending angles follow a third order polynomial. For what concerns dihedral angles we found that many of them show a double well profile for the potential energy with an energy barrier of ~ 1.3 kcal mol^{-1}. The force field para-

		New		Amber
Angle	θ_0	k_{θ_2}	k_{θ_3}	k_{θ_2}
ox-cx-os	124.970	71.43	-6.48	75.4
cx-os-ch	108.140	107.25	-3.33	62.0
ch-ch-os	102.050	119.09	-3.03	67.8
os-cx-os	110.200	139.74	-12.28	72.4
os-ch-h	108.600	65.09	-22.94	50.8
ch-ch-h	114.030	47.85	-16.44	46.5
h-ch-h	110.610	41.47	-21.59	39.3

Table 6.9. Values for the bending intramolecular potential constants (Units: $[\theta_0]$=degrees, $[k_{\theta_2}]$=kcal mol^{-6}rad^{-2}, $[k_{\theta_3}]$=kcal mol^{-1}rad^{-3}) and comparison between our new and the Amber force field.

meters have been determined by imposing that every single rPES energy profile (computed with an in-house Molecular Mechanics code) matches the corresponding quantum chemically derived one over a whole range of values of the internal coordinate (not only at the minimum).

The following functional form has been used for the intramolecular potential (PES), which is the typical expansion in terms of valence coordinates plus anharmonic terms for stretchings (4^{th} order) and bendings (3^{rd} order):

$$V(r,\theta,\phi) = \sum_{bonds}[k_{r_2}(r-r_0)^2 + k_{r_3}(r-r_0)^3 + k_{r_4}(r-r_0)^4] + \sum_{angles}[k_{\theta_2}(\theta-\theta_0)^2 + k_{\theta_3}(\theta-\theta_0)^3] + \sum_{dihedrals} A_n[1+cos(n\phi-\delta)] + \sum_{improper} k_{\phi_2}(\phi-\phi_0)^2 = V_{stretchings}(r) + V_{bendings}(\theta) + V_{dihedrals}(\phi) + V_{improper}(\phi) \quad (6.1)$$

where (r), (θ) and (ϕ) denote bond lengths, bending angles, and dihedral angles.

	New			Amber		
Dihedral	A_n	δ	n	A_n	δ	n
ox-cx-os-ch	1.400	180.0	1	1.400	180.0	1
ox-cx-os-ch	3.200	180.0	2	2.700	180.0	2
os-ch-ch-os	0.175	0.0	2	0.144	0.0	3
os-ch-ch-os	0.469	0.0	5	1.175	0.0	2
os-ch-ch-h	0.250	0.0	1	0.250	0.0	1
ch-ch-os-cx	0.800	180.0	1	0.800	180.0	1
ch-ch-os-cx	0.383	0.0	3	0.383	0.0	3
os-cx-os-ch	2.700	180.0	2	2.700	180.0	2
Improper	ϕ_0	k_{ϕ_2}		ϕ_0	k_{ϕ_2}	
ox-cx-os-os	180.0	45.0d0		—	—	

Table 6.10. Values for the constants obtained for dihedrals (Units: $[\phi_0]$=$[\delta]$=degrees, $[A_n]$=kcal mol^{-1}, $[k_{\phi_2}]$=kcal mol^{-1}rad^{-2} and comparison between our new and the Amber force field.

The initial approximation for the constants appearing in this expansion has been obtained from the *ab initio* rPES. For instance, the rPES for the ox-cx stretching has been fitted up to fourth order, and the corresponding constants have been introduced in formula 6.1. Though it is clear that rPES constants are in principle different from the corresponding internal coordinate contribution to the total PES, they constitute a convenient first guess. In an iterative procedure (in which classical rPES are computed for each set of PES constants) all the parameters in the PES expansion have been scaled until the ratio of quantum and classical rPES converged to a value better than 95 % for *all* internal coordinates. It should be

noted that an rPES profile does not only depend on its associated internal coordinate, but also on the rest of internal coordinates (which are optimized at each point), so that the cross coupling between valence coordinates is implicitly taken into account. The final force field is reported in tables 6.7, 6.9 and 6.10.

Figure 6.2 shows the remarkable goodness of the fit by comparing the *ab initio* and classical rPES for some selected examples. Panels (a) and (c) also display (dashed line) the potential profile computed with the AMBER force field for comparison. In the case of the bond stretching (panel (a)) we can appreciate that both the width and anharmonicity of the curve are better reproduced with the new parameters. Regarding the dihedral angles (panel (d)), the positions of the minima in the AMBER curve are displaced by $\sim \pm 33^{\circ}$ and the height of the barrier is underestimated with respect to the quantum chemically derived profile. Panel(d) displays one internal coordinate whose rPES shows a discontinuity (also found for another coordinate as well). This feature can be interpreted as a sudden jump between stability basins along the minimum energy path represented by the rPES. It is remarkable that the force field developed is able to reproduce even unusual aspects like this one.

Finally, the harmonic part of this force field also provides satisfactory results in the low frequency range, previously argued to be potentially important for liquid state dynamics. The harmonic frequencies obtained for a single EC molecule are shown in table 6.8. A *maximum* deviation of less than ≈ 10 % is found for the six lowest frequencies (< 700 cm^{-1}) when compared with the experimental values or with the *ab initio* harmonic frequencies. This good level of accord is maintained up to the highest frequencies, although in this range it is not manifestly superior to AMBER. Nevertheless, it is to be noted that for such an important mode like the C=O stretch (mode ν_3), the harmonic estimation with the present PES is larger than the experimental value (by ≈ 167 cm^{-1}, while that of AMBER is *lower* by ≈ 244 cm^{-1}). It is obvious that when introducing anharmonic effects (contained in the present force field) the resulting frequency will be lower than the harmonic one, and therefore it is reasonable to expect that our PES will come closer to the experimental value (a throughout study of the anharmonic frequencies is beyond the scope of this work and shall be addressed by the self consistent methods of Ref. [30]).

6.3 Classical Computations

We have performed MD classical simulations with flexible molecules implementing our intramolecular force field. The following systems have been studied:

- one EC molecule;
- 215 EC molecules;
- 214 EC molecules + 1 lithium ion;

atom type	σ_i (Å)	ϵ_i (kcal mol^{-1})	charge (e)
ox	2.96	0.210	-0.6452
cx	3.75	0.105	1.0996
os	3.00	0.170	-0.4684
ch	3.50	0.066	0.0330
h	2.50	0.030	0.1041
Li^+	1.46	0.191	1.0000

Table 6.11. Lennard Jones parameters and charges for intermolecular interactions [35]; the values of atom-atom LJ constants are obtained with geometric mixing rules: $\sigma_{ij} = (\sigma_i \times \sigma_j)^{\frac{1}{2}}$ and $\epsilon_{ij} = (\epsilon_i \times \epsilon_j)^{\frac{1}{2}}$

All simulations were performed in the NVE ensemble with a time step of 0.2 fs. The reference temperature and density were set to 323.15 K and 1.3214 g cm^{-3} respectively in order to compare with previous works [13, 21]. Table 6.11 contains the parameters used for the intermolecular potential. Lennard-Jones parameters for EC are taken from Carlson et al. [35] (with geometric average combination rules). Partial charges on the atoms and LJ parameters for lithium ion are given by Soetens at al. [21] (fitted to the electrostatic potential energy surface obtained by *ab initio* HF/6-31G** calculations). The Ewald sum was employed for the calculation of long range interactions. Vibrational spectra were obtained by fast Fourier transform (FFT) of the dipole moment autocorrelation function [36–41] (see below).

6.3.1 Solvation Structure

In agreement with previous experimental [16] and theoretical studies [13, 15, 21], our MD results for one lithium ion in liquid EC support the fact that four solvent molecules can be found within the first solvation shell. A more detailed study of the coordination structure around Li^+ shows its similarity with the *ab initio* calculation for the complex $[Li(EC)_4]^+$, with the carbonyl oxygen being the nearest site to the lithium ion (see panel (a) in figure 6.4, which displays the atom-atom radial distribution functions for li-ox, li-cx and li-os). The probability distribution

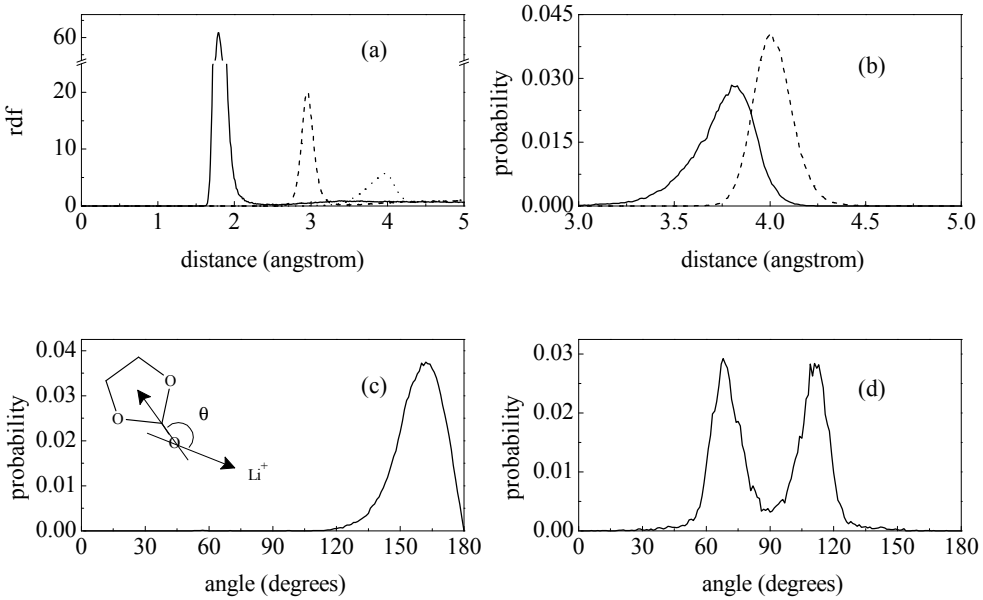

Figure 6.4. Results from MD simulation of the system EC-Li. Panel (a): atom-atom radial distribution function for li-ox (solid line), li-cx (dashed line) and li-os (dotted line); notice the broken scale on the y axis. Panel (b): probability distribution for the distance li-os_1 (solid line) and li-os_2 (dashed line), os_1 and os_2 being respectively the nearest and furthest carbonate oxygen in the same molecule. Panel (c): probability distribution for the angle θ between EC dipole moment and the vector li-ox (see inset). Panel (d): probability distribution for the dihedral angle formed by the 4 carbonyl oxygens nearest to lithium.

of the li-os distance (panel (b)), restricted to molecules in the first coordination shell, clearly shows that one of the carbonate oxygens is nearer to the lithium ion than the other, the most probable distances being 3.8 and 4.0 Å respectively (to be compared with 3.6 and 4.2 Å found in the four coordinated cluster, see section 6.2.1). The mean orientation of the EC molecules can be expressed by the angle between the molecular dipole moment (which, for symmetry reasons, is parallel to the ox-cx bond) and the vector pointing from the carbonyl oxygen to lithium. In panel (c) it is shown that the most probable value for this angle is $\sim 162°$. Therefore the average $Li^+ \cdots O{=}C$ angle in the liquid is larger than the optimized angle in the isolated dimer (see subsection 6.2.1). Finally, the dihedral angle formed by the four carbonyl oxygens around lithium is shown in panel (d). It has two probability maxima at $\sim 68°$ and $\sim 111°$. These values coincide with the *ab initio* results ($\sim 68°$ and $\sim 112°$). We can conclude that a tetrahedral-like structure is preserved in liquid phase (the dihedral angle formed by the vertexes

of a perfect tetrahedron is either 70.5° or 109.5°), with a slightly more parallel alignment between the EC dipole moment and the O$\cdots$Li$^+$ vector in the liquid phase.

6.3.2 Vibrational Spectrum

Experiments so far mostly measured of the ion induced shifts in liquid EC. Here we will address this issue by means of MD simulations. It is important to emphasize that for this purpose the inclusion of anharmonicity is capital. The C=O stretch (which for the sake of the argument we can approximate as a local mode), can be used to illustrate this point. From first order perturbation theory (*classical or quantal*) the induced shift on the simple vibration of a diatomic molecule is given by [42]

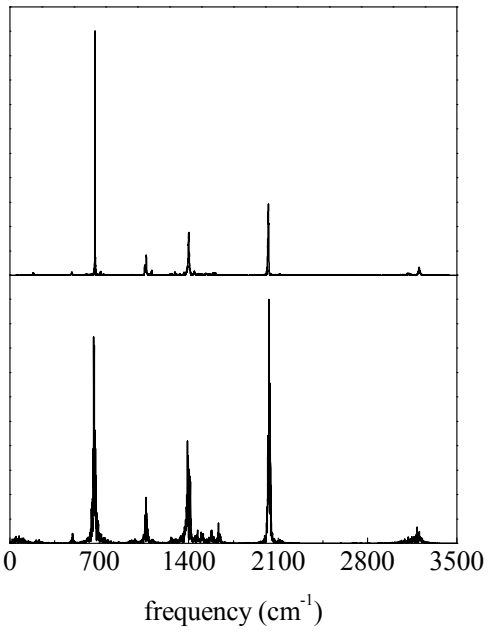

Figure 6.5. Simulated spectra for EC: for a single molecule (upper panel) and for 215 molecules in the condensed phase (lower panel).

$$\delta\omega(t) = -\frac{3f}{\mu^2\omega_0^3}F_1(t) + \frac{1}{\mu\omega_0}F_2(t), \tag{6.2}$$

where f is the coefficient of the cubic term in the gas phase internal potential of the diatomic, μ is the reduced mass of the pair and ω_0 is the gas phase frequency. The following expansion in terms of the vibrational mode (Q) is used for the coupling (V) with the surrounding medium

$$V = \left[\frac{dV}{dQ}\right]_{Q=0} Q + \frac{1}{2}\left[\frac{d^2V}{dQ^2}\right]_{Q=0} Q^2 + \ldots \equiv F_1Q + F_2Q^2 + \ldots \tag{6.3}$$

It is often found [42–44] that only the first term in Eq. 6.2 contributes, so that the shift is mainly determined by the cubic anharmonicity (f), (only in the case

of CN^- the second term in formula 6.2 has been found to dominate [45]). Similar formulas, leading to the same conclusions regarding the importance of the cubic anharmonicity can be derived in the general polyatomic case [39]. Therefore, if anharmonicity is not included (as it is the case in many conventional force fields), the computed shift is probably missing its main contribution. The fact that anharmonic terms are included in the intramolecular potential developed gives us confidence in the calculated shifts and it will be shown below that they are indeed consistent with both the trends found for the clusters and with the absolute shifts found in liquid phase experiments.

Following Berens et al. [36–38] the absorption lineshape is given by:

$$S(\omega) = (2\pi)^{-1} \int_{-\infty}^{\infty} dt \exp(-i\omega t) \langle \vec{M}(t) \cdot \vec{M}(0) \rangle, \tag{6.4}$$

where $\vec{M}$ denotes the total dipole moment.

Consequently, the vibrational spectrum can be obtained from the Fourier transform (FT) of the total dipole moment time correlation function computed during a simulation, which is the simple approach that has been taken for the pure liquid. A central issue is how the ion affects the vibrational frequencies of the first shell solvent molecules. To this end the dipole moments of these molecules were stored separately during the simulation of an ion immersed in a EC liquid, extracting the ion-perturbed spectrum from this time series. Since solvent exchanges take place between first and second ionic solvation shells, we were able to follow a single molecule residing in the first shell only up to a maximum of ~ 48 ps, this being the largest residence time observed in a simulation of 200 ps. The shortness of this time series results in a nonnegligible degree of noise, so that a filter is required. To illustrate the effect of this smoothing, the raw spectrum and the filtered one of the carbonyl stretching mode are shown in figure 6.6.

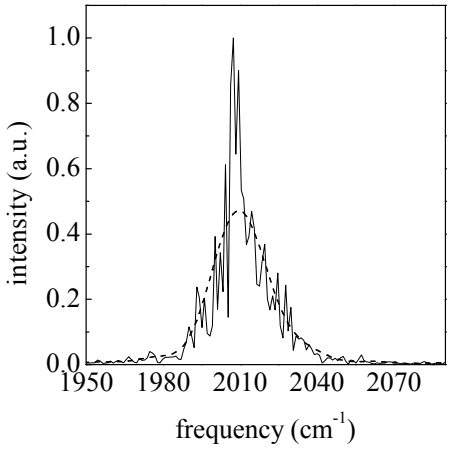

Figure 6.6. Original (noisy) spectrum (solid line) filtered spectrum (dashed line) of EC as used for the FFT of the dipole moment correlation function.

The whole vibrational spectrum of the neat liquid is compared with that of a single EC molecule in figure 6.5. They are displayed on different panels due to their overall similarity: the peak positions are coincident and the only difference is the usual broadening of the bands in the liquid state. The coincidence of vibrational frequencies can be explained by the weak interactions among EC molecules in condensed phase. Indeed, by means of *ab initio* calculations Li et al. [12] found that there is no strong attractive interaction between EC molecules.

From our *ab initio* calculation of the harmonic spectrum of EC and of the complexes $[Li(EC)_n]^+$ it is clear that all modes involving the ring and the carbonyl oxygen should be affected by solvation. The shifts reported in table 6.3 can be considered as an upper bound to those in the liquid phase, since as discussed in section 6.2 and 6.2.2 the interaction among Li^+ and EC is strongest for the dimer. Nevertheless they are indicative of the changes that might be found upon solvation of the lithium ion: the most important shifts (higher than 30 cm^{-1} in the dimer) are calculated to occur for ν_3, ν_{10}, ν_{11}, ν_{12}, ν_{16}, ν_{18}, ν_{19} and ν_{24}. Indeed, liquid phase experiments have focused on ν_3, ν_{10}, ν_{11}, ν_{16} and ν_{19}. In figure 6.7 we show the comparison between the MD spectrum for the pure liquid and the one for the first shell molecules. Five important regions, corresponding to the above cited bands, are enlarged in order to better discern the shifts induced by ion coordination in the liquid phase, which will be addressed in turn.

Experimentally it has not been possible to determine if a shift exists for the C=O stretch mode (ν_3), due to the overlap with Fermi resonances [31]. Only a broadening of the band is clearly found to be an effect of the lithium ion. Hyodo et al. [16] extracted a little redshift, pointing out that this mode is unsuitable for the investigation of ion-solvent interactions; Wang et al. [19] reported a change in the carbonyl stretching but they did not quantify it; Klassen et al. [11] observed a change of the band shape in their Raman spectra as lithium perchlorate concentration was increased. Moreover, for the system PC-lithium (very similar to EC-lithium) Battisti et al. [46] observed a broadening of 27 cm^{-1} in the FWHM of this spectral line at high ionic concentrations. These results are consistent with what was found in section 6.2.2 for the four coordinated complex: both red and (smaller) blue shifts exist for the carbonyl stretching, resulting in an average small resdshift of ~ 17 cm^{-1}. The second panel of figure 6.7 shows the C=O stretching band both for neat EC and for those molecules within the first solvation shell, as obtained from the MD simulations of the liquid. A red shift of ~ 20 cm^{-1} is observed (much lower than the 88 cm^{-1} predicted for the dimer in the higher

level calculations). This shift is comparable both with the cited line broadening observed experimentally [11, 46] and with the result of *ab initio* calculation on the four coordinated complex. Therefore, the present results support the notion that the observed broadening is mainly due to an ion induced red shift of the molecules within the first solvation shell.

Some frequencies are missing in the simulated spectrum, usually corresponding to the ones with lower intensity in the experiment. Although in a harmonic analysis of a single molecule all frequencies are obtained, the liquid phase spectrum is computed from the total dipole moment time correlation function and, therefore, the change of dipole moment and the signal-to-noise ratio determines which modes can be detected.

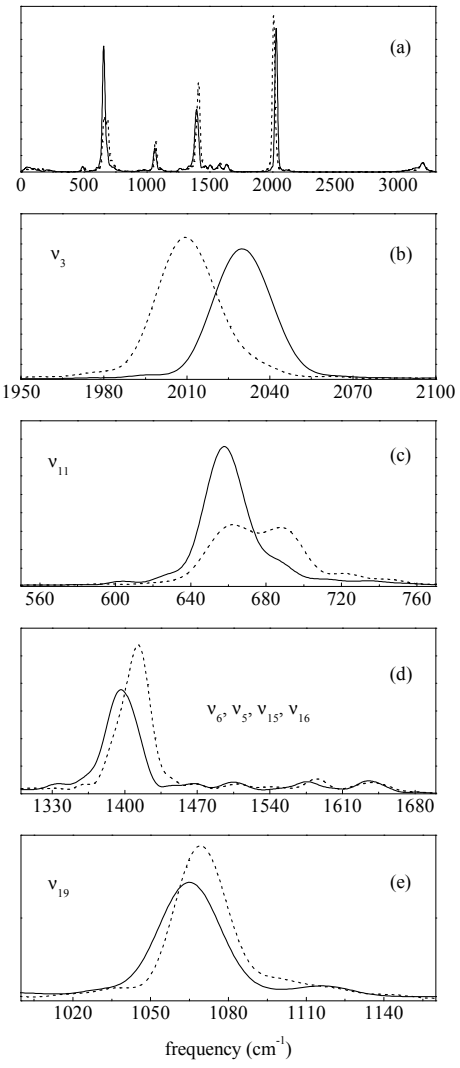

Figure 6.7. Comparison of the simulated spectra of EC (solid line) and EC-Li^+ (dashed line). The whole spectra are shown in the panel (a). Subsets of spectral regions as discussed in the text are shown in the lower panels.

In particular, the ring breathing mode at $\sim$ 900 cm^{-1} (ν_{10}) cannot be discerned. Experimentally, this mode seems to split when EC coordinates lithium, an effect that depends on lithium concentration [16]. A similar case is that of the ν_{18} band, which is also missing. This is the mode which, in our quantum chemical calculations, undergoes the highest blueshift. In line with the initial considerations, no experimental observations have been reported for this mode as its intensity is very weak (see table 6.8).

The ring stretching mode (ν_{11}) is shown in the third panel. Hyodo et al. [16] found that this band shows a typical shoulder or splitting of $\sim$ 15 cm^{-1} upon solvation of the electrolyte (though they attributed the vibration to the carbonyl-bending mode). This mea-

sured splitting clearly appears in our spectrum. Similarly to the behaviour found for ν_3 the *ab initio* calculated blueshift for this mode in the dimer is 67 cm^{-1}, while in the MD simulation we obtain a smaller blueshift of $\sim$ 28 cm^{-1}, which compares very well with the experiment. It is to be noted that this is not a simple shift of the band for those molecules in the first shell, as it occurred for the carbonyl stretching mode. Here, the first shell molecules contribute equally to both peaks. This suggests that, while the average structure is tetrahedral, interconversions between metastable substructures in the first shell might take place on a shorter timescale.

Experimentally, the hydrogen-carbon stretching and bending modes (ν_{16}, ν_{15}, ν_6 and ν_5) are largely unaffected by the coordination to the ion [11]. This is also the basic conclusion of this work: in the *ab-initio* calculations we find small shifts (see section 6.2.2 and tables 6.4 6.5) and in our MD simulations we find only small blueshifts of these bands as well. Panel (d) of figure 6.7) displays this for the CH_2 twisting (ν_6), for which the largest shift ($\sim$ 15 cm^{-1}) is found. The other bands are shifted by only $\sim$ 9 cm^{-1} (ν_{16}) and $\sim$ 5 cm^{-1} (ν_{15} and ν_5) respectively.

Finally, Klassen et al. [11] pointed out that the ring C-O stretching vibrations (ν_{19}) are affected by the presence of lithium ions, although quantitative estimations were not given. For this vibration, we obtain from the quantum chemical calculation, a red shift of 37 cm^{-1} (see table 6.4), while the simulated shift is of $\sim +5$ cm^{-1} for the ν_{19} band (panel (e)).

6.4 Conclusions

Structural and dynamical properties of EC in gas and liquid phase have been studied. High level *ab initio* calculations support the notion of a C_2 equilibrium symmetry for this molecule. This nonplanar structure persists upon solvation of the lithium ion, with a slight tendency to planarity for small solvation numbers. The barriers to internal motion are in all cases in the thermal range, what suggests that a nonneglibigle coupling with first shell dynamics might exist. A new assignment of vibrational modes is proposed that takes into account the nonplanarity in contrast to previous assignments. Lithium ion coordination induces substantial red and blue vibrational frequency shifs in the gas phase, resulting in a reordering of modes in a few cases. In order to handle properly the low energy vibrations at typical liquid state conditions, an intramolecular force field has been specifically developed for EC. The methodology devised for this purpose is aimed

at faithfully reproducing the rPES for all valence coordinates, a goal that has been achieved to a considerable degree. This force field has allowed the computation of the vibrational spectrum via classical simulation for the condensed phase. Both in the case of the neat liquid and in the close vicinity of the ion, the results reproduce satisfactorily the experimental measurements. Lithium coordination induces shifts mainly in the ring motions and in the carbonyl stretching bands of the 4 EC molecules lying in the first coordination shell. Most of the vibrations are shifted to higher wavenumbers except for the carbonyl stretching mode which exibits a redshift tipically found in the bond containing an oxygen atom directly coordinating to a metal cation. The broadening of the band observed experimentally seems thus related to this shift and supports the notion that the carbonyl groups are oriented towards the ion.

References

[1] J. Y. Song, Y. Y. Wang and C .C. Wan *J. Power Sources* **77**, 183 (1999).

[2] S. S. Sekhon, M. Deepa and S. A. Agnihotry *Solid State Ionics* **136-137**, 1189 (2000).

[3] C. L. Angell *Trans. Faraday Soc.* **52**, 1178 (1956).

[4] J. Wang, C. O. Britt and J. E. Boggs *J. Am. Chem. Soc.* **87**, 4950 (1965).

[5] B. Fortunato, P. Mirone and G. Fini *Spectrochim. Acta* **27A**, 1917 (1971).

[6] J. L. Alonso, R. Cervellati, A. D. Esposti, D. G. Lister and P. Palmieri *J. Chem. Soc., Faraday Trans. 2* **82**, 337 (1986).

[7] J. L. Alonso, R. Cervellati, A. D. Esposti, D. G. Lister and P. Palmieri *J. Chem. Soc., Faraday Trans. 2* **82**, 357 (1986).

[8] P. M. Matias, G. A. Jeffrey, L. M. Wingert and J. R. Ruble *J. Mol. Struct. (Theochem)* **184**, 247 (1989).

[9] A. D. Esposti, D. G. Lister and P. Palmieri *J. Mol. Struct.* **223**, 235 (1990).

[10] R. Blint *J. Electrochem. Soc.* **142**, 696 (1995).

[11] B. Klassen, R. Aroca, M. Nazri and G. A. Nazri *J. Phys. Chem. B* **102**, 4795 (1998).

[12] T. Li and P. B. Balbuena *J. Electrochem. Soc.* **146**, 3613 (1999).

[13] J. C. Soetens, C. Millot, B. Maigret and I. Bakó *J. Mol. Liq.* **92**, 201 (2001).

[14] Y. Wang and P. B. Balbuena *J. Phys. Chem. A* **105**, 9972 (2001).

[15] Y. Wang, S. Nakamura, M. Ue and P. B. Balbuena *J. Am. Chem. Soc.* **123**, 11708 (2001).

[16] S. A. Hyodo and K. Okabayashi *Electrochim. Acta* **34**, 1551 (1989).

[17] E. Cazzanelli, F. Croce, G. B. Appetecchi, F. Benevelli and P. Mustarelli *J. Chem. Phys.* **15**, 5740 (1997).

[18] M. Castriota, E. Cazzanelli, I. Nicotera, L. Coppola, C. Oliviero and G. A. Ranieri *J. Chem. Phys.* **118**, 5537 (2003).

[19] Z. Wang, B. Huang, H. Huang, R. Xue, L. Chen and F. Wang *J. Electrochem. Soc.* **143**, 1510 (1996).

[20] Z. Wang, B. Huang, R. Xue, L. Chen and X. Huang *J. Electrochem. Soc.* **145**, 3346 (1998).

[21] J. C. Soetens, C. Millot and B. Maigret *J. Phys. Chem. A* **102**, 1055 (1998).

[22] Gaussian 98, Revision A.11.2, M. J. Frisch, G. W. Trucks, H. B. Schlegel, G. E. Scuseria, M. A. Robb, J. R. Cheeseman, V. G. Zakrzewski, J. A. Montgomery, Jr., R. E. Stratmann, J. C. Burant, S. Dapprich, J. M. Millam, A. D. Daniels, K. N. Kudin, M. C. Strain, O. Farkas, J. Tomasi, V. Barone, M. Cossi, R. Cammi, B. Mennucci, C. Pomelli, C. Adamo, S. Clifford, J. Ochterski, G. A. Petersson, P. Y. Ayala, Q. Cui, K. Morokuma, N. Rega, P. Salvador, J. J. Dannenberg, D. K. Malick, A. D. Rabuck, K. Raghavachari, J. B. Foresman, J. Cioslowski, J. V. Ortiz, A. G. Baboul, B. B. Stefanov, G. Liu, A. Liashenko, P. Piskorz, I. Komaromi, R. Gomperts, R. L. Martin, D. J. Fox, T. Keith, M. A. Al-Laham, C. Y. Peng, A. Nanayakkara, M. Challacombe, P. M. W. Gill, B. Johnson, W. Chen, M. W. Wong, J. L. Andres, C. Gonzalez, M. Head-Gordon, E. S. Replogle, and J. A. Pople, Gaussian, Inc., Pittsburgh PA, 2001.

[23] M. J. Frisch, J. A. Pople and J. S. Binkley *J. Chem. Phys.* **80**, 3265 (1984).

[24] DL_POLY is a package of molecular simulation routines written by W. Smith and T. R. Forester, copyright The Council For The Central Laboratory Of The Research Council, Daresbury Laboratory at Daresbury, Nr. Warrington (1996).

[25] `http://www.dl.ac.uk/TCSC/Software/DL_POLY/main.html`

[26] `http://www.originlab.com`

[27] D. Cremer and J. A. Pople *J. Am. Chem. Soc.* **97**, 1354 (1975).

[28] H. B. Schlegel *J. Comp. Chem.* **3**, 214 (1982).

[29] C. Peng, P. Y. Ayala, H. B. Schlegel and M. J. Frish *J. Comp. Chem.* **17**, 49 (1996).

[30] G. M. Chaban, J. O. Jung and R. B. Gerber *J. Phys. Chem. A* **104**, 10035 (2000).

[31] E. B. Wilson, J. C. Decius and P. C. Cross, Molecular Vibrations, Dover Publications Inc., New York (1980).

[32] S. J. Weiner, P. A. Kollman, D. T. Nguyen and D. A. Case *J. Comp. Chem.* **7**, 230 (1986).

[33] W. D. Cornell, P. Cieplak, C. Bayly, I. R. Gould, K. M. Merz, D. M. Ferguson, D. C. Spellmeyer, T. Fox, J. W. Caldwell and P. A. Kollman *J. Am. Chem. Soc.* **117**, 5179 (1995).

[34] `http://www.amber.ucsf.edu/amber/dbase.html`

[35] H. A. Carlson, T. B. Nguyen, M. Orozco and W. L. Jorgensen *J. Comp. Chem.* **14**, 1240 (1993).

[36] P. H. Berens and K. R. Wilson *J. Chem. Phys.* **74**, 4872 (1981).

[37] P. H. Berens, S. R. White and K. R. Wilson *J. Chem. Phys.* **75**, 515 (1981).

[38] P. H. Berens, D. H. J. Mackay, G. M. White and K. R. Wilson *J. Chem. Phys.* **79**, 2375 (1983).

[39] T. Katō, K. Machida, M. Oobatake and S. Hayashi *J. Chem. Phys.* **93**, 3970 (1990).

[40] T. Nakagawa, J. Umemura, S. Hayashi, M. Oobatake, Y. Miwa and K. Machida *Mol. Phys.* **88**, 1635 (1996).

[41] E. Henssge, D. Dumont, D. Fischer and D. Bougeard *J. Mol. Struct.* **482-483**, 491 (1999).

[42] D. W. Oxtoby, D. Levesque and J.-J. Weiss *J. Chem. Phys.* **68**, 5528 (1978).

[43] A. Laaksonen and P.-O. Westlund *Mol. Phys.* **73**, 663 (1991).

[44] R. Rey, K. B. Møller and J. T. Hynes *J. Phys. Chem. A* **106**, 11993 (2002).

[45] R. Rey and J. T. Hynes *J. Chem. Phys.* **108**, 142 (1998).

[46] D. Battisti, G. A. Nazri, B. Klassen and R. Aroca *J. Phys. Chem.* **97**, 5826 (1993).

Chapter 7

A computational study of γ-butyrolactone and Li^+/γ-butyrolactone in gas and liquid phases

γ-Butyrolactone (GBL, 4-hydroxybutyric acid gamma-lactone, figure 7.1), the simplest cyclic ester, is a major chemical compound with extensive application in pharmaceuticals, pesticides and petrochemicals [1–6]. It is also known to be a building block of many natural products of biological activity, like the sesquiterpene lactones, flavour components, alkaloids, antileukemics and pheromones [7–11]. Its biological relevance is attributed to its similarity with cyclic peptides.

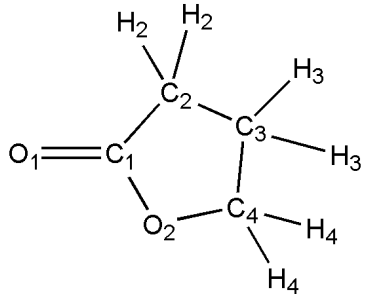

Figure 7.1. γ-butyrolactone with the atom labelling used in the text (notice that hydrogens are grouped in classes).

Recently, GBL has become the focus of increasing technological interest for its application in lithium ion batteries (LIBs). Its physicochemical properties

make it suitable to enhance LIBs capabilities (reciclability, power, etc.) [12]. It is an aprotic polar solvent of moderate viscosity with a dielectric constant of 41.7 at ambient temperature, that shows a good solubilizing power for lithium salts. Contrary to other good plasticizers employed in LIBs, the liquid phase exists over a wide range of temperatures (the melting and the boiling points are -42°C and 206°C respectively). Takami et al. [6] have recently reported that the mixture of GBL with ethylene carbonate (EC) is a promising liquid electrolyte for thin LIBs.

Despite its importance for basic and applied areas, to our knowledge there are no complete ab initio studies of its structure and vibrational manifold, nor any Molecular Dynamics (MD) simulation in the liquid phase, particularly in the vicinity of the lithium ion. The only theoretical studies to date concern Molecular Mechanics calculation of structures [13–15], and ab initio computations of some partial aspects [16–20] (see below). In contrast, and probably due to the aforementioned high technological impact on LIBs, a substantial amount of experimental work has been reported for Li^+-GBL [1, 2, 18, 21–28] and for its mixtures with other plasticizers [6, 29].

Here we have aimed to obtain a comprehensive theoretical understanding at the molecular level: from the isolated molecule up to the solvation of the lithium ion in the liquid phase. Both ab initio and MD calculations have been used to that purpose. For the gas phase, the optimal structure and vibrational frequencies have been computed for the monomer, including a complete assignment of bands. Structure and vibrational frequencies have also been studied for clusters of Li^+, with up to four GBL molecules, as a function of solvation number. Finally, and still within the gas phase, an accurate anharmonic intramolecular force field has been developed, following a novel procedure for parameterization based on the concept of relaxed potential energy profiles along internal coordinates. Concerning the liquid state, both neat liquid GBL and Li^+ dissolved in GBL have been studied. To this end, a standard intermolecular force field has been refined, checking its goodness against counterpoise corrected potential energy profiles. Finally, a detailed study of diffusion and vibrational shifts for molecules within the first solvation shell of lithium has been performed.

The paper is organized as follows: in section 7.1 the computational details are described, section 7.2 contains the results of the ab initio calculations in the gas phase, and section 7.3 contains those for the liquid phase. Finally, the main aspects are summarized in the conclusions section.

atom	x	y	z	σ (Å)	ϵ (kcal mol^{-1})	charge (e)
O_1	0.00000	0.00000	0.00000	2.96	0.210	-0.532
C_1	0.00000	0.00000	1.20280	3.75	0.105	0.723
C_2	1.19147	0.00000	2.15166	3.50	0.066	-0.165
O_2	-1.15362	-0.00118	1.93714	3.00	0.170	-0.432
C_3	0.57957	0.47337	3.46735	3.50	0.066	-0.059
C_4	-0.84004	-0.08158	3.34160	3.00	0.105	0.153
H_2	0.54938	1.56630	3.50044	1.80	0.030	0.069
H_2	1.09264	0.10562	4.35823	1.80	0.030	0.069
H_3	-1.59565	0.49234	3.87823	1.80	0.030	0.042
H_3	-0.88941	-1.13199	3.64882	1.80	0.030	0.042
H_4	1.55847	-1.03058	2.22354	1.80	0.030	0.045
H_4	1.99083	0.62373	1.75112	1.80	0.030	0.045

Table 7.1. Cartesian coordinates for the minimum energy structure, Lennard-Jones parameters and charges for the intermolecular interaction.

7.1 Computational Details

All ab initio calculations were performed with Gaussian 98 [30]. Vibrational analysis and geometry optimization were performed at the MP2 level with the 6-311G basis set augmented with diffuse and polarization functions [31]. The same model chemistry has been employed for a relaxed potential energy surface scan. Because of the high memory requirements, the study of the complexes $[Li(GBL)_n]^+$ with n ranging from 1 to 4 is performed using the MP2/6-31G model chemistry.

Classical calculations were performed with an in-house Molecular Mechanics (MM) code, together with the DL_POLY [32,33] suite. The MM code was used for the scan of the potential energy surface of a single GBL molecule using a classical intramolecular force field, and for the vibrational analysis. Finally, the DL_POLY package was used to perform the liquid phase simulations. Data analysis (FFT, curve smoothing and curve fitting) was performed with the commercial package Microcal Origin 6.1 [34].

7.2 Ab initio calculations

7.2.1 Structure

Single molecule

On the experimental side, infrared [21, 24], Raman [24] and microwave spectra [22,23,25] of GBL have been reported. On the other hand, most of the theoretical studies correspond to MM calculations (with generic force fields) of properties such as heats of formation and minimum energy structures [13–15, 17]. To our knowledge previous ab initio calculations for GBL (using lower levels of theory) were aimed to study partial aspects such as ring inversion [16], the effect of isotopic substitution on vibrational circular dichroism [18], intrinsic basicities [19] and thermal decomposition [20]. In consequence most of the structural and vibrational measures remain to be addressed at the ab initio level.

dihedral	ϕ_0	MM	AI
O_1-C_1-C_2-C_3	161.523	-	-
O_1-C_1-O_2-C_4	176.531	-	177.391
C_1-C_2-C_3-C_4	31.142	29.0	-
C_1-O_2-C_4-C_3	24.112	16.4	20.484
O_2-C_1-C_2-C_3	-18.664	-21.2	-
C_2-C_3-C_4-O_2	-34.080	-28.3	-
C_2-C_1-O_2-C_4	-3.295	3.2	-2.355

Table 7.2. Comparison of the equilibrium values for the most representative dihedral angles (degrees) with previous studies: molecular mechanics (MM [14], the sign conventions have been adapted to the ones used here) and ab initio (AI [18]) calculations.

In first place, a geometry optimization of the molecule at the MP2/6-311++G(d,p) level has been performed. The cartesian coordinates obtained for the minimum energy structure are given in table 7.1. Tables 7.2, 7.3 and 7.4 contain the equilibrium values obtained for the internal coordinates, together with those reported in previous works (obtained experimentally [24], with MM methods [14] or with lower level quantum chemical calculations [18]). A good agreement among all results is achieved for bond lengths and bending angles, while the values for some dihedral angles show somewhat larger deviations, particularly for the O_2-C_1-C_2-C_3 angle (to our knowledge no experimental results are available for dihedral angles). A basic aspect to consider is that of molecular planarity. Confirming previous works [13, 14, 16, 25], we found that the β-carbon lies out of the plane of the remaining four ring atoms resulting in C_1 symmetry. With the assumption that the two ring puckering coordinates could be treated separately, Lopez et al. [25] demonstrated that the barrier for inversion of the GBL ring could be reliably described using a one dimensional

Bond	k_{r_2}	k_{r_3}	k_{r_4}	r_0	MM	Exp.	AI
O_1 - C_1	921.20	-2225.23	3362.30	1.2028	1.211	1.239	1.180
C_1 - C_2	266.95	-544.87	644.95	1.5231	1.514	1.515	1.517
C_1 - O_2	331.50	-920.47	1344.25	1.3675	1.359	1.347	1.335
C_2 - C_3	295.60	-573.20	633.08	1.5263	1.527	1.529	-
C_3 - C_4	276.30	-561.17	627.53	1.5294	1.530	1.530	1.531
C_4 - O_2	286.80	-649.33	848.48	1.4412	1.421	1.411	1.419
C_2 - H_2	398.00	-812.10	1017.75	1.0930	-	-	-
C_3 - H_3	398.00	-812.10	1017.75	1.0930	-	-	-
C_4 - H_4	398.00	-812.10	1017.75	1.0930	-	-	-

Table 7.3. Intramolecular Force Field Parameters For Stretchings; units: [k_{r_i}] = kcal mol^{-1} Å^{-i}, [r_0] = Å. Comparison of the equilibrium values with previous studies: molecular mechanics calculations (MM [14]), experiment (Exp. [24]) and ab initio (AI [18]).

potential function. Indeed, a typical double well potential for inversion is obtained from a relaxed potential energy scan of the C_2-C_3-C_4-O_2 dihedral angle (Fig. 7.2, see details in section 7.2.3). Microwave spectroscopy measurements [25] predict a barrier height for ring inversion of $\approx$ 8.0 kJ mol^{-1}.

Our quantum chemical calculation produces a slightly higher value ($\approx$ 9.0 kJ mol^{-1}), with the maximum located at 0° (*i.e.* a planar conformation). This conclusion agrees with the expectation of Cremer and Pople in their study on general monocyclic rings [35], according to which a planar ring should imply a more highly strained ring angle at the carbonyl atom than a twisted conformation. Regarding other dihedrals (table 7.2) our results are very similar to previous ab initio calculations [18] but show deviations of up to 8° if compared with MM results [14].

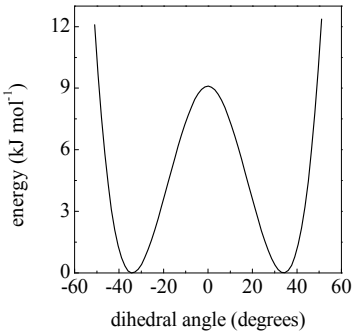

Figure 7.2. rPES profile along the C_2-C_3-C_4-O_2 dihedral angle.

Some final remarks can be made on the structure: the carbonyl bond axis (O_1-C_1) is slightly tilted (3°) with respect to the bisetrix of the C_2-C_1-O_2 angle, what results in a distance among the two oxygens shorter than the O_1-C_2 separation. For what concerns the hydrogen atoms, differences in their distances from the carbons ($\sim$ 1.09 Å), or in the H-C-H bending angle ($\sim$ 109°) are negligible.

Angle	k_{θ_2}	k_{θ_3}	θ_0	MM	Exp.	AI
O_1 - C_1 - C_2	44.95	-40.10	128.5350	-	-	-
O_1 - C_1 - O_2	95.20	-49.23	122.4780	-	-	-
C_1 - C_2 - C_3	92.10	0.00	102.9020	103.0	102.2	-
C_2 - C_3 - C_4	92.45	0.00	100.8770	101.4	99.4	-
C_3 - C_4 - O_2	100.40	0.00	105.1830	106.2	105.1	105.2
C_4 - O_2 - C_1	70.95	10.07	109.8680	111.2	110.2	112.0
O_2 - C_1 - C_2	100.95	-31.54	108.9870	108.9	109.7	109.1
C_1 - C_2 - H_2	47.85	-16.43	108.9000	-	-	-
C_3 - C_2 - H_2	47.85	-16.43	113.6700	-	-	-
C_2 - C_3 - H_3	47.85	-16.43	112.2700	-	-	-
C_4 - C_3 - H_3	47.85	-16.43	111.1200	-	-	-
C_3 - C_4 - H_4	47.85	-16.43	112.9150	-	-	-
O_2 - C_4 - H_4	65.10	-22.93	107.9540	-	-	-
H_2 - C_2 - H_2	41.45	-21.57	108.4510	-	-	-
H_3 - C_3 - H_3	41.45	-21.57	108.9570	-	-	-
H_4 - C_4 - H_4	41.45	-21.57	109.6030	-	-	-

Table 7.4. Intramolecular Force Field Parameters For Bendings; units: [k_{θ_i}] = kcal mol^{-1} rad^{-i}, [θ_0] = rad. Comparison of the equilibrium values with previous studies: molecular mechanics calculations (MM [14]), experiment (Exp. [24]) and ab initio (AI [18]).

$[Li(GBL)_n]^+$ ($n = 1 - 4$) clusters

In a recent study of ethylene carbonate [36], a molecule very similar to GBL (the α-methylene group is substituted by an oxygen) we found that the interaction with lithium affects the structure causing the distortion of the molecule. A high level calculation (MP2/6-31++G(d,p)) of the complex $[Li(GBL)]^+$ has been performed to look into the most important changes in the equilibrium geometry of the molecule (figure 7.3 a). In the previous subsection it was observed that the carbonyl axis of the single molecule is slightly tilted towards the lactone oxygen; this would suggest that the lithium ion might be coordinated by both oxygens if the oxygen atoms could get closer upon ion coordination. This possibility has to be discarded because both the angle among the carbonyl axis and the bisetrix of the C_2-C_1-O_2 angle and the O_1-O_2 distance remain fixed. On the other hand our calculations clearly show that the lithium ion is only coordinated by O_1, but still lying out of the carbonyl axis, a muted signal of the presence of the lactone oxygen. Compared to EC, GBL seems to be slightly more rigid: coordination affects some bond lengths (mainly O_1-C_1, C_1-O_2 and C_4-O_2), while bending and dihedral angles are almost unaffected. A representative example is given by the

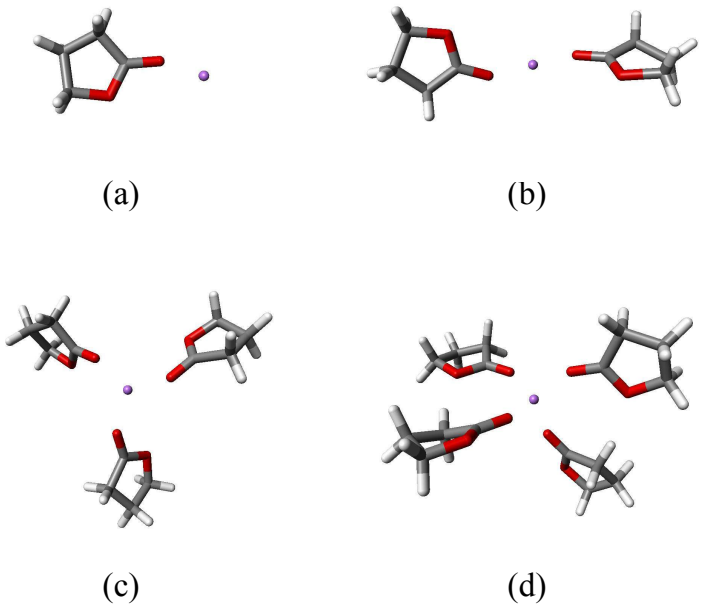

Figure 7.3. γ-butyrolactone and its complexes $[Li(GBL)_n]^+$ with $1 \leq n \leq 4$. The following colours are assigned to different atomic species: red to oxygen, grey to carbon, white to hydrogen and violet to lithium.

change of the torsional angle C_2-C_3-C_4-O_2 upon coordination: when passing from the monomer to the dimer it diminishes by $\sim 13°$ in EC, while in GBL it only varies by $\sim 5°$. To convey a clearer idea of the changes induced by the complexation, in table 7.5 we report the values for the most affected internal coordinates.

Experimental results obtained with Raman spectroscopy for the liquid state suggest that the lithium ion is coordinated by four GBL molecules [37] (a coordination number that has been found both for small molecules as water and for larger ones such as EC). We studied the structure of all GBL complexes (from 1 to 4 molecules plus the lithium ion, figure 7.3) with a MP2/6-31G model chemistry (the calculations for the single molecule have also been repeated at this lower level of theory, in order to facilitate a consistent comparison along the series). The minimum energy geometry for the two-coordinated complex has a linear arrangement with the lithium ion coordinated at opposite sides by the carbonyl oxygens, with the two GBL molecules lying on perpendicular planes. The three-coordinated complex shows a trigonal configuration with the GBL molecules slightly tilted to reduce the repulsion. The four-coordinated complex shows a tetrahedral like

	MP2/6-311++G(d,p)		MP2/6-31G				
	GBL	$[Li(GBL)]^+$	GBL	$[Li(GBL)]^+$	$[Li(GBL)_2]^+$	$[Li(GBL)_3]^+$	$[Li(GBL)_4]^+$
Li^+-O_1		1.786		1.778	1.831	1.900	1.934
O_1-C_1	1.203	1.233	1.240	1.267	1.261	1.255	1.253
C_1-O_2	1.367	1.315	1.417	1.353	1.364	1.378	1.383
C_1-C_2	1.523	1.505	1.535	1.519	1.521	1.523	1.525
C_2-C_3	1.526	1.531	1.548	1.555	1.554	1.552	1.551
C_3-C_4	1.529	1.527	1.551	1.550	1.550	1.550	1.551
C_4-O_2	1.441	1.471	1.499	1.537	1.529	1.522	1.515
Li^+-O_1-C_1		154.2		157.6	150.9	143.5	139.9
O_1-C_1-O_2	122.5	121.1	122.0	120.5	120.8	121.1	121.4
O_1-C_1-C_2	128.5	127.1	128.7	127.2	127.4	127.6	127.9
C_2-C_3-C_4-O_2	-34.08	-31.03	-29.2	-24.1	-24.8	-26.1	-27.7

Table 7.5. Values for the most affected coordinates by ion coordination both for high and low level calculations.

arrangement as the carbonyl oxygens form a dihedral angle of $\sim 75°$. Similar results for the structure of these complexes where also obtained for EC. As in that case, distortions of the molecular structure become smaller upon increasing the coordination number, most probably due to the increasing distance between lithium and the carbonyl oxygens. Again, if we compare the distortion induced in the torsional angle in EC and GBL, we notice that the GBL molecule is more rigid than EC. Finally, the angle between carbonyl axis and the vector joining the ion with the oxygen decreases from $\sim 157°$ to $\sim 140°$ as the coordination number increases, an aspect of interest in the analysis of liquid phase results.

7.2.2 Vibrations

Single molecule

In table 7.6 we report the harmonic frequencies obtained from ab initio calculations, those obtained with the force field developed in this work (see section 7.2.3), the experimental measures and, finally, the band assignment. It is known that the neglect of anharmonicity is a source of disagreement with experimental results, mainly for high frequency modes. Recently Scott et Radom [38] published generic scaling factors for these frequencies so that ab initio results can be brought to better agreement with experiment. For MP2/6-311G(d,p) quantum chemical calculations they proposed a scaling factor of 0.9496. Even though our model chemistry is slightly different (for the inclusion of the ++ diffuse function in the basis set), using the same factor for the highest frequencies, the corrected ab initio frequencies agree very well with experiment.

mode	GBL-G98	Classical	IR	Raman	assignment	$[Li(GBL)]^+$-G98	Shift
ν_1	3188.1 (3027.4)	3229.1	3000	2990	CH_2 asym. stretching	3185.8 (3025.2)	-2.3
ν_2	3183.0 (3022.6)	3224.0	3000	2990	CH_2 asym. stretching	3224.3 (3049.9)	+41.3
ν_3	3170.6 (3010.8)	3220.4	3000	2990	CH_2 asym. stretching	3195.2 (3022.3)	+24.6
ν_4	3106.4 (2949.8)	3148.9	2930	2920	CH_2 sym. stretching	3123.1 (2965.7)	+16.7
ν_5	3096.3 (2940.2)	3146.0	2930	2920	CH_2 sym. stretching	3093.3 (2937.4)	-3.0
ν_6	3090.4 (2934.6)	3144.5	2930	2920	CH_2 sym. stretching	3135.5 (2977.4)	+45.1
ν_7	1844.0 (1751.0)	1949.3	1770	1765	C_1=O_1 streching	1767.1 (1678.0)	-76.9
ν_8	1543.9 (1466.1)	1594.3	1487	1488	CH_2 scissoring	1543.6 (1465.8)	-0.3
ν_9	1511.5 (1435.3)	1576.9	1463	1464	CH_2 scissoring	1541.9 (1464.2)	+30.4
ν_{10}	1478.6 (1404.1)	1560.8	1425	1425	CH_2 scissoring	1469.3 (1395.2)	-9.3
ν_{11}	1417.9 (1346.4)	1521.5	1378	1378	**CH_2 wagging**	1455.5 (1382.1)	+37.6
ν_{12}	1361.6	1420.6	1318	-	CH_2 wagging	1378.5	+16.9
ν_{13}	1320.6	1400.7	1288	-	CH_2 wagging	1336.8	+16.2
ν_{14}	1285.5	1316.9	1280	1280	**CH_2 twisting**	1268.2	-17.3
ν_{15}	1232.4	1280.1	1240	1245	CH_2 twisting	1238.3	+5.9
ν_{16}	1214.0	1180.3	1200	1200	CH_2 twisting	1217.4	+3.4
ν_{17}	1179.3	1171.2	1180	1180	**C_1-O_2 stretching**	1295.0	+115.7
ν_{18}	1106.7	1079.4	1140	-	**CH_2 rocking**	1116.6	+9.9
ν_{19}	1087.1	1027.0	1085	1085	**O_2-C_4 stretching**	1074.8	-12.3
ν_{20}	1022.4	967.4	1038	1040	**C_2-C_3 stretching**	1017.0	-5.4
ν_{21}	961.6	926.7	994	995	**C_3-C_4 stretching**	964.0	+2.4
ν_{22}	911.4	902.6	934	933	**CH_2 rocking**	928.2	+16.8
ν_{23}	889.5	840.9	870	870	**CH_2 rocking**	901.7	+2.2
ν_{24}	817.8	747.0	805	805	ring breathing / C_2-C_1 stretching	832.3 (-)	+14.5
ν_{25}	681.5	634.1	675	678	**ring stretching**	732.3	+50.8
ν_{26}	640.5	603.7	637	638	**ring distortion**	655.0	+14.5
ν_{27}	529.4	545.8	539	540	**out of plane ring-C_1=O_1 torsion**	522.2	-7.2
ν_{28}	491.7	459.2	492	493	**in plane ring-C_1=O_1 bending**	454.5	-37.2
ν_{29}	231.3	230.3	205	-	ring twisting	229.7	-1.6
ν_{30}	152.5	152.4	-	170	**in plane ring-C_1=O_1 torsion**	184.4	+31.9

Table 7.6. Vibrational analysis: high level ab initio, classical and experimental [24] frequencies (cm^{-1}) and mode assignments. The results for the mono-coordinated lithium complex are ordered following the assignment for the single molecule. The numbers in brackets are the high frequency ab initio scaled values. The shifts with respect to the single molecule are given in the last column (positive sign is used for blueshifts).

The most recent vibrational analysis is the one by McDermott [24], who used a modified Urey-Bradley force field, with structural assumptions based on experimental measures [22,23] and previous theoretical works [13]. 14 modes differ from our assignment (see table 7.6, bold typeface), although only a few of them can be considered to be substantial. Particularly important is that the ν_{11} mode had been assigned to the C_1-O_2 stretching while we find that this stretch probably corresponds to ν_{17} (what agrees with typical results for lactones [39]). Moreover, CH_2 rocking modes had been assigned to bands for which we find C-C or O-C stretching modes and viceversa, a shuffling that can probably be explained if we notice that this zone of the spectrum is particularly crowded (7 bands in circa 300 cm^{-1}). At lower frequencies we find important differences for ν_{27}, ν_{28} and ν_{30} which had been previously assigned respectively to the in-plane ring-C=O torsion, the out of plane and the in-plane bending of the carbonyl, while here they are assigned to the out of plane ring-C=O torsion, the in-plane carbonyl bending and the in-plane ring-C=O torsion respectively.

$[Li(GBL)_n]^+$ ($n = 1 - 4$) clusters

As pointed out in subsection 7.2.1 the coordination of lithium bears non-negligible structural changes, what suggests that the strong interaction between GBL and the cation also may also induce noticeable shifts of the vibrational frequencies. With high level quantum calculations (MP2/6-311++G(d,p)) substantial shifts (higher than 30 cm^{-1}) have been found for the following modes: ν_6, ν_7, ν_{11}, ν_{17}, ν_{25}, ν_{28}, ν_{30}. Actually, these modes are associated to the most affected degrees of freedom upon ion coordination (see section 7.2.1). Table 7.6 contains the shifts for all modes of the mono-coordinated complex. It should be noted that a reordering of modes takes place in some cases upon coordination. It is the case, for instance, of ν_{17}, which frequency is upshifted by $\sim$ 115 cm^{-1}; since this large big shift is not experienced by ν_{14-16}, it results in a swapping of modes.

A preliminary understanding of condensed phase effects might be obtained from the study of n-coordinated complexes. As it has been shown in the previous subsection, the structural changes on the GBL molecule decrease with increasing coordination number, an effect that can be expected as well for the vibrational shifts (an issue that was studied in detail for the EC molecule [36]). According to experimental results [37], the four coordinated complex is the most likely in liquid phase. A detailed study of the shifts as a function of the coordination number (with up to four molecules) has been performed with a MP2/6-31G model chemistry. As the number n of coordinating molecules increases, also the number m of modes increases (according to $m = 3 \times (12 \times n + 1) - 6$). The majority of modes are localized on single molecules so that in a n-coordinated complex one can usually discern n frequencies that can easily be associated to a single mode (the average of these n frequencies is taken as the mode frequency). In some cases there is a non-negligible dispersion of frequencies (more than 10 cm^{-1}), so that the average value might not be fully informative. The carbonyl stretching for the four-coordinated complex is a relevant example, with frequencies: 1708, 1710, 1720 and 1736 cm^{-1}. As it will be shown, this behaviour is probably a precursor of the broadening of the absorption band found in the liquid state, both in experiments and MD simulations (see section 7.3.4). Obviously, a subset of modes is associated to vibrational motion of the whole cluster and have a complex character, most of them fall at wavenumbers lower than 150 cm^{-1}. An exception corresponds to some lithium-O=C modes which are found within the range of ring distortion vibrations; in the four-coordinated complex there are 3

normal mode	single GBL	$\Delta\nu$ $n=1$	$\Delta\nu$ $n=2$	$\Delta\nu$ $n=3$	$\Delta\nu$ $n=4$
ν_7	1726.9	-35.9	-21.6	-14.8	-7.9
ν_8	1587.2	-6.8	-5.3	-4.0	-3.7
ν_9	1568.4	2.0	2.2	1.7	1.5
ν_{10}	1548.6	-8.6	-6.5	-4.5	-1.0
ν_{11}	1406.4	21.9	15.7	9.6	5.8
ν_{12}	1395.3	8.1	6.6	5.2	4.3
ν_{13}	1357.7	2.1	2.7	2.7	3.8
ν_{14}	1277.5	-1.3	-2.5	-2.2	1.5
ν_{15}	1250.4	15.9	-50.7	9.6	7.8
ν_{16}	1195.6	48.6	67.9	6.1	3.4
ν_{17}	1145.3	54.6	80.8	52.6	34.0
ν_{18}	1122.9	18.6	18.5	16.9	16.6
ν_{19}	1054.4	5.5	5.0	3.9	4.1
ν_{20}	976.1	-12.4	-11.7	-11.5	-9.4
ν_{21}	942.7	4.8	2.4	-0.7	-0.9
ν_{22}	912.6	13.5	10.2	3.5	2.3
ν_{23}	877.5	19.8	20.9	18.9	12.8
ν_{24}	781.2	21.7	25.7	20.6	17.5
ν_{25}	661.8	66.6	18.3	27.2	19.1
ν_{26}	641.4	29.6	-6.6	18.7	12.0
ν_{27}	524.5	38.3	16.5	25.1	17.3
ν_{28}	473.4	44.6	2.5	38.7	20.2
ν_{29}	194.8	18.9	12.8	2.7	3.9
ν_{30}	143.7	16.9	30.0	13.9	23.2

Table 7.7. Vibrational analysis: ab initio low level frequencies (cm^{-1}) for single GBL and the relative shifts with its lithium complexes $[Li(GBL)_n]^+$. Positive and negative values of $\Delta\nu$ correspond to blue and red shifts respectively.

of them: $\omega_1 = 441.108$, $\omega_2 = 428.185$ and $\omega_3 = 421.648$ cm^{-1}, which will be discussed when the vibrational spectrum for the liquid phase is addressed.

Table 7.7 illustrates how the shifts become smaller when the coordination number increases. As will be shown in section 7.3.4, the results for the four coordinated complex are rather similar to those obtained in the liquid phase. Several other features are worth noticing in the shifts experienced by GBL molecules for clusters. One would expect a monotonic variation of the shifts with the coordination number; remarkably this is not the case for many degrees of freedom, as the shifts for the bis coordinated complex do not follow this trend (see for example ν_9, ν_{14}, ν_{15}, ν_{16}, ν_{17}, ν_{23}, ν_{24}, ν_{25}, ν_{26}, ν_{27}, ν_{28}, ν_{30} in table 7.7). Finally, the frequency shift decreases at different rates depending on the mode, it is not possible to find

a simple relation for the magnitude of the shift as a function of the coordination number.

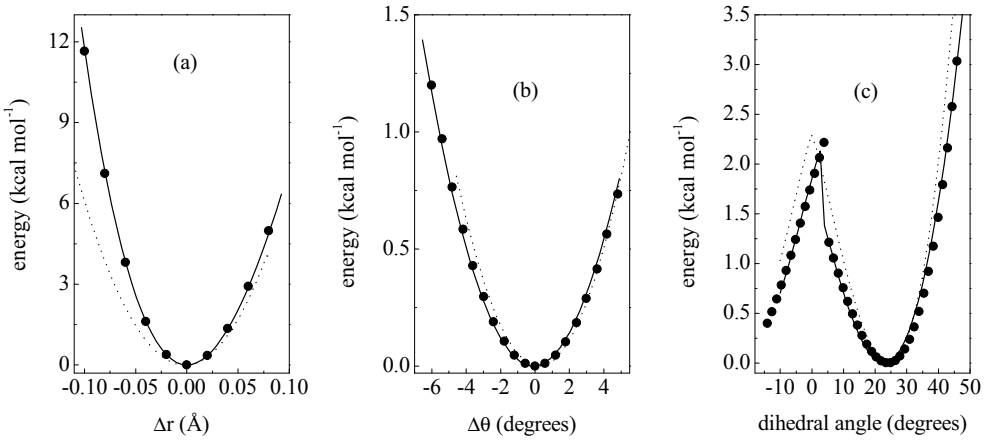

Figure 7.4. rPES profiles along selected internal coordinates: (a) O_1-C_1 bond, (b) O_1-C_1-C_2 angle and (c) C_3-C_4-O_2-C_1 dihedral. Filled circles, solid line and dotted line are used respectively for ab initio, our force field and AMBER results.

7.2.3 Intramolecular Force Field

There are indeed many intramolecular force fields available in the literature, like UFF [40], AMBER [41–43], MM3 [44–51], CHARMM [52,53], OPLS [54–59] and COMPASS [60]. They can be roughly divided into three classes: (i) generic ones with a large coverage (UFF), (ii) improved models restricted to some area of applications (e.g. biochemistry, AMBER, CHARMM), (iii) optimized parameterizations for condensed matter simulations. In the present work we add to the view that, given the increased computational power, force fields tailored to each system can be developed (at least for molecules of the size of GBL) using as a source of reference data quantum mechanical results. This is the path followed for instance to parameterize very flexible force fields for transition metal complexes, where an accurate description of the quantum mechanical PES far from the minimum is needed [61,62].

Recently [36] we applied an efficient methodology to develop a force field from first principles, an applied it to the EC molecule. The starting point is the usual expansion of the intramolecular potential in terms of internal coordinates (note that anharmonic terms are included for stretchings and bendings):

$$V(r,\theta,\phi) = \sum_{bonds}\left[k_{r_2}(r-r_0)^2 + k_{r_3}(r-r_0)^3 + k_{r_4}(r-r_0)^4\right] + \tag{7.1}$$

$$\sum_{angles}\left[k_{\theta_2}(\theta-\theta_0)^2 + k_{\theta_3}(\theta-\theta_0)^3\right] +$$

$$\sum_{dihedrals} A_n\left[1+\cos(n\phi-\delta)\right] + \sum_{impropers}\left[k_\phi(\phi-\phi_0)^2\right] =$$

$$V_{stretchings}(r) + V_{bendings}(\theta) + V_{dihedrals}(\phi) + V_{improper}(\phi)$$

where r, θ and ϕ denote respectively bond lengths, bending angles, and dihedral angles.

The method used to determine the parameters in the previous expansion makes use of the relaxed potential energy surface (rPES) concept [63]. In a rPES scan the energy is computed along a given internal coordinate simultaneously optimizing all the unconstrained degrees of freedom, so that the minimum total energy is obtained along the chosen internal coordinate. Such procedure can be performed both at the ab initio level and with the classical potential embodied in Eq. 7.1. Since the calculation is done for all internal coordinates, more rPES profiles are obtained than intramolecular degrees of freedom. This redundant description indirectly takes into account cross effects that are apparently neglected with the functional form used for the potential. The constants in eq. 7.1 are obtained in an iterative way: after a first guess, the parameter set is refined until the classical rPES profiles reach a good convergence with the ab initio ones. While for the stretching degrees of freedom few iterations are required to get a 100% convergence, for bending and torsional coordinates the fitting procedure is slower. The resulting force field is summarized in tables 7.3, 7.4 and 7.8. Figure 7.4 displays some examples of rPES profiles obtained with ab initio (black circles)

Dihedral	A_n	δ	n
O_1 - C_1 - C_2 - C_3	0.57	0.0	3
O_1 - C_1 - O_2 - C_4	0.84	0.0	3
C_1 - C_2 - C_3 - C_4	2.00	0.0	1
C_1 - C_2 - C_3 - C_4	1.90	180.0	2
C_1 - O_2 - C_4 - C_3	2.50	180.0	2
C_2 - C_1 - O_2 - C_4	1.87	180.0	2
O_2 - C_1 - C_2 - C_3	1.17	180.0	2
O_2 - C_1 - C_2 - C_3	0.63	180.0	3
O_2 - C_1 - C_2 - C_3	0.57	0.0	5
C_2 - C_3 - C_4 - O_2	1.71	0.0	3
C_2 - C_3 - C_4 - O_2	0.38	0.0	5

Improper	ϕ_0	k_ϕ
O_1 - C_1 - C_2 - O_2	180.0	19.0

Table 7.8. Intramolecular Force Field Parameters For Dihedrals; units: [A_n] = kcal mol^{-1}, [ϕ_0]=[δ]=degrees, [k_ϕ] = kcal mol^{-1} rad^{-2}.

and classical calculations using both our (solid line) and AMBER (dotted line) force fields. Here AMBER is used as a benchmark since it probably is the most popular force field used in atomistic simulations (nevertheless we have obtained similar results with other force fields such as CHARMM, MM3 and OPLS). Our parameterization produces profiles in excellent agreement with the ab initio ones (the same degree of accord is obtained for *all* intramolecular degrees of freedom, not shown). As mentioned before, our functional form includes the anharmonic terms along stretching and bending coordinates. The quantitative importance of an anharmonic description to better address solvent induced shifts is discussed in section 7.3.4. Panels (a) and (b) display the qualitative differences in the potential curves when anharmonicity is considered (our force field) and when not (AMBER): the ab initio profile is clearly anharmonic. Even for dihedral angles, which are obviously anharmonic in all force fields, there are noticeable differences. Panel (c) shows how AMBER fails to faithfully reproduce the discontinuity for the C_3-C_4-O_2-C_1 dihedral angle. The vibrational frequencies obtained with the model developed here are reported in table 7.6, which also contains the quantum chemical results. The maximum discrepancy with ab initio results is ≈ 8 % (≈ 15 % with AMBER).

7.3 Molecular Dynamics

7.3.1 Simulation Details

Molecular Dynamics simulations of the pure liquid and of one lithium ion dissolved in liquid GBL have been performed. Table 7.1 contains the parameters used for the intermolecular potential. Partial charges on the atoms were obtained by fitting the electrostatic potential energy surface (obtained by ab initio MP2/6-311G++(d,p) calculations) at points selected according to the Merz-Singh-Kollman scheme [64, 65], constraining them to reproduce the total molecular dipole moment. The latter is slightly overestimated (4.708 Debye versus the experimental value of 4.270 Debye [22]), which is a desirable feature in order to balance the absence of polarization effects with fixed charge models [65].

Lennard-Jones parameters for GBL are taken from Carlson et al. [66] (with geometric average combination rules: $\sigma_{ij} = (\sigma_i \times \sigma_j)^{1/2}$, $\epsilon_{ij} = (\epsilon_i \times \epsilon_j)^{1/2}$). Indeed, with this parameter set the diffusion coefficient is lower than the experimental one. The origin of this discrepancy lies in the radius taken for H. The value used ($\sigma =$

2.5 Å) is the one typical for hydrocarbons, while in GBL (and EC) the hydrogens are connected to carbon atoms that are near to electron-withdrawing groups (carbonate oxygens). This suggests that the electronic cloud for the hydrogen should be smaller. Indeed Sun et al. [67] have proposed that in the simulation of polycarbonates a value of $\sigma = 1.8$ Å should be used for hydrogen atoms which are hydrogen bonded to oxygens (it will be shown in the analysis of liquid structure that the carbonate oxygen tends to bind to hydrogens).

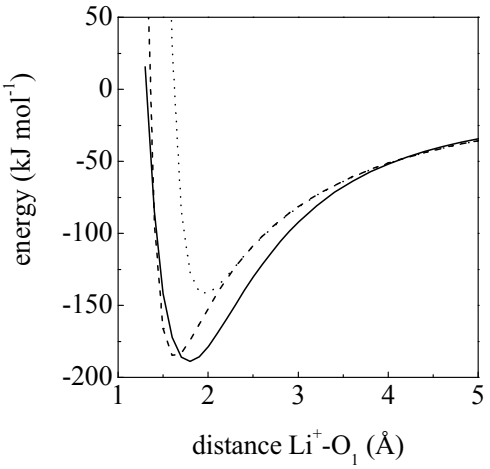

Figure 7.5. Potential energy for the GBL-Li^+ dimer; ab initio results (solid line), and classical results with the new (dashed line) and old (dotted line) set of Lennard-Jones parameters (see text).

We found that with this smaller hydrogen radius the diffusion coefficient is very near to the experimental one. Along the same line of reasoning it has been found that an optimal value for the lithium ion parameters is: $\sigma = 1.3$ Å and $\epsilon = 0.191$ kcal mol^{-1}. After this parameter fine-tuning it is important to check that the modified force field is consistent with ab initio calculations. Figure 7.5 displays the potential curves obtained with quantum chemical, and with the modified classical force field just described, for the Li^+-GBL dimer. The ab initio result is obtained with a counterpoise [68] correction using an MP2/6-311G(d,p) model chemistry. As can be seen the refined parameterization performs substantially better in reproducing the interaction between GBL and the lithium ion. Obviously the dimer potential is an approximation to the interaction in the liquid phase, where many body effects will be present, but we do not expect them to be important given the low degree of association of the neat liquid (see next section).

All simulations were done in the NVE ensemble with a time step of 0.2 fs. The reference temperature and density were set to 298.15 K and 1.1290 g cm^{-3} (as reported in the catalogue for the pure product). After an equilibration run of 50 ps, 3 productions runs of 100 ps each were completed to calculate structural and dynamical properties of the system. Two more calculations of 250 ps each were

done to compute vibrational spectra. For the intramolecular interactions we used the intramolecular force field developed in section 7.2.3 and the AMBER force field for comparison. The Ewald sum was employed for electrostatic interactions.

7.3.2 Structural properties

Pure GBL

The radial distribution function (RDF) corresponding to the molecular center of mass is displayed in panel (a) of figure 7.6. Its overall structure is very similar to that of dense simple liquids, what can be further confirmed by analysis of the solvation number N_s, defined as

$$N_s = 4\pi\rho \times \int_0^{r_{min}} r^2 g(r) dr, \tag{7.2}$$

where $g(r)$ denotes the RDF, ρ is the number density and r_{min} is the first minimum of the RDF (7.1 Å). A solvation number of 12 is found, which is typical of nonassociated liquids. Although this is a signal of a low degree of order, some further insight can be obtained from the analysis of partial RDFs. Panel (b) of figure 7.6 displays the O_1-oxygen and O_1-carbon radial distribution functions for representative oxygen and carbon atoms. For the O_1-O_1 case there is no first peak at 3 Å, the contact oxygen-oxygen distance, and the same result is obtained for O_1-O_2 (not shown). The corresponding RDFs are flat and start at larger separations. These features indicate that the oxygens in different molecules tend to stay away from each other, what can be explained by the strong electrostatic repulsion. Concerning

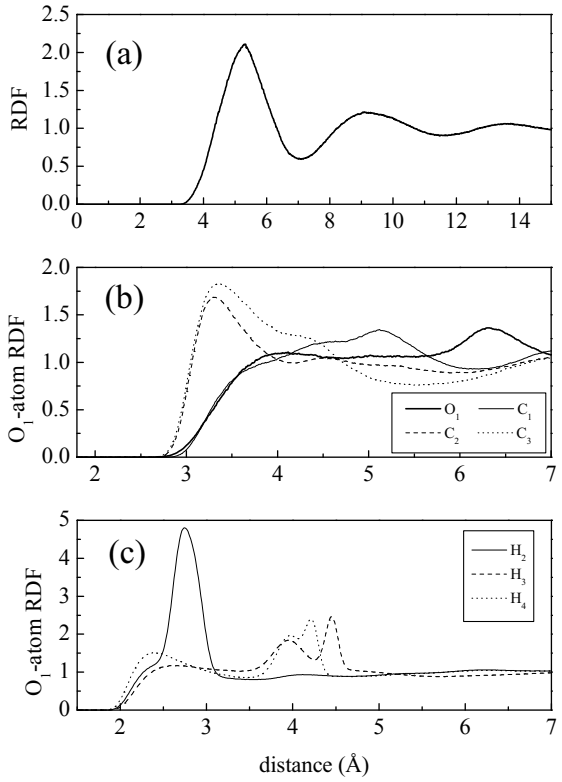

Figure 7.6. Molecular Dynamics simulation results: (a) radial distribution function for GBL molecules' center of mass, (b) and (c) O_1-atom radial distribution functions.

the carbons, the result for O_1-C_1 are almost identical to those just discussed for the oxygen-oxygen RDFs, so that the configuration in which the carbonyl oxygen would point to C_1 of a neighbouring molecule is not found. The behaviour for the other carbons differs markedly, with a first peak at the contact oxygen-carbon distance ($\approx$ 3.2 Å). The slight differences in peak position among different carbons correspond to their different radius (see Table 7.1). The results for C_4 are not shown for clarity, they are very similar to those for C_3 but slightly shifted to shorter distances due to the somewhat smaller carbon radius. The picture that results is one for which the carbonyl oxygen preferentially solvates the methylene groups. This is supported by the analysis of the O_1-H RDFs, with the representative examples displayed in panel (c) of figure 7.6. Two rather different behaviours are found: for the hydrogens close to C_3 and C_4 there is a (small) first peak located at $\approx$ 2.4 Å, which corresponds to the contact O-H distance, while for the hydrogens close to C_2 there is a rather high peak located at a somewhat larger distance ($\approx$ 2.8 Å). The latter is consistent with a bifurcated configuration in which the carbonyl oxygen of one molecule would be located midway between both hydrogens of the C_2 group (as a simple geometric calculation confirms). Such configuration is consistent with the lower height of the O_1-C_2 RDF as compared with those for O_1-C_3 or O_1-C_4: when coordinating the C_2 methylene group of one molecule, the carbonyl oxygen of the coordinating molecule tends to attach preferentially to both hydrogens rather than directly to the carbon. The peaks located at a shorter distance for the hydrogens belonging to C_3 and (to a lesser extent) C_4 are indicative of a collinear C-H...O configuration. It is also interesting to note the double peak that appears at $\approx$ 4 Å in both cases, which are consistent with the distances corresponding to the case in which the carbonyl oxygen is coordinated by both C_2 hydrogens. In conclusion this analysis points to a substantial amount of hydrogen bonding between the carbonyl oxygen and the methylene hydrogens.

GBL + Li^+

The structural properties of the liquid around lithium are collected in figure 7.7. The radial distribution function for lithium ion is shown in panel (a) (the inset contains the solvation number for the first two solvation shells). We find that the solvation number is exactly four (in accord with the experimental estimation [37]), and that the radius of the first solvation shell is 4.0 Å. The structure of the complex can be compared to the one obtained with quantum chemical

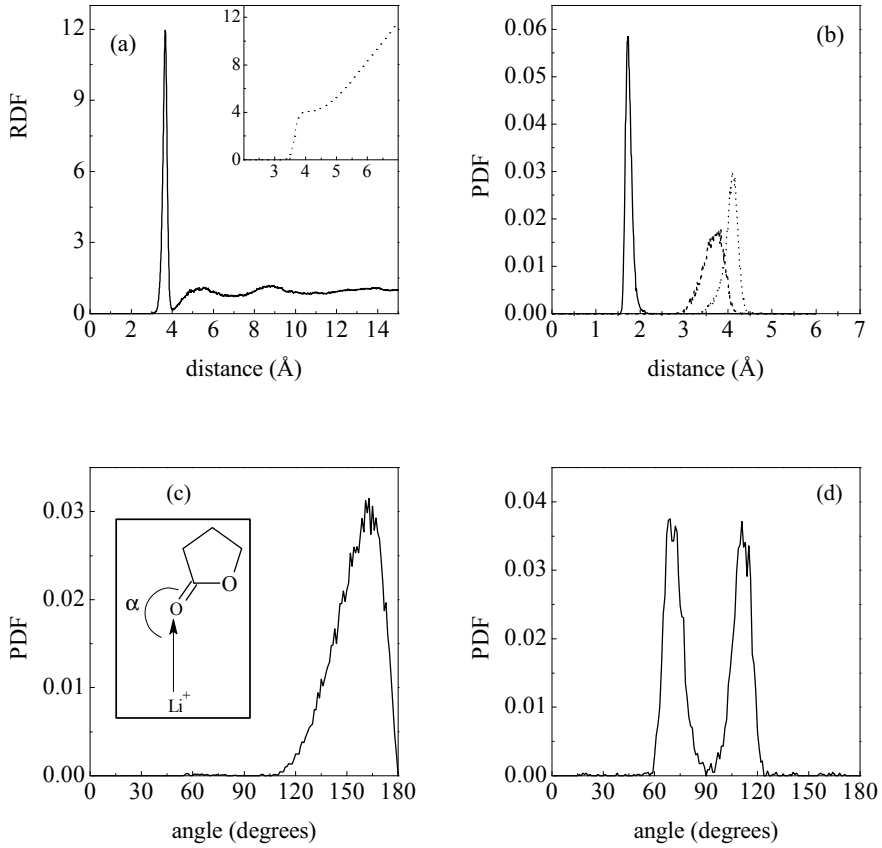

Figure 7.7. Structural properties of liquid GBL around lithium ion. Panel (a): Li^+-GBL center of mass radial distribution function, and solvation number (inset). Panel (b): probability distribution for the distance Li^+-O_1 (solid line), Li^+-O_2 (dashed line) and Li^+-C_2 (dotted line). Panel (c): probability distribution for α (see inset for definition). Panel (d): probability distribution for the dihedral angle formed by the 4 carbonyl oxygens nearest to lithium.

calculations for clusters (section 7.2.1). In panel (b) the probability distribution functions for the distances Li^+-O_1, Li^+-C_2 and Li^+-O_2 are shown. The most probable distances to O_1, O_2 and C_2 are respectively 1.73, 3.74 and 4.1 Å: as in the ab initio calculations, the lithium ion is coordinated by the carbonyl oxygen and the molecule is tilted allowing the ester oxygen to lie nearer to the ion than the α-carbon. To more clearly ascertain the distortion from a linear arrangement of the Li^+-O_1-C_1 atoms, we computed the probability distribution for the angle (α) formed between the Li^+-O_1 and the O_1-C_1 axis (see inset in panel (c) for a graphical definition). A maximum exists at $\sim 160°$, well above the result found in gas phase for the four-coordinated complex ($\sim 140°$) and near to the value obtained

for the mono-coordinated one ($\sim 158°$). Similar results were obtained for the EC case [36], and are explained by the attractive interaction with the carbonyl oxygen of second shell molecules, which tends to draw the methylene groups of first shell molecules away from the lithium ion, resulting in an angle closer to 180°. Finally, the dihedral angle formed by the carbonyl oxygens coordinating the cation (last panel) is typical of a tetrahedral structure, the distribution is peaked at $\sim 71°$, just 4° less than the ab initio result.

7.3.3 Diffusion

Diffusion coefficients are calculated both from the mean square displacement (MSD):

$$D_{MSD} = \lim_{t\to\infty} \frac{\langle|\mathbf{R}(\mathbf{t}) - \mathbf{R}(\mathbf{0})|^2\rangle}{6t} \tag{7.3}$$

and from the velocity autocorrelation function (VACF):

$$D_{VACF} = \frac{1}{3}\int_0^\infty \langle \mathbf{V}(\mathbf{0}) \cdot \mathbf{V}(\mathbf{t})\rangle dt \tag{7.4}$$

where $\langle \ldots \rangle$ denotes the average for all time origins and all molecules' positions (velocities) of the center of mass. The actual cutoffs used in these formulas are 25 ps (for the MSD, see figure 7.8) and 5 ps (for the VACF integration). The experimental value of the GBL diffusion coefficient has been recently measured by means of Pulsed Gradient Spin-Echo ^{1}H NMR [26], at ambient temperature it is $\approx 0.90 \times 10^{-9}\mathrm{m^2s^{-1}}$, with which our results agree satisfactorily ($D_{VACF} = 0.84(\pm 0.03)\times 10^{-9}\mathrm{m^2s^{-1}}$ and $D_{MSD} = 0.76(\pm 0.04) \times 10^{-9}\mathrm{m^2s^{-1}}$). For what concerns lithium diffusion we found very good agreement with experiment as well: Kikuko et al. [26] measured a

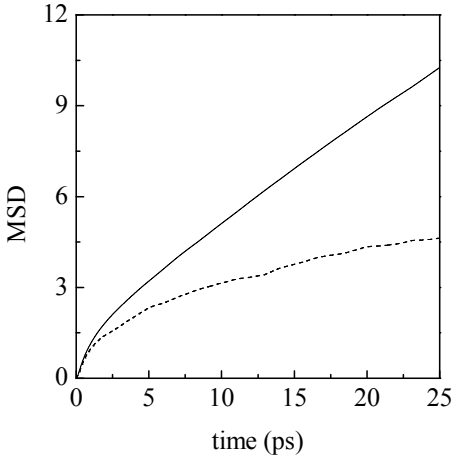

Figure 7.8. Molecular Dynamics simulation results for the mean square displacement of GBL molecules' center of mass (solid line) and of lithium ion (dashed line).

value of $\approx 0.25 \times 10^{-9}\mathrm{m^2s^{-1}}$, while we obtain $D_{VACF} = 0.32(\pm 0.04) \times 10^{-9}\mathrm{m^2s^{-1}}$ and $D_{MSD} = 0.20(\pm 0.05) \times 10^{-9}\mathrm{m^2s^{-1}}$.

According to Dünweg et al. [69], due to the finite size of the simulation box, the diffusion coefficient arising from the simulation usually underestimates the value for infinite size systems. They proposed that this could be corrected by adding a constant term (χ) that depends on the simulation box dimension (L), temperature (T) and viscosity (η)

$$\chi = \frac{2.867 k_B T}{6\pi\eta L}. \tag{7.5}$$

In our case, considering $\eta = 1.727$ cP [70] we have $\chi = 0.119 \times 10^{-9}\mathrm{m^2s^{-1}}$. Taking into account this correction, the diffusion coefficients for the pure liquid are even in better agreement with the experimental one.

7.3.4 Vibrational Spectrum

Vibrational spectra were obtained by fast Fourier transform (FFT) of the total dipole moment autocorrelation function computed during the simulation (including all GBL molecules or just those within the first shell of the ion, see below). According to Berens et al. [71–73] the absorption lineshape is given by:

$$S(\omega) = (2\pi)^{-1} \int_{-\infty}^{\infty} dt \exp(-i\omega t) \langle \vec{M}(t) \cdot \vec{M}(0) \rangle, \tag{7.6}$$

where $\vec{M}$ denotes the total dipole moment. The shortness of the time series available results in a no negligible degree of noise, so that a filter is required. We used an FFT filter with 20 points for a correlation function of 100000 points (we checked in a previous study [36] that this smoothing allows to get a clearer representation of the spectrum without losing important information).

Pure GBL

The whole spectrum of liquid GBL is shown in the middle panel of figure 7.9. Contrary to EC, where a number of bands did not appear in the simulated spectrum [36], here almost all vibrational frequencies are visible. To ease the comparison with the vibrational analysis done in subsection 7.2.2, the spectrum is divided into four zones (ν_{29} and ν_{30} modes are not considered because they have a very low intensity). Panel (a) contains all ring modes (ν_{28} to ν_{24}); of particular intensity is the band for the out of plane ring-C=O torsion (ν_{27}). In panel (b) we show

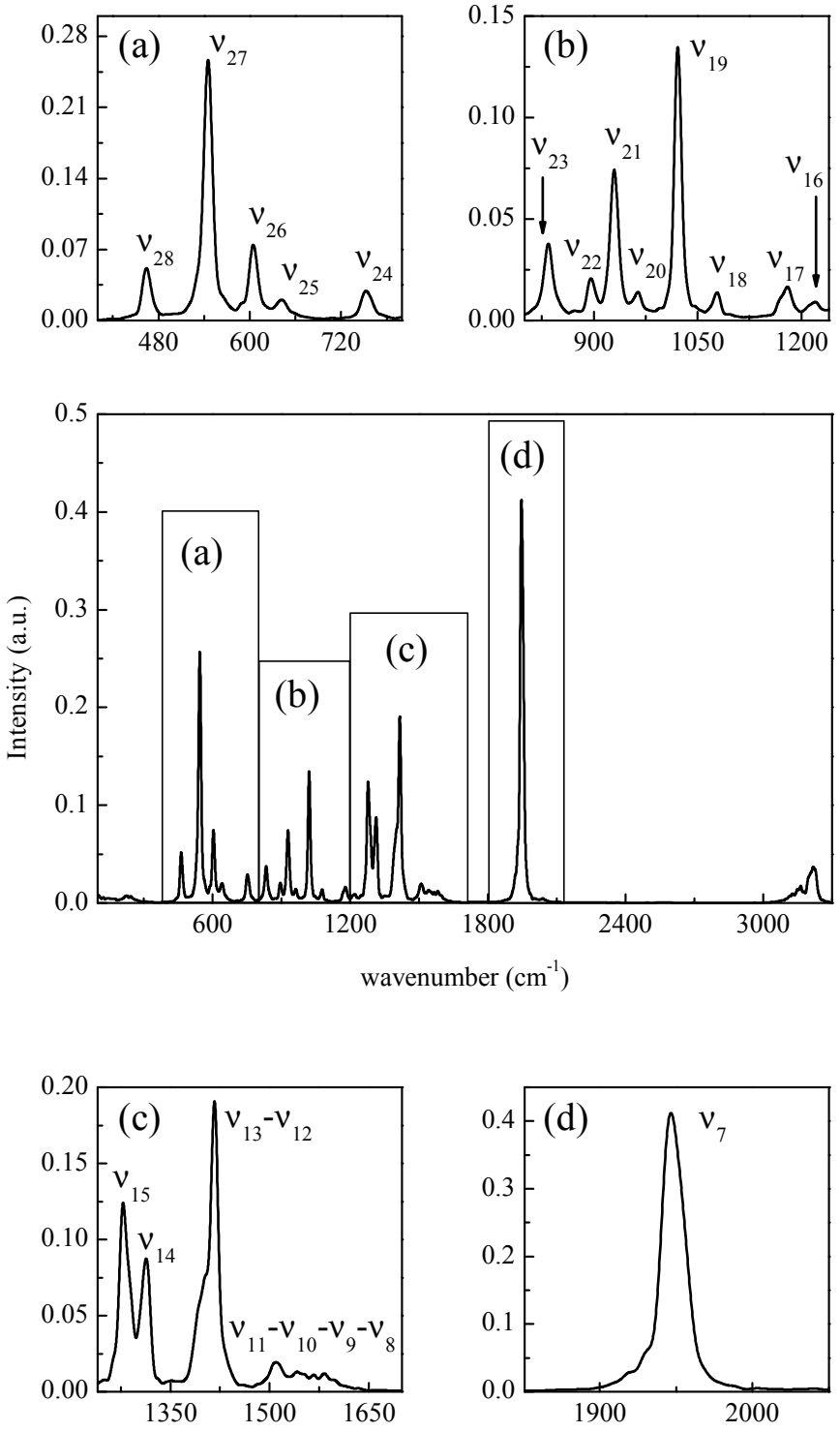

Figure 7.9. Middle panel: whole vibrational spectrum of pure GBL. Smaller panels: details of zone (a), (b), (c) and (d).

all the stretching modes for the ring bonds and the CH_2 rocking modes (ν_{23} to ν_{16}). For what concerns the remaining CH_2 modes (ν_{15} to ν_8), we can see in panel (c) that the scissoring and the highest frequency wagging modes (ν_{11} to ν_8) form a broad band of low intensity where the peaks cannot be easily distinguished. ν_{15} to ν_{12} modes have higher intensity and two wagging modes coalesce in a single band with a shoulder due to the ν_{13} mode. The important carbonyl stretching mode is depicted in panel (d): it shows an asymmetric band which width at half height is ~ 18 cm^{-1}. Very small shifts (maximum of ~ 10 cm^{-1}) of the frequencies are noticed if we compare the condensed phase and the harmonic analysis for the isolated molecule. They can be observed mainly in the CH_2 twisting and rocking modes and, of minor entity, in ring modes.

GBL + Li^+

In order to discern the effect of the lithium ion on the liquid phase spectrum, the dipole moment autocorrelation function was computed during the simulation only for the molecules belonging to the first solvation shell. Figure 7.10 shows the details of what we called zones (a) and (d) for the pure solvent spectrum (previous subsection); both the pure solvent and the coordinating GBL frequencies are shown. These zones contain most of the vibrational frequencies that can be compared with experimental results: Wang et al. [27] found, with IR and Raman spectroscopy, that the most important shifts correspond to ν_7, ν_{16}, ν_{22}, ν_{24}, ν_{27} and ν_{28}, which will be addressed in turn. It should be noted that it is not straightforward to compare with experiment because, in contrast to simulated ones, experimental spectra contain contributions of bulk and ion-coordinating molecules. Besides experimentally there are substantial contributions from overtone and combination bands (the carbonyl stretching being a prominent example), which in contrast are muted in the simulation results.

The carbonyl stretching normal mode (ν_7) is depicted in panel (a) of figure 7.10: upon cation coordination we notice a redshift of ~ 14 cm^{-1} and a broadening of the spectral band of ~ 6 cm^{-1}. Experimentally Wang et al. found a bigger broadening and a shoulder at lower frequencies (which might be indicative of a shift of ~ 24 cm^{-1}).

On the other hand there is a study of Deepa et al. [29] who found a redshift of 10 cm^{-1}. Our result thus falls midway between both experimental estimations. The same panel dramatically illustrates the effect of neglecting anharmonicity. If

only the harmonic terms of the force field are considered, instead of a red shift, a blueshift is obtained. In order to discard that this is not a particular feature of the force field employed, similar simulations have been run using the AMBER force field (which we recall does not contain any anharmonicity for stretchings or bendings). Again the same result is obtained: upon ion coordination, the carbonyl stretching mode is upshifted to higher wavenumbers. In short, a fully harmonic force field is not able to reproduce the correct sign of the shift, what should be regarded as an important limitation of most force fields if they are to be used to interpret spectroscopic measures of solvated molecules.

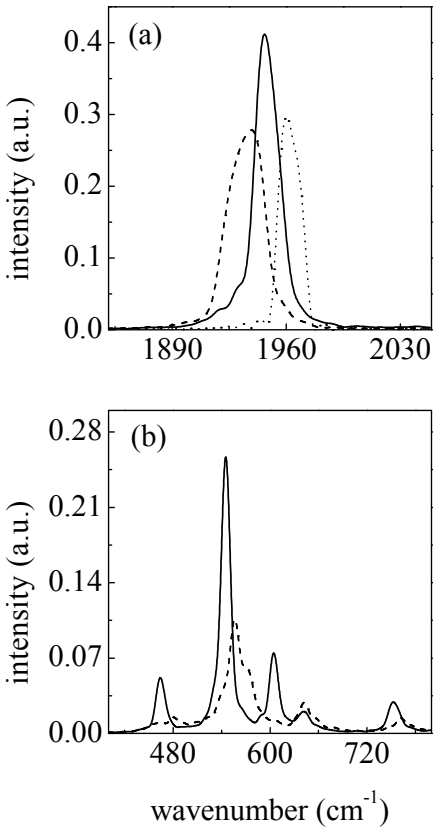

Figure 7.10. Comparison between the simulated vibrational spectra of bulk GBL (solid line) and first shell molecules (dashed line) for the two most representative regions, corresponding respectively to zones (d) and (a) of figure 7.9. In panel (a) the result with an harmonic force field is included (dotted line).

For what concerns ν_{16} (CH_2 twisting mode) and ν_{22} (CH_2 rocking mode) we observed, consistently with experiment, a blueshift of respectively $\sim$ 27 cm^{-1} (experimental $\sim$ 30 cm^{-1}) and $\sim$ 6 cm^{-1} (experimental $\sim$ 10 cm^{-1}). The low intensity obtained for these bands is consistent with experiment as well, as they are only observed at high ionic concentrations. The remaining modes on which we focus are shown in panel (b) of figure 7.10. This part of the spectrum seems to be rather sensitive to coordination. The ν_{28} mode shows a blueshift of $\sim$ 20 cm^{-1}. Experimentally the presence of a new band which intensity grows with salt concentration is observed (with a blueshift of $\sim$ 5 cm^{-1}). The ν_{27} mode is upshifted by $\sim$ 15 cm^{-1}, in line with the experimental blueshift of $\sim$ 8 cm^{-1}. In addition, this band shows a shoulder that might be interpreted as the contribution of lithium-GBL intermolecular modes: while in quantum chemical calculations the majority of intermolecular modes are found below 150 cm^{-1}, three of them are found in this

zone of the spectrum (see subsection 7.2.2), what might explain the broad profile of the ν_{27} mode.

Finally, for what concerns ν_{24}, there is a broadening of the band which peak is upshifted by ~ 11 cm^{-1}; a blueshift of ~ 22 cm^{-1} is found experimentally. Wang et al. [27] observed that the contour becomes more asymmetric as lithium salt concentration is raised, followed by the splitting of the band at high concentrations. We should mention that in this zone of the spectrum we also observe the change in intensity of ν_{26} and ν_{25}: the former lowers substantially and the latter increases in intensity, while both are slightly upshifted (the entity of these shifts is within the order of experimental precision). Small shifts (less than 5 cm^{-1}) are also found in all low lying vibrations. Even if they are not observed experimentally, this result is consistent with our ab initio calculation on complexes as explained in section 7.2.2. We can conclude that as a result of the strong interaction between lithium and GBL, the most affected vibrational modes are the ring distortions, the methylene rocking and twisting modes, and, obviously, the carbonyl stretching.

7.4 Conclusions

Concerning structural properties, it has been found in first place that the GBL monomer is non-planar with a barrier of ≈ 9 kJ/mol for ring inversion, with the carbonyl bond axis slightly tilted towards the lactone oxygen. This structure is somewhat deformed in the presence of the lithium ion but to a lesser extent than what is found for instance in the ethylene carbonate case. As the number of molecules solvating the ion increases, the distance between the carbonyl oxygen and the ion increases as well, reducing the molecular distortion. For the important case of the four coordinated cluster the structure is tetrahedral. In addition, the carbonyl axis is not collinear with the lithium ion, but the lactone oxygen is closer to lithium than the α-carbon. Such configuration is maintained in the liquid phase, but with an increased tendency to a collinear configuration due to the attractive effect of second shell molecules. This attraction is explained by the analysis of radial distribution functions for neat liquid GBL: the carbonyl oxygen tends to solvate the methylene groups. Particularly, the solvation of the α-carbon differs from the two other methylene groups in that the oxygen tends to sit midway between both hydrogens.

Given that the main probes of GBL are spectroscopic, an special emphasis

has been put on vibrational properties, starting with a full new assignment of bands. Substantial shifts have been found upon lithium coordination. The cases of the C-O stretches are particularly remarkable for the Li^+-GBL dimer: the carbonyl stretch frequency is downshifted by ≈ 77 cm^{-1} while, on the contrary, the C_1-O_2 stretch (which is not directly linked to the ion) is upshifted by a larger value (≈ 100 cm^{-1}). Ring modes are substantially affected as well. The shifts decrease upon increasing the solvation number, but not necessarily in a monotonic way for all modes. This is the case for instance of the C_1-O_2 stretch, which shift is increased for the trimer compared to the dimer, followed by a gradual decrease as the number of GBL molecules is increased. A direct comparison with experimental results is possible in the liquid phase. To this end an intramolecular force field has been specially tailored to the GBL molecule, following a procedure founded on the concept of relaxed potential energy profiles. This new potential includes anharmonic terms for stretches (up to quartic contributions) and bends (cubic), and has been shown to be superior to conventional force fields regarding potential profiles and harmonic frequencies for the monomer. More importantly, the analysis of the carbonyl stretch in the liquid phase has illustrated how the neglect of anharmonic contributions results in a wrong sign for the predicted shift. This is a critical feature to take into consideration if one wants to use generic force fields to theoretically interpret spectroscopic measures. Finally, the calculation of the spectrum for the molecules belonging to the first shell produces results which are in fair agreement with experimental shifts. This has allowed to interpret several shoulders and/or broadenings appearing in experimental spectra as due to lithium induced shifts on first shell molecules.

References

[1] Y.-L. Zhu, H.-W. Xiang, G.-S. Wu, L. Bai and Y.-W. Li *Chem. Commun.* **3**, 254 (2002).

[2] M. Tarvainen, R. Sutinen, M. Somppi, P. Paronen and A. Poso *Pharm. Res.* **18**, 1760 (2001).

[3] U. Herrmann and G. Eming *Chem. Eng. Technol.* **21**, 285 (1998).

[4] N. Harris and M. W. Tuck *Hydrocarbon Process.* **69**, 79 (1990).

[5] G. S. Banker *J. Pharm. Sci.* **55**, 81 (1966).

[6] N. Takami, M. Sekino, T. Ohsaki, M. Kanda and M. Yamamoto *J. Power Sources* **97-98**, 677 (2001).

[7] J. Vose, T. Tighe, M. Schwartz and E. Buel *J. Forensic Sci.* **46**, 1164 (2001).

[8] H. M. R. Hoffmann and J. Rabe *Angew. Chem., Int. Ed. Engl.* **24**, 94 (1985).

[9] S. S. C. Koch and A. R. Chamberlin *J. Org. Chem.* **58**, 2725 (1993).

[10] H. C. Brown, S. V. Kulkarni and V. S. Racherla *J. Org. Chem.* **59**, 365 (1994).

[11] P. M. Donate, D. Frederico, R. Da Silva, M. G. Constantino, G. Del Ponte and P. S. Bonatto *Tetrahedron Asym.* **14**, 3253 (2003).

[12] A. Chagnes, B. Carré , P. Willmann, R. Dedryvère, D. Gonbeau and D. Lemordant *J. Electrochem. Soc.* **150**, A1255 (2003).

[13] N. L. Allinger and S. H. M. Chang *Tetrahedron* **33**, 1561 (1977).

[14] N. L. Allinger *Pure and Appl. Chem.* **1982** 54 (12), 2515.

[15] J. H. Lii *J. Phys. Chem. A* **106**, 8667 (2002).

[16] A. D. Esposti, J. L. Alonso, R. Cervellati, D. G. Lister, J. C. Lopez and P. Palmieri *J. Chem. Soc. Faraday Trans.* **86**, 459 (1990).

[17] N. L. Allinger, L. R. Schmitz, I. Motoc, C. Bender and J. K. Labanowski *J. Comput. Chem.* **1992** 13 (7), 838.

[18] P. Malon, L. J. Mickley, K. M. Sluis, C. N. Tam, T. A. Keiderling, S. Kamath, J. Uang and J. S. Chickos *J. Phys. Chem.* **1992** 96, 10139.

[19] G. Bouchoux, D. Leblanc, O. Mó and M. Yáñez *J. Org. Chem.* **1997** 62, 8439.

[20] Z.-H. Li, W.-N. Wang, K.-N. Fan, M. W. Wong, H.-H. Huang and W. Huang *Chem. Phys. Lett.* **1999** 305, 474.

[21] J. R. Durig, G. L. Coulter and D. M. Wertz *J. Mol. Spectrosc.* **1968** 27, 285.

[22] J. R. Durig, Y. S. Li and C. C. Tong *J. Mol. Struct.* **1973** 18, 269.

[23] A. C. Legon *Chem. Commun.* 838 (1970).

[24] P. McDermott *J. Phys. Chem.* **90**, 2569 (1986).

[25] J. C. Lopez, J. L. Alonso, R. Cervellati, A. D. Esposti, D. G. Lister and P. Palmieri *J. Chem. Soc. Faraday Trans.* **86**, 453 (1990).

[26] K. Hayamizu, Y. Aihara, S. Arai and C. G. Martinez *J. Phys. Chem. B* **103**, 519 (1999).

[27] J. Wang, X. Xuan, J. Lu, N. Pei and Y. Mo *Z. Phys. Chem.* **215**, 437 (2001).

[28] S. K. Mandal, A. R. Amin and W. E. Crowe *J. Am. Chem. Soc.* **123**, 6457 (2001).

[29] M. Deepa, N. Sharma, P. Varshney, S. A. Agnihotry and R. Chandra *Ionics* **6**, 408 (2000).

[30] Gaussian 98, Revision A.11.2, M. J. Frisch, G. W. Trucks, H. B. Schlegel, G. E. Scuseria, M. A. Robb, J. R. Cheeseman, V. G. Zakrzewski, J. A. Montgomery, Jr., R. E. Stratmann, J. C. Burant, S. Dapprich, J. M. Millam, A. D. Daniels, K. N. Kudin, M. C. Strain, O. Farkas, J. Tomasi, V. Barone, M. Cossi, R. Cammi, B. Mennucci, C. Pomelli, C. Adamo, S. Clifford, J. Ochterski, G. A. Petersson, P. Y. Ayala, Q. Cui, K. Morokuma, N. Rega, P.

Salvador, J. J. Dannenberg, D. K. Malick, A. D. Rabuck, K. Raghavachari, J. B. Foresman, J. Cioslowski, J. V. Ortiz, A. G. Baboul, B. B. Stefanov, G. Liu, A. Liashenko, P. Piskorz, I. Komaromi, R. Gomperts, R. L. Martin, D. J. Fox, T. Keith, M. A. Al-Laham, C. Y. Peng, A. Nanayakkara, M. Challacombe, P. M. W. Gill, B. Johnson, W. Chen, M. W. Wong, J. L. Andres, C. Gonzalez, M. Head-Gordon, E. S. Replogle, and J. A. Pople, Gaussian, Inc., Pittsburgh PA, 2001.

[31] M. J. Frisch, J. A. Pople and J. S. Binkley *J. Chem. Phys.* **80**, 3265 (1984).

[32] DL_POLY is a package of molecular simulation routines written by W. Smith and T. R. Forester, copyright The Council For The Central Laboratory Of The Research Council, Daresbury Laboratory at Daresbury, Nr. Warrington (1996).

[33] `http://www.cse.clrc.ac.uk/msi/software/DL_POLY/`

[34] `http://www.originlab.com`

[35] D. Cremer and J. A. Pople *J. Am. Chem. Soc.* **97**, 1354 (1975).

[36] M. Masia, M. Probst and R. Rey *J. Phys. Chem. B* **108**, 2016 (2004).

[37] M. Caillon-Caravanier, G. Bosser, B. Claude-Montigny and D. Lemordant *J. Electrochem. Soc.* **149**, E340 (2002).

[38] A. P. Scott and L. Radom *J. Phys. Chem.* **100**, 16502 (1996).

[39] E. Pretsch, T. Clerk, J. Seibl and W. Simon, Tablas para la determinación estructural por metodós espectroscopicos, Springer-Werlag Ibérica (1998).

[40] A. K. Rappé, C. J. Casewit, K. S. Colwell, W. A. Goddard III and W. M. Skiff *J. Am. Chem. Soc.* **114**, 10024 (1992).

[41] S. J. Weiner, P. A. Kollman, D. T. Nguyen and D. A. Case *J. Comput. Chem.* **7**, 230 (1986).

[42] W. D. Cornell, P. Cieplak, C. I. Bayly, I. R. Gould, K. M. Merz, D. M. Ferguson, D. C. Spellmeyer, T. Fox, J. W. Caldwell and P. A. Kollman *J. Am. Chem. Soc.* **117**, 5179 (1995).

[43] `http://amber.scripps.edu/`

[44] N. L. Allinger, Y. H. Yuh and J.-H. Lii *J. Am. Chem. Soc.* **111**, 8551 (1989).

[45] J.-H. Lii and N. L. Allinger *J. Am. Chem. Soc.* **111**, 8566 (1989).

[46] J.-H. Lii and N. L. Allinger *J. Am. Chem. Soc.* **111**, 8576 (1989).

[47] N. L. Allinger, H. J. Geise, W. Pyckhout, L. A. Paquette and J. C. Gallucci *J. Am. Chem. Soc.* **111**, 1106 (1989).

[48] N. L. Allinger, F. Li and L. Yan *J. Comput. Chem.* **11**, 848 (1990).

[49] N. L. Allinger, F. Li, L. Yan and J. C. Tai *J. Comput. Chem.* **11**, 868 (1990).

[50] J.-H. Lii and N. L. Allinger *J. Phys. Org. Chem.* **7**, 591 (1994).

[51] Lii J.-H. and Allinger N. L. *J. Comput. Chem.* **19**, 1001 (1998).

[52] A .D. MacKerrell Jr., D. Bashford, M. Bellot, R. L. Dunbrack Jr., J. D. Evanseck, M. J. Field, S. Fisher, J. Gao, H. Guo, S. Ha, D. Joseph-McCarthy, L. Kuchnir, K. Kuczera, F. T. K. Lau, C. Mattos, S. Michnick, T. Ngo, D. T. Nguyen, B. Prodhom, W. E. Reiher III, B. Roux, M. Schlenkrich, J. C. Smith, R. Stote, J. Straub, M. Watanabe, J. Wiórkiewicz-Kuczera, D. Yin and M. Karplus *J. Phys. Chem. B* **102**, 3586 (1998).

[53] N. Foloppe and A. D. MacKerell Jr. *J. Comput. Chem.* **21**, 86 (2000).

[54] W. L. Jorgensen, D. S. Maxwell and J. Tirado-Rives *J. Am. Chem. Soc.* **117**, 11225 (1996).

[55] D. S. Maxwell, J. Tirado-Rives and W. L. Jorgensen *J. Comput. Chem.* **16**, 984 (1995).

[56] W. L. Jorgensen and N. A. McDonald *J. Mol. Struct. (Theochem)* **424**, 145 (1998).

[57] N. A. McDonald and W. L. Jorgensen *J. Phys. Chem. B* **102**, 8049 (1998).

[58] R. C. Rizzo and W. L. Jorgensen *J. Am. Chem. Soc.* **121**, 4827 (1999).

[59] M. L. P. Price, D. Ostrovsky and W. L. Jorgensen *J. Comput. Chem.* **22**, 1340 (2001).

[60] H. Sun *J. Phys. Chem. B* **102**, 7338 (1998).

[61] A. Villa, U. Cosentino, D. Pitea, G. Moro and A. Maiocchi *J. Phys. Chem. A* **104**, 3421 (2000).

[62] P.-O. Norrby and P. Brandt *Coord. Chem. Rev.* **212**, 79 (2001).

[63] J. B. Foresman and Æ. Frisch, Exploring Chemistry with Electronic Structure Methods (second edition), Gaussian, Inc. (1996).

[64] U. C. Singh and P. A. Kollman *J. Comput. Chem.* **5**, 129 (1984).

[65] B. H. Besler, K. M. Merz Jr. and P. A. Kollman *J. Comput. Chem.* **11**, 431 (1990).

[66] H. A. Carlson, T. B. Nguyen, M. Orozco and W. L. Jorgensen *J. Comput. Chem.* **14**, 1240 (1993).

[67] H. Sun, S. J. Mumby, J. R. Maple and A. T. Hagler *J. Am. Chem. Soc.* **116**, 2978 (1994).

[68] F. B. van Duijneveldt, J. G. C. M. van Duijneveldt-van de Rijdt and J. H. van Lenthe *Chem. Rev.* **94**, 1873 (1994).

[69] B. Dünweg and K. Kremer *J. Chem. Phys.* **99**, 6983 (1993).

[70] M. Ue *J. Electrochem. Soc.* **141**, 3336 (1994).

[71] P. H. Berens and K. R. Wilson *J. Chem. Phys.* **74**, 4872 (1981).

[72] P. H. Berens, S. R. White and K. R. Wilson *J. Chem. Phys.* **75**, 515 (1981).

[73] P. H. Berens, D. H. J. Mackay, G. M. White and K. R. Wilson *J. Chem. Phys.* **79**, 2375 (1983).

Part IV

Polarization

This Part contains a detailed study of the most popular molecular polarization methods as applied to ion-molecule dimers, following the outline given below:

Chapter 8 The three main methods to implement molecular polarization (point dipoles, fluctuating charges and shell model) are tested against high level ab initio calculations for a molecule (water, carbon tetrachloride) close to a point charge (at the distance of a lithium or magnesium ion). The goal is to check whether an approximation (linear polarization) strictly valid at large intermolecular distances is sufficiently accurate for liquid state molecular dynamics simulations, where strong polarization effects are to be expected at short separations. The monitored observable is the molecular dipole moment as a function of the charge-molecule distance for selected molecular orientations. Analytic formulas are derived for the components of the molecular polarization tensor, facilitating the optimization of the performance for each polarization method as a function of its underlying parameters. Overall, the methods studied provide a remarkably good representation of the induced dipole, with no divergences appearing even at the shortest distances. For water close to a monovalent point charge the point dipole model, implemented with one or three dipoles, accurately reproduces the water dipole moment at all distances. Deficiencies appear as the molecular polarizability and/or charge increase: basically, the ab initio induced moments grow faster at intermediate distances than the linear increase characteristic of the phenomenological polarization methods, suggesting that nonlinear effects (hyperpolarizability) can not be neglected in these cases. Regarding the capabilities of each method, the point dipole method is the one that performs best overall, with the shell model achieving acceptable results in most instances. The fluctuating charge method shows some noticeable limitations for implementations of comparable complexity (in terms of number of sites required).

Chapter 9 Our initial study on the performance of molecular polarization methods close to a positive point charge (J. Chem. Phys. **121**, 7362 (2004)) is extended to the case in which a molecule interacts with a real cation. Two different methods (point dipoles and shell model) are applied to both the ion and the molecule. The results are tested against high level *ab initio* calculations for a molecule (water or carbon tetrachloride) close to Li^+, Na^+, Mg^{2+} and Ca^{2+}. The monitored observable is in all cases the dimer

electric dipole as a function of the ion-molecule distance for selected molecular orientations. The moderate disagreement previously obtained for point charges at intermediate distances, and attributed to the linearity of current polarization methods (as opposed to the nonlinear effects evident in *ab initio* calculations), is confirmed for real cations as well. More importantly, it is found that at short separations the phenomenological polarization methods studied here substantially overestimate the dipole moment induced if the ion is described quantum chemically as well, in contrast to the dipole moment induced by a point charge ion, for which they show a better degree of accord with *ab initio* results. Such behaviour can be understood in terms of a decrease of atomic polarizabilities due to the repulsion between electronic charge distributions at contact separations. It is shown that a reparametrization of the Thole method for damping of the electric field, used in conjunction with any polarization scheme, allows to satisfactorily reproduce the dimer dipole at short distances. In contrast with the original approach (developed for intramolecular interactions), the present reparametrization is ion and method dependent, and corresponding parameters are given for each case.

Chapter 10 High level *ab initio* calculations show that the self induced dipole moment of a halide-water dimer deviates from the usually employed point dipole model, with a substantial nonlinear damping at separations corresponding to the first hydration shell. The total dipole moment is rather similar along the halide series, with the maximum value decreasing as anionic polarizability increases. A new implementation of the Thole damping method satisfactorily reproduces the dipole moment at all separations for the most probable configurations.

Chapter 8

On the performance of molecular polarization methods. I. Water and carbon tetrachloride close to a point charge.

It is widely accepted that the inclusion of polarization is indispensable for the next generation of molecular force fields in order to confidently simulate heterogeneous environments. Indeed, a substantial amount of work has already been directed towards this goal, mainly motivated by the accuracy required in biomolecular simulations [1, 2] (as reflected for instance in the recent upgrading of the CHARMM force field with the inclusion of a fluctuating charge parameterization [3], or an initial version of an atomic dipole model implemented in AMBER [4]). At this point it might be convenient to critically examine the performance of the simple polarization methods that are being used, and the way in which polarizable force fields are constructed. In standard practice one of the available polarization meth-

ods is added to a force field functional (with *e.g.* Lennard-Jones and Coulomb interactions) and parameters are optimized so that selected liquid state properties get acceptably close to experimental values or, in an alternative approach, to ab initio energies computed for several cluster configurations. Both methods share two basic problems related to the description of the electrostatic part: first, the performance of the polarization methods at short distances is seldomly addressed in detail (while there is no guarantee that they provide reasonable results in regions with highly nonhomogenous electric fields) and, second, the electrostatic parameters get mixed with energetic or condensed phase properties, while this could in principle be avoided. An example should clarify these points: in the vast literature on ion solvation [5–27] (a scenario in which short range polarization effects can be expected to be particularly important) that makes use of classical polarizable methods, we are not aware of any work in which the induced dipole moment is computed as a function of the ion-molecule distance, and the results compared with ab initio calculations. Such a comparison might allow a reassessment of the way in which polarizability is handled prior to the development of the force field. It is a test of this sort that will be undertaken here for the most popular polarization methods. Moreover, considering that high quality electrostatic multipoles are readily obtained in ab initio calculations, it is suggested that the electrostatic part might be decoupled from liquid state properties and/or cluster energies to better understand the effect of polarization. The contradictory results obtained to date on the contribution of molecular polarization might result from comparing force fields that have been optimized mixing electrostatic with energetic and/or condensed phase aspects in variable proportions, and using different polarization methods with uncontrolled or unclear behaviours at short distances.

As already emphasized, the environment of an ion in solution is of particular interest, which justifies to study polarization effects for ion-molecule dimers instead of, for instance, addressing molecules under strong homogeneous fields. Regarding the molecules selected, water is a mandatory choice. As stated for instance in a review by Elrod and Saykally [28], many body effects can have important manifestations in a number of bulk water properties and, unlike in most atomic and molecular systems, many-body effects in hydrated ion systems can result in substantial structural changes. Considering this critical role of water, it is remarkable that a simple and reliable polarizable model is not yet available although, starting with the pioneering work of Barnes et al. [29], a large number of polarizable models have been developed in the past and new ones are being de-

veloped at an increasing pace [30–61] (the study of phase coexistence constitutes a relevant example of the difficulties encountered [62–64]). It is obvious that there is a need for such a model in order to replace the (nonpolarizable) workhorses of liquid state simulation (like SPC/E [65] and TIP4P [66]). Comparison with high level ab initio results for the dipole moment (or even higher multipoles) in strong nonhomogeneous electric fields (like those in the presence of an ion) might be a convenient and systematic way to guide future work. In this connection, only the work by Alfredsson et al. [67] on the water dimer, where the polarization was modelled by a single point dipole and the most probable configurations were compared with ab initio calculations, is along the lines of what is reported here. Although different from the present approach, the concept of molecular polarization potential map has also been used to help understand the performance of different polarization models for the water molecule [68]. The main limitation of water, when looking for general guidelines, lies in its low polarizability. As an example of a highly polarizable molecule we selected carbon tetrachloride, which displays a number of interesting features: its polarizability is almost one order of magnitude larger than the one of water, it has no permanent dipole moment and no polarization anisotropy.

Regarding the ions chosen, Li^+ should provide upper bounds on the polarization that a monovalent ion induces on neighbouring molecules. Similarly, Mg^{++} is the smallest divalent ion of biochemical interest. It is important to keep in mind, though, that the present calculations correspond to a molecule in the vicinity of a point charge (singly or doubly charged), rather than to an actual lithium or magnesium ion. This is the case for both the ab initio results and for those with classical polarization methods (where only the molecule is allowed to be polarized). Although in principle there is no obstacle in computing the total induced dipole moment of an ion-molecule dimer (which will be addressed in a forthcoming contribution), several considerations justify this simplified approach. First, almost all simulation studies of solvated cations have neglected ion polarizability, so that it is important to assess to which extent these models hold when compared with ab initio calculations. An interesting issue is that of polarization divergence which has been often invoked to introduce damping schemes at short separations and ascribed to the use of point charge models. Although this claim has been disproved for the water dimer [67], it might be possible that such divergence exists under the stronger fields created by small cations. Moreover, this simplified approach should provide a simple picture of molecular polarization, but one that

can still be rigorously compared with ab initio results. Real ions would introduce a higher degree of complexity since the total polarization depends then on both ionic and molecular contributions as well as on charge transfer. Together with the fact that the total dipole moment for charged systems depends on an arbitrary origin, the result would not be intuitively clear. In short, the molecules have been treated exactly but for the ions it is assumed that beyond the ionic radius (our induced moments have only been computed down to the closest distance for the real ion-molecule dimer) they behave as point charges (this approximation is virtually exact from rather small separations onwards, as will be shown).

There are three approaches for the inclusion of polarization that are amply used [2], and for which a comparative study is reported here: point dipoles [69–71], electronic equalization (fluctuating charges) [72] and Drude oscillators or shell models [73]. Methods that handle many-body effects by including 3-body terms (or higher) in the parameterization of energy [74–76], without making use of explicit polarization, are also rather popular but are not included in the present study. While they have the advantage of computational efficiency, and can accurately reproduce the energy landscape, they are unable to provide information on induced dipoles. We also do not analyse the extremely useful work on polarizable atoms designed to incorporate reaction fields into quantum chemical calculations [77]. Each of the methods studied here has, *a priori*, its strong and weak points. In the point dipole approach, the fact that dipoles are located on different sites substantially increases the complexity of Molecular Dyamics (MD) codes. This method, though, seems the most natural choice if a sort of hierarchical approach (feasible for increasing computational resources) is to be followed, since it would allow for the inclusion of higher multipoles [78]. The fluctuating charge method, in which site charges depend on the environment, is one of the most appealing because no significant changes need to be made in existing non-polarizable codes. It has also the conceptional advantage to describe charge transfer within a molecule (on which this approach is based). Unfortunately, it is difficult to model out-of-plane dipole moments for planar molecules [43] or even polarizable atomic ions [10]. Finally, the shell model has similar advantages regarding easiness of implementation. Its main problem might be the shortening of the time step that the inclusion of fast vibrating oscillators imposes, and the use of more interaction sites. One important point that has not been addressed so far is that of the equivalence between these methods. In principle all three are capable of providing at least the same mean polarizability under homogeneous fields,

and are therefore indistinguishable at long intermolecular distances. However, at short separations it is not clear if they are still interchangeable, since they can (and do) have different responses to nonhomogeneous fields. While computational convenience has been a major factor to decide which method to use, it will be here investigated if this different performance at short distances could provide a physically based criterion. These methods do not encompass all the possibilities at hand. Mixed methods are also possible: within the fluctuating charge model, charges can be allowed to depart from their equilibrium positions [79] (*i.e.* an electronic equalization-Drude oscillator model), or, again using fluctuating charges, polarizable point dipoles can be added [53,80,81] (*i.e.* an electronic equalization-point dipole method). Obviously, any other combination is in principle possible. It is not clear, though, if these approaches can solve the problems of simple methods: if non-linear effects turn out to be important (hyperpolarizability), none of these refinements would be capable of addressing them. This is one of the main focus of the present work. Another reason not to address mixed methods at the outset is that simple methods have not been optimized in most cases; it suffices to say that we know of no simple polarizable model of water that displays the experimental anisotropic polarizability. Therefore we decided to investigate their maximum performance before embarking in more sophisticated approaches. To this end we have also derived analytic formulas for the polarization tensor components for each of the methods, since these are helpful in guiding the optimization process.

The outline of the paper is as follows: a summary of the polarization methods used is given in the following section. Details of the ab initio calculations for the chosen systems are summarized in section III. The reader not interested in computational details can find the main results and the discussion of capabilities and shortcomings of each method in section IV. The main conclusions are summarized in section V.

8.1 Polarization methods

Here we summarize the fundamentals of the polarization methods studied, together with the corresponding parameters for water and carbon tetrachloride required in each method. Moreover, analytic formulas are given for the polarization tensor in each case (with the mathematical derivation outlined in an Appendix for illustrative examples).

8.1.1 Fluctuating charges

In the chemical potential equalization method (CPE) [72] variable discrete charges are located on atomic sites within the molecule. Their value is computed, for a given molecular geometry, by minimization of the electrostatic energy. Within the context of liquid state simulations it is most usually known as the fluctuating charge method [43].

For an isolated molecule, the molecular energy is expanded to second order in the partial charges

$$U_{molec} = U_0(\{r\}) + \sum_i^M \chi_i^0 q_i + \frac{1}{2}\sum_i^M J_i^0 q_i^2 + \frac{1}{2}\sum_i^M \sum_{j\neq i}^M J_{ij}(r_{ij}) q_i q_j, \qquad (8.1)$$

where $U_0(\{r\})$ denotes the charge independent contribution, χ_i^0 ("atomic electronegativity") and J_i^0 ("atomic hardness") are in principle characteristic of the atomic site i, and $J_{ij}(r_{ij})$ is a screening function, which is usually computed as the Coulomb integral of Slater ns atomic orbitals. In practice Eq. 8.1 is probably better regarded as a convenient expansion of the molecular energy, with parameters to be fitted from molecular properties, a perspective that will be here exploited to obtain the maximum possible performance of the method. Moreover, and although this possibility lies outside the scope of the present work, the $J_{ij}(r_{ij})$ coefficients are in principle dependent on the intramolecular distances if a flexible model is being considered (an Appendix in Ref [82] contains a detailed discussion of how the calculation of intramolecular forces is affected in such case).

The CPE tenet is that atom electronegativities within the molecule ($\chi_i \equiv \partial U_{mol}/\partial q_i$), should equalise ($\chi_1 = \chi_2, \ldots, \chi_1 = \chi_M$), while maintaining overall neutrality ($\sum_{i=1}^M q_i = 0$). This is equivalent to the minimisation of the molecular energy with respect to the partial charges, again with the added condition of charge neutrality.

Particularizing to the case in which the molecule is subject to an external homogeneous field, the total energy is given by

$$U = U_{molec} - \vec{p}\cdot\vec{E}, \qquad (8.2)$$

where $\vec{p}$ denotes the molecular dipole moment. If the energy is minimized, with the additional constraint of electroneutrality (with χ being the corresponding Lagrange multiplier),

$$\frac{\partial(U - \chi \sum_j q_j)}{\partial q_i} = 0, \tag{8.3}$$

the following set of equations is obtained (with the first one applying for each site i within the molecule)

$$\chi_i + J_i^o q_i + \sum_{j \neq i} J_{ij} q_j - \frac{\partial \vec{p}}{\partial q_i} \cdot \vec{E} = \chi \tag{8.4}$$

$$\sum_j q_j = 0, \tag{8.5}$$

from which the induced charges required to evaluate the molecular polarizability can be obtained.

We now give the analytic formulas for the polarization tensor components in the case of water and carbon tetrachloride. As a general rule, this tensor has no dependence on atomic electronegativities [83] (which are themselves linked to partial charges). This fact greatly facilitates the construction of fluctuating charge models: the J parameters can be optimized to reproduce the experimental values of the polarization tensor components, while the electronegativities can be tuned to reproduce any charge set of choice (often designed to reproduce multipole moments). Such approach has been successfully applied to neat carbon tetrachloride [84] and similar chloromethanes [85].

Water

The most popular fluctuating charge models of water [43] consist of three charges, located respectively on the two hydrogen sites and on the oxygen (SPC-FQ) or an auxiliary site (M) on the molecular plane (along the line bisecting the bending angle and towards the hydrogens, TIP4P-FQ). Defining the z axis along the bisector of the bending angle, and the x axis perpendicular to the molecular plane, the following expressions result [43] for the polarization components (see Appendix),

$$\alpha_{xx} = 0, \tag{8.6}$$

$$\alpha_{yy} = \frac{2d^2 \sin^2(\theta/2)}{J_H^0 - J_{HH}}, \tag{8.7}$$

$$\alpha_{zz} = \frac{2d^2 \cos^2(\theta/2)}{J_H^0 + J_{HH} - 4J_{HO} + 2J_O^0}. \tag{8.8}$$

where d denotes the oxygen-hydrogen (or M-hydrogen) distance and θ the angle between both bonds.

It is well known that neither of both models (SPC-FQ and TIP4P-FQ) does allow for induced dipoles perpendicular to the molecular plane (as reflected in the null value of α_{xx}). Within the present perspective, in which the emphasis is put on an accurate reproduction of induced moments, such behaviour is regarded as an important flaw. Possible solutions involve an increase in the number of sites or the use of mixed methods (as discussed in the Introduction), and will not be pursued here. The required parameters for the SPC-FQ and TIP4P-FQ models [43] are summarized in Table 8.1. The associated polarizabilities (obtained with Eqs. 8.6, 8.7, 8.8) are reported in Table 8.2.

	SPC-FQ	TIP4P-FQ
d_{OH} (Å)	1.0	0.9572
d_{OM} (Å)	0.0	0.15
$\theta_{H\hat{O}H}$ (degrees)	109.47	104.52
J^0_{OO} (kJ mol$^{-1}e^{-2}$)	1536.1	1555.3
J^0_{HH} (kJ mol$^{-1}e^{-2}$)	1641.5	1477.5
J_{OH} (kJ mol$^{-1}e^{-2}$)	1155.2	1198.7
J_{HH} (kJ mol$^{-1}e^{-2}$)	820.4	852.2

Table 8.1. Parameters for fluctuating charge models of water.

	SPC-FQ	TIP4P-FQ	PSPC	POL1	RPOL	PDM	RER	PD1-H2O	PD2-H2O	Exp.
$\bar{\alpha}$ (Å^3)	1.09	1.12	1.44	0.979	1.975	1.44	1.44	1.47	1.47	1.47
α_{xx} (Å^3)	0.0	0.0	1.44	0.922	0.933	1.44	1.44	1.428	1.415	1.415
α_{yy} (Å^3)	2.26	2.55	1.44	1.464	3.759	1.44	1.44	1.532	1.528	1.528
α_{zz} (Å^3)	1.02	0.82	1.44	0.550	1.234	1.44	1.44	1.451	1.468	1.468

Table 8.2. Experimental polarizabilities of water compared to those corresponding to the different classical models studied.

Carbon tetrachloride

In the case of carbon tetrachloride, with one fluctuating charge on each atomic site, all three polarization tensor components are equal

$$\alpha_{CCl_4} = \frac{4d\cos(tg^{-1}(\sqrt{2}))}{J^0_{Cl} - J_{ClCl}}, \tag{8.9}$$

where d stands for the carbon-chloride distance and tetrahedral symmetry is assumed. It is important to note that as long as the difference $J^0_{Cl} - J_{ClCl}$ is kept constant, the same molecular polarizability is obtained. Therefore the J values can be optimized so that the best possible accord for induced dipole moments at short distances is obtained (it is also interesting to note that the carbon hardness

does not contribute to the molecular polarizability). Subsequently, only the results with the model used by Llanta and Rey [84] to study induced absorption in liquid carbon tetrachloride will be reported since, as will be shown within, no significant improvement (based on Eq. 8.9) is possible. The corresponding parameters are [84] $J_C^o = 962.259$ kJ/(mol e^2), $J_{Cl}^o = 983.844$ kJ/(mol e^2), $J_{CCl} = 577.796$ kJ/(mol e^2), $J_{ClCl} = 432.919$ kJ/(mol e^2), $d = 1.766$ Å, which reproduce the experimental polarizability (10.5 Å^3) when inserted in Eq. 8.9.

8.1.2 Point dipoles

In this method both fixed partial charges and induced dipoles are located within the molecule. The value of the induced dipoles ($\vec{p_i}$) can be derived starting from the electrostatic energy of a polarizable particle (of polarizability α_i) subject to an external field [86, 87]

$$U_i = -\vec{p_i} \cdot \vec{E}_i + \frac{p_i^2}{2\alpha_i}, \tag{8.10}$$

where $\vec{p_i}$ denotes the induced dipole.

The field is produced by the external partial charges ($\vec{E^o}$) and by both the intramolecular and external induced dipole moments

$$\vec{E}_i = \vec{E}_i^o + \sum_{j \neq i} T_{ij} \cdot \vec{p_i}, \tag{8.11}$$

where T_{ij} denotes the dipole field tensor

$$T_{ij} = \frac{1}{r_{ij}^3} \left[3\frac{\vec{r}_{ij}\vec{r}_{ij}}{r_{ij}^2} - I \right]. \tag{8.12}$$

The following expression results for the electrostatic energy associated to induced dipoles

$$U_p = -\frac{1}{2} \sum_i \sum_{j \neq i} \vec{p_i} \cdot T_{ij} \cdot \vec{p_j} - \sum_i \vec{p_i} \cdot \vec{E}_i^o + \sum_i \frac{p_i^2}{2\alpha_i}, \tag{8.13}$$

which, if minimized with respect to $\vec{p_i}$, yields an implicit expression for the induced dipole

$$\vec{p_i} = \alpha_i \left[\vec{E}_i^o + \sum_{j \neq i} T_{ij} \cdot \vec{p_j} \right], \tag{8.14}$$

that can be solved iteratively in numerical simulations.

Since interactions are allowed between induced dipole moments located on different sites within a molecule, the present model has a non-additive character. Consistent sets of non-additive atomic polarizabilities have been derived that allow to satisfactorily reproduce the molecular polarizabilities of different molecular families [69]. According to our knowledge no analytic formulas are available in the literature for the polarization tensor principal components for polyatomic molecules, not even in the very important case of water.

Water

Adopting the same geometrical definitions as for the fluctuating charge model, the following expressions result for the polarizability along the z axis (see Appendix)

$$\begin{aligned}\alpha_{zz} &= (\alpha_O + 2\alpha_H) + \\ + &\quad \frac{16\alpha_O^2\alpha_H \sin^3(\theta) - 32\alpha_O\alpha_H d^3 \sin^3(\theta) + 32\alpha_O\alpha_H^2 \sin^3(\theta) - 2\alpha_h^2 d^3}{8d^6 \sin^3(\theta) - 16\alpha_O\alpha_H \sin^3(\theta) + \alpha_H d^3}\end{aligned} \tag{8.15}$$

The terms within the first parenthesis correspond to the result that would be obtained if the model had an additive character (in this limit different -additive- atomic polarizabilities should be used, which are also available [69]). The somewhat involved last term thus represents the effect of intramolecular interactions between induced dipoles. We have not attempted to partition the polarization tensor component in a similar way for the two other cases, in order to avoid unnecessarily increasing the complexity of the formulas,

$$\begin{aligned}\alpha_{yy} &= \frac{\alpha_O(1 - \frac{\alpha_H}{4d^3\sin^3(\theta)}) + 2\frac{\alpha_H\alpha_O(3\sin^2(\theta)-1)}{d^3}}{(1 - 144\frac{\alpha_O\alpha_H \sin^5(\theta)\cos^2(\theta)}{8d^6\sin^3(\theta)-\alpha_H d^3})(1 - \frac{\alpha_H}{4d^3\sin^3(\theta)}) - 2\frac{\alpha_O(3\sin^2(\theta)-1)\alpha_H(3\sin^3(\theta)-1)}{d^6}} + \\ + &\quad \frac{2\alpha_H(1 - 144\frac{\alpha_O\alpha_H \sin^5(\theta)\cos^2(\theta)}{8d^6\sin^3(\theta)-\alpha_H d^3}) + 2\frac{\alpha_O\alpha_H(3\sin^3(\theta)-1)}{d^3}}{(1 - 144\frac{\alpha_O\alpha_H \sin^5(\theta)\cos^2(\theta)}{8d^6\sin^3(\theta)-\alpha_H d^3})(1 - \frac{\alpha_H}{4d^3\sin^3(\theta)}) - 2\frac{\alpha_O(3\sin^2(\theta)-1)\alpha_H(3\sin^3(\theta)-1)}{d^6}}\end{aligned} \tag{8.16}$$

$$\begin{aligned}\alpha_{xx} &= \frac{\alpha_O(1 + \frac{\alpha_H}{8d^3\sin^3(\theta)}) + 2\frac{\alpha_H\alpha_O(3\cos^2(\theta)-1)}{d^3}}{(1 - 72\frac{\alpha_O\alpha_H \sin^5(\theta)\cos^2(\theta)}{4d^6\sin^3(\theta)+\alpha_H d^3})(1 + \frac{\alpha_H}{8d^3\sin^3(\theta)}) - 2\frac{\alpha_O(3\cos^2(\theta)-1)\alpha_H(3\cos^3(\theta)-1)}{d^6}} + \\ + &\quad \frac{2\alpha_H(1 - 72\frac{\alpha_O\alpha_H \sin^5(\theta)\cos^2(\theta)}{4d^6\sin^3(\theta)+\alpha_H d^3}) + \frac{2\alpha_O\alpha_H(3\cos^3(\theta)-1)}{d^3}}{(1 - 72\frac{\alpha_O\alpha_H \sin^5(\theta)\cos^2(\theta)}{4d^6\sin^3(\theta)+\alpha_H d^3})(1 + \frac{\alpha_H}{8d^3\sin^3(\theta)}) - 2\frac{\alpha_O(3\cos^2(\theta)-1)\alpha_H(3\cos^3(\theta)-1)}{d^6}}\end{aligned} \tag{8.17}$$

A large number of models exist for water, ranging from those with only one point dipole (located on the oxygen or on the M site), to those that have three

	PSPC	POL1	RPOL	PDM	RER	PD1-H2O	PD2-H2O
d_{OH} (Å)	1.0	1.0	1.0	0.9572	0.9572	0.9572	0.9572
d_{OM} (Å)	0.0	0.0	0.0	0.215	0.15	0.22	0.0606
$\theta_{H\hat{O}H}$ (degrees)	109.47	109.47	109.47	104.52	104.52	104.52	104.52
α_O (Å^3)	1.44	0.465	0.528	0.0	1.44	0.0	0.0
α_M (Å^3)	0.0	0.0	0.0	1.444	0.0	1.42048	1.4099
α_H (Å^3)	0.0	0.135	0.170	0.0	0.0	0.00192	0.0038

Table 8.3. Parameters for point dipole models of water.

point dipoles, respectively located on the hydrogens and, again, on the oxygen or M sites. A summary of the parameters for each of the models studied here is given in Table 8.3 (although only the most successful will be discussed). The associated polarizabilities, obtained with Eqs. 8.15, 8.16, 8.17 for the cases with three point dipoles, are reported in Table 8.2.

It should be noted that models with only one dipole are isotropic, while the water molecule displays anisotropic polarizabilities. Although this is in principle a reasonable approximation (the difference between polarization tensor components is less than 10 %), it is not clear to what extent it can be trusted at short distances, a point that will be addressed here. It is somewhat surprising that none of the models with three point dipoles available in the literature have aimed to reproduce the experimental anisotropic components, while an excellent match can be attained by optimizing the oxygen (or M site), and hydrogen, polarizabilities with the help of Eqs. 8.15, 8.16, 8.17. The result of such optimization is denoted PD1-H2O in Table 8.3 (there the charge is located on the M site characteristic of the TIP4P model, as this turns out to be superior to locating it on the oxygen). We have also included the position of M in the optimization process, and denoted the resulting model PD2-H2O; it reproduces correctly the (gas phase) experimental anisotropic polarizabilities (see Table 8.2).

Carbon tetrachloride

If induced dipoles are located on each atomic site and tetrahedral symmetry is assumed the following expression is obtained

$$\begin{aligned} \alpha_{CCl_4} &= (\alpha_C + 4\alpha_{Cl}) + (4\sqrt{2}\alpha_C + \frac{9\sqrt{3}}{8}\alpha_{Cl}) \times \\ &\times \frac{2048\alpha_C\alpha_{Cl} + 288\sqrt{2}\alpha_{Cl}^2}{1024\sqrt{2}d^6 - 8192\sqrt{2}\alpha_{Cl}\alpha_C - 243\sqrt{2}\alpha_{Cl}^2 + 96\sqrt{3}\alpha_{Cl}d^3}. \end{aligned} \quad (8.18)$$

Similar to the case of fluctuating charges, the molecular polarizability (α_{CCl_4}) depends on two parameters (α_C,α_{Cl}), so that an infinite number of pairs can be obtained that yield the same molecular polarizability. Again, this feature has been exploited to explore the maximum performance of the method. Results for two different sets are reported (Table 8.4): the model proposed in Ref. [69], and an optimized point dipole model (PD-CCl4) developed here along the lines just described.

8.1.3 Shell model

Several denominations (Drude oscillator, charge-on-spring, shell model) exist for closely related versions of this method. Essentially, induction is represented by charged particles attached by springs to several sites within the molecule. In its most simple (albeit rather popular) form only one charge is used which, for instance in the case of water, might be attached to the oxygen site. Under the effect of an external field the position of each auxiliary charge is adjusted to minimize the electrostatic energy.

	Ref. [69]	PD-CCl4	PD-central
α_C (Å^3)	0.878	-1.000	10.51
α_{Cl} (Å^3)	1.910	2.880	0.00

Table 8.4. Site polarizabilities for the different CCl_4 point dipole methods discussed.

The total partial charge for each site (q_i) is split between a fixed charge ($q_i - q_{Di}$) and an auxiliary charge (q_{Di}) that is allowed to move in the vicinity of the site (so that in absence of external field, both charges will overlap, with a net charge q_i). Note that, in the present formulation, this is an additive model since no intramolecular interactions are considered between charges, the displacement of auxiliary charges stems from external fields only. Each auxiliary charge is harmonically bound to its site (with position vector $\vec{r_i}$) by a spring of force constant k_i. Under the effect of the external field it will settle on an equilibrium position $\vec{r_i}+\vec{d_i}$. The part of the total energy associated to the induced dipoles generated when the molecule is under the effect of an external field is given by

$$U = \sum_i \frac{1}{2} k_i d_i^2 - \sum_i \vec{p_i} \cdot \vec{E}, \tag{8.19}$$

where the first term stands for the energy of the oscillators and the second for that of the induced dipoles in the presence of the external field.

The equilibrium position will be found by solving

$$\frac{\partial U}{\partial \vec{d}_i} = 0, \tag{8.20}$$

which, considering that $\vec{p_i} = \sum_i q_{Di}\vec{d}_i$, yields

$$k_i\vec{d}_i - q_{Di}\vec{E} = 0, \tag{8.21}$$

so that

$$\vec{d}_i = \frac{q_{Di}}{k_i}\vec{E}. \tag{8.22}$$

Inserting into the formula for the induced dipoles, we get

$$\vec{p_i} = \sum_i \frac{q_{Di}^2}{k_i}\vec{E}, \tag{8.23}$$

from which the polarizability in the direction of $\vec{E}$ is identified as

$$\alpha = \sum_i \frac{q_{Di}^2}{k_i}. \tag{8.24}$$

Since the result is independent of the electric field direction, an important limitation is that molecular polarization in this method is isotropic (even if more than one site per molecule is used). Regarding parameter optimization, somewhat different approaches are possible. In principle each term of the sum could be identified with the corresponding atomic polarizability ($\alpha_i \equiv q_{Di}^2/k_i$), what makes more evident the additive nature of the model (as Eq. 8.24 reduces to $\alpha = \sum_i \alpha_i$). If these atomic polarizabilities are taken as given [69] then only one free parameter is left for each site (q_{Di}^2 or k_i). In another approach, since the (average) molecular polarizability is the only observable, atomic polarizabilities are used as first guess of the quotients (q_{Di}^2/k_i) but all parameters are subsequently varied (with the only restriction

	Ref. [56]	Ref. [58]	Ref. [76]	SH-H2O
d_{OH} (Å)	1.0	1.0	1.0	0.9572
d_{OM} (Å)	0.0	0.0	0.0	0.215
$\theta_{H\hat{O}H}$ (degrees)	109.47	109.47	109.47	104.52
k_O (kJ/(mol Å^2)	61535.44	4185.5	65784.0	0.0
k_M (kJ/(mol Å^2)	0.0	0.0	0.0	62597.64
k_H (kJ/(mol Å^2)	0.0	0.0	4597.0	29096.44
q_{DO} (e)	-8	2.08241	-5.00	0.0
q_{DM} (e)	0.0	0.0	0.0	8.0
q_{DH} (e)	0.0	0.0	-0.75	0.2

Table 8.5. Parameters for shell models of water.

that the total molecular polarizability remains unchanged). Both approaches have been followed here in order to explore the maximum performance of the method. Actually, numerical efficiency also puts an important restriction on the sort of models that are acceptable. Since in its most popular form the method is applied making use of a generalized lagrangian, with the dynamics of the auxiliary sites integrated together with that of the nuclei, spring stiffness cannot be too large since this would require a rather short time step. Conversely, the charges cannot be large either, with approximately 10 e being a rough upper bound of the values that can be found in the literature.

Parameters for the different models available for water, and for the optimized one developed in this work (SH-H2O), are summarized in Table 8.5. The corresponding polarizabilities can be found in Table 8.2. For carbon tetrachloride there are no available models, an optimized version has been developed here (SH-CCl4, with parameters $k_C = 0.0$, $q_{DC} = 0.0$, $k_{Cl} = 13206$ kJ mol^{-1}Å^2, $q_{DCl} = 5e$), which yields the experimental polarizability.

8.2 Ab initio calculations

The performance of the polarization models discussed in this work is examined by comparing the induced dipole moments with those from ab initio calculations on the same systems. Therefore it must be ensured that the reference calculations are of sufficient accuracy. From a quantum chemical viewpoint, electrostatic properties like induced dipole moments (and polarizabilities) are one-electron properties or properties of the (linear response of the) ground-state electron density and can be calculated semiquantitatively already on the Hartree-Fock level if sufficiently flexible basis sets are used. Qualitatively wrong Hartree-Fock dipole moments [88] are found for small dipole moments, however, and accurate calculations of these properties require inclusion of electron correlation. For polarizabilities, Hartree-Fock calculations underestimate polarizabilities typically by up to 10%. The low accuracy of Hartree-Fock calculations with respect to polarizability calculations is also evident from the well-known approximate character of Koopmans' theorem since, to the first order of perturbation theory, the polarizability is proportional to the sum of the reciprocal excitation energies ($\alpha \approx 1/(E_0 - E_n)$; E_n is the n^{th} excited state). Just opposite to Hartree-Fock, density functional calculations with simple functionals (VWN [89], BLYP [90]) overestimate polarizabilities. Newer density functionals like B3LYP [91] perform better [92] and give an error around

2% [93] or less [94] if used with specially designed basis sets [95]. For our calculations we decided to use the B3LYP density functional with the aug-cc-pVTZ [96] basis set since a vast number of studies has already demonstrated its accuracy also for other quantities we are interested in with respect to future investigations. A good overview of the performance of density functionals for the calculation of electrical properties is given in [97].

In order to find the minimum of the potential energy curves Li^+ and Mg^{2+} were described with the 6-311G* basis set [98] since for these metals no aug-cc-pVTZ basis is available. Then the potential curves were calculated by moving the ions in the directions relative to H_2O and CCl_4 described in the subsequent sections. The curves of the induced dipole moments as function of the distance were calculated in the same way except that the ions are replaced by point charges without basis functions.

8.3 Molecule close to monovalued charge

We first address molecular polarization in the proximity of a monovalued charge with the radius of a lithium cation.

8.3.1 Water

The performance of molecular polarization methods only needs to be studied for distances that are physically relevant, so we start by estimating the distance of closest approach. Fig. 8.1 displays the Li^+-H_2O energy profiles computed ab initio for several molecular orientations (full lines). The same calculation has been performed for a point charge (dashed lines) instead of a lithium ion in order to ascertain from which separation on the approximation used here for the ion is accurate. Five molecular orientations have been selected: *C_{2v}-face*, with the molecular dipole pointing away from the

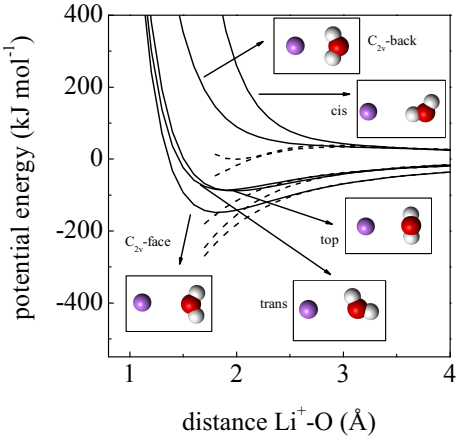

Figure 8.1. Ab initio potential energy curves for Li^+-H_2O (solid lines) and for (+)-H_2O (dashed lines).

ion, corresponds to the most probable orientation in the vicinity of a cation, as reflected in the deeper minimum; *trans* corresponds to a similar configuration with the molecule slightly tilted, so that there is a collinear ion-oxygen-hydrogen arrangement; *top* is a rather different geometric configuration which remarkably has almost the same energy profile as *trans*, and in which the ion approaches the water molecule perpendicular to the molecular plane and towards the oxigen; C_{2v}-*back* and *cis* have been included for completness, since they have dissociative profiles and therefore will be rather unprobable; in C_{2v}-*back* the water molecule has been inverted with respect to C_{2v}-*face* and in *cis* the water molecule has been inverted with respect to *trans*.

The distance of maximum approach has been determined in each case as that in which the interaction energy is ≈ 10 k_BT, what guarantees that no shorter distances will be reached during a typical liquid state simulation. This criterion results in a "radius" slightly smaller than 1.5 Å for C_{2v}-*face*, *trans* and *top* configurations, what seems a safe estimation since it is substantially smaller than the shortest distances found (≈ 1.7 Å) in Molecular Dynamics simulations of Li^+ in water for a broad range of thermodynamic conditions [99] (using an effective potential). This minimal distance for C_{2v}-*back* and *cis* was chosen to be 4 Å. Compared with a real cation, the point charge approximations is virtually exact down to 3 Å for C_{2v}-*back* and *cis* (the distance at which the solid and dashed lines start to diverge), and down to 2.5 Å for C_{2v}-*face*, *trans* and *top*. These values can be taken as indicative of the closest distances where the induced dipole moments computed here faithfully represent those of the real ion-molecule dimer.

The first five panels in Fig. 8.2 display the modulus of the total dipole moment of the water molecule for each of the chosen orientations (the last panel displays the x component of the induced dipole moment for the *top* configuration). In each case, the results are shown only for the physically relevant range (see above). Vertical dashed lines indicate the distance at which the potential energy profiles obtained for the ion or for a point charge are still indistinguishable. Each plot includes the ab initio result together with the best point dipole, shell and fluctuating charge models. Before discussing each one in turn, several things can be observed at the outset. First, inspection of the shortest distances shows that induced dipoles can substantially exceed the permanent dipole moment (1.85 D) (with total dipole moments that reach up to 4.5 D for the most probable orientation, *i.e.* an induced dipole of 2.65 D), what highlights the importance of including polarization in order to properly describe these strong induction

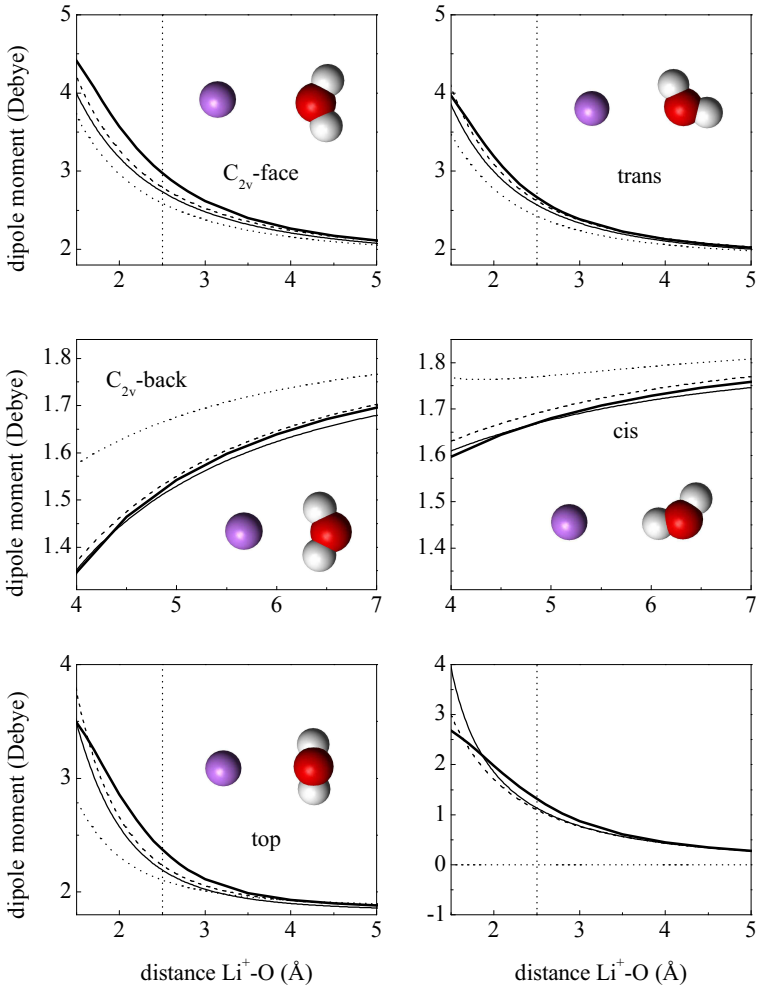

Figure 8.2. Water-monovalued charge: total dipole moments for representative configurations (sketched in the insets). Ab initio (thick solid line), shell model (thin solid line), point dipoles (dashed line), fluctuating charges (dotted line). The last panel displays the x component of the induced dipole moment for the *top* configuration. Vertical dashed lines indicate the distance at which the point charge model of the ion is still accurate.

effects. Conversely, inspection at larger distances shows that all methods are interchangeable from a distance of 4-5 Å (*i.e.* two molecular radius), which signals the distance from which the linear polarizability approximation is virtually exact. Regarding the performance of each method, the shell and point dipole method reproduce fairly well the ab initio profiles, the latter method coming even closer at the shortest distances. Finally, another important conclusion can be already drawn: when compared with the ab initio results, no overestimations are observed

for any of the polarization methods. This is in line with the conclusion obtained for water dimers [67], according to which the high dipole moments obtained in molecular dynamics simulations of polarizable water using the point dipole approximation cannot be ascribed to a failure of the method. Actually, this notion is considerably reinforced here since it is tested close to a monovalent ion for several polarization methods. If any, the only noticeable deviation goes in the opposite direction and is to be found at intermediate distances (2-3 Å), for which the ab initio results predict slightly higher induced dipoles than those obtained with the phenomelogical methods. This discrepancy will be shown to be stronger for higher ionic charge or molecular polarizability, and is thus ascribed to nonlinear polarization (not reproducible by the classical methods tested here), which in this case is only barely noticeable. Finally, concerning the validity of the present results for a real ion-molecule dimer, all the above conclusions are equally valid for distances larger than those indicated by vertical dashed lines.

We now turn to a case per case analysis of each polarization method, although given the large number of models studied, only the main aspects will be included (for the best models). The point dipole models can be classified in two distinct groups: those with one point dipole and those with three dipoles. Within the first group the differences lie in the position of the dipole. Several possibilities have been tried: the oxygen site [30, 40], the center of mass [29, 47] and, finally, those that locate it on the M site [48], with oxygen-M distances that can be varied [67]. From the comparison (not included) of all these models, and again in line with the results for the water dimer [67], the best accord with the ab initio profiles is obtained when the point dipole is located on an M site, with a distance of approximately 0.2 Å from the oxygen. Therefore the single-dipole models reported in Ref. [48] and (the best model) in Ref. [67] provide an optimal representation of the molecular induced dipole on the water molecule (and will be denoted PDM). Actually, a single point dipole model is optimal since none of the models with three point dipoles that have been tried is able to outperform it. A comparison between the best one-dipole and three-dipoles models, for a selected number of orientations, is displayed in Fig. 8.3. Several three point models have been tried (with parameters summarized in Table 8.3), which include two new optimized models (PD1-H2O and PD2-H2O, described in section 8.1.2). The best model with three dipoles is PD2-H2O, and although its description of the induced dipole is excellent in all cases (Fig. 8.3), it is still slightly worse than a one-dipole model at contact. This is good news from the simulation point of view since there

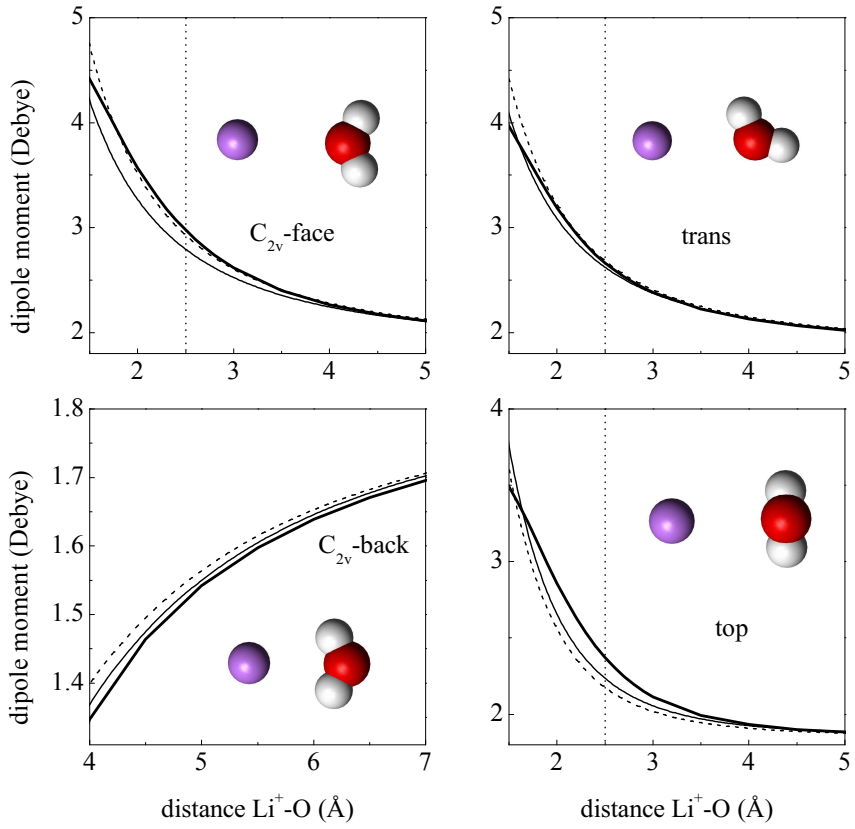

Figure 8.3. Water-monovalued charge: comparison of the best results using point dipoles. Ab initio (thick solid line), PDM (thin solid line) and PD2-H2O (dashed line).

is no need to include more than one dipole per molecule, although it is somewhat surprising given that PD2-H2O displays the exact experimental anisotropic polarizabilities (see Table 8.2) in contrast with the isotropic polarizabilitiy of a one dipole model.

Regarding the shell model, the best implementation is the one optimized here (SH-H2O, see Table 8.5 and Table 8.2), and displayed in Fig. 8.2. As stated above its performance is excellent, although it slightly overestimates the induced dipoles at contact, particularly for the *top* configuration (although it is important to recall that such close separations are not observed in MD simulations). The result that a method without anisotropic polarizabilities displays such a good agreement is in line with the results obtained with the point dipole method, according to which a one dipole (isotropic) model is excellent. In this case, contrary to what has been observed for point dipoles, the shell model performs better if the polarizability

on hydrogens is included.

Finally, both fluctuating charge models are clearly inferior to optimized shell or point dipole models for all configurations, as can be seen in Fig. 8.2 (where only the best one, SPC-FQ, is displayed). It is known that the main failure is to be expected for the *top* configuration, as displayed in the sixth panel of Fig. 8.2. There, instead of the total dipole moment, only the component of the induced dipole moment along the x axis is plotted (flat dashed line), showing that the fluctuating charge model yields a null induced dipole perpendicular to the molecular plane, while the other two methods predict the right ab initio result at all distances. Again, as for the other orientations, this induced dipole is substantial (up to 2.5 D) and certainly cannot be considered a small discrepancy. However, the fluctuating charge model can predict part of the *total* dipole in the *top* configuration (ion perpendicular to the molecular plane), since such configuration also induces some polarization on the molecular plane due to the hydrogen sites polarizability (fifth panel in Fig. 8.2). Moreover, in all other configurations (first four panels in Fig. 8.2) the fluctuacting charge models underestimate the induced dipole moment as well, what is consistent with the fact that both have a mean molecular polarizability which is approximately 20 % lower than the experimental one. This underestimation is not only due to neglecting the perpendicular component but also to a low in-plane polarizability along the direction perpendicular to the molecular dipole (y axis), which is roughly half of the experimental value. It is also the case that the polarizability along the dipole axis (z) is substantially higher than the experimental one. While it would be relatively easy to get the correct experimental polarizabilities along the y and z axis by optimizing the parameters in Eqs. 8.7, 8.8, the fact that no improvement is possible for the x axis precludes this option. It is obvious that a higher number of sites is required for a real improvement (or the use of a mixed model) with the consequent computational burden in MD simulations, and that this is probably not worth being pursued given the success of, for instance, point dipole models with only one dipole.

8.3.2 Carbon Tetrachloride

Its much higher polarizability (10.5 Å^3 compared with 1.4 Å^3 for water), together with its spherically symmetric polarizability, make this molecule an ideal case to study the limits of some of the conclusions drawn from water. Fig. 8.4 displays the Li^+-CCl_4 energy profiles computed for several molecular orientations

(full lines), together with the corresponding profiles for the point charge approximation (dashed lines). Three molecular orientations have been studied (with sketches included in Fig. 8.5), with two of them being almost equally stable (as shown in Fig. 8.4): in the *face* configuration the ion occupies a position above the center of the triangle defined by three chlorine atoms and its minimum occurs at the shortest distance ($\approx$ 2.5 Å), in the *edge* configuration the ion sits above the line between two chlorine atoms with the minimum at a somewhat larger distance ($\approx$ 3 Å). It is noteworthy that the well depth in both cases is not far from that of the water-dimer (see Fig. 8.1), showing that electrostatic interactions due to induced dipoles are not per se weaker than interaction energies from permanent ones (a phenomenon that is known to occur in other cases, see Sec. 15 in Ref. [86]). Finally, for the *corner* configuration, with a colinear ion-chlorine-carbon alignment, the well is shallower and occurs at a larger distance ($\approx$ 4 Å). Concerning the accuracy of the point charge approximation for the ion, it is virtually exact down to 4.5 Å for the *corner* configuration and down to 3.5 Å for the *face* and *edge* orientations. The distance of maximum approach is $\approx$ 1.8 Å for the *face* configuration, $\approx$ 2.2 Å for *edge*, and $\approx$ 3.6 Å for *corner* (note the different origins of the horizontal axis in Fig.8.5).

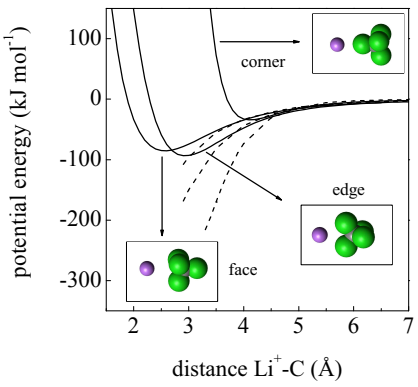

Figure 8.4. Ab initio potential energy curves for Li^+-CCl_4 (solid lines) and for (+)-CCl_4 (dashed lines).

The results from several models are displayed in Fig. 8.5. We first note that the ab initio calculations predict rather high induced dipole moments (of up to 8 D for the *corner* configuration), much larger than those of the water molecule, and roughly one order of magnitude larger than those in neat liquid CCl_4 (which have a mean value of 0.19 D and a maximum value of $\approx$ 0.7 D, see Ref. [84]). From the preceding analysis of the water molecule, and the spherical symmetry of CCl_4, one may think that only one point dipole (with the molecular polarizability) located on the carbon site might be adequate. Indeed, this model is fairly reasonable for distances for which the point charge approximation for the ion is accurate (vertical dashed lines). However, and as displayed in Fig. 8.5, such model would produce strong divergences at short distances, particularly for the most stable configuration (*face*). For this orientation

the single point dipole model overestimates the induced dipole for all distances. Therefore, the optimal model for water performs rather poorly for carbon tetrachloride, indicating that the selection of a model should be decided on a case per case basis. Although a definitive conclusion will require computing the total dipole moment for the ion-molecule complex, the low polarizability of the lithium ion (the only aspect that is not included here), as compared with that of CCl_4, strongly suggests that the present conclusion will not change appreciably. The natural choice is then a model with point dipoles on each atomic site. The only available model is that proposed in Ref. [69] and used in MD simulations of the neat liquid and ionic solutions in Ref. [9] (see Sec 8.1.2 and Table 8.4). From the third panel in Fig. 8.5, we see that it is rather accurate for the *corner* configuration at all distances. This good degree of accord is reduced for the *edge* configuration and gets even poorer for the *face* configuration, so that the performance reduces for the most probable configurations. Also in Fig. 8.5 the results from a fluctuating charge model [84] are included. Its performance is almost identical to the five point dipole model that has been just discussed.

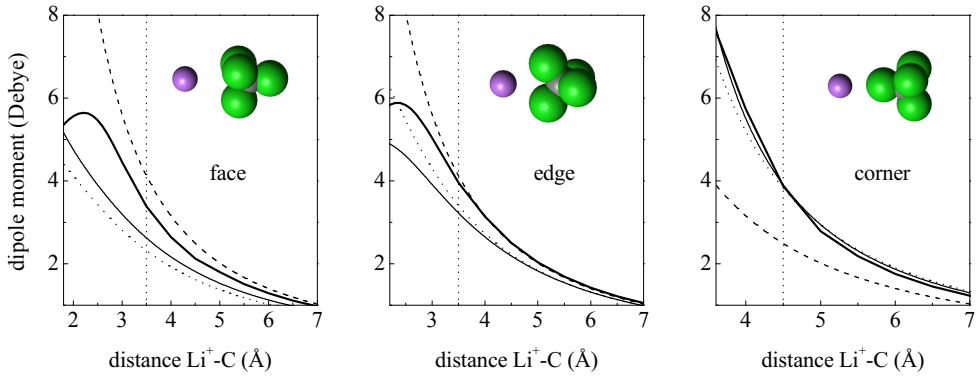

Figure 8.5. CCl_4-monovalued charge: total dipole moments for representative configurations. Ab initio (thick solid line), point dipole of Ref. [69] (thin solid line), PD-central (dashed line) and fluctuating charges (dotted line). Vertical dashed lines indicate the distance at which the point charge model of the ion is still accurate.

On the basis of the polarizability formulas for CCl_4 (Eqs. 8.9,8.18,8.24) we have optimized each method for the two most probable configurations (*face* and *edge*). Remarkably, no optimization of the fluctuating charge model is possible. From Eq. 8.9 we have that α_{CCl4} only depends on the difference $J^o_C - J_{ClCl}$, so that these two parameters have to be increased or decreased proportionally, in

order to keep the difference (and therefore the molecular polarizability) constant. Following this procedure, no changes are observed on the curves displayed in Fig. 8.5. Since this method fails particularly for the most probable configuration (*face*) we conclude that, as in the case of water, it has the worst performance and that, again, a more complex approach (with more point charges or mixed methods) is required in order to be comparable with the shell or point dipole methods. Together with the aforementioned difficulties for planar molecules and atomic ions, and despite its computational convenience, it seems fair to conclude that it should not be recommended as the method of choice if an accurate and fast calculation of induced dipoles is required.

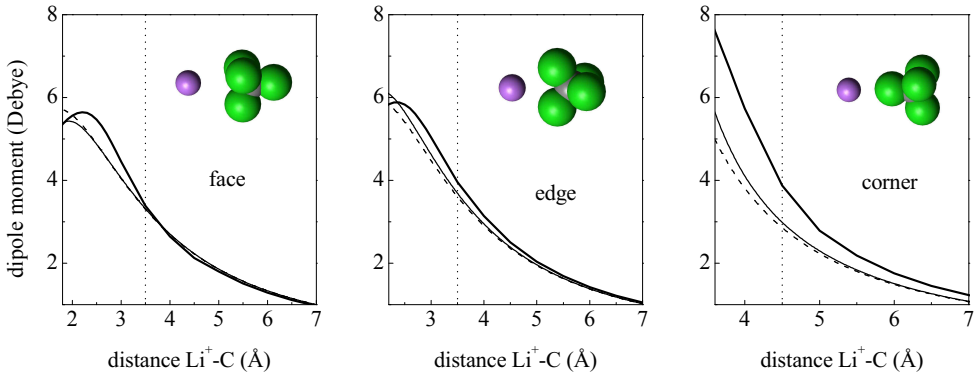

Figure 8.6. CCl_4-monovalued charge: comparison of the best models. Ab initio (thick solid line), point dipole PD-CCl4 (thin solid line) and SH-CCl4 (dashed line).

Regarding the optimized shell and point dipoles methods, the results are displayed in Fig. 8.6. Parameters for the optimized shell model (SH-CCl4) are reported in Sec. 8.1.3, and those for the optimized point dipole (PD-CCl4) are given in Table 8.4. It can be seen that now they both satisfactorily reproduce the ab initio curves for the most probable configurations (*face* and *edge*), what highlights the importance of parameter optimization for each molecule in order to get the maximum performance, while at the same time keeping the behaviour at long distances (molecular polarizability) intact. It is interesting to note that this optimization process, in the case of point dipoles, leads to a *negative* polarizability located on the carbon site (see parameters in Table 8.4). This possibility, which to our knowledge has never been considered before [69], can be physically motivated if one considers that the main deficiency of the point dipole method lies in its inability to model intramolecular charge transfer. We see, as

a result of the optimization process, that by using negative polarizabilities (for a *buried* atom), this approach is able to mimic alternating partial charges in a molecule that result from polarisation by an ion. The fact that an ion often induces alternating changes in atomic partial charges if, for example, positioned on one end of a hydrocarbon molecule, is known since a long time. Semiempirical calculations that showed such results were among the first ones in coordination chemistry [100]. Finally, for the less probable configuration (*corner*) both methods underestimate the induced dipole (by a ≈ 25 % in the worst case). It is to be noted that this stronger disagreement occurs for the configuration in which higher dipole moments are induced: for *face* and *edge* the maximum induced dipole is 6 D, while it goes up to almost 8 D for *corner*. As in the (much less pronounced) case of water close to lithium, where the ab initio curve is slightly above each method at intermediate distances, a likely explanation is that there are nonlinear polarization effects (with the consequent higher induced dipole in the ab initio calculation) that the classical methods are unable to reproduce. It is this particular issue that will be the focus of the next section.

8.4 Molecule close to divalent charge

The models for water and for carbon tetrachloride that have been found to accurately reproduce the dipole moment close to a (point charge) lithium ion will be now tested in the environment of the (point charge) magnesium ion. No further optimization is now possible, any disagreement that may appear will signal unavoidable deficiencies of simple polarization methods, that would need to be addressed with *ad hoc* improvements.

8.4.1 Water

A single point dipole located on a M site close to the oxygen or, to a lesser extent, a three point shell model, are the simplest models that accurately predict the induced dipole of a monvalued charge for all relevant distances (see Sec. 8.3). Only these two optimal methods will be now compared with the ab initio results for a divalent point charge. Fig. 8.7 displays the Mg^{++}-H_2O energy profiles computed for several molecular orientations (full lines), together with the corresponding profiles for the point charge approximation (dashed lines). Qualitatively the results are very similar to those for the monovalent charge: C_{2v}-*face* is the

most stable configuration (with the well depth increasing by about a factor of 2 with respect to the corresponding curve for Li^+), *top* and *trans* have similar but shallower attractive profiles, while *cis* and C_{2v}-*back* are dissociative. Concerning the accuracy of the point charge approximation it is virtually exact down to 3 Å for all configurations displayed in Fig. 8.7. The distance of maximum approach is of roughly 1.3 Å for C_{2v}-*face* and *trans* configurations, increases to ≈ 1.5 Å for *top* and, finally, is of about ≈ 2.3 Å for C_{2v}-*back*.

The results for the total dipole moment are displayed in Fig. 8.8. Each plot includes the ab initio result together with the best point dipole and shell models. Notice that in the case of the C_{2v}-*back* configuration the point dipole which is directed towards the ion at long separations, reverses its direction at ≈ 3.5 Å due to the contribution of the induced dipole, yielding negative values at shorter distances. Vertical dashed lines indicate the distance at which the potential energy profiles obtained for the ion or for a point charge are still indistinguishable. Although still not substantial, marked divergences already exist at these separations (where the point charge approximation for the ion is exact) between the ab initio and classical polarization methods (themselves almost identical within all the range). These differences grow for smaller distances, although at the shortest separations the ab initio curves display a turnover (with a maximum of ≈ 8 D for the total dipole), what allows the classical methods to come closer again to the ab initio results (except for the C_{2v}-*back* configuration, due to a larger contact distance).

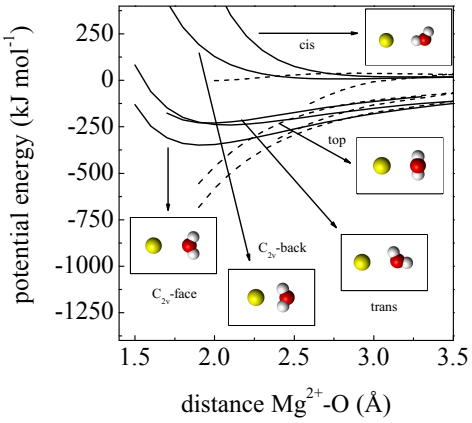

Figure 8.7. Ab initio potential energy curves for Mg^{2+}-H_2O (solid lines) and for (++)-H_2O (dashed lines).

Regarding the interpretation of these results, we first note that for distances larger than 4-5 Å both methods provide highly accurate results, confirming the good performance of classical polarization methods for distances larger than about two molecular diameters (as observed for the Li^+-H_2O dimer). However, for smaller distances the performance is not as good as for the monovalent charge. The differences between classical an ab initio results can be rationalized as re-

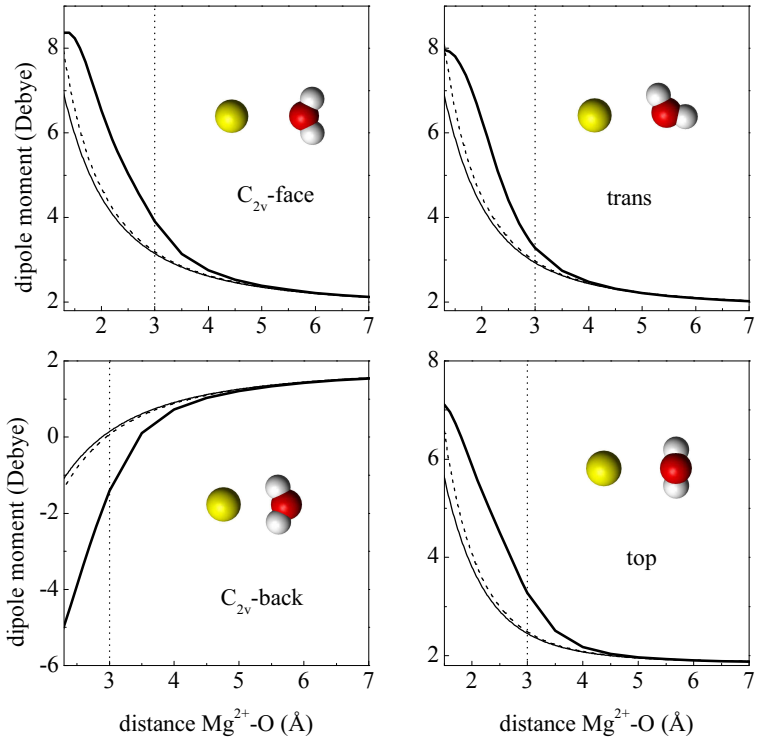

Figure 8.8. Water-divalent charge: comparison of the best models. Ab initio (thick solid line), SH-H2O (thin solid line) and PDM (dashed line).

sulting from two sources, depending on the separation.

First, the underestimation of the induced dipole at "intermediate" separations (1.5-4 Å) should probably be ascribed to the lack of nonlinear contributions in the classical methods (hyperpolarizability), to a higher degree than what has already been observed in the analysis for the monovalent charge. Here the difference can go up to 2 D between the ab initio and classical curves (a substantial 50 % in some cases, while for the *edge* configuration of the Li^+-CCl_4 dimer it was of about 30 % in the worst case). Nonlinear effects can be better appreciated if we compare, for a fixed distance, the dipole induced by a monovalent charge with that induced by a divalent one. We take the case of the C_{2v}*-face* configuration for the ion-water dimer, with the distance fixed at 2 Å (that is, the most probable orientation close to the minimum of the corresponding potential energy profile, see Figs. 8.1 and 8.7). The total ab initio dipole for a lithium-water dimer is 3.57 D, *i.e.* an induced dipole moment of 1.72 D (given that water has a permanent dipole of 1.85 D). For the magnesium-water pair we get 6.53 D for the total ab initio dipole, *i.e.* and

induced dipole of 4.68 D. The crucial point is that the latter is a factor 2.7 larger (compared to 1.72 D), while the charge has only increased by a factor of 2. If we now turn to the corresponding results obtained with the best classical model (PDM, which has one point dipole located at the M site), we find that the induced dipole is 1.4 D for the lithium-water dimer and 2.8 D for the magnesium-water dimer. Therefore, the induced dipole increases by exactly a factor of 2 when the charge is doubled, consistent with the expected linear behaviour. In conclusion, it does not seem possible that any of the (linear) polarizable models studied is capable of reproducing the nonlinear increases with charge predicted by ab initio calculations.

Second, at separations close to contact the ab initio curves go through a maximum and slightly decrease at the closest separations, while the classical curves continue increasing. This damping that is here observed for the ab initio calculations supports the notion that a decrease of atomic polarizabilities at short distances should be expected due to the overlap of electronic charge distributions [42]. The better accord with the classical methods that is observed at contact is probably fortuituous, in the sense that polarization methods seem to perform better while they do not contain any mechanism to mimick electronic overlap. These results stem from two opposing trends: the underestimation at "intermediate" distances and the overestimation that can be expected at very short distances (in most cases classical methods tend to diverge for unphysically short separations). Put another way, if the classical methods would have yielded a better accord at intermediate distances, then one should expect to find divergences at contact. In this connection, it is important to note that no divergences are found at contact separations even for this doubly charged ion, while they would probably appear in any method that would include nonlinear effects (what would require the use of damping schemes).

8.4.2 Carbon Tetrachloride

Finally, we turn to CCl_4, for which it is to be expected that the features just discussed may become even more evident. Fig. 8.9 displays the energy profiles computed for several molecular orientations (full lines), together with the corresponding profiles for the point charge approximation (dashed lines). Again, the qualitative results for the Mg^{++}-CCl_4 profiles are very similar to those for Li^+. The *face* and *edge* configurations have almost the same stability, albeit the well depth has increased by *more* than a factor of 3 (while the charge has only been

doubled). The *edge* configuration also increases its well depth although, again, its position is located at a much larger distance and is therefore less probable. In contrast with all previous examples, there is a substantial disagreement with the point charge approximation for the ion (dashed lines) at all distances. Consequently, the comparison with ab initio results will only apply for the point charge-CCl_4 system. The distances of maximum approach barely change compared to those reported in Sec. 8.3.2.

Fig. 8.10 displays the results from the ab initio calculations together with those from the optimized point dipole (PD-CCL4) and shell (SH-CCl4) models (see Sec. 8.3.2). The most remarkable aspect probably is the huge induced dipole moments predicted by the ab initio calculations, which go up to 25 D for the *edge* configuration. Certainly, these results correspond to the point charge-CCl_4 system and will have to await confirmation from a computation for the real Mg^{++}-CCl_4 dimer. Concerning the point that is of interest here, the comparison of the induced dipoles between ab initio and classical methods for a point charge, the basic results obtained for water are here reinforced. Basically, classical methods produce exact results for distances larger than one molecular diameter [101] ($\approx$ 5 Å), and underestimate the ab initio results for shorter distances. In this case the underestimation can be as large as a 50 %. Again the ab initio results display a turnover for the closest distances, which in this case the classical methods are able to mimick to a certain extent. Again, there are no signs of divergence for the classical methods at contact separations, and no significant differences exist between point dipoles or shell models.

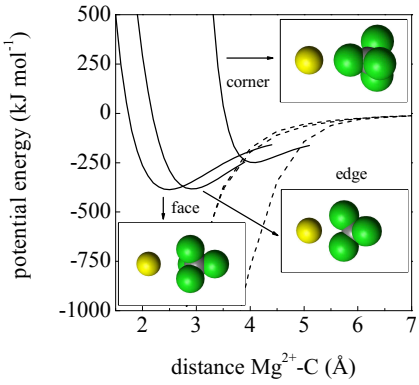

Figure 8.9. Ab initio potential energy curves for Mg^{2+}-CCl_4 (solid lines) and for (++)-CCl_4 (dashed lines).

8.5 Conclusions

To summarize, the point dipole or shell models are remarkably accurate at all distances in the vicinity of a small monovalent charge. The analysis close to a divalent charge (or to a monovalent charge for highly polarizable molecules) suggests that the inclusion of hyperpolarizability might be required to cure the

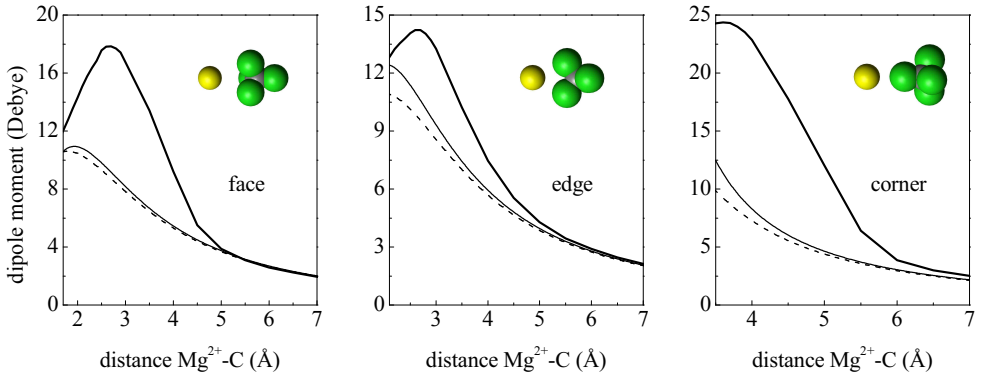

Figure 8.10. CCl_4-divalent charge: comparison of the best models. Ab initio (solid bold line), PD-CCl4 (thin solid line) and SH-CCl4 (dashed line).

underestimation of the dipole moment at intermediate distances. It should be noted that in no case is damping required, so that the use of damping schemes based on divergences taking place during MD simulation of the liquid phase does not seem justified on physical grounds. Actually, in most configurations classical polarization methods tend to underestimate the induced dipole.

The present results discourage the use of the fluctuating charge method. Besides its known limitations for planar molecules and atomic ions, it has been shown that for carbon tetrachloride (a spherical molecule with five sites) it cannot describe, even if optimized, the induced dipole for the most probable molecular orientation. While a better performance might probably be obtained using a higher number of site charges, this solution is in conflict with the requirements of efficiency in MD simulations. In contrast, the point dipole and shell models display a high degree of flexibility, what has allowed to optimize their parameters and obtain a much better accord with ab initio calculations than would be possible by simply using transfereable sets of parameters. In this sense, given the present feasibility of an ab initio analysis for each molecule of interest, it is probably advisable to perform a case per case parameter optimization instead of using reduced sets of atomic parameters which, although yielding acceptable results for wide a range of molecules, are not able to exploit the full capabilities of simple polarization methods. The example of the point dipole method applied to carbon tetrachloride illustrates this point: while it is improbable that a negative polarizability for the carbon atom is transfereable, it is the one that yields the best accord with ab initio results for this particular molecule. Following this

approach, and for the cases studied, the use of mixed methods does not seem necessary, specially considering that they do not seem to have the potential to reproduce nonlinear effects either.

Certainly, it is necessary to check whether the present conclusions hold for the real ion-molecule dimer and for this purpose the total induced dipole will be computed ab initio and with classical methods that include ion polarizability. No substantial changes are anticipated, though, given the low cation polarizability and the fact that the basic conclusions already hold in the region where the point charge approximation for the ion is highly accurate. Assuming that this is the case, schemes for including nonlinear effects will be studied. In this connection, although damping schemes seem not to be required in the cases studied here, if an additional nonlinear polarization is included, it might actualy require the use of damping at contact. Finally, given the very good accord obtained with ab initio calculations for dimers in the gas phase, it seems essential to ascertain the possible variations of polarizability that may take place in condensed phase [102–104], since at the present level of accuracy they may constitute the limiting factor in order to get a satisfactory representation of many body effects in the condensed phase.

8.6 Appendix

Here we outline the derivation of one of the polarization tensor components (α_{zz}) for the case of water. It should be reminded that the z axis is directed along the water symmetry axis, bisecting the angle between both oxygen-hydrogen stretches, with the origin located on the oxygen site (or the auxiliary site M characteristic of TIP models). Only the cases of fluctuating charges and point dipoles will be addressed, as the general expression for the shell method is already derived in Sec. 8.1.3.

8.6.1 Fluctuating charges

The molecular dipole moment in the z direction is given by $(q_{H_1} + q_{H_2})d\cos(\theta/2)$, where d denotes the O-H bond length and θ the bending angle. If the set of Eqs. 8.4 is particularized for this case (only the equation for one of the two hydrogens is given), we obtain

$$\chi_H + J^o_H q_{H_1} + J_{H_1H_2} q_{H_2} + J_{HO} q_O - d\cos(\theta/2)E = \chi$$

$$\chi_O + J_O^o q_O + J_{HO} q_{H_1} + J_{HO} q_{H_2} = \chi$$
$$q_O + q_{H_1} + q_{H_2} = 0.$$

Together with the fact that both hydrogens have the same charge ($q_{H_1} = q_{H_2}$), it is straightforward to obtain for the *induced* charge on each hydrogen

$$q_H^{ind} = \frac{Ed\cos(\theta/2)}{J_H^o + J_{H_1H_2} + 2J_O^0 - 4J_{HO}}.$$

The induced dipole in the z direction is thus given by

$$p_z^{ind} = 2q_H^{ind} d\cos(\theta/2) = \frac{E2d^2\cos^2(\theta/2)}{J_H^o + J_{H_1H_2} + 2J_O^0 - 4J_{HO}},$$

from which α_{zz} is readily identified [43] (see Eq. 8.8).

8.6.2 Point dipoles

Under the effect of an external field in the z direction there are in principle nine induced dipole cartesian components to be determined, which are reduced to only three due to symmetry considerations: the z component of the oxygen dipole moment (p_z^O), the z component of the hydrogen dipoles ($p_z^{H_1}$ and $p_z^{H_2}$, which will be equal), and possibly the y components of the hydrogen dipoles ($p_y^{H_1}$ and $p_y^{H_2}$, again equal in magnitude but of opposite signs).

We can compute for instance p_z^O expanding formula 8.14 and retaining terms different from zero

$$\begin{aligned} p_z^O &= \alpha_O \left[E + (T_{O-H_1})_{zz} p_z^{H_1} + (T_{O-H_1})_{zy} p_y^{H_1} + (T_{O-H_2})_{zz} p_z^{H_2} + (T_{O-H_2})_{zy} p_y^{H_2}\right] = \\ &= \alpha_O \left\{E + \left[(T_{O-H_1})_{zz} + (T_{O-H_2})_{zz}\right] p_z^{H_1} + \left[(T_{O-H_1})_{zy} - (T_{O-H_2})_{zy}\right] p_y^{H_1}\right\}. \end{aligned}$$

From Eq. 8.12, the polarization tensor components are

$$(T_{O-H_1})_{zz} = (T_{O-H_2})_{zz} = \frac{1}{d^3}\left[3\cos^2(\theta) - 1\right]$$
$$(T_{O-H_1})_{zy} = -(T_{O-H_2})_{zy} = \frac{3\cos(\theta)\sin(\theta)}{d^3},$$

which if inserted in the expression for p_z^O yield

$$p_z^O = \alpha_O \left[E + \frac{2}{d^3}(3\cos^2(\theta) - 1) p_z^{H_1} + \frac{6\cos(\theta)\sin(\theta)}{d^3} p_y^{H_1}\right].$$

In a similar way corresponding expressions can be derived for the other two components

$$p_z^{H_1} = \alpha_H \left[E + \frac{3\cos^2(\theta) - 1}{d^3} p_z^O - \frac{1}{8d^3\sin^3(\theta)} p_z^{H_1}\right]$$
$$p_y^{H_1} = \alpha_H \left[\frac{3\cos(\theta)\sin(\theta)}{d^3} p_z^O - \frac{1}{4d^3\sin^3(\theta)} p_y^{H_1}\right].$$

From the last three equations it is straightforward to express the dipole components in terms of E. When inserted in the expression for the total dipole moment ($p_z = p_z^O + 2p_z^{H_1}$), α_{zz} is readily identified (see Eq. 8.17).

References

[1] A. van der Vaart, B.D. Bursulaya, C.L. Brooks and K.K. Merz, *J. Phys. Chem. B* **104**, 9554 (2000).

[2] T.A. Halgren and W. Damm *Curr. Opin. Struc. Biol.* **11**, 236 (2001).

[3] S. Patel and C.L. Brooks, *J. Comp. Chem.* **25**, 1 (2004).

[4] P. Cieplak, J. Caldwell and P. Kollman, *J. Comp. Chem.*, **22**, 1048 (2001).

[5] L.X. Dang, J.E. Rice, J. Caldwell and P.A. Kollman, *J. Am. Chem. Soc.* **113**, 2481 (1991).

[6] L.X. Dang and D.E. Smith *J. Chem. Phys.* **99**, 6950 (1993).

[7] W.L. Jorgensen and D.L. Severance, *J. Chem. Phys.* **99**, 4233 (1993).

[8] D.E. Smith and L.X. Dang, *J. Chem. Phys.* **100**, 3757 (1994).

[9] T.M. Chang, K.A. Peterson and L.X. Dang, *J. Chem. Phys.* **103**, 7502 (1995).

[10] S.J. Stuart and B.J. Berne, *J. Phys. Chem.* **100**, 11934 (1996).

[11] M.A. Carignano, G. Karlström and P. Linse, *J. Phys. Chem. B*, **101**, 1142 (1997).

[12] T.M. Chang and L.X. Dang, *J. Phys. Chem. B*,**101**, 10518 (1997).

[13] A.A. Chialvo, P.T. Cummings, J.M. Simonson and R.E. Mesmer *Fluid Phase Equilib.* **150-151**, 107 (1998).

[14] L.X. Dang *J. Chem. Phys.* **113**, 266 (2000).

[15] S. Nagakawa, *J. Phys. Chem. A* **104**, 5281 (2000).

[16] G.H. Peslherbe, B.M. Ladanyi and J.T. Hynes, *J. Phys. Chem. A* **104**, 4533 (2000).

[17] J.M. Martínez, J. Hernández-Cobos, H. Saint-Martin, R.R. Pappalardo, I. Ortega-Blake and E. Sánchez Marcos *J. Chem. Phys.* **112**, 2339 (2000).

[18] S. Koneshan, J.C. Rasaiah and L.X.Dang, *J. Chem. Phys.* **114**, 7544 (2001).

[19] R. Ayala, J.M. Martínez, R.R. Pappalardo, H. Saint-Martín, I Ortega-Blake and E. Sánchez Marcos *J. Chem. Phys.* **117**, 10512 (2002).

[20] R. Fischer, J. Richardi, P.H. Fries and H. Krienke, *J. Chem. Phys.* **117**, 8467 (2002).

[21] E. Oyen and R. Hentschke, *Langmuir* **18**, 547 (2002).

[22] M. Kubo, R.M. Levy, P.J. Rossky, N. Matubayasi and M. Nakahara, *J. Phys. Chem. B* **106**, 3979 (2002).

[23] R. Ayala, J. M. Martínez, R.R. Pappalardo and E. Sánchez Marcos, *J. Chem. Phys.* **119**, 9538 (2003).

[24] M. Carrillo-Tripp, J. Saint-Martin and I. Ortega-Blake, *J. Chem. Phys* **118**, 7062 (2003).

[25] A. Grossfield, P. Ren and J.W. Ponder, *J. Am. Chem. Soc.* **125**, 15671 (2003).

[26] T.V. Nguyen and G. H. Peslherbe, *J. Phys. Chem. A*, **107**, 1540 (2003).

[27] S. Yoo, Y.A. Lei and X.C. Zeng, *J. Chem. Phys.* **119**, 6083 (2003).

[28] M.J. Elrod and R.J. Saykally, *Chem. Rev.*, **94**, 1975 (1994).

[29] P. Barnes, J.L. Finney, J.D. Nicholas and J.E. Quinn, *Nature* **282**, 459 (1979).

[30] P. Alström, A. Wallqvist, S. Engström and B. Jönsson, *Mol. Phys.* **68**, 563 (1989).

[31] A. Wallquist, P. Alström and G. Karlström, *J. Phys. Chem.* **94**, 1649 (1990)

[32] U. Niesar, G. Corongiu, E. Clementi, G.R. Kneller and D.K. Bhattacharya, *J. Phys. Chem.* **94**, 7949 (1990)

[33] J. Caldwell, L.X. Dang and P.A. Kollman, *J. Am. Chem. Soc.* **112**, 9144 (1990).

[34] H. Saint-Martin, C. Medina-Llanos and I. Ortega-Blake, *J. Chem. Phys.* **93**, 6448 (1990)

[35] M. Sprik, *J. Phys. Chem.* **95**, 2283 (1991).

[36] S.B. Zhu, S. Singh and G.W. Robinson, *J. Chem. Phys.* **95**, 2791 (1991).

[37] C. Millot and A.J. Stone *Mol. Phys* **77**, 439 (1992).

[38] L.X. Dang, *J. Chem. Phys.* **97**, 2659 (1992).

[39] R.E. Kozack and P.C. Jordan *J. Chem. Phys.* **96**, 3120 (1992).

[40] A. Wallqvist and B.J. Berne, *J. Phys. Chem.* **97**, 13841 (1993).

[41] J.W. Halley, J.R. Rustad and A. Rahman *J. Chem. Phys.* **98**, 4110 (1993).

[42] D.N. Bernardo, Y. Ding, K. Krogh-Jespersen and R.M. Levy, *J. Phys. Chem.* **98**, 4180 (1994).

[43] S.W. Rick, S.J. Stuart and B.J.Berne, *J. Chem. Phys.* **101**, 6141 (1994).

[44] B.J. Palmer *Chem. Phys.* **184**, 163 (1994).

[45] D. Borgis and A. Staib, *Chem. Phys. Lett.* **238**, 187 (1995).

[46] J.C. Soetens and C. Millot *Chem. Phys. Lett.* **235**, 22 (1995).

[47] A.A. Chialvo and P.T. Cummings, *J. Chem. Phys.* **105**, 8274 (1996).

[48] L.X. Dang and T.M. Chang, *J. Chem. Phys.* **106**, 8149 (1997).

[49] B. Chen, J. Xing and J.I. Siepmann, *J. Phys. Chem. B* **104**, 2391 (2000).

[50] H. Saint-Martin, J. Hernandez-Cobos, M.I. Bernal-Uruchurtu, I. Ortega-Blake and H.J.C. Berendsen *J. Chem. Phys.* **113** 10899 (2000).

[51] B. Guillot and Y. Guissani, *J. Chem. Phys.* **114**, 6720 (2001).

[52] G. Ferenczy and C.A. Reynolds, *J. Phys. Chem. A* **105**, 11470 (2001).

[53] H.A. Stern, F. Rittner, B.J. Berne and R.A. Friesner, *J. Chem. Phys.* **115**, 2237 (2001).

[54] K.H. Cho, K.T. No and H.A. Scheraga, *J. Mol. Struc.* **641** 77 (2002).

[55] C.J. Burnham and S.S. Xantheas, *J. Chem. Phys.* **116**, 5115 (2002).

[56] H. Yu, T. Hansson and W.F. van Gunsteren, *J. Chem. Phys.* **118**, 221 (2003).

[57] P. Ren and J.W. Ponder, *J. Phys. Chem. B* **107**, 5933 (2003).

[58] G. Lamoreoux and B. Roux, *J. Chem. Phys.* **119**, 3025 (2003).

[59] E. M. Mas , *J. Chem. Phys.* **118**, 4386 (2003)

[60] G.A. Kaminski, R.A. Friesner and R.Zhou, *J. Comp. Chem.* **24**, 267 (2003).

[61] Z.Z. Yang, Y. Wu and D.X. Zhao *J. Chem. Phys.* **120** 2541 (2004).

[62] E.M. Yezdimer and P.T. Cummings, *Mol. Phys.* **97**, 993 (1999).

[63] B. Chen, J. Xing and J.I. Siepmann, *J. Phys. Chem. B* **104**, 2391 (2000).

[64] M. Predota, A.A. Chialvo and P.T. Cummings, *Fluid Phase Equilib.* **183-184**, 295 (2001).

[65] H.J.C. Berendsen, J.R. Grigera adn T.P. Straatsma, *J. Phys. Chem.* **91**, 6269 (1987).

[66] W.L Jorgensen, J. Chandrasekar, J.D. Madura, R.W. Impey and M.L. Klein, *J. Chem. Phys.* **79**, 926 (1983).

[67] M. Alfredsson, J.P. Brodholt, K. Hermansson and R. Vallauri, *Mol. Phys.* **94**, 873 (1998).

[68] I. Alkorta, M. Bachs adn J.J. Pérez, *Chem. Phys. Lett.* **224**, 160 (1994).

[69] J. Applequist, J.R. Carl and K.K. Fung, *J. Am. Chem. Soc.* **94**, 2952 (1972).

[70] B.T. Thole, *Chem. Phys.* **59**, 341 (1981).

[71] R. R. Birge, *J. Chem. Phys.* **72**, 5312 (1980).

[72] A.K. Rappé and W.A. Goddard III, *J. Phys. Chem.* **95**, 3358 (1991).

[73] P. Drude, The Theory of Optics, Longmans, New York (1902).

[74] H.H. Loeffler, *J. Comp. Chem.* **24**, 1232 (2003)

[75] R. Armunanto, C.F. Schwenk and B.M. Rode, *J. Phys. Chem. A*, **107**, 3132 (2003).

[76] D. Spangberg and K. Hermansson, *J. Chem. Phys.* **120**, 4829 (2004).

[77] B. T. Thole and P. T. Van Duijnen, *Chemical Physics* **72** (2), 211 (1982); B. T. Thole and P. T. Van Duijnen, *Theoretica Chimica Acta* **55** (4), 307 (1980); P. T. Van Duijnen and J. A. C. Rullmann, *International Journal of Quantum Chemistry* **38** (2), 181 (1990).

[78] A.J. Stone, *Mol. Phys.* **56**, 1065 (1985).

[79] U. Dinur, *J. Phys. Chem.* **97**, 7894 (1993).

[80] H.A. Stern, G.A. Kaminski, J.L. Banks, R. Zhou, B.J. Berne and R.A. Friesner, *J. Phys. Chem. B* **103**, 4730 (1999).

[81] G.A. Kaminiski, H.A. Stern, B.J. Berne, R.A. Friesner, Y. X. X. Cao, R.B. Murphy, R. H. Zhou and T. A. Halgren, *J. Comp. Chem.* **23**, 1515 (2002).

[82] E.L. Sibert III and R. Rey, *J. Chem. Phys.* **116**, 237 (2002).

[83] R. Chelli, S. Ciabatti, G. Cardini, R. Righini and P. Procacci, *J. Chem. Phys.* **111**, 4218 (1999).

[84] E. Llanta and R. Rey, *Chem. Phys. Lett.* **340**, 173 (2001).

[85] E. Llanta, K. Ando and R. Rey, *J. Phys. Chem. B* **105**, 7783 (2001).

[86] C.J.F. Böttcher, *Theory of Electric Polarisation*, 2nd. Edn. (Elsevier, 1973).

[87] D. van Belle, M. Froeyen, G. Lippens and S.J. Wodak, *Mol. Phys.* **77**, 239 (1992).

[88] A. J. Cohen, and Y. Tantirungrotechai, *Chem. Phys. Lett.* **299**, 465 (1999).

[89] P. Hohenberg and W. Kohn, *Phys. Rev.* **136**, B864 (1964); S. H. Vosko, L. Wilk and M. Nusair, *Can. J. Phys.* **58**, 1200 (1980).

[90] A. D. Becke, *Phys. Rev. A* **38**, 3098 (1988); C. Lee, W. Yang and R. G. Parr, *Phys. Rev. B* **37**, 785 (1988).

[91] A. D. Becke, *J. Chem. Phys.* **98**, 5648 (1993).

[92] P. Fuentalba and Y. Simn-Manso, *J.Phys. Chem. A* **101**, 4231 (1997).

[93] D. J. Tozer and N. C. Handy *J. Chem. Phys.* **109**, 10180 (1998).

[94] J. P. Perdew, K. Burke and M. Ernzerhof, *Phys. Rev. Lett.* **77**, 3865-3868 (1996).

[95] A. J. Sadlej, *Theor. Chim. Acta* **79**, 123 (1992)

[96] D. E. Woon and T. H. Dunning Jr., *J. Chem. Phys.* **98**, 1358 (1993); K. A. Peterson, D. E. Woon, and T. H. Dunning Jr., *J. Chem. Phys.* **100**, 7410 (1994).

[97] W. Koch and M.C. Holthausen, A Chemist's Guide to DFT, Wiley-VCH (2001).

[98] A. D. McLean and G. S. Chandler, *J. Chem. Phys.* **72**, 5639 (1980).

[99] M. Masia and R. Rey, *J. Phys. Chem. B* **107**, 2651 (2003).

[100] V. Gutmann, The donor-acceptor approach to molecular interactions, Plenum Press, New York (1978).

[101] R. Rey, L.C. Pardo, E. Llanta, K. Ando, D.O. López, J. Ll. Tamarit and M. Barrio, *J. Chem. Phys.* **112**, 7505 (2000).

[102] A. Morita and S. Kato, *J. Chem. Phys.* **110**, 11987 (1999).

[103] A. Morita, *J. Comp. Chem.* **23**, 1466 (2002).

[104] T. J. Giese and D. M. York *J. Chem. Phys.* **9903**, 120 (2004).

Chapter 9

On the Performance of Molecular Polarization Methods. II. Water and carbon tetrachloride close to a cation.

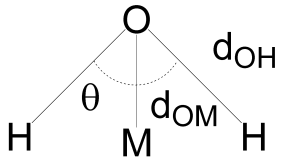

Figure 9.1. Geometrical parameters for water molecule. Site M is represented out of scale for sake of clarity in the drawing.

Molecular polarization methods play a central role in the next generation of force fields for molecular simulations [1–5] and much effort is being devoted to the development of methods and parameters [6–53]. This is mainly due to the fact that it is increasingly important to simulate heterogeneous environments, what requires that a given molecular model is able to provide an environment dependent response. For example, it seems clear that modelling a water molecule with fixed point charges is not adequate to simultane-

POINT DIPOLES				SHELL MODEL	
	PDM	PD1-H2O	PD2-H2O		SH-H2O
d_{OH} (Å)	0.9572	0.9572	0.9572	d_{OH} (Å)	0.9572
d_{OM} (Å)	0.215	0.22	0.0606	d_{OM} (Å)	0.215
θ (degrees)	104.52	104.52	104.52	θ (degrees)	104.52
α_M (Å^3)	1.444	1.42048	1.4099	k_M (kJ mol^{-1} Å^2)	62597.64
α_H (Å^3)	0.0	0.00192	0.0038	k_H (kJ mol^{-1} Å^2)	29096.44
$\bar{\alpha}$ (Å^3)	1.44	1.47	1.47	q_{DM} (e)	8.0
α_{xx} (Å^3)	1.44	1.428	1.415	q_{DM} (e)	0.2
α_{yy} (Å^3)	1.44	1.532	1.528		
α_{zz} (Å^3)	1.44	1.451	1.468		

Table 9.1. Water molecule parameters for the methods studied. The polarizability tensor components of model PD2-H2O are equal to the experimental ones. For the meaning of geometrical parameters we refer to figure 9.1.

ously describe bulk water molecules and those close to hydrophilic or hydrophobic sites. This is more critical if it is considered that a given molecule may visit these environments within the course of the simulation. Therefore, the inclusion of molecular polarizability seems a basic requirement in order to develop transfereable force fields.

Several, rather different, computational approaches have been devised to take into account molecular (and atomic) polarizability. In all cases they are constructed to reproduce the molecular response under homogeneous fields, and are therefore indistinguishable at long intermolecular distances. However, at the short separations typical of liquid state simulation it is not clear whether they are still interchangeable, as they can have different responses to nonhomogeneous fields. While computational convenience has been a major factor to decide which method to use, it is important to investigate if performance at short distances could be a relevant factor. More important might be the fact that all these methods share a common characteristic, basically they are linear methods and as such they can be expected to fail as nonlinear effects become important. In the simple case study of a point charge-molecule interaction this was demonstrated to occur at intermediate distances: as the molecule approaches the increasing electric field of the charge [47, 53] polarization methods consistently underestimate the induced dipole. It will be shown within that as the distance is further reduced (to values typical of first solvation shell molecules) different nonlinear effects set in due to electronic cloud overlapping. This aspect, which obviously could not be addressed for point charge models, will be central to the present work. The problem here is

POINT DIPOLES			SHELL MODEL	
	Ref. [68]	PD-CCl4		SH-CCl4
d_{CCl} (Å)	1.766	1.766	d_{CCl} (Å)	1.766
α_C (Å^3)	0.878	-1.000	k_C (kJ mol^{-1} Å^2)	0
α_{Cl} (Å^3)	1.910	2.880	k_Cl (kJ mol^{-1} Å^2)	13206.0
$\bar{\alpha}$ (Å^3)	10.52	10.52	q_{DCl} (e)	5

Table 9.2. CCl_4 parameters for the methods studied.

just the opposite, polarization methods overestimate the induced dipole as they tend to diverge for decreasing ion-molecule separation, while in the real system there is a decrease of induced dipoles.

In our previous studies [47, 53] (hereafter I and II) we investigated how the most popular polarization methods perform for water or carbon tetrachloride near to a mono- or bi-valent positive point charge. These two molecules were chosen for their almost complementary electrostatic properties. Water is a polar molecule with a moderate anisotropic polarizability ($\bar{\alpha} = 1.47$ Å^3), while CCl_4 is an apolar molecule with a high isotropic polarizability ($\alpha = 10.5$ Å^3). For these two molecules, we found that simple point dipoles (PD) and shell (SH) models available in the literature are the best approaches to reproduce the induced dipole moments (although in some cases they required parameter refitting). Fluctuating charge (FQ) models with charges (only) on each atomic site showed a poorer performance. In tables 9.1 and 9.2 we give a brief description of the best models for both molecules and methods. It is interesting to note that for water a description with a single point dipole (a model termed PDM, see Ref. [27]), although characterised by an isotropic polarizability, is the one that works best in the case of point charges. In general terms, the main conclusion was that for the important case of singly charged ions in water the phenomenological models produced acceptable results for all distances. This satisfactory behaviour is progressively lost as the ion charge and/or molecular polarizability is increased.

With this contribution, we look into the limits of molecular polarization models when the molecule interacts with a polarizable cation instead of a point charge. Since the ions also polarize, the electrostatic property we consider in this study is the first electric moment of the system cation-molecule as a whole [54] which, slightly abusing the nomenclature, will be referred to as total dipole moment (even if this term is only unambiguously defined for a neutral system). To keep the study of different methods (and ion-molecule systems) within a manageable

limit, we will restrict to cases where all polarizable species (ion and molecule) are modelled with the same method. Indeed one could treat each polarizable site with different methods [55] but it is to be expected that, given the essentially similar nature of the various methods available, such approach would not change the essence of our conclusions. Therefore, in this study we compare the accuracy of PD and SH methods, applying them to the whole ion-molecule system. We present the results obtained for a set of mono- and bi-valent cations: Li^+, Na^+, Mg^{2+} and Ca^{2+}. A basic characteristic is that both ionic polarizability and radius increase in the group, and decrease as the ionic charge increases [56–58] (see table 9.3).

	polarizability (Å^3)	charge (e)
(+)	0.0	1.0
Li^+	0.02875	1.0
Na^+	0.14833	1.0
(++)	0.0	2.0
Mg^{2+}	0.0784	2.0
Ca^{2+}	0.522	2.0

Table 9.3. Electrostatic properties of point charges and cations. Calculated polarizabilities taken from Ref. [56–58].

The work of Alfredsson et al. [27] for a water dimer is illustrative of the novel features that the study of ions brings in. As the water dimer separation is varied the PDM model faithfully represents the total dipole moment of the system at all physically reasonable distances [27]. In I and II, though, it was shown that if a water molecule is displaced in the vicinity of a point charge, the PDM model (and other schemes as well) are not able to reproduce the nonlinear increase in dipolar moment obtained in *ab initio* calculations at intermediate and contact separations. While this effect is modest for univalent ions, it becomes more important as the ion charge/molecular polarizability increase. In I and II it was emphasized that, for real ions, these conclusions could only be expected to hold for distances for which the point charge approximation embedded in a rigid sphere is a reasonable model for the ion. This criterion was quantified as the distance at which the potential energy (computed *ab initio*) for the real ion/molecule and point-charge/molecule start to diverge. The study of cations reported here aims to explore this region, so that two new effects will emerge. First, ion polarizability will contribute to the total dipole moment, although given the characteristic low polarizability of cations this effect cannot be expected to alter the conclusions obtained for point charges. Electronic overlap at separations close to contact, though, will represent a substantial change below the limiting distance referred above and its study constitutes the first main theme of the present work. While in the case of the water dimer [27] no particular feature

is found within the range where electronic overlap effects could manifest themselves, this is not the case for cations. A strong damping of the induced dipole moment is found in *ab initio* calculations that the molecular polarization methods are not able to cure without modification, what forces the inclusion of damping schemes: while the neglect of polarization results in underestimations of the dipole moment by roughly a factor of two, the neglect of damping at short separations results in an overestimation of roughly a 30% as well. A detailed discussion of the Thole electric field damping, its relation with polarization methods, and its fine tunning for different ion-molecule dimers will thus constitute the second main theme of this paper. Basically it will be shown that, when used together with the polarization method of choice, it is possible to satisfactorily reproduce the total dipole moment of the complex for all distances and, simultaneously, for different molecular orientations.

The outline of this article is as follows: in section 9.1 we discuss the computational details and the methods used; results and conclusion are given respectively in sections 9.2 and 9.3, while an Appendix summarizes the Thole method for a set of different "flavors".

9.1 Computational details

Different configurations were considered for the ion-molecule system (see figure 9.2). For each arrangement the distance was varied in an interval of ~ 5 Å. The closest distance for each configuration was chosen where the potential energy was ≈ 25 kJ mol^{-1} ($\approx 10 k_B T$ at standard temperature) above the potential energy minimum. In the case of real ions, it is important to note that the closest approach estimated for the dimer at thermal conditions might be larger than that found in the liquid phase to some extent. In the case of Li^+ the minimum distance reached in *ab initio* molecular dynamics simulations of the liquid is 1.7 Å [59], while with the criterium used here we consider distances down to 1.6 Å, which are probably inaccessible in condensed phase. This fact should be kept in mind in order to properly assess the significance of the results at very short distances.

Regarding the definition for the total dipole moment of the ion-molecule dimer, and given that for charged systems the dipole moment depends on the origin of coordinates [54], the position of the ion has been taken as origin of the reference system. In this way, in the limit of zero polarizability for the ion the total dipole moment of the system will be that of the molecule (water or carbon

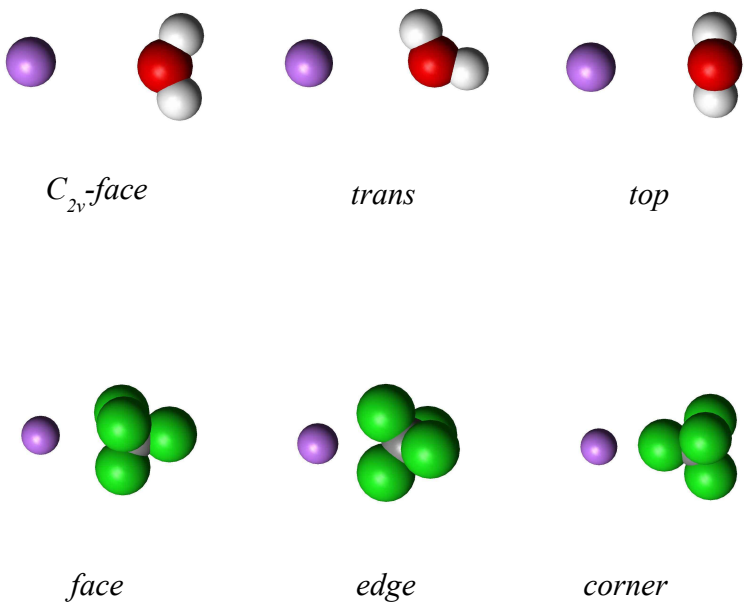

Figure 9.2. Configurations studied for the ion-water (left column) and ion-CCl_4 (right column) systems.

tetrachloride).

9.1.1 Ab Initio Calculations

All quantum chemical calculations where performed with the commercial package Gaussian 03. The B3LYP density functional [60] was used with the aug-cc-pvtz basis set [61,62]. For Mg^{2+} and Ca^{2+} we used a modified cc-pVDZ basis set, from which 3s, 2p and outer shells for Mg^{2+} and 4s, 3p and outer shells for Ca^{2+} were removed to avoid the charge transfer that otherwise occurs in vacuum at intermediate distances when the M^{2+}-X state becomes less stable than the M^{+}-X^{+} state. Counterpoise calculations with the same density functional and basis sets were done for all the systems to compute the ion-molecule potential energy. The density functional used was choosen because it is known to perform well, with estimated errors of 2% or less for the computed dipole moments and polarisabilities [63]. As a hybrid functional it averages between the underestimation of the polarizability typical of Hartree-Fock calculations and the opposite behaviour of pure density functionals. This was also checked by comparing selected calculations with results from Sadleij's basis sets [64, 65] and the PBE1PBE functional [66] The model chemistries used in our calculations demonstrated to be accurate also

in the evaluation of other quantitites of interest [67].

9.1.2 Polarization Methods

A detailed description of polarization methods was given in I. Here we just outline the main features of the two methods used in this work. In the point dipoles method, a polarizability α is associated to one or more sites [68]. The total electric field acting on each site is produced by the external partial charges ($\vec{E}^o$) and by both the intramolecular and external induced dipole moments

$$\vec{E}_i = \vec{E}_i^o + \sum_{j \neq i} T_{ij} \cdot \vec{p}_i, \tag{9.1}$$

where T_{ij} denotes the dipole field tensor, which for a point dipole located at the origin can be written

$$T = 3\frac{\vec{r}\vec{r}}{r^5} - \frac{I}{r^3}. \tag{9.2}$$

The induced point dipole on site i is obtained from the total field according to

$$\vec{\mu}_i = \alpha_i \vec{E}_i, \tag{9.3}$$

and can be computed iteratively until a given threshold of convergence for the induced dipole is reached (we refer to Ref. [5] for issues concerning the efficiency of the different methods for liquid state simulations).

The shell model (also known as Drude oscillator or charge on spring model, see Ref. [5] for suggested nomenclature) is based on a similar approach. Again, a polarizability is assigned to one or more sites. These sites are composed of two charges: one is fixed while the other (q_D) is free to move, linked to the first one via a spring. The sum of both charges is equal to the charge of the atomic site. The spring constant is related to the charge on the moving shell and to the polarizability of the site:

$$k_D = q_D^2/\alpha. \tag{9.4}$$

An advantage of this method is that it is easy to implement in typical molecular dynamics codes, while an important drawback is that it increases the number of interaction sites and therefore the number of relative distances to be computed.

In I we reparameterized standard models for both methods; the values of site polarizabilities were fitted in order to reproduce i) the polarizability tensor of the molecules and ii) the distance dependence of the total dipole moment in the presence of a point charge.

9.1.3 Damping Functions

As it will be shown within, a basic finding is that the methods explored in I and II are unable to reproduce the substantial decrease of the total dipole moment at distances close to contact which is obtained in *ab initio* calculations. A way to deal with this limitation is the inclusion of electrostatic damping, what can be achieved through a reparametrization of the Thole method [69]. In this seminal work it was recognized that in the interacting point dipoles model of molecular polarizability [68] there is a too sharp variation of molecular polarizability with interatomic distances. This is usually illustrated with the diatomic molecule (AB) case, for which the parallel and normal components of its polarizability are proportional to $1/(1-\alpha_A\alpha_B/r^6)$. For $r=(\alpha_A\alpha_B)^{1/6}$ the molecular polarizability diverges and therefore it will be unphysically high in its neighbourhood as well. Thole proposed to address this problem using charge distributions instead of point charges, what results in a damping (see below) of the electric field created by point charges and/or point dipoles. The extend of this damping was fit so that the experimental polarizabilities of a given set of molecules were reproduced satisfactorily. While the mathematical framework will be adopted with few changes, an important difference will be that the method will be implementated recoursing to *ab initio* calculations. The rationale is that given that the method will be applied to *intermolecular* interactions, it is not to be expected that the same parameters found for intramolecular interactions will be optimal in this context, although in some cases it has been transferred without modification to liquid phase simulations due to its ability to eliminate polarization divergences. Here the method will be parametrized so that the *ab initio* dipole moment of the dimer is reproduced all along the ion-molecule distance (with particular emphasis at contact separations) *and* for several orientations of the molecule. These stringent condition is meant to provide some confidence in that the resulting models are physically sound for their use in liquid phase simulations.

A mathematical derivation of the Thole method [69], that impinges on the pair additive nature of this approach and on the fact that is not logically connected with polarization, is given in the Appendix. Here we just give the fundamental formulas required for its implementation. Basically, Eqs. 9.1,9.2,9.3 retain their validity with the only change being that both the electric field created by a fixed charge and/or that created by a point dipole (depending on the molecular model)

are damped by functions $f_1(r)$ and $f_2(r)$

$$\vec{E}^o = f_1(r) \cdot q\frac{\vec{r}}{r^3} \tag{9.5}$$

$$T = f_2(r) \cdot 3\frac{\vec{r}\vec{r}}{r^5} - f_1(r) \cdot \frac{I}{r^3}. \tag{9.6}$$

In the limit of *point* charges and/or *point* dipoles we have $f_1(r) = f_2(r) = 1$, and the usual expressions are recovered. If on the contrary they are thought to be spatially extended, the form of the damping depends on the charge distribution assumed. Thole concluded that a linear decrease of charge density (up to a cutoff, a) was rather ideal for the purpose it had been designed for (fitting of the molecular polarizability). In this approximation we have for the damping functions (see Appendix)

$$f_1(r) = 4\left(\frac{r}{a}\right)^3 - 3\left(\frac{r}{a}\right)^4 \tag{9.7}$$

$$f_2(r) = \left(\frac{r}{a}\right)^4, \tag{9.8}$$

up to the cutoff a (for $r > a$ we simply use the point like expressions for the fields). As noticed by Bernardo et al. [20], the somewhat pathological behaviour at $r = a$ might be problematic in Molecular Dynamics simulations. Although *ad hoc* corrections are possible [20], they complicate the resulting expressions and therefore, other distributions might be more convenient. The most popular alternative seems to be an exponential distribution [28,39,69] (see Appendix), for which the correction factors are

$$f_1(r) = 1 - e^{-(\frac{r}{a})^3} \tag{9.9}$$

$$f_2(r) = 1 - \left[1 + \left(\frac{r}{a}\right)^3\right] e^{-(\frac{r}{a})^3}, \tag{9.10}$$

Finally, while the latter two distribution functions have already been used in the literature, we have also explored the capabilities of using a gaussian distribution function for each charge (see Appendix), given the good performance that such distributions have shown in electronic structure theory. In this approximation the interaction energy has a simple form (as compared for instance with that of an exponential distribution) at the cost of somewhat more complicated correction factors

$$f_1(r) = \mathrm{erf}\left(\frac{r}{a}\right) - \frac{2}{\sqrt{\pi}}\left(\frac{r}{a}\right) e^{-(\frac{r}{a})^2} \tag{9.11}$$

$$f_2(r) = \mathrm{erf}\left(\frac{r}{a}\right) - \frac{2}{\sqrt{\pi}}\left(\frac{r}{a}\right) e^{-(\frac{r}{a})^2}\left[1 + \frac{2}{3}\left(\frac{r}{a}\right)\right]. \tag{9.12}$$

In any of the above possibilites a plays de role of the characteristic distance of maximum approach. This is particularly clear in the example of two charges "dressed" with gaussian distributions (described in the Appendix), where it is shown that a is roughly equal to the sum of the widths of both gaussians (see Eq. 9.15). Obviously the precise value will depend on the functional form chosen, but will be rather similar in all cases (as will be shown within) and close to the sum of atomic radius as one would expect. It should be noted that in the present approach no use of the scaling concept introduced by Thole is made. The original approach would assume the following relation

$$a = w \cdot (\alpha_1 \alpha_2)^{1/6}, \tag{9.13}$$

where α_i denotes the polarizatility of each member of the pair and w was assumed to be a universal adimensional scaling parameter, independent of the pair. While such scaling did work in order to fit the molecular polarizability of a set of molecules, it does not seem possible to extend its validity to the intermolecular interactions studied here. Neither the original value of w, nor any optimization, are able to cope with the stringent requirements described above (reproducing the *ab initio* induced dipole moment for all distances and molecular orientations). In addition, such assumption (Eq. 9.13) is to some extend a source of confusion as it may lead to the idea that the method is dependent on atomic polarizabilities, while indeed (as shown in the Appendix) the relevant physical parameter is the atomic radius. It is the generally monotonic dependence of polarizability on atomic radius which makes these two rather different concepts approximately interchangeable for numerical purposes.

Regarding the flexibility of the method, the above possibilities illustrate the potentially unending variety of functional forms from where to choose from. In addition, the a parameter, as just discussed, can be made dependent on each different pair. In this connection, while the formulas given assume the same value of a for the charge and for the dipole, this is not a necessary condition [28]. If a site contains both a charge and a dipole (a typical scenario for many molecular models), its interaction with an external charge and/or dipole can be characterised by different values of a for the charge-charge, dipole-charge, etc. Despite this potential, in the present case of ion-molecule interaction (which is probably one of the most demanding, particularly for doubly charged ions) it has not been necessary to recourse to such possibility, and the value of a for a given pair of sites is in all cases taken to be unique, i.e. independent of the interaction class.

Finally, in the cases that have been studied, a is very close to the simple sum of atomic radius, therefore easing considerably the task of developing parameter sets for different pairs.

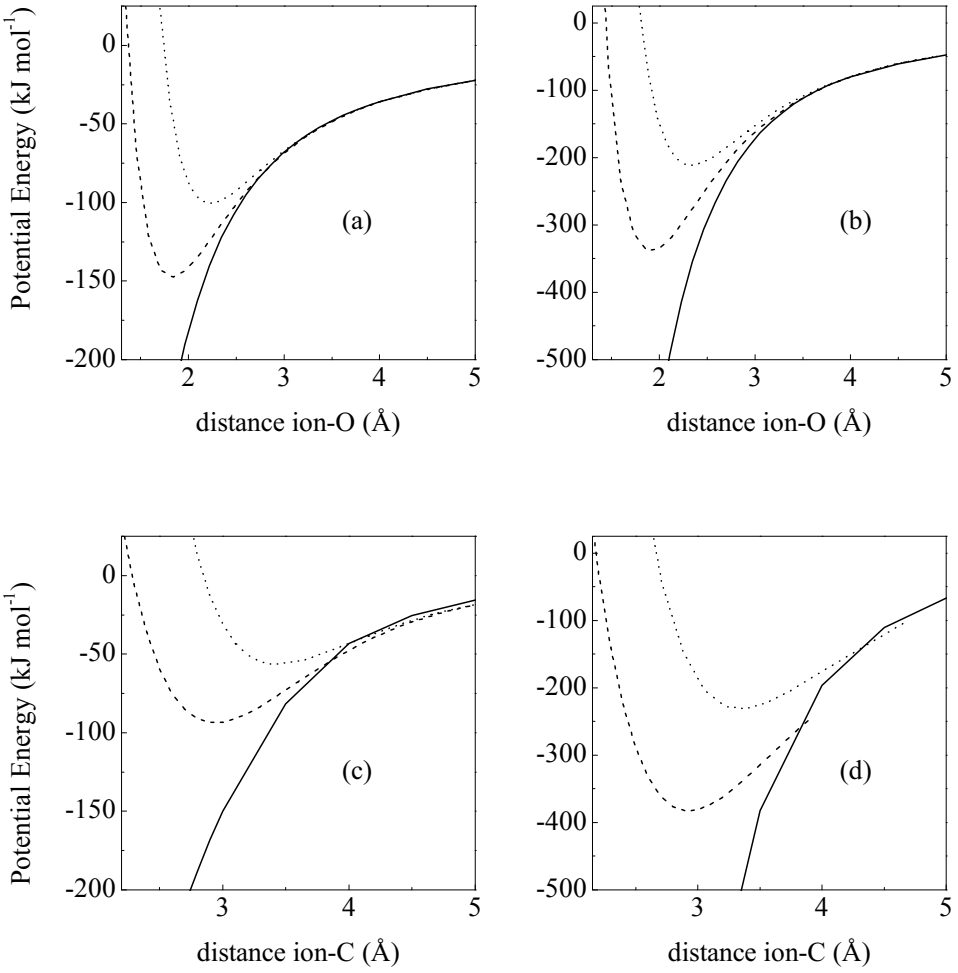

Figure 9.3. Potential energy for C_{2v}-*face* configuration of (a) monovalent and (b) divalent ion-water, and for the *edge* configuration of (c) monovalent and (d) divalent ion-CCl_4 system. Solid line is used in all panels for point charges. Panels (a) and (c): Li^+ (dashed line) and Na^+ (dotted line). Panels (b) and (d): Mg^{2+} (dashed line) and Ca^{2+} (dotted line) The values for contact distance of each ion and configuration are reported in tables 9.4 and 9.5.

We close this section emphasizing that this electric field damping scheme is totally independent of the polarization method used. If, for instance, this approach is used in combination with a point charge model of polarization (shell method or fluctuating charges) only Eq. 9.5 is required. If, on the other hand, the molecular

model uses point charges and point dipoles (like in the point dipole method) one should use both Eq. 9.5 and Eq. 9.6.

9.2 Results

9.2.1 Dimer Potential Energy

	H_2O			CCl_4		
	face	trans	top	face	edge	corner
(+)	1.6	1.6	1.6	2.1	2.5	3.7
Li^+	1.6	1.6	1.6	2.1	2.5	3.7
Na^+	1.9	1.95	2.05	2.5	3.0	4.1
(++)	1.7	1.75	1.85	2.2	2.6	3.8
Mg^{2+}	1.7	1.75	1.85	2.2	2.6	3.8
Ca^{2+}	2.1	2.1	2.2	2.5	3.0	4.0

Table 9.4. Minimum distances considered for each system and configuration (units Å).

For each configuration considered (see Fig. 9.2) the potential energy has been computed as a function of the ion-molecule distance. In figure 9.3 we show the results for the C_{2v}-*face* configuration of the system ion-water and those of the *edge* configuration for ion-CCl4; similar profiles are found for the other configurations of both systems (not shown). As it can be expected, with decreasing ionic radius, the equilibrium distance gets smaller and the well depth increases. This happens both for mono- and di-valent cations. The well depth for di-valent ions is at least twice that of mono-valent ones (in the case of, the highly polarizable, CCl_4 the ratio is of roughly a factor of four for ions of similar ionic radius, e.g. Na^+ and Ca^{2+}). The comparison with the point charge is also given. At large distances the potential energy curves are identical, while at intermediate distances the curves diverge from each other. In principle the breakdown of the point charge approximation should take place at distances directly related to the ion dimension. This simple rule is indeed valid for cations of the same group, but does not apply between different rows of the periodic table. One would expect that, since the ionic radius of second group cations is smaller or comparable to that of the first group, the point charge approximation would hold for smaller distances. Contrary to this notion, we notice that it holds down to shorter distances for mono-valent than for di-valent ions (compare panels (a) and (c) respectively with (b) and (d) of figure 9.3). This effect can be rationalised in terms of the higher attraction exerted by the double charge on the molecular electronic cloud (as reported in I the dipole moment induced from a double charge is more than double of the one induced by a single charge). As a consequence the molecular

	H_2O			CCl_4		
	face	trans	top	face	edge	corner
Li^+	- 147.61	- 84.91	- 87.86	- 85.34	- 93.48	- 34.26
Na^+	- 100.71	- 54.26	- 53.08	- 55.78	- 56.46	- 18.29
Mg^{2+}	- 337.75	- 218.80	- 226.11	- 386.45	- 382.79	- 248.91
Ca^{2+}	- 211.05	- 126.36	- 115.93	- 238.96	- 230.98	- 144.70

Table 9.5. Potential energy minimum for each system and configuration (units kJ mol^{-1}).

electronic cloud is more shifted towards the cation and interacts with the ion outer shell more strongly than for mono-valued ion (for a given ion-molecule distance). Finally, the distance where the repulsive energy is above the potential energy minimum more than 25 kJ mol^{-1}, is considered as the lower limit for our calculations. Shorter distances will rarely be found in liquid state simulation. In tables 9.4 and 9.5 we report respectively the minimum distances obtained and the well depths for all configurations of each system.

9.2.2 Induced Dipole Moments

The total *ab initio* dipole moments for the ion-molecule complex are depicted in Figs. 9.4 and 9.5. The results for a point charge are almost identical to those of "real" cations down to rather small distances :$\approx$ 2.5 Å for water, and down to $\approx$ 3.5 Å in the case of CCl_4 (for CCl_4 close to a divalent ion, Fig. 9.5(b), this distance is increased to $\approx$ 4.5 Å). However, a dramatic difference exists at shorter distances: the dipole moment for a point charge keeps increasing with decreasing distance while for the ions this increase is considerably slowed down and, eventually, a turnover is reached, beyond which the dipole moment decreases with decreasing distance (notice that the results are only displayed up to maximum approach distance as defined above with a energetic criterium, what results for instance in that in some cases the turnover is not reached and only the slow-down of the dipole increase is observed). It is to be noted that the distances at which such effects occur correspond to those typical of molecules within the first solvation shell of the ion in the liquid state [70], and therefore it does not seem advisable to neglect them.

It is important to understand the physical origin of the total dipole damping. To illustrate the discussion we take for instance the C_{2v}-face configuration of water (first configuration in Fig 9.2). As the molecule approaches the ion, the total dipole is expected to grow mostly due to molecular polarization, with a

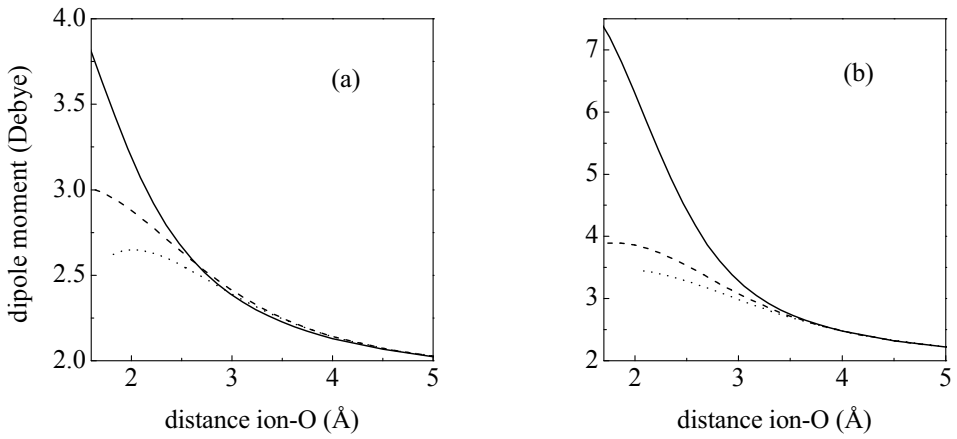

Figure 9.4. Ab initio electric moment for the *trans* configuration of cation-water dimer. Results for (a) monovalent point charge (solid line), Li^+ (dashed line), Na^+ (dotted line) and (b) divalent point charge (solid line), Mg^{2+} (dashed line), Ca^{2+} (dotted line).

small contribution from the cation polarization. Given that the molecular dipole is oriented to the right (which we will consider the positive direction), the induced dipole on the ion will also be directed to the right (or, in terms of the shell model, the auxiliary -negative- charge harmonically bonded to the -positive- ion site will be shifted to the left). Both effects (increase of the ionic and molecular dipole with decreasing distance) can be mimicked by any polarization method (except of course the moderate nonlinear increase discussed in I and II), and therefore should not be a cause of concern to phenomenological molecular polarization methods.

If the ion-molecule distance is reduced to contact, though, a different mechanism sets in as evident from the *ab initio* calculations: repulsion between the electronic clouds of the ion and the molecule, which can be understood as a "mechanical" polarization [5, 71]. For the cation this effect is translated in an additional push to the left of its electronic cloud, i.e. this effect will add to that of the purely electrostatic polarization. In short, the ionic contribution will tend to further increase (nonlinearly) the total dipole moment of the complex. However, given its low polarizability, this effect will not be relevant and is superseded by electronic shift within the molecule. Indeed, a similar reasoning applied to the molecule, leads to the conclusion that its electronic cloud will be shifted to the right and therefore will tend to *reduce* the molecular dipole. Given the much

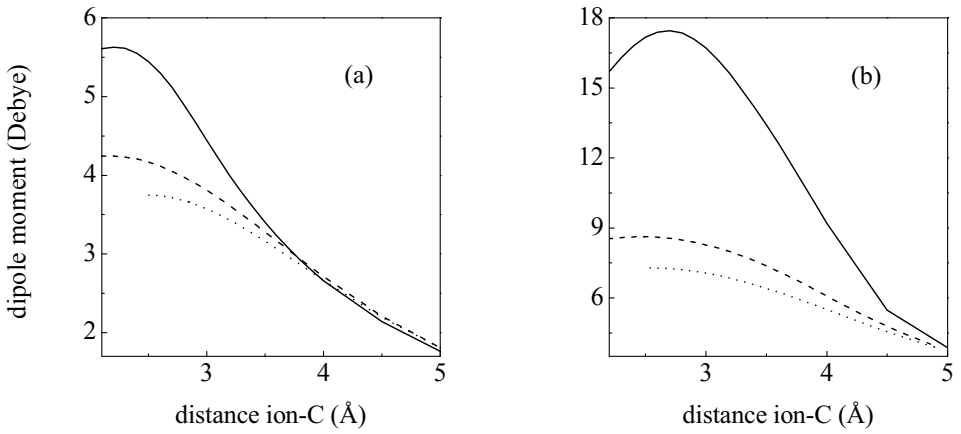

Figure 9.5. Ab initio electric moment for the *face* configuration of cation-CCl_4 dimer. Results for (a) monovalent point charge (solid line), Li^+ (dashed line), Na^+ (dotted line) and (b) divalent point charge (solid line), Mg^{2+} (dashed line), Ca^{2+} (dotted line).

higher molecular polarizability, this will be the dominant effect (a similar conclusion is reached if one considers an inverted orientation for the molecule). To summarize, molecular polarization at contact distances results from two opposite effects: a dipole increase due to the presence of the positive ion's charge (which can in principle be represented by any of the methods discussed for electric polarization), and a dipole decrease due to the mechanical shift of electronic clouds. Unfortunately, the latter effect clearly dominates, as can be seen from the *ab initio* results, and is not contained in any of the polarization methods, what will require *ad hoc* modifications at short distances. It is important to note that the two opposing mechanisms can be linked to two different physical aspects: the dipole increase basically depends on electric polarizability while the dipole decrease due to electronic overlap depends on geometrical parameters (ionic and molecular radius).

In connection with the last point, an additional aspect is to be noted: the damping of the dipole moment increases with increasing ionic radius, as the curves get lower along the series (Li^+ and Na^+ or Mg^{2+} and Ca^{2+}). This behaviour is common to the most probable configurations of both H_2O and CCl_4 (Figs. 9.4 and 9.5), and is a corollary of the previous discussion: for a fixed ion-molecule distance the molecular electronic cloud will have a higher overlap with ions of larger radius. This will result in a stronger shift of this cloud and, therefore,

in a smaller molecular dipole. This secondary effect has important consequences for the construction of damping methods. It is possible to imagine a convenient damping model (in terms of ease of simulation) which includes a damping of the electric field felt by the molecule if this field is larger than some threshold, irrespective of the origin of this electric field. In this way it is in principle possible to mimick the dipole decrease with increasing electric field (i.e. proximity to the ion). Unfortunately, the dependence on the ion just discussed, makes such simple approach only approximate at best: we find for instance that while the positive charge on Li^+ and Na^+ create the same field on the molecule, the polarization induced at contact differs substantially. In consequence a damping of the field of this sort might work for one ion but would not do for other ions. The damping method should thus take into account geometric aspects. In its simpler form it should depend on the ion and molecule radius, and this is where the Thole method comes in, as it is based on the inclusion of mutual size effects on the computation of the electric field at short separations.

9.2.3 Performance of undamped methods

Before exploring the utility of this damping method, we analyse the shortcomings of the uncorrected polarization methods in the light of the two mechanisms just discussed. Only the results for a single configuration and for the molecular polarization models that performed better for the point charge model of the ion will be shown (the behaviour is highly similar for other configurations and models). The unability of the unmodified point dipole and shell methods to reproduce the dipole moment at small distances is manifest in Fig. 9.6 for water and in Fig. 9.7 for carbon tetrachloride. The fundamental problem is that the total dipole of the complex is predicted to grow monotonically as the distance is reduced, in contrast with the already discussed damped increase (followed by a turnover) of the *ab initio* results.

The case of water close to a monovalent ion (Fig. 9.6(a)) can serve to illustrate the main features. First, it is evident that the differences at contact separations are quantitively important even for this case of low ionic charge/low molecular polarizability: for Li^+ there is a 40% difference between the dipole moment predicted by the polarisable model and the *ab initio* result. Second, the effect of ion polarizability is minor: the curves for Li^+ and Na^+ are rather close to each other and to the curve that corresponds to a point charge. This feature illus-

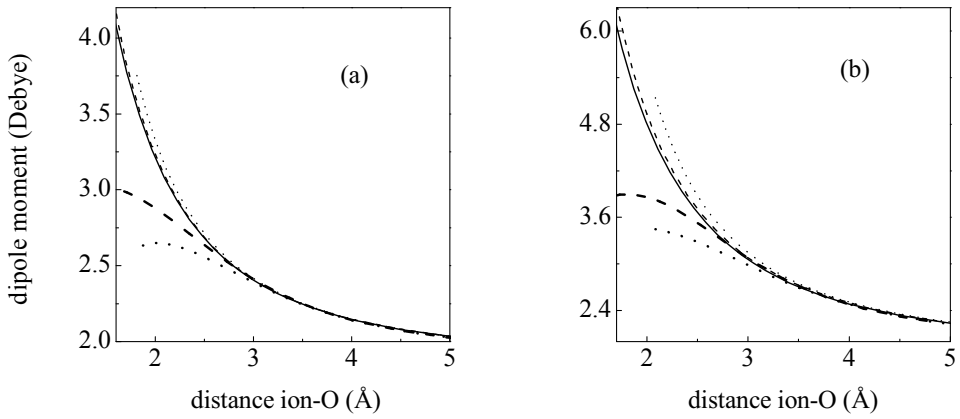

Figure 9.6. Electric moment for the *trans* configuration of cation-water system. Thick lines are for ab initio calculations and thin lines are for PD2-H2O curves. Results for (a) monovalent point charge (solid line), Li^+ (dashed line), Na^+ (dotted line) and (b) divalent point charge (solid line), Mg^{2+} (dashed line), Ca^{2+} (dotted line).

trates the feeble effect of the dipole moment induced on the ion as compared with the molecular induced dipole. In connection with the two mechanisms described in the previous section, we see how the curves are slightly steeper as the ion's polarizability increases, i.e. the predicted polarization is slightly higher for the case of Na^+ than for Li^+ due to the higher ionic polarizability of the former, what illustrates that the polarization methods only take into account this sort of ion dependent polarization. As was described in the previous section, there is no electronic overlap effect included, while it is precisely this finite size effect which results in the *ab initio* results showing exactly the opposite trend, i.e. the induced dipole is smaller for the Na^+ case than for Li^+. The same basic trends are found for all cases studied (see Figs. 9.6,9.7). One can notice for instance that for divalent ions close to water (Fig. 9.6(b)) the differences are qualitatively very similar, although quantitatively larger. For carbon tetrachloride the scenario is rather similar to that of water as well (Fig. 9.7(a,b)). Again, the *ab initio* results show the opposite trend of classical methods: the dipole moment of the system lowers as the ion polarizability increases.

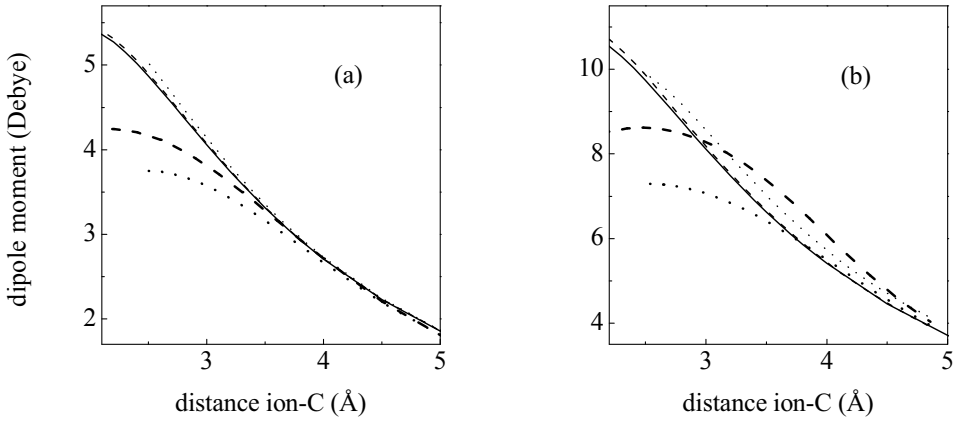

Figure 9.7. Electric moment for the *face* configuration of cation-CCl_4 system. Thick lines are for ab initio calculations and thin lines are for PD-CCl4 curves. Results for (a) monovalent point charge (solid line), Li^+ (dashed line), Na^+ (dotted line) and (b) divalent point charge (solid line), Mg^{2+} (dashed line), Ca^{2+} (dotted line).

9.2.4 Polarization plus Thole damping

The previous section makes evident the need for a damping scheme. This can be achieved to a great extend by using the Thole method described in section 9.1.3 and the Appendix. As shown there, this method can be implemented in different "flavours", which depend on the chosen joint charge distribution: linear (LIN, Eqs. 9.7,9.8), exponential (EXP, Eqs. 9.9,9.10) or gaussian (GAUSS, Eqs. 9.11,9.12). Any of the three can be used in conjunction with the point dipoles or shell models of polarization. It will be shown that once the parameter on which they depend (a) is optimized for each distinct pair, every possible combination of polarization and damping method performs reasonably well.

Figure 9.8 illustrates the performance of the different combinations for the Li^+-water dimer, which will center most of the discussion. Panels (a) and (b) correspond to PDM (point dipoles) and SH (shell method) respectively. The crucial point to observe is that the three damped curves closely follow the *ab initio* results, resulting in a much better performance with respect to the undamped models. While only a subset of the results will be shown, this behaviour is also found for the rest of the ions, for the different molecular orientations studied (see Fig. 9.2), and for the CCl_4 molecule as well. Coming to the finer level of detail, the PDM-LIN and SH-LIN give the best results, followed by the EXP distribu-

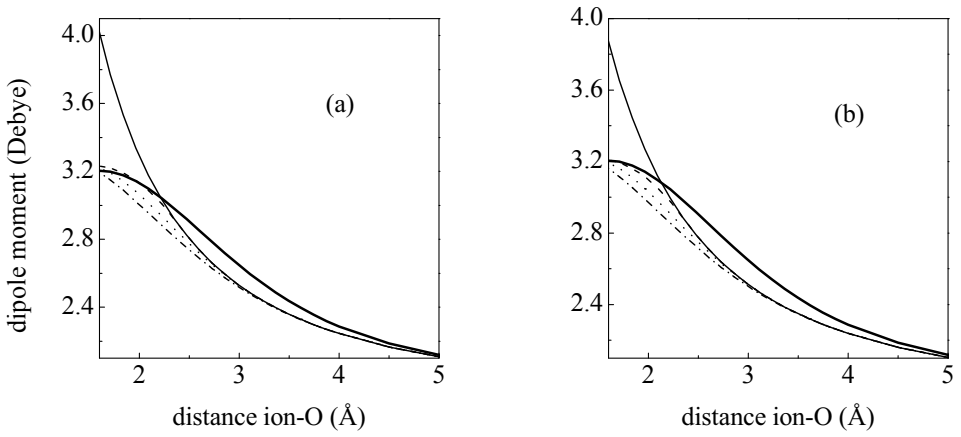

Figure 9.8. Comparison among the methods discussed in the text for the C_{2v}-*face* configuration in the Li^+-water dimer. Panel (a): PDM-H2O (thin solid line), PDM-LIN (dashed line), PDM-EXP (dotted line) and PDM-GAUSS (dash-dot line). Panel (b): SH-H2O (thin solid line), SH-LIN (dashed line), SH-EXP (dotted line) and SH-GAUSS (dash-dot line). Thick solid line in both panels is used for ab initio results.

tion, and with GAUSS coming last. Indeed, the LIN distribution showed to be the best performing scheme for all the ions considered (in the case of water), the results are shown in Figure 9.9. We now discuss in more depth some additional aspects of the fits.

First, it can be noticed that for each method (LIN, EXP, GAUSS) the corresponding curves are almost equal in panels (a) and (b) of Fig. 9.8, i.e. each charge distribution performs equally well for any of the two polarization methods (point dipoles or shell). The almost imperceptible differences can be adscribed to two factors: i) the PD method includes a damping of the dipolar interaction while in SH only the charge-charge interaction is damped (indeed the high similarity between the curves illustrates the feeble contribution of the dipole field damping); ii) since in the SH model, the shell charge is displaced with respect to the zero-field position, the (distance dependent) damping will be slightly different from the one used for PD (where the charges remain fixed).

Second, while the three schemes are able to satisfactorily reproduce the ab initio results at short distances, the underestimation found in I and II at intermediate distances ($2.2 < r < 4$ Å) is left unchanged. This drawback derives, as discussed in I and II, from the fact that the polarization methods studied are linear and thus cannot reproduce the system hyperpolarizability obtained

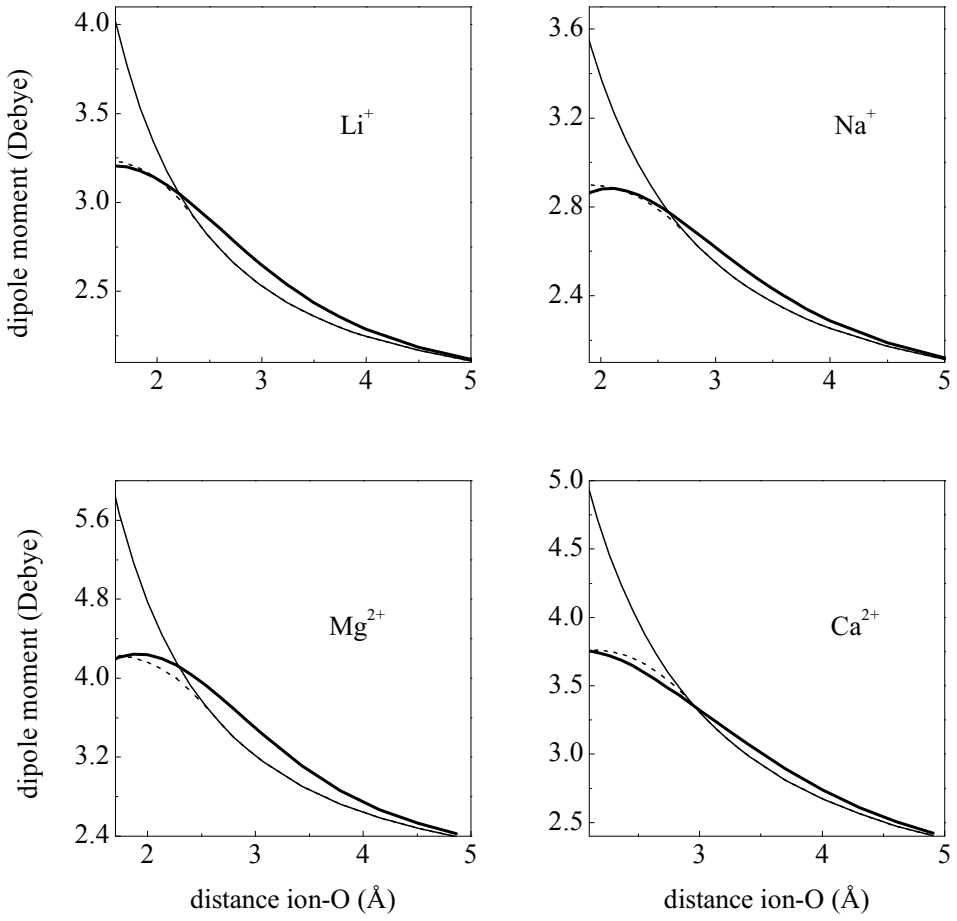

Figure 9.9. Total electric moment for the C_{2v}-*face* configuration of ion-water. Ab initio results (thick solid line), PDM-H2O (thin solid line) and PDM-LIN (dotted line).

with quantum chemical calculations. The present implementation of the Thole damping cannot be a solution for this either, as it is a larger polarization what is required instead of a damping (although it is possible to imagine that this deviation might be tackled with more complex charge distributions). This limitation, though, should not be overemphasized, the worst disagreement for any of the different combination of methods yields a relative error in the range 5-6 % of the total dipole moment (the largest deviation occurs for the unprobable *top* configuration, see Fig. 9.2, and does not exceed a 10 %), what justifies limiting the present study to the simple charge distributionds described. For the linear and exponential cases the deviation takes place close to 3 Å, i.e. in the region where there is still no damping, and can thus be totally adscribed to the lack of

hyperpolarizability. For the gaussian method, the largest deviation (≈ 6 %) occurs at ≈ 2.5 Å, and thus also includes a small contribution from an (undesired) non-zero damping in this region.

The latter point highlights how the damping differs somewhat between different charge distributions. It is possible to get some additional insight by considering the total electric field felt by the ion. Figure 9.10 displays the results for both damped and undamped calculations within the physically meaningful range of distances. The main feature of the LIN scheme (the one that produces better results) is that it stays close to the undamped curve down to a shorter distance than the EXP or GAUSS distributions. The larger steepness of this damping seems thus to be important in order to get a better fit. Nevertheless, since the present results are rather satisfactory, a marginal improvement along these lines has not been pursued.

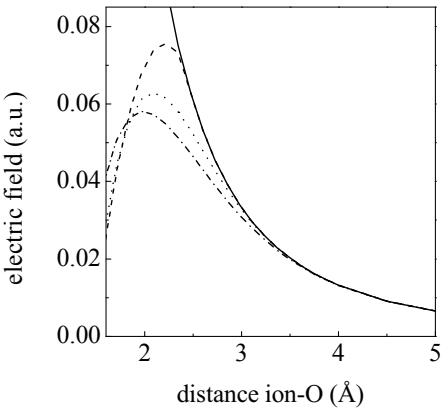

Figure 9.10. Distance dependence of the total electric field on the ion; PDM-H2O (solid line), PDM-LIN (dashed line), PDM-EXP (dotted line) and PDM-GAUSS (dash-dot line).

Regarding the precise values for the a_{ij} parameters (with i denoting an ion and j and atomic site within the molecule), in the case of water *only* the cation-oxygen interaction was damped, while the cation-hydrogen interaction was left unchanged, so that a single parameter is needed for each ion (a_{IO}). The results are summarized in Table 9.6. As a result of the fitting, a_{IO} has the nice characteristic of being independent of the polarization method used (point dipoles or shell method). The last column contains the estimated value for a_{IO}, calculated as $a_{IO}^{est} = (r_{ion}^2 + r_O^2)^{1/2}$(see Eq. 9.15), where r_{ion} and r_O denote respectively the ionic radius [78–81] and the oxygen Van der Waals radius [82]. For the GAUSS distribution the fitted values are very close to the estimated

	LIN	EXP	GAUSS	a_{IO}^{est}
Li^+	2.59	1.79	1.44	1.63
Na^+	2.98	2.05	1.64	1.79
Mg^{2+}	2.79	1.92	1.57	1.65
Ca^{2+}	3.13	2.14	1.72	1.81

Table 9.6. Parameter a used for the ion-oxygen interaction (in Å) for the linear, exponential and gaussian dampings. The radius (a_{IO}^{est}) estimated from the experimental values of the atomic radius is reported in the last column.

	LIN		EXP		GAUSS		a^{est}	
	a_{ICl}	a_{IC}	a_{ICl}	a_{IC}	a_{ICl}	a_{IC}	a_{ICl}	a_{IC}
Li^+	3.05	2.8	2.0	1.8	1.6	1.5	1.85	1.80
Na^+	3.65	2.9	2.28	1.9	1.84	1.7	1.99	1.95
Mg^{2+}	3.0	2.7	1.9	1.4	1.6	1.5	1.87	1.82
Ca^{2+}	3.46	3.0	2.35	2.0	1.9	1.9	2.01	1.97

Table 9.7. Parameter a (in Å) used for the ion-chlorine (a_{Cl}) and ion-carbon (a_C) interactions; values for the linear, exponential and gaussian dampings. The radius (a^{est}) estimated from the experimental values of the atomic radius is reported in the last two columns.

ones: as a rule of thumb the fitted ones are $\approx 10\%$ lower than the estimated ones. This approximate rule also applies for the CCl_4 results (Table 9.7), and could thus be used as a reasonable estimate if the method should be applied to other atomic sites. For the EXP distribution the fitted values are $\approx 15\%$ higher than the estimated ones, while for the LIN distribution they are consistently higher by $\approx 70\%$.

So far the discussion has been mainly centered on the water molecule, for carbon tetrachloride the results are rather similar although some differing details have to be considered. The a_{ij} parameters were fitted for both the ion-chlorine and ion-carbon interactions (Table 9.7). Contrary to the case of water, for this system the EXP scheme is the one that performs better, although as it was clear in the case of Li^+-water the differences are rather minor. The results for the PD-EXP models are displayed in Figure 9.11, showing similar features as those for the water case.

9.3 Conclusions

The aim of this work has been to explore the possibility of reproducing the mutually induced dipole moment of a molecular complex with simple phenomenological methods that can be easily implemented in Molecular Dynamics codes. This has been done in a demanding environment like that corresponding to polarizable molecules in the presence of polarizable cations, using high level *ab initio* results as benchmark. It has been shown that a reparametrization of the Thole electric field damping method, combined with almost any simple polarization method, is able to reproduce rather satisfactorily the induced dipole moment of the cation-molecule dimer. This has been demonstrated for several (mono- and di-valent)

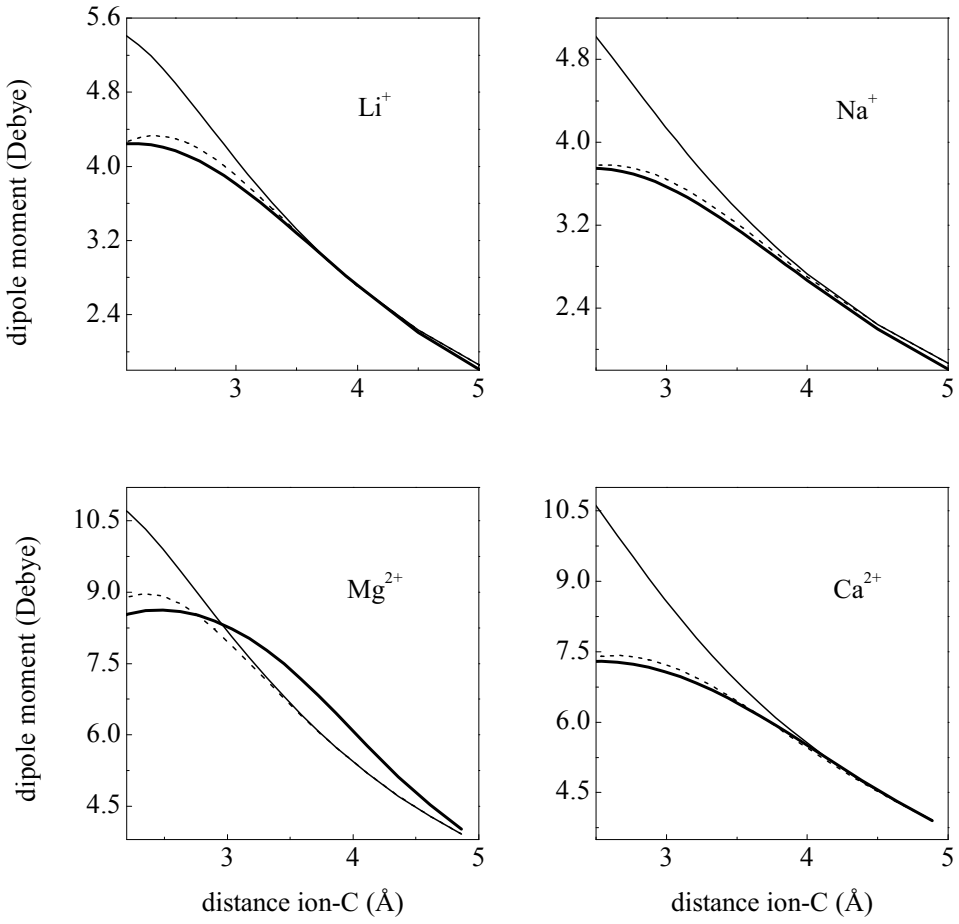

Figure 9.11. Total electric moment for the *face* configuration of ion-CCl_4. Ab initio results (thick solid line), PD-CCl4 (thin solid line) and PD-EXP (dashed line).

cations, molecules (water and carbon tetrachloride), and for an extended set of molecular orientations and ion-molecule distances. The largest deviations are due to the nonlinear behaviour at intermediate separations, although in no case these reach a 10 % of the total dipole moment and therefore it does not seem necessary to resort to more sophisticated charge densities. The study of this approach for anions (with the increased complexity that stems from their higher polarizabiity) and to clusters larger than the dimer will constitute stringent tests of the present approach.

Finally, the present work can be regarded as a preliminary step for a novel strategy in the development of a force field. The usual route has been to include a simple polarization method within a typical nonpolarizable force field, and

subsequently fine tune the parameters using for instance *ab initio* results for the energy of clusters and/or thermodynamic properties for condensed phase, etc. A first casualty of such approach is that there is no guarantee that the resulting dipole moment (a crucial quantity for the calculation of spectra) is physically meaningful. Moreover, the divergent behaviour shown here for simple polarization methods at short distances can be a source of an undesired strain on the whole force field: the important overestimation of the coulomb interaction forces a consequent damping by other pair-additive terms (like Lennard-Jones parameters), which might not work properly in all environments. In short, it seems more advisable to first construct a polarisable electrostatic model recoursing to *ab initio* calculations and, in a second stage, to include additive terms in order to develop a force field that reproduces the potential energy landscape.

9.4 Appendix

Here we summarize the basic aspects of the Thole method. It should be recognized at the outset that, despite the fact that this theory was developed to improve the point dipole method of molecular polarizability, it has no direct connection with polarization. Indeed it could be described as a theory to substitute a set of point charges by a corresponding set of *rigid* charge distributions, neglecting any induced deformation due to mutual interaction (polarization). In fact, related schemes were developed, for example, to replace a point-charge nucleus by a finite-size nucleus in Dirac-Fock calculations [72–74]. The final result is a scheme in which the pair additive nature is maintained and the fields at contact separation between pairs of charges are damped due to their finite extent. It is this damping of the electric field which, when used in conjunction with a polarization method of choice, results in a corresponding damping of the induced dipole.

The method can be motivated by the form of the interaction energy between two gaussian charge distributions, a well known case in electronic structure theory. The distributions are taken to have total charges q_1 and q_2 respectively, so that they can be written in terms of normalized (N) gaussians ($\rho_1(r) = q_1 \cdot \rho_1^N(r)$, $\rho_2(r) = q_2 \cdot \rho_2^N(r)$). The total interaction energy is [75, 76]

$$U = q_1 q_2 \int\int \frac{\rho_1^N(r_1)\rho_1^N(r_2)d\vec{r_1}d\vec{r_2}}{r_{12}} = q_1 q_2 \frac{\mathrm{erf}(r_{12}/a)}{r_{12}}, \tag{9.14}$$

where $\mathrm{erf}(r)$ denotes the error function (the Coulomb interaction is recovered in the long distance limit as this function tends to 1). The parameter a depends on

the width of each of the gaussians by the simple relation

$$a = \sqrt{a_1^2 + a_2^2}, \tag{9.15}$$

with the normalized three dimensional gaussian being

$$\rho^N(r) = (\pi a^2)^{-3/2} e^{-(r/a)^2}. \tag{9.16}$$

Thole's method is based on the observation that Eq. 9.14 can be interpreted as resulting from the interaction of a point charge (q_1) with a distributed charge (q_2), which creates a potential of the form $V(r) = q_2\varphi(r;a)$ (in this case $\varphi(r;a) = \mathrm{erf}(r/a)/r$). It should be noted that this potential depends on a parameter (a) which contains information on *both* interacting distributions (reflected in relation 9.15 for the gaussian case). This interpretation can be extended to systems of more than a couple of charges as the theory is pair additive (see the dipole case below for an example).

We can immediately derive the electric field generated by such a distribution

$$\vec{E} = -\nabla[q\varphi(r;a)] = -q\dot{\varphi}\frac{\vec{r}}{r} = [-r^2\dot{\varphi}]q\frac{\vec{r}}{r^3} \equiv f_1(r)\cdot q\frac{\vec{r}}{r^3}. \tag{9.17}$$

Notice that the following correction has been defined

$$f_1 = -r^2\dot{\varphi}, \tag{9.18}$$

which acts on the field that would be created by a point charge, and which depends on the derivative of the electric potential by unit of charge ($\dot{\varphi}$). The latter function can be related with the charge distribution that creates it by applying Gauss' theorem. For an spherically symmetric distribution

$$\vec{E} = \frac{\vec{r}}{r^3}\int_0^r 4\pi r^2\rho(r)dr, \tag{9.19}$$

which together with Eq. 9.17 yields

$$\dot{\varphi} = -\frac{1}{r^2}\int_0^r 4\pi r^2\rho^N(r)dr. \tag{9.20}$$

In the original Thole approach one would start by assuming a given functional form for $\rho^N(r)$ (related in a nontrivial way with the -unknown- atomic distributions of each member of the pair). With this normalized charge density one can compute $\dot{\varphi}$ (Eq. 9.20), and finally the damping of the electric field (Eq. 9.18).

In the form just described Thole's approach can be applied to models with only point charges. Originally, though, it was developed for models for which only

point dipoles exist. The extension to this case [28] starts from a finite dipole, with charge $-q$ at the origin plus a charge q at a position $\vec{l}$. Each of both charges is assumed to consist of a charge distribution of the type just described above. Therefore, thanks to the mentioned pair additive character of this approach, the interaction with an external charge Q is

$$U = Q \cdot q\varphi(r) + Q \cdot (-q)\varphi(r') = Q \cdot q[\varphi(r') - \varphi(r)]. \tag{9.21}$$

The position vector of charge Q with respect to q (denoted $\vec{r'}$) can be expressed as $\vec{r'} = \vec{r} - \vec{l}$, what together with a Taylor expansion yields

$$U \cong Qq\nabla\varphi \cdot (-\vec{l}). \tag{9.22}$$

With the usual definition for the dipole moment ($\vec{p} \equiv q\vec{l}$), the above expression becomes exact in the limit $\vec{l} \to 0$

$$U = -Q\nabla\varphi \cdot \vec{p}, \tag{9.23}$$

so that the potential created by such a dipole can be identified as

$$\psi = -\nabla\varphi \cdot \vec{p}. \tag{9.24}$$

Like in the case of a charge, it is now straightforward to derive the electric field it creates

$$\vec{E} = \nabla\left(\nabla\varphi \cdot \vec{p}\right) = \nabla\nabla\varphi \cdot \vec{p} \equiv T \cdot \vec{p}, \tag{9.25}$$

where the dipole field tensor has been defined ($T \equiv \nabla\nabla\varphi$). Its components can be readily computed

$$\begin{aligned} T_{ij} &= \frac{\partial}{\partial r_i}\frac{\partial}{\partial r_j}\varphi = \frac{\partial}{\partial r_j}(\frac{\dot{\varphi}}{r}r_i) = \\ &= \frac{r^3}{3}\left[\ddot{\varphi} - \frac{\dot{\varphi}}{r}\right]3\frac{r_i r_j}{r^5} - \left[-\dot{\varphi}r^2\right]\frac{\delta_{ij}}{r^3} \equiv [f_2]3\frac{r_i r_j}{r^5} - [f_1]\frac{\delta_{ij}}{r^3}, \end{aligned}$$

from which we conclude that usual expression (Eq. 9.2) is corrected by factors $f_1(r;a)$ (see Eq. 9.18) and $f_2(r;a) = \frac{r^3}{3}\left[\ddot{\varphi} - \frac{\dot{\varphi}}{r}\right]$

With this general framework, it is now possible to deduce the correction factors corresponding to any joint charge distribution ($\rho^N(r)$) of choice. Thole favoured the use of a linear behaviour

$$\rho^N(r) = \begin{cases} \frac{3}{\pi a^3}\left(1 - \frac{r}{a}\right) & \text{for } r < a \\ 0 & \text{for } r > a, \end{cases} \tag{9.26}$$

which results in the corrections displayed in Eqs. 9.7,9.8. The corresponding interaction potential can be obtained after integration of this distribution (see Eq. 9.20)

$$\varphi(r) = \begin{cases} \frac{1}{r} & \text{for } r > a \\ \frac{1}{a}\left[2 - 2\left(\frac{r}{a}\right)^2 + \left(\frac{r}{a}\right)^3\right] & \text{for } r < a \end{cases} \tag{9.27}$$

The most popular distribution for Molecular Dynamics simulation seems to be an exponential one [28, 39, 69]

$$\rho^N(r) = \frac{3}{4\pi a^3} e^{-\left(\frac{r}{a}\right)^3}, \tag{9.28}$$

with the corresponding correction factors displayed in Eqs. 9.9,9.10, while the interaction potential having a somewhat involved form [28]

$$\varphi(r) = \frac{1}{r} - \frac{e^{-\left(\frac{r}{a}\right)^3}}{r} + \frac{1}{a}\Gamma(2/3)Q\left(\frac{2}{3}, \left(\frac{r}{a}\right)^3\right), \tag{9.29}$$

where $Q(s, w)$ is the *incomplete gamma function* defined as

$$Q(s, w) = \frac{\Gamma(s, w)}{\Gamma(s)} = \frac{\int_w^\infty t^{s-1}\exp(-t)\mathrm{d}t}{\int_0^\infty t^{s-1}\exp(-t)\mathrm{d}t}. \tag{9.30}$$

Finally, we have also included the distribution that has been used to motivate the initial part of this Appendix, characterized by a rather simple form of the interaction potential

$$\varphi(r) = \frac{\mathrm{erf}(r/a)}{r} \tag{9.31}$$

and for which the correction factors that result are displayed in Eqs 9.11,9.12. The (so far unknown) joint charge distribution corresonding to this case can be obtained by derivation of Eq 9.20. A three dimensional normalized gaussian (Eq 9.16) is obtained, as should be expected from the very well known properties of gaussian pairs.

References

[1] T. Halgren and W. Damm *Curr. Opin. Struct. Biol.* **11** (2), 236 (2001).

[2] A. van der Vaart, B.D. Bursulaya, C.L. Brooks and K.K. Merz *J. Phys. Chem. B* **104**, 9554 (2000).

[3] S. Patel and C.L. Brooks *J. Comp. Chem.* **25**, 1 (2004).

[4] P. Cieplak, J. Caldwell and P. Kollman *J. Comp. Chem.*, **22**, 1048 (2001).

[5] S. W. Rick and S. J. Stuart *Rev. Comp. Chem.* **18**, 89 (2002).

[6] P. Alström, A. Wallqvist, S. Engström and B. Jönsson *Mol. Phys.* **68**, 563 (1989).

[7] A. Wallquist, P. Alström and G. Karlström *J. Phys. Chem.* **94**, 1649 (1990).

[8] U. Niesar, G. Corongiu, E. Clementi, G.R. Kneller and D.K. Bhattacharya *J. Phys. Chem.* **94**, 7949 (1990).

[9] J. Caldwell, L.X. Dang and P.A. Kollman *J. Am. Chem. Soc.* **112**, 9144 (1990).

[10] H. Saint-Martin, C. Medina-Llanos and I. Ortega-Blake *J. Chem. Phys.* **93**, 6448 (1990).

[11] M. Sprik *J. Phys. Chem.* **95**, 2283 (1991).

[12] S.B. Zhu, S. Singh and G.W. Robinson *J. Chem. Phys.* **95**, 2791 (1991).

[13] C. Millot and A.J. Stone *Mol. Phys* **77**, 439 (1992).

[14] L.X. Dang *J. Chem. Phys.* **97**, 2659 (1992).

[15] R.E. Kozack and P.C. Jordan *J. Chem. Phys.* **96**, 3120 (1992).

[16] A. Wallqvist and B.J. Berne *J. Phys. Chem.* **97**, 13841 (1993).

[17] J.W. Halley, J.R. Rustad and A. Rahman *J. Chem. Phys.* **98**, 4110 (1993).

[18] L. X. Dang and D. E. Smith *J. Chem. Phys.* **99**, 6950 (1993).

[19] M. Wilson and P. A. Madden *J. Phys. Cond. Matter* **5**, 2087 (1993).

[20] D. N. Bernardo, Y. Ding, K. Krogh-Jespersen and R. M. Levy *J. Phys. Chem.* **98**, 4180 (1994).

[21] S.W. Rick, S.J. Stuart and B.J.Berne *J. Chem. Phys.* **101**, 6141 (1994).

[22] B.J. Palmer *Chem. Phys.* **184**, 163 (1994).

[23] D. Borgis and A. Staib *Chem. Phys. Lett.* **238**, 187 (1995).

[24] J.C. Soetens and C. Millot *Chem. Phys. Lett.* **235**, 22 (1995).

[25] A.A. Chialvo and P.T. Cummings *J. Chem. Phys.* **105**, 8274 (1996).

[26] L.X. Dang and T.M. Chang *J. Chem. Phys.* **106**, 8149 (1997).

[27] M. Alfredsson, J.P. Brodholt, K. Hermansson and R. Vallauri, *Mol. Phys.* **94**, 873 (1998).

[28] J. C. Burnham, J. Li, S. S. Xantheas and M. Leslie *J. Chem. Phys.* **110**, 4566 (1999).

[29] B. Chen, J. Xing and J.I. Siepmann *J. Phys. Chem. B* **104**, 2391 (2000).

[30] H. Saint-Martin, J. Hernandez-Cobos, M.I. Bernal-Uruchurtu, I. Ortega-Blake and H.J.C. Berendsen *J. Chem. Phys.* **113** 10899 (2000).

[31] K. Ando *J. Chem. Phys.* **115**, 5228 (2001)

[32] B. Guillot and Y. Guissani *J. Chem. Phys.* **114**, 6720 (2001).

[33] G. Ferenczy and C.A. Reynolds *J. Phys. Chem. A* **105**, 11470 (2001).

[34] H.A. Stern, F. Rittner, B.J. Berne and R.A. Friesner *J. Chem. Phys.* **115**, 2237 (2001).

[35] K.H. Cho, K.T. No and H.A. Scheraga *J. Mol. Struc.* **641** 77 (2002).

[36] P. Ren and J. W. Ponder *J. Comput. Chem.* **23**, 1497 (2002).

[37] R. Chelli and P. Procacci *J. Chem. Phys.* **117**, 9175 (2002).

[38] H. Yu, T. Hansson and W.F. van Gunsteren *J. Chem. Phys.* **118**, 221 (2003).

[39] P. Ren and J. W. Ponder *J. Phys. Chem. B* **107**, 5933 (2003).

[40] G. Lamoreoux and B. Roux *J. Chem. Phys.* **119**, 3025 (2003).

[41] E. M. Mas *J. Chem. Phys.* **118**, 4386 (2003).

[42] G.A. Kaminski, R.A. Friesner and R.Zhou *J. Comp. Chem.* **24**, 267 (2003).

[43] H. Yu and W.F. van Gunsteren *J. Chem. Phys.* **121**, 9549 (2004).

[44] Z.Z. Yang, Y. Wu and D.X. Zhao *J. Chem. Phys.* **120** 2541 (2004).

[45] T. Yan, C. J. Burnham, M. G. Del Popolo and G. A. Voth *J. Phys. Chem. B* **108**, 11877 (2004).

[46] T. J. Giese and D. M. York *J. Chem. Phys.* **120**, 9903 (2004).

[47] M. Masia, M. Probst and R. Rey *J. Chem. Phys.* **121**, 7362 (2004).

[48] V. M. Anisimov, G. Lamoureux, I. V. Vorobyov, N. Huang, B. Roux and A. D. MacKerell Jr. *J. Chem. Theory Comput.* **1** 153 (2005).

[49] E. V. Tsiper *Phys. Rev. Lett.* **94** 013204 (2005).

[50] E. Harder, B. Kim, R. A. Friesner and B. J. Berne *J. Chem. Theory Comput.* **1** 169 (2005).

[51] R. Chelli, M. Pagliai, P. Procacci, G. Cardini and V. Schettino *J. Chem. Phys.* **122**, 074504 (2005).

[52] S. Yu. Noskov, G. Lamoureux and B. Roux *J. Phys. Chem. B* asap, DOI: 10.1021/jp045438g (2005).

[53] M. Masia, M. probst and R.Rey *Comp. Phys. Comm.* **169**, 331 (2005).

[54] C. J. F. Böttcher, Theory of Electric Polarization, Elsevier, Amsterdam (1973).

[55] S. J. Stuart and B. J. Berne *J. Phys. Chem.* **100**, 11934 (1996).

[56] H. Coker *J. Phys. Chem.* **80**, 2078 (1976).

[57] W. R. Johnson and K. T. Cheng *Phys. Rev. A* **53**, 1375 (1996).

[58] I. S. Lim, J. K. Laerdahl and P. Schwerdtfeger *J. Chem. Phys.* **116**, 172 (2002).

[59] A.P. Lyubartsev, K. Laasonen and A. Laaksonen, J. Chem. Phys. 114, 3120 (2001).

[60] A. D. Becke *J. Chem. Phys.* **98**, 5648 (1993).

[61] D. E. Woon and T. H. Dunning Jr. *J. Chem. Phys.* **98**, 1358 (1993).

[62] K. A. Peterson, D. E. Woon and T. H. Dunning Jr. *J. Chem. Phys.* **100**, 7410 (1994).

[63] D. J. Tozer and N. C. Handy *J. Chem. Phys.* **109**, 10180 (1998).

[64] A. J. Sadlej, *Collection Czech Chem. Commun.* **53**, 1995 (1988).

[65] A. J. Sadlej, *Theoret. Chim. Acta* **79**, 123 (1991).

[66] J. P. Perdew, K. Burke and M. Ernzerhof, *Phys. Rev. Lett.* **77**, 3865 (1996).

[67] W. Koch and M.C. Holthausen, A Chemist's Guide to DFT, Wiley-VCH (2001).

[68] J. Applequist, J.R. Carl and K.K. Fung *J. Am. Chem. Soc.* **94**, 2952 (1972).

[69] B. T. Thole *Chem. Phys.* **59**, 341 (1981).

[70] M. Masia and R. Rey *J. Phys. Chem. B* **107**, 2651 (2003).

[71] J. E. Hanlon and A. W. Lawson *Phys. Rev.* **113**, 472 (1959).

[72] A. K. Mohanty and E. Clementi, *Int. J. Quantum Chem.* **39**, 487 (1991).

[73] A. K. Mohanty and E. Clementi, *Int. J. Quantum Chem.* **40**, 429 (1991).

[74] Y. Ishikawa, R. Baretty and R. C. Binning Jr., *Chem. Phys. Lett.* **121**, 130 (1985).

[75] L. Jensen, P.-O. Åstrand, A. Osted, J. Kongsted and K. V. Mikkelsen *J. Chem. Phys.* **116**, 4001 (2002).

[76] T. Helgaker, P. Jørgensen, and J. Olsen, Molecular Electronic-Structure Theory, Wiley, Chichester, (2000).

[77] W. H. Press, S. A. Teukolsky, W. T. Vetterling and B. P. Flannery, Numerical Recipes in Fortran 77 - 2nd ed., Cambridge University Press, Cambridge (1992).

[78] R. D. Shannon, *Acta Cryst.* **A32**, 751 (1976).

[79] R. D. Shannon and C.T. Prewitt, *Acta Cryst.* **B25**, 925 (1969).

[80] R. D. Shannon and C.T. Prewitt, *Acta Cryst.* **B26**, 1046 (1970).

[81] J.E. Huheey, E.A. Keiter and R.L. Keiter, Inorganic Chemistry: Principles of Structure and Reactivity, 4th edition, Harper Collins, New York, (1993).

[82] A. Bondi *J. Phys. Chem.* **68**, 441 (1964).

Chapter 10

Distance dependent polarization damping in halide-water dimers

Halide hydration, an old topic in chemical physics, has regained experimental and theoretical interest. Recently, ultrafast spectroscopy has allowed to directly probe the dynamics of the solvation shell in the bulk [1], offering a potential tool for the study of shell exchange [2]. It is the behaviour at the air-water interface, though, that has been the focus of more intense research within the last decade. The initial theoretical [3] and experimental [4] hints of an enhanced anion concentration at the surface, have been recently confirmed experimentally both for halides [5] and for a molecular anion [6]. This finding contradicts the accepted picture for over a century (in which anions would prefer interior solvation) and has far reaching implications for atmospheric chemistry [7, 8].

Surface solvation seems to be particularly sensitive to the different types of interactions. Polarization forces are considered the direct cause for the emergence of surface states [9, 10], and indeed polarization has also been suggested to be relevant for bulk hydration [11]. This crucial role of polarization was already

highlighted in the initial work by Perera and Berkowitz [3], and confirmed by a number of simulations (see the review by Jungwirth and Tobias [9] and references within), although it has also been questioned from different angles [12–14].

The evidence for the role of polarization forces stems from classical molecular dynamics (MD) simulations, as in *ab initio* MD (which also predicts the propensity for the interface [9]) decomposition of the various contributions in order to judge the importance of each type of force is not completely straightforward. It is interesting to note that in almost all classical simulations to date polarization has been treated in the same way: the point dipole model of polarization [15] is applied without further refinements [16]. In this model, point dipoles are located on the ion and on one or several sites within the molecule. As it is known that classical simulations can be sensitive to the force field parametrization [5], a considerable effort is currently directed towards the accurate *ab initio* calculation of polarizability (the single adjustable parameter) in the liquid phase, starting by that of the water molecule [19] and continued with those for halides in water [20, 21].

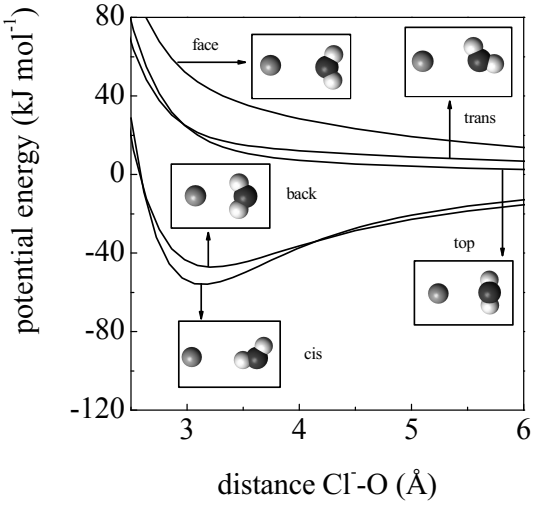

Figure 10.1. *Ab initio* potential energy curves for Cl^--H_2O.

Remarkably, the point dipole model itself has not been questioned, albeit its limitations are known for the fitting of gas phase molecular polarizabilities [15, 22] and for the simulation of crystal and molten salts [23]. In both cases a divergent behaviour at short distances is at the root of the problems that arise. Indeed, the very use of a point dipole model for condensed phase, where direct contact between neighbours is so important, seems doubtful as it is an approximation valid for long distances. In this connection calculations that aim to estimate polarizability in condensed phase may not be answering the real question, as what they are indeed optimizing is the response (of the ion surrounded by a set of solvent molecules) to an homogeneous external field, while it is the response

to the field originated by first shell neighbours that should be of concern.

The tenet of this work is that the failings of the current polarization models at short separations may have been overlooked, with the potential impact that this might have on the contribution of polarization. We adopt a perspective in which, also relying on *ab initio* calculations, special attention is paid to the behaviour at close ion-molecule distances. The induced dipole moment is computed for varying anion-molecule distances (for five molecular orientations), and the results are compared with the predictions of the point dipole model. This program has already been carried out for a molecule close to a positive point charge [18] and for a molecule close to a cation [24].

10.1 Computational Details

Different configurations were considered for the ion-molecule system (see figure 10.1), and for each arrangement the distance was varied in an interval of $\sim$ 5 Å. All quantum chemical calculations were performed with the commercial package Gaussian 03. The B3LYP/aug-cc-pvtz model chemistry was used for all atoms but Iodide, for which the aug-cc-pvtz_pp basis set was required. For the most probable configuration (*cis* and *back*, see below) coupled cluster (CCSD) calculations with the same basis set have also been performed, although only for five points due to the high computational cost (it is found that B3LYP slightly overestimate CCSD calculations, the largest difference being $\sim$ 4%). The total dipole moment of the ion-molecule dimer has been defined taking the position of the ion as the origin of the reference system.

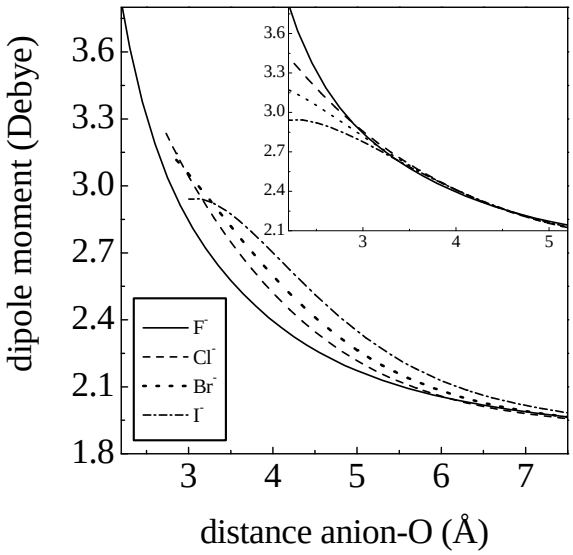

Figure 10.2. *Ab initio* dipole moment profiles for the *cis* configuration. In the inset the same curves are shifted to obtain the maximum overlap.

10.2 Results and Discussion

Figure 10.1 displays the potential energy profiles for each Cl^--water configuration. The *cis* configuration (with the characteristic linear hydrogen bond) is the most probable, followed by the *back* orientation. Similar features are found for the other halides, with the most probable stable configuration occurring at larger distances for increasing ionic radius. In this connection, in the study of the dipole moment that follows, the closest distance for each configuration was chosen where the potential energy was ≈ 25 kJ mol^{-1} ($\approx 10k_BT$ at standard temperature) above the potential energy minimum. For Br^- this definition yields 2.8 Å, which matches that found in *ab initio* MD simulations of Br^- in liquid water [11].

	$a_{\mathrm{Ion-M}}$	$b_{\mathrm{Ion-M}}$	$a_{\mathrm{Ion-H}}$	$b_{\mathrm{Ion-H}}$
F^-	0.0	30.0	1.75	0.0
Cl^-	0.0	7.38	2.14	0.0
Br^-	0.0	7.05	2.29	0.0
I^-	0.0	5.79	2.41	0.0

Table 10.1. Parameters for the anion-water interaction using the gaussian Thole damping (Eqs. 10.5 and 10.6).

Figure 10.2 displays the dipole moment profiles for the *cis* configuration (results for the *back* configuration follow a similar pattern). Contrary to what might have been expected, considering the rapidly growing anion polarizability along the halide series, the differences are rather small and seem to be due to the slight increase of ionic radius. This point is highlighted in the inset of Figure 10.2, in which the same profiles have been shifted along the radial coordinate until the maximum overlap is obtained. All the curves are rather similar and show that the maximum induced dipole moment follows a trend opposite to what might be expected, decreasing along the F^-, Cl^-, Br^-, I^- series. These features cast some doubts on the notion that the propensity for surface states is proportional to anion polarizability, and seems to suggest that it is the increasing radius which might be a more relevant factor. Finally, it should be noted that this polarization damping is nonlinear, a feature particularly clear for iodide, for which a turnover exists.

We now turn to the comparison with the phenomenological point dipole method, in which polarizabilities (α_i) are associated to one or more sites [15]. The total electric field acting on each site is produced by the external partial charges ($\vec{E}^o$) and by both the intramolecular and external induced dipole moments

$$\vec{E}_i = \vec{E}_i^o + \sum_{j \neq i} T_{ij} \cdot \vec{p}_i, \tag{10.1}$$

where T_{ij} denotes the dipole field tensor. The induced point dipole on site i is obtained from the total field according to

$$\vec{\mu}_i = \alpha_i \vec{E}_i. \tag{10.2}$$

Thole proposed to address the divergences that appear, when this method is applied to intramolecular interactions, by using charge distributions instead of point charges [22]. Eqs. 10.1 and 10.2 still hold, but the contributions to the electric field from a fixed charge and/or point dipole are damped by functions $f_1(r)$ and $f_2(r)$

$$\vec{E^o} = f_1(r) \cdot q \frac{\vec{r}}{r^3} \tag{10.3}$$

$$T = f_2(r) \cdot 3 \frac{\vec{r}\vec{r}}{r^5} - f_1(r) \cdot \frac{I}{r^3}. \tag{10.4}$$

The damping depends on the functional forms assumed for the charge distributions. While the original distributions proposed by Thole can be reparameterized with acceptable results for cations, in the present case it has been necessary to recourse to gaussian distribution functions [24], for which

$$f_1(r) = \operatorname{erf}\left(\frac{r}{a}\right) - \frac{2}{\sqrt{\pi}} \left(\frac{r}{a}\right) e^{-(\frac{r}{a})^2} \tag{10.5}$$

$$f_2(r) = \operatorname{erf}\left(\frac{r}{b}\right) - \frac{2}{\sqrt{\pi}} \left(\frac{r}{b}\right) e^{-(\frac{r}{b})^2} \left[1 + \frac{2}{3}\left(\frac{r}{b}\right)\right], \tag{10.6}$$

where a and b are adjustable parameters (see table 10.1) dependent on each ion-molecular site pair (the single point dipole polarizable water model -PDM- of Alfredsson et al. [18, 24, 25] was used).

Figure 10.3 displays the results for Cl^- in the *cis* configuration, again representative of those for the other halides and molecular orientations. Two *ab initio* sets of results are shown (the points correspond to the CCSD computation and represent the highest level currently reported for halides). We notice first the strong deviation between the point dipole method prediction (using the theoretical gas phase polarizability [20] of 5.5 $Å^3$) and the *ab initio* results. A quantitative measure of this deviation is the value at contact, which is ≈5 D according to the point dipole model in front of ≈3 D from the *ab initio* calculations. The deviation takes place over a range that corresponds to the full first shell hydration region as marked by the vertical dotted line (located at the first minimum of the liquid

phase chlorine-oxygen radial distribution function), and highlights the potential relevance of including damping in MD simulations. As previously stated, a lower value of the anion polarizability is currently recommended, with the best estimate being 4.0 Å^3 [20]. As shown in Fig. 10.3 with this value the divergence at short distances is cured to some extend, but still results in a substantial overestimation. In contrast, the curve obtained with the damped point dipole method satisfactorily reproduces the *ab initio* curves.

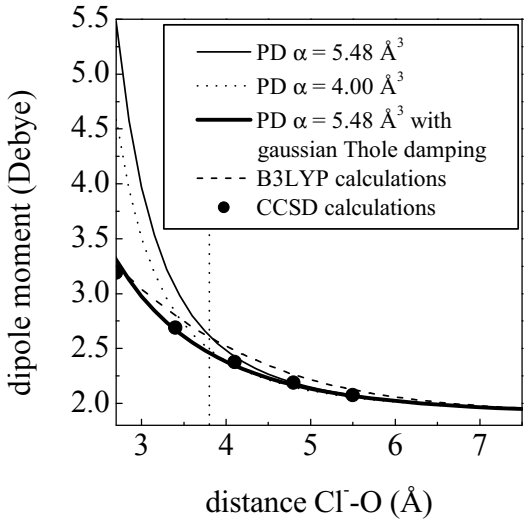

Figure 10.3. Dipole moment for the *cis* configuration of the Cl^--H_2O dimer. Results from *ab initio* and point dipoles (PD) calculations. Vertical dotted line marks the limit of the first solvation shell.

The situation is rather similar for all halides, as displayed in figure 10.4. The prediction with the point dipole method, with the theoretical gas phase polarizabilities [26], is always substantially higher than the one obtained from a first principles calculation (for distances corresponding to the first shell). The damped version proposed here is in all cases rather satisfactory and, although only the results for the *cis* configuration are shown, those for the *back* configuration show the same level of agreement (the same is true for the energetically unfavourable *top*, *trans* and *face* configurations). Finally, the substantial damping that occurs for all cases is consistent by the observation made for clusters [27] according to which classical polarizable force fields (employing the point dipole method) are unable to reproduce the structures found in *ab initio* calculations. Indeed, this is only achieved [27] at the cost of unphysical reductions of ionic polarizabilities (for instance a value of 2 Å^3 is required for Cl^-). The present work demonstrates that one can keep the correct behaviour at long distances, while at the same time the behaviour at short distances is substantially damped, in line with these previous findings.

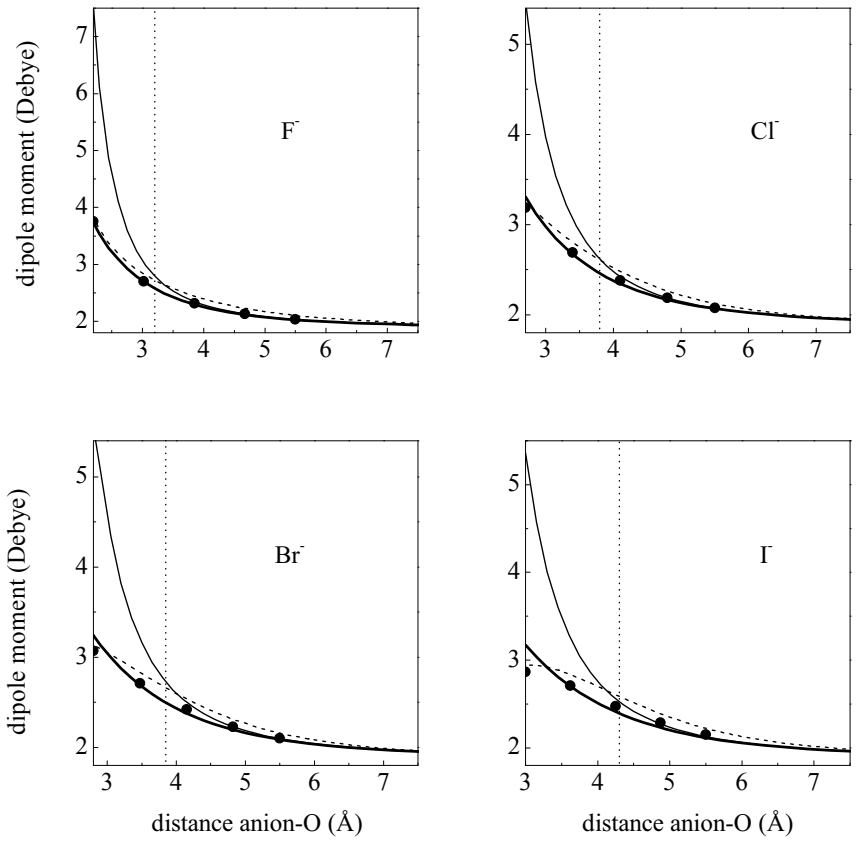

Figure 10.4. Results for all anions in the *cis* configuration (same legend as in figure 10.3).

10.3 Conclusions

It is interesting to note that we are not aware of any work in which damping has been considered, despite of the vast literature on classical simulations of ionic solutions. This might be of special interest in order to ascertain the precise role of polarization in the emergence of surface states for halides in water. There are some additional points to consider. First, the present proposal is computationally convenient as the modifications required are minimal (Eqs. 10.3, 10.4, 10.5, 10.6), and the computational overload negligible, for codes that already include the point dipole method. It should be noted, in addition, that these modifications only affect the polarization part, and therefore are compatible with any force field. A third point, which we consider capital, is that only the short range part is affected, while the polarizability at long distances is that of the gas phase. So

far, the changes suggested in the literature in order to include the solvent effect consist in a scaling of the polarizability, which is usually diminished from its gas phase value. An important drawback of this approach, besides the fact that it does not solve satisfactorily the short range problems as demonstrated above, is that the force field is no longer transfereable. This strongly contradicts the notion according to which the inclusion of polarization is required in order to obtain transfereable force fields.

Finally, the present results might have more general implications in connection with the theory of polarization in condensed phase. The neglect of short range damping in MD is a reflection of the standard theoretical approach, where each atom/molecule is characterised by a single dipolar polarizability [28]. It seems desirable that the theoretical description would explicitly consider short range damping, what might result in a reassesment of the polarizabilities inferred from experiment. This would resemble somewhat the spirit in which environment dependent polarizabilities are used to model ionic crystals [29].

References

[1] M.F. Kropman and H.J. Bakker *Science* **291**, 2118 (2001); M.F. Kropman, H.K. Nienhuys, and H.J. Bakker *Phys. Rev. Lett.* **88**, 077601 (2002).

[2] B. Nigro, R. Rey, and J.T. Hynes *J. Phys. Chem. A* (submitted).

[3] L. Perera and M.L. Berkowitz *J. Chem. Phys.* **95**, 1954 (1991).

[4] J.H. Hu, Q. Shi, P. Davidovits, D.R. Worsnop, M.S. Zahniser, C.E. Kolb *J. Phys. Chem.* **99**, 8768 (1995).

[5] S. Ghosal, J.C. Hemminger, H. Bluhm, B.S. Mun, E.L.D. Hebesbreit, G. Ketterler, D.F. Ogletree, F.G: Requejo, and M. Salmeron *Science* **307**, 563 (2005).

[6] P.B. Petersen and R.J. Saykally *Chem. Phys. Lett.* **397**, 51 (2004).

[7] E.M. Knipping, M.J. Lakin, K.L. Foster, P. Jungwirth, D.J. Tobias, R.B. Gerber, D. Dabdub, and B.J. Finlayson-Pitts *Science* **288**, 301 (2000).

[8] A. Laskin, D.J. Gaspar, W. Wang, S.W. Hunt, J.P. Cowin, S.D. Colson, and B.J. Finlayson-Pitts *Science* **301**, 340 (2003).

[9] P. Jungwirth and D.J. Tobias *J. Phys. Chem. B* **106**, 6361 (2002).

[10] B.C. Garrett *Science* **303**, 1146 (2004).

[11] S. Raugei and M.L. Klein *J. Chem. Phys.* **116**, 196 (2002).

[12] W.L. Jorgensen and D.L. Severance *J. Chem. Phys.* **99**, 4233 (1993).

[13] D. Marx *Science* **303**, 634 (2004).

[14] D.H. Herce, L. Perera, T.A. Darden, and C. Sagui *J. Chem. Phys.* **122**, 024513 (2005).

[15] J. Applequist, J.R. Carl and K.K. Fung *J. Am. Chem. Soc.* **94**, 2952 (1972).

[16] Although different implementations of polarization are possible, as in Ref. [17], they all share the same basic characteristics [18].

[17] S.J. Stuart and B.J. Berne *J. Phys. Chem.* **100**, 11934 (1996).

[18] M. Masia, M. Probst and R. Rey *J. Chem. Phys.* **121**, 7362 (2004); *Comp. Phys. Comm.* **169**, 331 (2005).

[19] A. Morita and S. Kato *J. Chem. Phys.* **110**, 11987 (1999); A. Morita *J. Comp. Chem.* **23**, 1466 (2002).

[20] P. Jungwirth and D.J. Tobias *J. Phys. Chem. A* **106**, 379 (2002).

[21] L. Frediani, B. Menucci, and R. Cammi *J. Phys. Chem. B* **108**, 13796 (2004).

[22] B.T. Thole *Chem. Phys.* **59**, 341 (1981).

[23] M. Wilson and P. A. Madden *J. Phys. Cond. Matter* **5**, 2687 (1993).

[24] M. Masia, M. Probst, and R. Rey *J. Chem. Phys.* (in press).

[25] M. Alfredsson, J. P. Brodholt, K. Hermansson, and R. Vallauri *Mol. Phys.* **94**, 873 (1998).

[26] C. Hättig and B. A. Heß *J. Chem. Phys.* **108**, 3863 (1998).

[27] L. X. Dang and D. E. Smith *J. Chem. Phys.* **99**, 6950 (1993); L.X. Dang *J. Chem. Phys.* **110**, 1526 (1999).

[28] C. J. F. Böttcher, Theory of Electric Polarization, Elsevier, Amsterdam (1973).

[29] A. Aguado and P. A. Madden *Phys Rev. B.* **70**, 245103 (2004).

Part V

Conclusions

Detailed conclusions for each subject of study have been given in the respective chapters. In this part, overall concluding remarks and perspectives are given, following the topics division of the thesis.

Solvation and Ionic Mobility

1. The main features of water exchange around the lithium ion are largely independent of the thermodynamic state both in liquid and supercritical water.

2. At short times, the mean square displacement of first solvation shell molecules results from ion translation, plus rotation around the ion, while at longer times, after rotational correlation is lost, both MSD differ by a constant.

3. For the cases studied, the mobility of the ion is higher during solvent exchange, irrespective of the exchange mechanism.

4. Analytic probability distributions have been derived for the stereochemistry of the exchange, which relate the probabilities of entrance/exit with the instantaneous ion velocity.

Perspectives

- Since for multiply charged ions the exchange times are very high at ambient conditions, the study of their dynamics in supercritical water might provide clues on the exchange behaviour, given the independence on thermodynamic conditions found for Li^+.

- Given the strong variation in solvent polarity within the supercritical regime, the above conclusions should be tested with, e.g., the polarizable model developed here.

- The rotational motion of the ion first shell complex suggests that it might be of interest to study the internal dynamics, and how it is affected when an exchange occurs.

Plasticizers

1. The structural properties at gas and liquid phases of two plasticizers of high technological interest (EC and GBL) have been studied. The molecules show a barrier for the internal isomerization of a non planar structure, which remains substantially unaltered in the bulk liquid.

2. A new approach for the develpment of tailored intramolecular force fields for small/medium sized molecules has been introduced. It has been implemented with satisfactory results.

3. A new vibrational mode assignment has been done for EC and GBL, which takes into account the degree of symmetry found.

4. The lithium ion is coordinated by 4 molecules through the carbonyl oxygen; the ligand structure is affected by coordination, mainly in the C=O bond lenght, which is sligthly stretched.

5. The effect of lithium ion coordination on the vibrational shifts has been studied. Ligands show substantial shifts in several vibrational modes (particularly the ones related to the esteric moiety), which compare satisfactorily with experiments.

Perspectives

- The properties of the lithium ion in EC/GBL mixtures (and eventually in a polymer matrix) should be studied, as this environment constitutes the core of modern batteries.

- The study, both theoretical and experimental, of the induced shifts for different cations (Li^+, Mg^{2+} etc.) might shed some light on the information contained in the carbonyl Fermi doublet.

- The limits of the technique developed for force field parametrization should be probed by applying it to smaller molecules, and solving the nuclear motion with quantum mechanical methods.

Polarization

1. An approach, based on ab initio results, has been developed to check the performance of phenomenological polarization methods. It focuses on the electrostatic part instead of on the full potental energy surface.

2. Analytic formulas have been derived for the molecular polarizability tensor for both water and carbon tetrachloride.

3. New polarizable models have been developed for water and carbon tetrachloride, which reproduce the behaviour of charge-molecule dimers.

4. In contrast to the models usually employed in the literature, it has been shown that due to orbital overlap effects, a polarization damping correction is required at short distances.

5. Short range polarization is satisfactorily reproduced if the Thole damping method is used.

6. The point dipole method with Thole damping shows the highest flexibility, and accurate parameter sets have been developed for all ion-molecule dimers studied.

Perspectives

- The same sort of study should be extended to water-water dimers in order to obtain a complete set of parameters for aqueous electrolyte solutions.

- To test this set, the results for clusters of molecules should be equally compared with ab initio calculations.

- The work done constitutes a starting point for the development of a new force field where dipolar interactions are properly taken into account.

- The present approach might be relevant for the interpretation of surface states for halides in water, a point that should be tested once a complete force field is developed.